Interaction of Metal-Based Nanoparticles with Proteins: Relation to Structure, Function and Amyloid Forming Propensity of Lysozyme and α-Lactalbumin

Dissertation submitted in partial fulfillment

of the requirements of the degree of

Doctor of Philosophy

in
Biotechnology and Medical Engineering

by

Deependra Kumar Ban

(Roll Number: 510BM112)

based on research carried out

under the supervision of

Prof. Subhankar Paul

and

Prof. Swadesh Kumar Pratihar

December 2016

Department of Biotechnology and Medical Engineering
National Institute of Technology Rourkela

Department of Biotechnology and Medical Engineering

National Institute of Technology Rourkela

Certificate of Examination

Roll Number: 510BM112

Name: *Deependra Kumar Ban*

Title of Dissertation: *Interaction of metal-based nanoparticles with proteins: Relation to structure, function and amyloid forming propensity of lysozyme and α-lactalbumin.*

We the below signed, after checking the dissertation mentioned above and the official record book (s) of the student, hereby state our approval of the dissertation submitted in partial fulfillment of the requirements of the degree of Doctor of Philosophy in Department of Biotechnology and Medical Engineering at National Institute of Technology Rourkela. We are satisfied with the volume, quality, correctness, and originality of the work.

Swadesh Kumar Pratihar
Co-Supervisor

Subhankar Paul
Principal Supervisor

Amit Biswas
Member, DSC

Raj Kishore Patel
Member, DSC

K. C. Biswal
Member, DSC

External examiner

Krishna Pramanik
Chairperson, DSC

Mukesh Gupta
Head of the Department

Department of Biotechnology and Medical Engineering
National Institute of Technology Rourkela

Prof. Subhankar Paul
Associate Professor, Biotechnology and Medical Engineering Department

Prof. Swadesh Kumar Pratihar
Associate Professor, Ceramic Engineering Department

December 2016

Supervisors' Certificate

This is to certify that the work presented in the dissertation entitled "*Interaction of metal-based nanoparticles with proteins: Relation to structure, function and amyloid forming propensity of lysozyme and α-lactalbumin*" submitted by *Deependra Kumar Ban,* Roll Number 510BM112 is record of original research carried out by him under our supervision and guidance in partial fulfillment of the requirement for the degree of *Doctor of Philosophy in Biotechnology and Medical Engineering.* Neither this dissertation nor any part of it has been submitted earlier for any degree or diploma to any institute or university in India or abroad

.

Swadesh Kumar Pratihar
Co-Supervisor

Subhankar Paul
Principal Supervisor

Declaration of Originality

I, Deependra Kumar Ban, Roll Number 510BM112 hereby declare that this dissertation entitled *Interaction of metal-based nanoparticles with proteins: Relation to structure, function and amyloid forming propensity of lysozyme and α-lactalbumin* presents my original work carried out as a Doctoral student of NIT Rourkela and, to the best of my knowledge, contains no material previously published or written by another person, nor any material presented by me for the award of any degree or diploma of NIT Rourkela or any other institution. Any contribution made to this research by others, with whom I have worked at NIT Rourkela or elsewhere, is explicitly acknowledged under the sections "Reference." I have also submitted my original research records to the scrutiny committee for evaluation of my dissertation.

I am fully aware that in the case of any non-compliance detected in future, the Senate of NIT Rourkela may withdraw the degree awarded to me based on the present dissertation.

Deependra Kumar Ban
NIT Rourkela December 2016

ACKNOWLEDGEMENT

This research was supported by the Department of Biotechnology and Medical Engineering, National Institute of Technology, Rourkela, India. During the last five years, I have gained one of the most valuable experiences of my life. At this juncture, I would like to express my appreciation to one and all who have contributed to successfully complete the work. I owe my sincere gratitude to my supervisor Prof. Subhankar Paul, for his continuous encouragement of my research instincts and for allowing me to grow as a researcher. His advice on both research as well as on my career has been priceless. I also like owe sincere gratitude to my Co-supervisor Prof. Swadesh Kumar Pratihar from Department of Ceramic Engineering for his guidance and providing priceless suggestions during the whole tenure of my Ph.D.

My special thanks are due to Prof. Animesh Biswas, Director, National Institute of Technology, Rourkela for all the facilities provided to successfully complete this work.

I am also very thankful to all the members of my doctoral scrutiny committee Prof. R. K. Patel, Prof. K. C. Biswal, Prof. A. Biswas and Prof. K. Pramanik (chairperson, DSC) for their thoughtful suggestions, inspiration and continuous encouragement throughout the research work. I take this opportunity to thank Prof. M. K. Gupta (HOD, BM), all faculty members, and the supporting staff members of the Department of Biotechnology and Medical Engineering for their timely cooperation and support at various phases of experimental work.

I would like to extend special thanks to my dear friends Pratap S, Sailendra Kumar Mahanta, Subhadip Mukhopadhyay, Krishna Kumar Ramajyam, Dipto Sengupta, , Vidya Lata Koli, and all the previous members of the lab for their valuable suggestions and encouragement. I am also grateful to my beloved wife who had always been supportive through this venture.

I will be failing in my duty if I do not acknowledge the constant cooperation and support of my parents, sisters and elder brother who have always been a source of inspiration for me.

Above all, I would like to thanks the world research community whose research work inspired me. Finally, I want to devote my work to Almighty for his enormous blessings and guiding me in the right direction in life.

ABSTRACT

Metal nanoparticles (NPs) such as gold (AuNP), silver (AgNP), and zinc oxide (ZnONP) demonstrate variety of applications including drug delivery, imaging, nanomedicine, and sensing. However, many of their applications involve biological systems, which might trigger their interaction with various biomolecules such as proteins. Proteins are highly sensitive to various stresses and ligand interaction due to the intimate correlation of their structure with biological function. Moreover, it is also a well-known fact that protein misfolding and aggregation process is the prime cause of a number of neurodegenerative disorders like Alzheimer's disease, Parkinson disease, Prion disease, etc. The interaction of NP with the proteins can cause the change of structure as well as the function of proteins and can generate a new identity such as 'nanoparticle-protein' complex.

Here, in our present study, we investigated the interaction of two small homologous proteins: bovine α-lactalbumin (BLA) and hen egg white lysozyme (HEWL) with three different nanoparticles (AuNP, AgNP, ZnONP) in vitro. The structure, function, stability and amyloid forming propensity of the proteins were studied during the interaction with three different NPs using various spectroscopic and microscopic techniques. We synthesized NPs by chemical as well as semi-green methods using non-toxic materials such as starch, PEG, and NaOH with precursor salts with a size of below 20 nm. Moreover, we synthesized the self-assembly of ZnONP of an average size of 163 nm. The NPs were further characterized using field emission scanning electron microscopy (FESEM), transmission electron microscopy (TEM), X-ray diffraction (XRD) as well as dynamic light scattering (DLS) zeta sizer for the analysis of size and shape and stability of NP.

The conformational change of proteins, due to the interaction of NP with proteins was analyzed by fluorescence as well as circular dichroism (CD) spectroscopy. The fluorescence spectroscopic analysis showed quenching of Trp fluorescence as well as a shift in emission peak. This fact indirectly confirmed the alteration of protein structure to a different extent. The CD spectroscopy of BLA and HEWL revealed a drastic alteration of β-sheet as well as α-helix contents substantially during their interaction with NP. Further, DLS and FESEM analysis showed that BLA and HEWL both formed multilayer protein corona over NPs. The stability of both the proteins was analyzed under thermal, strong denaturant (GdnHCl) and Proteinase K stress. Protein in conjugation with AuNP$_{ST}$, AgNP$_{ST}$ and ZnONP$_{ST}$ showed alteration in susceptibility to Proteinase K, and stability in thermal as well as in presence of GdnHCl. This study proved that NP-protein interaction not only alters the structure and function of protein but also can alter its stability under stress condition.

Further, we investigated the effect of three NPs in the amyloid growth of HEWL. We found that all three starch capped NP demonstrated dose-dependent inhibition of fibrillar amyloid formation. Further, the effect of capping agent on HEWL amyloid growth was also observed and revealed that PEGylation of AuNP and AgNP increased their amyloid inhibition potential, contrary to uncapped, and assembly of ZnONP. Moreover, we observed that all NPs prolonged the nucleation and shorten elongation phase of amyloid growth with reduction of amyloid amount. Further, we also evaluated the cellular toxicity of various amyloid samples in vitro. While amyloid demonstrated substantial cellular toxicity in two different cell lines, amyloid prepared in the presence of all three NP showed much reduced cellular toxicity in both mouse carcinoma (N2a) as well as human keratinocytes (HaCaT) cells. We also observed that inhibition of amyloid formation was effective when NP was administered during the nucleation phase and less effective duirng elongation as well as maturation phase.

Therefore, from our study, we concluded that suitable tuning of core nanomaterial properties and surface capping could altered its interaction with proteins significantly, thus alter the structural and functional alteration of those proteins. Moreover, they also could inhibit amyloid forming inclination of proteins and thus might help to open a new avenue in the therapy in various neurodegenerative disorders.

***KEYWORDS*:** Lysozyme; bovine α-lactalbumin; conformational change; gold nanoparticles; silver nanoparticles; zinc oxide nanoparticles; amyloid; thioflavin-T; cellular toxicity.

Contents

LIST OF FIGURE

LIST OF TABLE

LIST OF ABBREVIATIONS

AFM	Atomic force microscopy
ANS	8-anilinonapthalene-1-sulfonic acid
$AuNP_{ST}$	starch capped gold nanoparticle
$AuNP_{PEG}$	polyethylene glycol capped gold nanoparticle
$AgNP_{ST}$	starch capped gold nanoparticle
$AgNP_{PEG}$	polyethylene glycol capped gold nanoparticle
BLA	Bovine α-lactalbumin
CD	Circular dichroism
DLS	Dynamic light scattering
DMEM	Dulbecco's Minimum Essential Medium
FESEM	Field emission scanning electron microscopy
GdnHCl	Guanidine hydrochloride
HEWL	Hen egg white lysozyme
NAC	N-acetylcysteine
BLA	bovine α-lactalbumin
PK	Proteinase K
PMSF	Phenylmethanesulfonyl fluoride
ROS	Reactive oxygen species
TEM	Transmission electron microscopy
ThT	Thioflavin-T
Trp	Tryptophan
Tyr	Tyrosine

XRD	X-ray Diffraction
$ZnONP_{uncap}$	uncapped capped zinc oxide nanoparticle
$ZnONP_{ST}$	starch capped zinc oxide nanoparticle
$ZnONP_{assmb}$	assembly of zinc oxide nanoparticle

CHAPTER 1

INTRODUCTION

Nanoparticles (NPs) attracted great interest in various research groups for exploring new biomedical, optical and electronic applications. The evolution of new properties at the nanoscale size and the increase in surface to volume ratio to make number of atoms available per unit surface for the reaction. Moreover, the tuning of optical, magnetic, electrical, and chemical properties of NP can be achieved by controlling size, shape, and surface functionalization of nanomaterials. These physical and chemical properties of NP showed numerous biological and non-biological applications. Among the inorganic NP, gold, silver, and zinc oxide NP exhibited great potential in the area of imaging [1-5], sensing [4, 6-10], drug delivery [11-14], and pharmaceuticals [15-19]. Since, their applications involve biological systems consisting of cells, tissues, and bio-molecules; it readily triggers the interaction between NP with biomolecules such as proteins, nucleic acid (DNA and RNA), lipids, and carbohydrates. However, the fate of these biomolecules after interaction with NPs such as proteins is not yet clear.

It was already reported by various research groups that administration of NPs in the biological system causes the interaction of proteins with the surface of NPs and form protein corona (soft and hard) over NP surface [20-23]. Such interactions not only change the surface properties of NPs but can also change structure and function of proteins [23, 24]. It was also found that the effect of NPs on the biological system depends on material composition [25], size [26, 27], shape [28], surface functionality [29] and surface charge [30] of NPs. Moreover, during the use of NPs, various groups reported that the possible cause of side effect or toxicity produced in biological system is due to generation of reactive oxygen species (ROS) [31], release of active ions [32], and interaction with specific biomolecules [33], which collectively might alter the structure and function of biomolecules.

To the best of our knowledge, all previous studies related to NP and protein interactions did not address the detailed study of few aspects such as the stability and fate of the protein present in the NP-protein conjugate with altered structure and function under various stress conditions like high temperature, denaturant, proteinase-K, etc. Moreover, the interaction was not studied with various NPs with different capping agents like starch, etc. Moreover, the detailed study of protein interaction with NP in self-assembly state, which usually achieved novel properties, was also not studied.

Protein misfolding and aggregation process are few most important cellular phenomena that can change the structure and function of proteins and sometimes can cause a series of neurodegenerative disorders such as an Alzheimer's disease [34], Parkinson's disease [34, 35], Prion disease [36], etc. However, the role/effect of NPs on such aggregation or amyloid formation have not been studied in detail except few reports with some nanoparticles such as a copolymer, cerium oxide, quantum dots, carbon nanotubes, gold [37] and titanium dioxide [38], which enhanced the protein amyloid formation by reducing the nucleation phase of amyloids. In some other studies, functionalized gold nanoparticles [39-41] and iron oxide magnetic NP [42] showed inhibition of amyloid growth. Therefore, it was clear that the interaction of proteins with a nanomaterial could affect the amyloid formation and growth. From all the above reports, it was also concluded that the interaction of NP with proteins highly depends on its surface properties that further depends on the core material and its assembly, type of functional molecules present, its density [43], and type of proteins. However, it is important to analyze in detail on the effect of NP on the amyloid formation of proteins under varying core materials, doses, administration time, and surface capping of NPs.

To address all these above issues, we synthesized gold (Au), silver (Ag), and zinc oxide (ZnO) NPs by using starch, and PEG as reducing as well as capping agent and NaOH as reaction accelerator and modifier. To study the NP-protein interaction, bovine α-lactalbumin (BLA) and hen egg lysozyme (HEWL) were used as model proteins. The conformational changes of proteins due to the interaction with AuNP, AgNP, and ZnONP were analyzed by fluorescence and circular dichroism (CD) spectroscopy. The effect of NPs on unfolding of protein in the presence of guanidine hydrochloride (GdnHCl) and heat was analyzed. The stability of protein in NP-protein conjugate to proteinase-K was also analyzed. The effect of NP on protein amyloid growth was also analyzed under various conditions by thioflavin-T fluorescence assay and microscopic techniques such as AFM, FESEM, and TEM. Further, cellular toxicity of amyloid formed in the presence of different NPs was also analyzed in N2a (neuroblastoma cells of mice) and HaCaT cells (human keratinocytes) by MTT assay and compared. The mechanism of cellular toxicity was also studied and reported.

CHAPTER 2

LITERATURE REVIEW

2.1 Metal-based nanoparticles (NP) and their Applications

Noble metal nanoparticles created great interest in various areas of research due its optical [44], electronic [45], mechanical [46], cellular toxicity [47, 48]. Moreover, availability of simple synthesis method to tune the size and surface of NP make the metal based NP, a material of choice for various studies. Among these metal based NP such as gold (AuNP), silver (AgNP), zinc oxide (ZnONP) were few well studied NP for their various applications.

2.1.1 Gold nanoparticle

Due to excellent surface plasmon resonance and photoluminescence properties, gold nanoparticles (AuNP) has become the material of choice for various applications such as nanosensors [49], electronic devices [2], nanomedicine, drug delivery [4], and photothermal therapy. To synthesize such nanoparticles for different applications, a number of methods like chemical [50-52], physical, and green/ biomolecule based route [53-60] can be used to produce desired shape, size, surface functionality. Cui et al. [61] used AuNP and carbon nanosphere-based hybrid material for electrochemical immunoassay. Phadtare et al. [62] used AuNP shells with polyurethane microsphere core as an enzyme immobilization template. Due to non-toxic nature of AuNP, it is used for drug and gene delivery for treatment of various diseases [13]. Liu et al. [63] developed an one-step immunoassay for detection of cancer biomarker using AuNP. Kim et al. [64] synthesized the drug loaded aptamer-AuNP conjugates that can be used for CT imaging and treatment of prostate cancer. Due to excellent optical and electrical properties, AuNP can be used for photothermal therapy of cancer [65].

Lee et al. [66] reported the application of AuNP-DNA-based reversible network as a diagnosis tool that specifically attached to cell surface marker. Yehezkeli et al. [67] developed an electrode for glucose sensing and biofuel cell application. They engineered the AuNP surface using flavin-dependent glucose dehydrogenase for application. Guerrero et al. [68]

synthesized the AuNP labeled with ^{18}F and conjugated with peptide for in vivo biomedical application. Yang et al. [69] used AuNP for label-free DNA detection by enhancing the charge transfer by it. Almeida et al. [70] used AuNP for delivery of peptide vaccine and observed the anti-tumor immune response in tumor models such as prophylactic and therapeutic tumor. Sinha et al. [71] used AuNP for enhancing the radiation-based damage to tumor cells in brachytherapy and observed the damage to tumor cells is increased due to AuNP administration.

2.1.2 Silver nanoparticles

Silver nanoparticle (AgNP) showed great potential as a broad spectrum antimicrobial agent [72-74]. Moreover, its optical properties also attracted the attention for various application such as SPR based sensor [75, 76], biomedical devices/ products [77-80], consumer products [81-83], and as an antimicrobial agent [84-87]. It was found that its properties can be manipulated by varying size [88], shape [89], surface properties [90, 91]. Moreover, the synthesis of AgNP can be performed by chemical, green and physical method for various applications such as fabrication of various biomedical and sensing devices [92]. Tai et al. [93] used AgNP for molecular imaging of cancer cells by generation of enhanced third harmonic plasmon resonance. AgNP has a very excellent antimicrobial property, which can be used to kill the many antibiotic resistance bacteria and fungus [73, 86]. Due to their excellent antimicrobial properties, AgNP can be used in developing polymeric, ceramic, and hybrid nanoparticle such as graphene oxide-AgNP based filter, which can be used for water purification [94-96]. Hence, AgNP has possible applications in pharmaceutical industry, water purification industry, and use in fabrication of various biomedical devices make a valuable NP for study.

2.1.3 Zinc oxide nanoparticles

Due to the unique properties of ZnONP such as wide band gap (3.37 eV), exciton binding energy (60 meV), it has been utilized in various fields of research such as electronics [36], sensing [37] and medicine [38, 4]. Various scientific groups have already developed ZnO nanostructure by mechanical [39], chemical [40], and green [41] method for different applications. Moreover, the properties of nanoparticle also vary with their size, shape, and functionality. The various applications like solar cell, semiconductor based electronic devices and photocatalysis use larger particle assembly. Ansari et al. [97] used Concanavalin layered ZnONP for β-galactosidase immobilization and showed that immobilized enzyme showed more than 60% activity. Reddy et al. [98] observed that ZnONP showed toxicity against *E. coli*, *S. aureus,* and primary human cells. Vigneshwaran et al. [99] reported the synthesis of soluble starch capped ZnONP of more than 50 nm and showed the UV absorption potential of ZnONP when doped in cotton fibers. Moreover, ZnONP showed potential to selectively kill the cancer cells and can be used in drug delivery system [18]. Huang et al. [100] reported that ZnONP can be used as imaging tool during apoptosis process of cell. Yuan et al. [101] prepared the chitosan encapsulated ZnONP for drug delivery response in tumor cells while Nie et al. [102] used tetrapod shape nanosized ZnO for plasmid DNA delivery. Zhao et al. [103] developed enzyme biosensor by using ZnONP. Zhang et al. [104] reported that ZnO nanorods can be used for photodynamic therapy due to its excellent light absorption property.

Therefore, broad applications of AuNP, AgNP, and ZnONP and reported cellular toxicity against various cells make them a suitable candidate for NP and biomolecule interaction study and possible side effects for developing safe and efficient NP based devices and therapies.

2.2 Importance of structure, folding, and aggregation of proteins

The 3D conformation and function of proteins are highly correlated with each other. Moreover, correct folding of a protein is essential to get the native structure and function of the protein [105]. However, misfolding of proteins due to internal and external factors causes protein aggregation [106]. Protein misfolding that produces cross β-sheet secondary structure causes assembly and deposition known as amyloid protein and causes amyloid-related disease [107-111]. Therefore, understanding the protein structure, folding and aggregation process is very important to manipulate the protein structure and function as well as find therapeutic avenues in protein misfolding-related problem. However, study the protein structure using very large protein is very difficult due to multistep folding mechanism followed by larger protein and complex secondary and tertiary structure. Therefore, small globular proteins are suitable to understand the protein structure and folding mechanism before study such complex phenomenon with larger proteins.

Moreover, small proteins are ideal for the study of interfacial interaction, conformational changes, and folding study. Small proteins (<20 kDa) have a high surface to volume ratio that makes them highly reactive to environmental changes and interfacial interactions. Moreover, half of their surface may be covered by nonpolar side chains. Therefore, small protein such as α-lactalbumin, cytochrome-C, lysozyme can be selected as a model protein for the study of the interfacial phenomenon. Moreover, α-lactalbumin, lysozyme showed evolutionarily conserved sequences from prokaryotic to mammalian protein. Therefore, analyzing the effect of NP on these proteins from one organism can be used to predict the effect of tested NP on these proteins from other organism.

Bovine α-lactalbumin (BLA) and hen white egg lysozyme (HEWL) were used as model protein, since the beginning of protein structure, and folding studies [112-116]. Due to their small size, well-known secondary structure and simple folding pathway make both the proteins an ideal choice for selecting as a model protein for understanding the protein folding pathway. Moreover, HEWL was also used as model protein for the study of the mechanism of amyloid formation [117] and effect of various molecules on amyloid formations to analyze the amyloid inhibition potential of tested molecules [118].

Moreover, both proteins received utter importance in recent research due to their anti-cancerous properties shown by a specific conformational state of the protein [119-123]. Therefore, use of these proteins might help to understand the effect of NP on protein structure, function, and stability in different conditions but also might create an opportunity to design NP surface to obtain the desired manipulation of protein structure in *in vivo* conditions, which can be utilized for the treatment of various diseases.

2.3 Overview of nanoparticle-protein interaction

Nanotechnology attracted the attention of different branches of sciences and engineering such as biomedical [124, 125], electronics, mechanical [126] for the development of nanomaterial-based technologies. It involves fabrication of nanoparticles (NP) and exploration of their new physiochemical properties for various applications. Moreover, the primary interest of current research is focused on various biomedical applications of NP such as bioimaging [127], sensing [128], drug delivery [129, 130], medicine [131], etc. Due to the small size and unique physical and chemical properties, NP can interact with cellular machinary [132] and can reach to the brain by crossing blood brain barrier [133]. Furthermore, the large-scale application of NP in a different area of research and industry causes direct or indirect exposure of NP to the biological systems and ultimately to biological fluids [134] and cells by different pathways such as oral, transdermal, pulmonary and intravenous (Figure 2.1). Therefore, active surface and novel properties at nanoscale provide opportunity as well as challenges regarding the assessment of nanotoxicity and safety of nanomaterials, which can be used to develop effective and safe nanomaterials for biological application [135, 136].

Moreover, the introduction of NP in biological system encounters a great identity crisis created by the interaction of nanoparticles (NP) and biomolecules (e.g. proteins, nucleic acid, carbohydrates, lipid and other natural molecules), which determines the biological distribution, cellular response and function of NP [22, 137-139]. Interestingly, NP interaction with biomolecules produces new responses, which is different from its bulk counterpart in similar conditions. Therefore, the new identity of NP depends on the outcome of interfacial interaction and biomolecular corona (e.g. protein) over NP surface. Hence, understanding of bio-nano interface become very important for biological applications of NP [140, 141]. Among biomolecular interaction study, protein interaction with NP surfaces created great interest due to the important role played by proteins in maintaining biological system. The study is more important due to the close correlation between protein structure and function and the active surface of NP might alter the structure and ultimately the function of proteins.

2.2.1 Effect of NP shape

The physiochemical properties of NP vary with variation in shape [44], which also determine the bio-nano interfacial response such as biomolecular interaction and protein corona formation over the surface, cellular uptake [142], and toxicity [88]. Therefore, NP with various shapes forms a different type of protein corona, which decides the biological identity of NP-protein complex and responsible for a cellular response. For example, variation in the shape of gold NP from spherical to rod changed the cellular uptake [143].

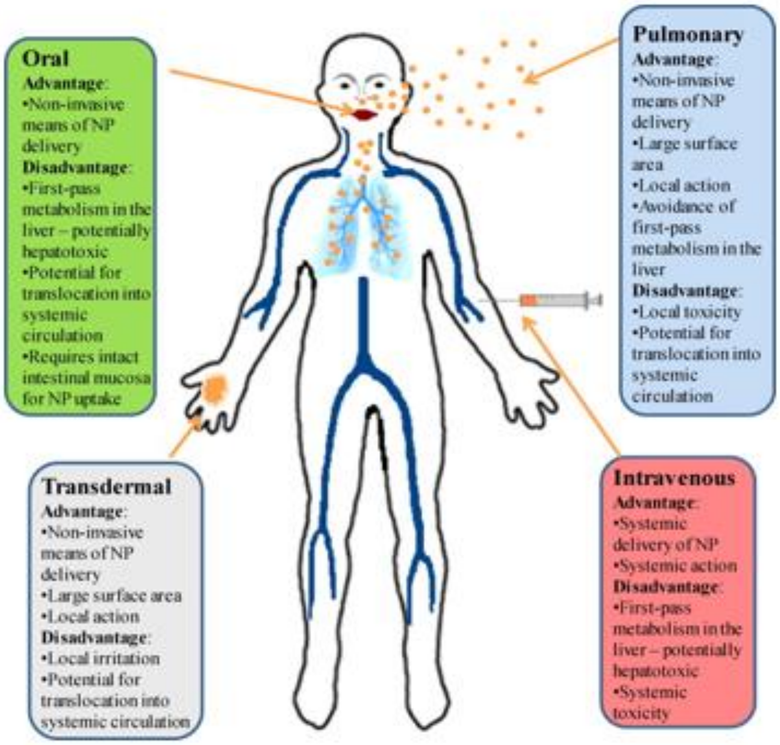

Figure 2.1 The advantage and disadvantage of nanoparticle administration were shown. (reproduced under the creative common licences) [144].

It was observed that cellular toxicity was also altered by variation in the shape of NP; for example, iron oxide nanorods showed higher toxicity than spherical particles [145]. Therefore, it is very important to analyze the effect of the different shape of NP on protein structure and function.

2.2.2 Effect of NP size:

The variation in size also changes the curvature of NP, which plays an important role in adsorption and conformational alteration in proteins. It was observed that various size of gold NP also determined the affinity and thickness of adsorbed protein on NP surface [146]. Moreover, some other reports showed that binding constant of protein to gold nanoparticles (AuNP) increased with increasing the size from 2-70 nm for Herceptin capped AuNP and 2-20 nm for citrate-capped AuNP. It was also reported that binding cooperativity of NP-protein interaction depends on the pair of NP and protein; for example human serum albumin (HSA), fibrinogen, histone, and γ-globulin proteins showed anticooperative interaction with AuNP while the contrary effect was observed with insulin. Another study with hydrophobic NP of different size showed that the amount of protein on NP surface depends on the size of NP [147]. It was observed that amount of surface coverage by protein is increased with increasing NP size while reducing the NP size from 200 to 70 nm also suppressed the protein adsorption. Klein et al. reported that reducing the curvature of NP also suppress the adsorption of certain proteins [139]. Hence, it is important to understand the effect of the different size of NP on the protein corona formation, structural as well as functional alteration.

2.2.3 Effect of NP synthetic identity:

The synthetic identity of NP plays an important role in cellular response and protein corona formation [148]. The reason is synthetic identity defined surface properties of NP and adsorbed ions and molecules on the surface. It includes the surface charge, surface smoothness/ roughness, hydrophilicity/ hydrophobicity, weak/ strong surface capping agent, surface functional groups, adsorbed ions or molecules from synthesis ingredient or by-product of synthesis. The surface charge of NP is an important factor in determining the composition of protein on NP surfaces. It was observed that some positively charged NP showed rapid removal from the excretory system due to the rapid interaction of opsonins with NP. Therefore, application of these NP is limited by its rapid removal in a biological system. There are high chances of absorption of reagents and by-product of synthesis on the NP surfaces. Even the use of various purification methods unable to completely remove the adsorbed molecules. Therefore, the biological response to these NP vary due to variation in chemicals used in the synthesis of NP and hence altered the outcome of same NP protein interaction and cellular response.

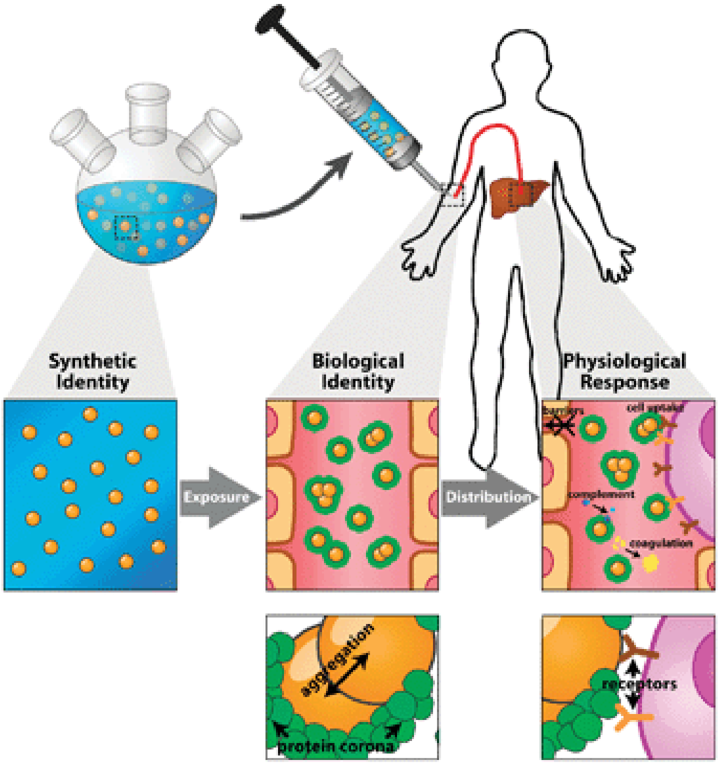

Figure 2.2 The relation between the different type of identity of NPs is shown. The synthetic identity includes structural and chemical identity, which link with the biological identity such as aggregation, interaction, and distribution of NP. The biological identity finally decides the physiological response of biological systems and biomolecules. (image is used under the copyright rule of RSC for the use of image in thesis) [149].

2.2.2 Effect of NP on protein aggregation and amyloid formation:

The deposition of the ordered cross β-sheet structure of protein causes Alzheimer's disease (AD), Parkinson's disease (PD), type-2 diabetes, Creutzfeldt-Jakob disease, and mad cow disease and symptoms such as inflammation [74]. The primary treatment method for these diseased conditions is inhibition and defibrillation of cross β-sheet assembly. Moreover, the available therapeutics such as short peptides and antibodies faces in vivo obstacle such as blood-brain barrier (BBB), complex synthesis process. The advent of NP-based therapeutics created new hope due to their small size and ability to cross BBB [75], the flexibility of designing NP surface [76-78].

Although NP has already been shown various kinds of surface reaction with biological systems, the effect of NP on amyloid growth have not been explored in detail. The highly active surface of nanomaterial and its unique physiochemical properties [62, 63] showed a new hope as well as a threat to the biological systems. Moreover, few in vitro studies demonstrated some NP such as a copolymer, cerium oxide, quantum dots, carbon nanotubes [66] and titanium dioxide [67] that enhanced the protein amyloid formation by reducing the nucleation phase of amyloids. In contrary, functionalized gold NP [68-70] and iron oxide, NP [71] demonstrated the inhibition of amyloid growth. Therefore, it was clear that interaction of proteins with a nanomaterial could affect the amyloid formation and growth. However, the toxicity and degradability of these NP in physiological condition have been a big concern.

Although consequences of the interaction of NP with proteins highly depends on its surface properties that further depends on the core material and its assembly, type of functional molecules present and its density [72]. It has already been established that intermediate state of amyloid fibrillation such as protofibrils is more toxic than their mature fibrils [73]. Therefore, it is very important to understand the effect of NP on a different state of amyloid growth. Moreover, biocompatibility and physiological stability of NPs is another issue. However, the use of non-biodegradable, self-assembly of inorganic NP could act as a new therapeutic agent by surface functionalization, variation in shape and size. Tuning surface and structure reduce the in vivo toxicity and enhance the target-specific interaction.

In this regards metal nanoparticle such as gold nanoparticle was used as a drug carrier [4], imaging [8], nano-sensing [12], and therapeutic agent [13], but existing report about its effect on the amyloid is controversial. It was reported that gold NP capped with citric acid inhibit the amyloid aggregation of bovine β-lactoglobulin [79], bovine insulin [80] but accelerate the growth of α-synuclein [81].

Moreover, bovine insulin fibrillation was inhibited by tryptophan and tyrosine capped AuNP and AgNP, while Aβ (1-42) fibrillation was inhibited by polymeric histidine, and Cys-PEP capped AuNP [82]. Further, some other studies reported that N-acetyl cysteine (NAC), and curcumin capped gold NP inhibit the amyloid growth [83]. Moreover, NAC [84], tyrosine, tryptophan, histidine [85] and curcumin [86] themselves showed inhibitory effect.

Table 2.1 The effect of different NP and their effect on amyloid fibrillation of different proteins.

Class of NPs	**NPs**	**Key findings**	**References**
Metal and Metal oxide NP	CdTe	N-acetyl cysteine-capped CdTe NP inhibit the Aβ(1-40) amyloid formation	[41]
	AuNP	Tryptophan and tyrosine capped NP inhibit the bovine insulin in vitro condition Histidine, polyacrylate capped AuNP inhibit Aβ(1-42) fibrillation	[40, 150]
	TiO_2	Enhance the Aβ amyloid growth	[38]
	ZrO_2	No effect on the Aβ	[38]
	CeO_2	Enhance the formation of amyloid by β2-microglobuline	[37]
	SiO_2	NO significant effect on fibril formation of Aβ	[38]
Carbon based NP	Fullerene	Inhibit the Aβ formation by interaction with hydrophobic region of protein	[151]
	C_{60} and C_{70}	No significant effect on the Aβ amyloid fibrillation	[38]
	Fluorinated carbon NP	Inhibit peptide fibrillation by enhancing α-helical content	[152]
Polymer NP	(NIPAM)/ (BAM) copolymer nanoparticle	Acceleration of β2-microglobulin amyloid formation by reducing nucleation time With Aβ and IAPP retard the amyloid growth by delaying nucleation	[37, 153]
	Amino-Modified Polystyrene NP	The NP showed a dual effect against Aβ. At low protein, to NP ratio amyloid growth increased by reducing lag phase time and at high ratio showed inhibition of amyloid formation	[154]
	Hydrophobic Dipeptide capped polyA-FF-ME	Slow down the transition of α-helix to β-sheet in $Aβ_{40}$ during amyloid growth	[155]

CHAPTER 3

OBJECTIVES AND SCOPE

The main aim of the current Ph.D. thesis was to study the effect of three metal-based nanoparticles; gold (AuNP) silver (AgNP) and zinc oxide (ZnONP) on the structure, function and amyloid growth of two small monomeric proteins upon their interaction. To achieve the aim following objectives were set:

1. Synthesis of gold, silver, and zinc oxide nanoparticles (NPs) by chemical as well as semi-green method, and their characterization with regard to their size, shape, and stability.
2. To study the formation and characterization of NP-protein conjugate in relation to the structure, function and the stability of the proteins under various stresses.
3. To study the role of nanoparticles on amyloid fibrillation process of hen egg white lysozyme under various condition.
4. To assess the cytotoxicity of amyloid prepared under various conditions and the mechanism of the cytotoxicity in two cell lines.

Scope of the work:

Nanoparticle (NP) interaction with proteins in a biological fluid is an unavoidable phenomenon. Moreover, the use of toxic chemicals in NP synthesis can act as a denaturant to many biomolecules including proteins, which makes this condition more severe. Hence, the focus has shifted to synthesize of biocompatible NPs using biomolecules as a capping agent. However, biomedical application of these NPs also requires detail characterization and understanding of their interaction with biomolecules such as proteins and subsequent possible side effects.

The current research work on the interaction of metal-based NPs (gold, silver, and zinc oxide) with model proteins (bovine α-lactalbumin, and hen egg white lysozyme) under different conditions has utter importance. In our work, we reported protein corona formation over NPs after their interaction. The structure, function, and stability of the protein during interaction (corona) might be changed, which could lead to substantial side effect to the biological system. Since metal nanoparticles are commonly used in various applications including biomedical areas, such kind of study must have utter importance. Therefore, understanding the characteristics of protein-NP interaction will be highly helpful to design and develop of suitable NPs that might cause the little or insignificant change to a protein during their interaction. Moreover, protein misfolding and aggregation process sometimes lead to form amyloid, which is indeed the prime cause of many neurodegenerations such as Alzheimer’s disease, Parkinson’s disease, Prion disease, etc. The interaction of NPs with proteins in relation to the amyloid formation propensity of the protein is also of huge curiosity. Here, we also studied the amyloid formation and growth under NP-rich environment to observe their effect on fiber formation, the outcome of which indeed might help to develop appropriate measure against multiple neurodegeneration.

Hence, in brief, understanding the role of NP on the structure, function, and stability of protein in solution can be used to design and develop a strategy for optimal use of NPs with least loss of protein’s inherent properties in various industrial applications. Moreover, the effect of metal-based NPs on the amyloid growth of proteins would provide an understanding of whether NPs based effective therapeutics strategy can be developed for various neurodegenerative disorders.

CHAPTER 4

SYNTHESIS OF GOLD, SILVER, AND ZINC OXIDE NANOPARTICLE AND CHARACTERIZATION

4.1 Materials and methods

4.1.1 Materials

$HAuCl_4.3H_2O$, $AgNO_3$, and $Zn(NO_3)_2.6H_2O$ were purchased from Sigma-Aldrich. NaOH, polyethylene glycol (PEG-400) and starch were purchased from Himedia, India and used without further purification. All the plastic wares were purchased from Tarson, India and glassware were purchased from Borosil, India. Before use, glass wares were cleaned using aquaregia and Milli-Q water. Milli-Q water was used throughout the study. The solution was filtered using membrane filter 0.2 μm (Millipore, India).

4.2 Synthesis of nanoparticles

4.2.1 Synthesis of gold nanoparticle

For the synthesis of AuNP, we prepared 1.0% (w/v) starch solution in Milli-Q water by heating in a microwave oven for 1 min. In the clear soluble starch solution, we added 1.0 mM $HAuCl_4.3H_2O$ and heated at 70 ^{0}C for 5.0 min with constant stirring. After heating, NaOH (6.0 mM) solution was added to $HAuCl_4.3H_2O$ solution within 2 min. The reaction proceeded for further 40 min and cooled down to room temperature (RT). The AuNP solution was kept in freeze at -20 ^{0}C for 1 h and thawed. This process precipitated the excess starch along with large size AuNP. The solution was centrifuged at 10,000 rpm for 10 min and supernatant was separated. This process was repeated three times to get a clear AuNP solution. The various parameters like temperature (RT, 40, 50, 60, 70, and 80 ^{0}C), concentration of $HAuCl_4.3H_2O$ (0.2, 0.5, and 1.0 mM), NaOH (2.0, 3.0, 4.0, 5.0, 6.0, 7.0, 8.0, 10, 20, 50, and 100 mM), and starch (0.05, 0.1, 0.2, 0.5 1.0, 2.0, and 3.0% w/v) were optimized. We also synthesized the polyethylene glycol (PEG) capped AuNP by using PEG (0.5% v/v) in place of starch in similar condition.

4.2.2 Synthesis of silver nanoparticle

Silver nanoparticle (AgNP) was synthesized by using $AgNO_3$, starch and sodium hydroxide (NaOH) as a precursor of the reaction. The reaction was performed at RT, 50, 60, 70, 80 and 90 ^{0}C, and boiling condition with 0.5 mM of $AgNO_3$, 1% (w/v) starch, and 0.5 mM of NaOH. The solution was continuously stirred for 30 min to get a yellow color solution. The effect of different concentrations of NaOH (3.0, 4.0, 5.0, 6.0, and 7.0 mM) in AgNP synthesis with 1% starch and 0.5 mM $AgNO_3$ at boiling condition was analyzed. Similarly, the different concentration of starch (0.2, 0.5, 1, and 2% w/v) was used with 0.5 mM $AgNO_3$ and 5 mM of NaOH and reaction performed at boiling of solution for 20 min. In another experiment, the different concentrations of $AgNO_3$ (0.2, and 0.5 mM) was used with 1% starch and 5 mM NaOH and reaction performed for 30 min by heating above 90 ^{0}C. The reaction temperature was optimized by performing reaction at 60, 70, and above 90 ^{0}C (i.e. 95-100 ^{0}C) condition. We also synthesized the polyethylene glycol (PEG) capped AgNP by using PEG (0.5% v/v) in place of starch in similar condition.

4.2.3 Synthesis of zinc oxide nanoparticle

We synthesized three different ZnONP (uncapped, starch capped, and larger assembly) by the wet chemical method. In brief, 1% (w/v) of starch was mixed with Milli-Q water to get a clear solution. Thereafter, 10.0 mM $Zn(NO_3)_2.6H_2O$ was incorporated in the starch solution and kept on a magnetic stirrer, and NaOH (20 mM) was added drop-wise while larger assembly of ZnONP synthesized by further heating at 60-65 ^{0}C for 2.0 h with stirring. To, get uncapped ZnONP, the reaction was performed without starch. The white precipitate was produced and washed three times with distilled water and centrifuged at 10,000 rpm for 10 min to remove impurities. The precipitate was dried in vacuum and calcinated at 70 ^{0}C for overnight. Dried powder was collected, and desired concentration of ZnONP was prepared by ultrasonication of the sample for 10 min.

4.3 Characterization of nanoparticles

4.3.1 UV-VIS spectroscopic analysis

The surface plasmon resonance (SPR) of AuNP, AgNP, and ZnONP were analyzed by UV-VIS spectrophotometer (Perkin Elmer, λ-35). The sample was prepared in Milli-Q water (18 mΩ) and scanned in the range of 200-700 nm, with a slit width of 2.0 nm and scanning speed of 100 nm/min. All the spectra were baseline corrected and plotted against wavelength.

4.3.2 Electron microscopy imaging

The samples were diluted and prepared on a silicon wafer by drop casting method and dried in a vacuum drier. The dried samples were gold coated for 30 seconds and analyzed. In addition, to perform the TEM analysis, NP sample was diluted with Milli-Q water and deposited on a copper grid (300 mesh) by drop casting method and dried in the vacuum. Transmission electron microscopic analysis of NP sample was performed by TEM (Jeol, JEM-2100F).

4.3.3 X-ray diffraction analysis

All the samples were deposited on the quartz slide and dried in vacuum. The baseline correction of spectra was done using a quartz slide. The samples were analyzed using XRD (XRD ULTIMA-IV, Rigaku, Japan) in the range of $25\text{-}90^0$, with 2θ/min scanning speed (2θ is scattering angle) and 0.5^0 step size. The peak position was matched using JCPDS card No. 040784 for gold, 040783 for silver, and 361451 for ZnO. The crystallite size of AuNP sample was analyzed using Scherrer's equation: **D = 0.94λ /β (1/2 Cosθ);** where λ is the wavelength of X-ray (1.54 A), β is line broadening, θ is Bragg's angle.

4.3.4 Dynamic light scattering

The hydrodynamic size of particles was measured with respect to number percent of nanoparticles by Zeta Sizer (Nano-ZS, Malvern pvt. Ltd.). Simultaneously, the stability of nanoparticles was analyzed by zeta potential analysis. Transparent samples were prepared in

Milli-Q water and analyzed. The data was analyzed using DTS 7.0 software provided by the company.

4.3.5 FTIR analysis of modification in starch

The structural modification in starch due to heating (60-80 ^{0}C) and the presence of NaOH was monitored by FTIR spectroscopy (Alpha-series, Malvern). The analysis was performed in the range of 500-4000 cm^{-1} with 2 nm resolution and average of 25 scans was evaluated for various vibrational bond analyses. We compared the transmission mode of starch without modification and after the heat and NaOH treatment. The transmission data of all the samples were analyzed. The baseline correction was performed with respect to water.

4.3.6 Analyzing the surface activity of NP

We have further analyzed the surface activity of synthesized NP. The surface activity of AuNP was analyzed by its heavy metal sensing potential with different heavy metal by SPR shift analysis and variation in color. The colorimetric and SPR based heavy metal sensing was performed with copper (Cu^{2+}), nickel (Ni^{2+}), zinc (Zn^{2+}), lead (Pb^{2+}), mercury (Hg^{2+}), and arsenic (As^{5+}) in water using $CuSO_4$, Ni $(CH_3COO)_2 \cdot 4H_2O$, $ZnSO_4 \cdot 7H_2O$, $Pb(CH_3COO)_2 \cdot 3H_2O$, $HgSO_4$, and $Na_2HAsO_4 \cdot 7H_2O$. The experiment was performed using a different dilution of a transparent 200 ppm stock solution of the heavy metal compound in deionized water. Initially, 50 ppm of metal was mixed with 100 μM of AuNP solution and incubated for 2 h and analyzed the sample after every 10 min. Visible color change was monitored, and SPR was measured for all samples

The surface activity of AgNP was analyzed by its heavy metal sensing potential was also analyzed for heavy metals (above mentioned). The surface activity of ZnONP was analyzed by its photocatalytic degradation of two dyes methyl green (MG) and rhodamine-B (Rho-B). To examine, the photocatalytic potential of ZnONP in methyl green (MG) and rhodamine-B (Rho-B) dye, 5 mg/ml of both the dyes was mixed with 0.5 mg/ml of ZnONP and incubated for 30 min at 25 ^{0}C in the dark condition. These mixtures were further incubated for 12 h in the wavelength of 254 nm (UV-C), and the absorbance of the dye was measured at 0, 2 h, 4 h, and 6 h, 8 h, 10 h interval up to 12 h. In addition, the baseline correction of the sample was done with respect to ZnONP. The absorption peak at 632 nm for MG and 554 nm for Rho-B plotted against time (h) and analyzed up to 12 h to get time-dependent photocatalytic degradation of the dye.

4.4 Results and discussion

To synthesize the AuNP, AgNP, and ZnONP of below 50 nm average sizes with variation in surface capping, we used different parameters such as variation in precursor concentration (NaOH, starch (0.1-2% w/v) and polyethylene glycol (0.5% v/v)), and reaction temperatures (50-1000 ^{0}C). The excess starch was separated by maintaining the solution at -20 ^{0}C for 1 h followed by thawing and centrifugation at 8,000 rpm for 10 min, while ZnONP solution was centrifuged and washed three times before calcination at 70 ^{0}C. The effect of various parameters on the development of the desired size of NP was discussed below.

4.4.1 Synthesis and characterization of AuNP

To synthesize the AuNP of below 20 nm average sizes, we varied different parameters such as NaOH, starch, gold salt concentrations and reaction temperatures. The excess starch was separated by maintaining the solution at -20 ^{0}C for 1 h followed by thawing and centrifugation at 10,000 rpm for 10 min. The effect of various parameters on the synthesis of AuNP was discussed in the following sections.

4.4.2 Effect of NaOH concentration

The different concentration of NaOH (2.0, 3.0, 4.0, 5.0, 6.0, 7.0, and 8.0 mM) with 1% starch (w/v) was used in the synthesis of AuNP when 1.0 mM of $HAuCl_4.3H_2O$ was used as initial precursor concentration at 70 ^{0}C (Figure 4.1). Here, we found that the use of increasing NaOH concentration like 2.0, 3.0, and 4.0 mM resulted in a gradual change in color from yellow to light black. However, when 5.0 mM NaOH was used, the solution color initially turned black. However, it turned dark ruby red after that. Further increasing of NaOH concentration to 6.0, 7.0, and 8.0 mM revealed no further change of ruby red color, indicates that the use of NaOH above 5 mM had the ability to produce AuNP while increasing concentration speed up the reaction rate. The SPR analysis also showed a red shift from 516 nm to 544 nm of an absorption peak that indicates the increased size of the particle (Figure 4.1 A). When we plotted the SPR shift with respect to NaOH concentration and interpolated it within the working range of NaOH concentration (See Appendix Figure S1. A), we found a redshift in SPR for NaOH concentration of below 5.0 mM while the use of 5.0 to 6 mM of NaOH showed blue SPR shift.

Further increase of NaOH concentration, i.e., 7 and 8 mM showed slight red shift (Appendix Figure S1. A). The fact collectively proved that the synthesis of AuNP and reaction rate was dependent on NaOH concentration. However, below and above a range of critical value of NaOH concentration, the synthesis of AuNP either not significant (below 5.0 mM) or produced larger particles (above 8.0 mM) as shown by the variation in SPR shift and color change. It was found that the application of higher concentration of NaOH (i.e. above 8 mM) caused immediate color change and for 20 mM or above, the color turned from violet to black (see Appendix Figure S3. A). This indicates that the NaOH accelerates the synthesis of AuNP while higher concentration speeds up the growth and produce larger AuNP.

The dynamic light scattering (DLS) analysis was also performed to analyze the hydrodynamic size of AuNP and examine the major population. The intensity of number percentage with size with peak width was analyzed (Figure 4.1 C). The results revealed that NaOH concentration was critical for the synthesis of a higher population of AuNP with less than 20 nm and low polydispersity. When NaOH concentration was below a critical value (i.e. less than 5 mM), the larger particle was produced while the increase of NaOH concentration to 6 mM synthesized AuNP with a smaller size (10-20 nm). To monitor the stability of the suspension, when zeta potential was measured, we found that the stability was highest at NaOH concentration of 5 and 6 mM (-25 to -20 mV). Further increase of NaOH concentration, i.e., 7 and 8 mM produced AuNP of larger size, higher polydispersity and reduced stability (Appendix Figure S1. C).

Therefore, the overall experimental results indicated that for obtaining reduced size with high stability, the critical concentration of NaOH was required. Dongxiang et al. [156] also reported the synthesis of AuNP of control size by varying pH using different concentration of NaOH and temperature. Goia and Matijevic reported that changing the pH alter the composition of gold (III) complex and this complex is very essential for formation of AuNP [157].

4.4.3 Effect of reaction temperature

To understand the role of reaction temperature, we also performed the reaction at room temperature (RT i.e. 25 ^{0}C), 50 ^{0}C, 60 ^{0}C, 70 ^{0}C, and 80 ^{0}C (Figure 4.1 B and D), when other parameters were constant (1.0 mM $AuCl_4$, 1% starch, and 6 mM NaOH). When we performed the reaction at RT for overnight and below 50 ^{0}C for more than 1.0 h, we found that the solution became transparent after addition of NaOH (6 mM), and no significant color change was observed. However, when the reaction was performed at 50 ^{0}C or above, the solution was initially found transparent, however, turned black thereafter, and finally turned ruby red after 40 min of reaction, indicated the synthesis of AuNP (Figure 4.1 B). When we plotted the temperature against SPR peak, we found that below 60 ^{0}C (i.e. RT and 50 ^{0}C) and above 70 ^{0}C (i.e. 80 ^{0}C), the SPR peak showed redshift (Appendix Figure S1. B) while reaction below the critical temperature (50 ^{0}C) revealed slow reaction rate.

However, when the reaction was performed at 80 ^{0}C with NaOH (5-8 mM), 1% starch and 1 mM of gold salt, the reaction rate became fast. It explains that the reaction requires minimum activation energy. However, the energy achieved was less by lower NaOH concentration (below 10 mM) and hence the reaction needed to be performed above 50 ^{0}C to overcome such threshold energy barrier. However, temperature above 80 ^{0}C perhaps caused a rapid burst of the nucleus and uncontrolled growth of particles that consequently produced poly-dispersity. In fact, the above result was also supported by the analysis of hydrodynamic size distribution (Figure 4.1 D) and zeta potential (see appendix Figure S1. D) measurement of AuNP suspension.

It showed that at a higher temperature (i.e. more than or at 80 ^{0}C) larger particle was formed with less stability while in the range of 60-70 ^{0}C more population of a smaller particle of 10-20 nm mean size were formed with higher stability (Figure 4.1 D & appendix Figure S1. D).

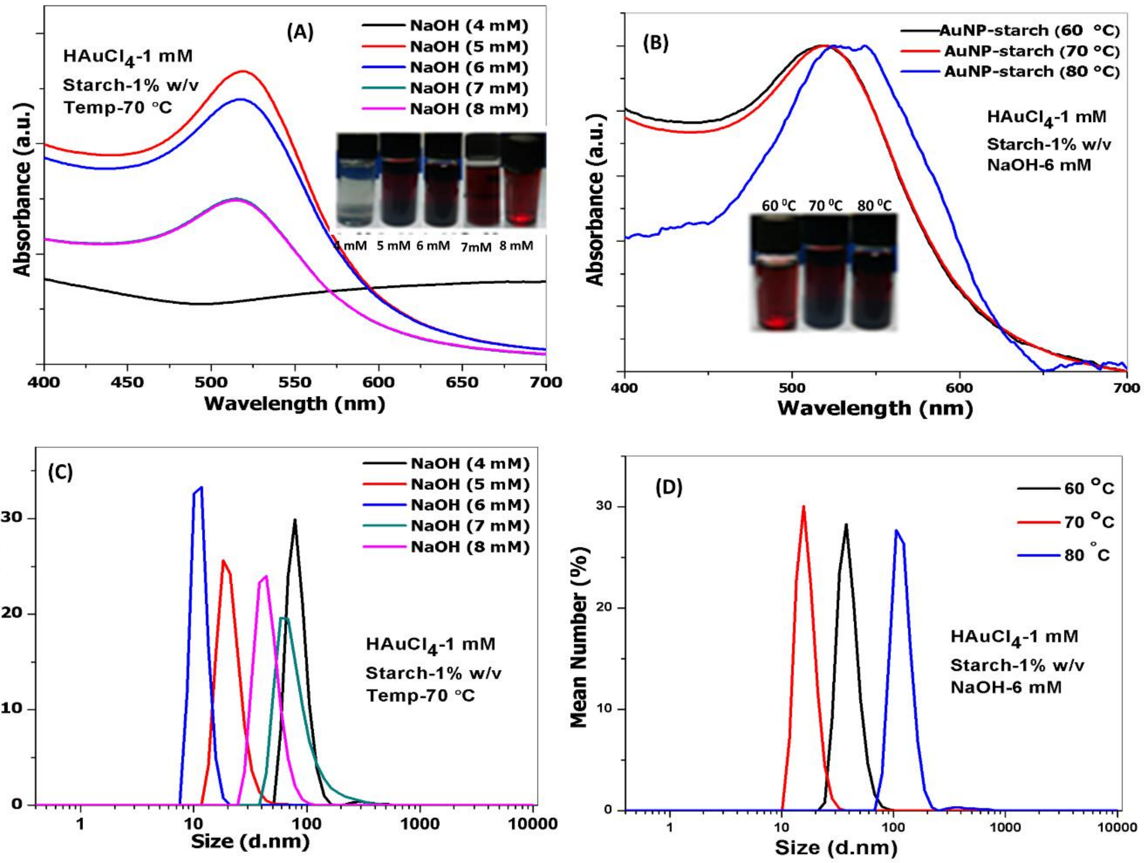

Figure 4.1 (A) The effect of NaOH concentration (4, 5, 6, 7, and 8 mM) on AuNP synthesis. Here, 1.0 mM $HAuCl_4.3H_2O$, 1% starch, and the 70 ^{0}C reaction temperature was used. (B) The effect of reaction temperature on the surface plasmon resonance (SPR). (C) DLS analysis of the hydrodynamic size of AuNP with various concentration of NaOH. (D) The effect of reaction temperature (60, 70, and 80 ^{0}C) in AuNP hydrodynamic size was analyzed by DLS particle size analysis.

Mountrichas et al. [158] reported that nanoparticle synthesis rate increased with increasing temperature and produce more homogenous nanoparticles while Muridharan et al. [159] reported that nanoparticle size increases with increment of reaction temperature. Therefore, the reaction temperature plays crucial role in size control synthesis of gold nanoparticle.

4.4.4 The effect of starch concentration

Further, we wanted to know the role of starch in controlling AuNP size when other parameters were kept constant (1.0 mM of $AuCl_4$, 6 mM of NaOH, and reaction temperature at 70 ^{0}C). Figure 4.2 A and C, showed how the variation in starch concentration affects SPR and subsequently the size of NP, which was further confirmed by color variation and DLS data.

The SPR analysis also revealed that at a lower concentration, larger particles were synthesized (shown by violet color for 0.05 % starch concentration) (see appendix Figure S3. B). With the increase of starch concentration, i.e., from 0.1 to 3%.

AuNP solution turned light to dark ruby red indicates a synthesis of small particles. When SPR was analyzed between starch concentrations of 0.05 to 3%, it showed initially a blue shift in SPR up to 0.2 % with an increase of SPR up to 1% of starch (Figure 4.2 A), However, it became constant thereafter i.e. till 3% (see appendix Figure S2. A) starch. A comparative study was performed using corn starch (0.2%) with the existing potato starch with and without D-glucose. It showed that corn starch-based synthesized AuNP without D-glucose showed relatively narrow SPR peak (see appendix Figure S3. C) than the synthesis method using D-glucose (see appendix Figure S3. D). This fact further validated that potato starch (reduction and capping) with NaOH for AuNP synthesis not only compatible with other starch but also eliminate the use of D-glucose in reduction process and other buffer ingredients to produce the smaller size of AuNP.

Further, we also analyzed the hydrodynamic size distribution with different starch concentration (0.2-1%). The results showed that increasing starch concentration from 0.2-1% also decreased the size of AuNP and produced a higher percentage of small particles (Figure 4.2 C). We also found that increasing starch concentration also increased the zeta potential of AuNP and stabilized the suspension up to 1% of starch (see appendix Figure S2. C). The initial shift of SPR was found up to 0.2% (shown by violet color for 0.05% and ruby red for 0.2%) of starch, but a further increase of starch produced a larger population of small particles. However, DLS analysis showed that slight red shift in SPR also indicated the presence of a higher concentration of surface capping species on the particles that caused a slight red shift. Moreover, the use of 1% to 3% starch demonstrated no significant shift in SPR, which indicated the saturation of AuNP for further interaction with available starch concentration. A further role of starch concentration was also observed during retrogradation of starch (see appendix Figure S6). We found that lower concentration of starch was unable to stabilize the AuNP during freezing and thawing and produced particle suspension with violet color due to aggregation. The Higher concentration, i.e., above 1% of starch, however, caused a higher amount of AuNP precipitation with starch although color variation was not found. Shimmin et al. [160] prepared gold nanoparticle of different size by varying size and concentration of capping agent and reported that the size of nanoparticle decrease with increasing capping agent molecular weight while nanoparticle showed polydispersity with less amount of thiol rich capping agent. Therefore, the surface capping agent play crucial role in size control synthesis.

4.4.5 The effect of gold chloride concentration

The effect of various concentration of gold salts was also observed when other parameters were constant (1% starch, 6 mM of NaOH, and reaction temperature at 70 ^{0}C). The results showed that SPR of various AuNP solutions varied with gold salt concentration exponentially (data below 0.5 mM and above 1 mM not shown). However, no significant change was found up to 0.5 mM of gold salt (Appendix Figure S2. B). The DLS analysis showed that both 0.5 mM and 1 mM concentration of gold salt produced AuNP of the equivalent hydrodynamic size of 10-15 nm (Figure 4.2 D) with a slightly broad peak width for AuNP synthesized from 0.5 mM gold salt. The zeta potential analysis also showed no significant change in stability of AuNP, as both showed zeta potential of -20 eV (see appendix Figure S2. D).

4.4.6 Electron microscopic analysis of AuNP

FESEM analysis of AuNP under various conditions and TEM imaging of the AuNP sample with the optimum condition (1 mM of $HAuCl_4.3H_2O$, 6 mM of NaOH, 1% of starch) was performed (Figure 4.3 A-F). The results showed that AuNP synthesized from 0.5 mM of $HAuCl_4.3H_2O$ contains smaller particles.

However, AuNPs synthesized by using 1.0 mM of $HAuCl_4.3H_2O$ produced larger particles with less polydispersity (Figure 4.3 B). In both cases, 6.0 mM NaOH and 70 ^{0}C reaction temperatures were used. However, when NaOH concentration was increased to 8.0 mM, the AuNP image revealed the formation of a large particle with high polydispersity and irregulars shape (Figure 4.3 C). When AuNP was prepared at high-temperature like 80 ^{0}C, the process produced large particles with the spherical shape (Figure 4.3 D) and little polydispersity. Furthermore, a precipitate of starch with AuNP was also analyzed (Figure 4.3 E), which showed large randomly distributed starch granule. The TEM analysis of optimized sample was performed (Figure 4.3 F). The TEM image revealed small AuNP of 7-10 nm size, which was in agreement with the results obtained from DLS analysis.

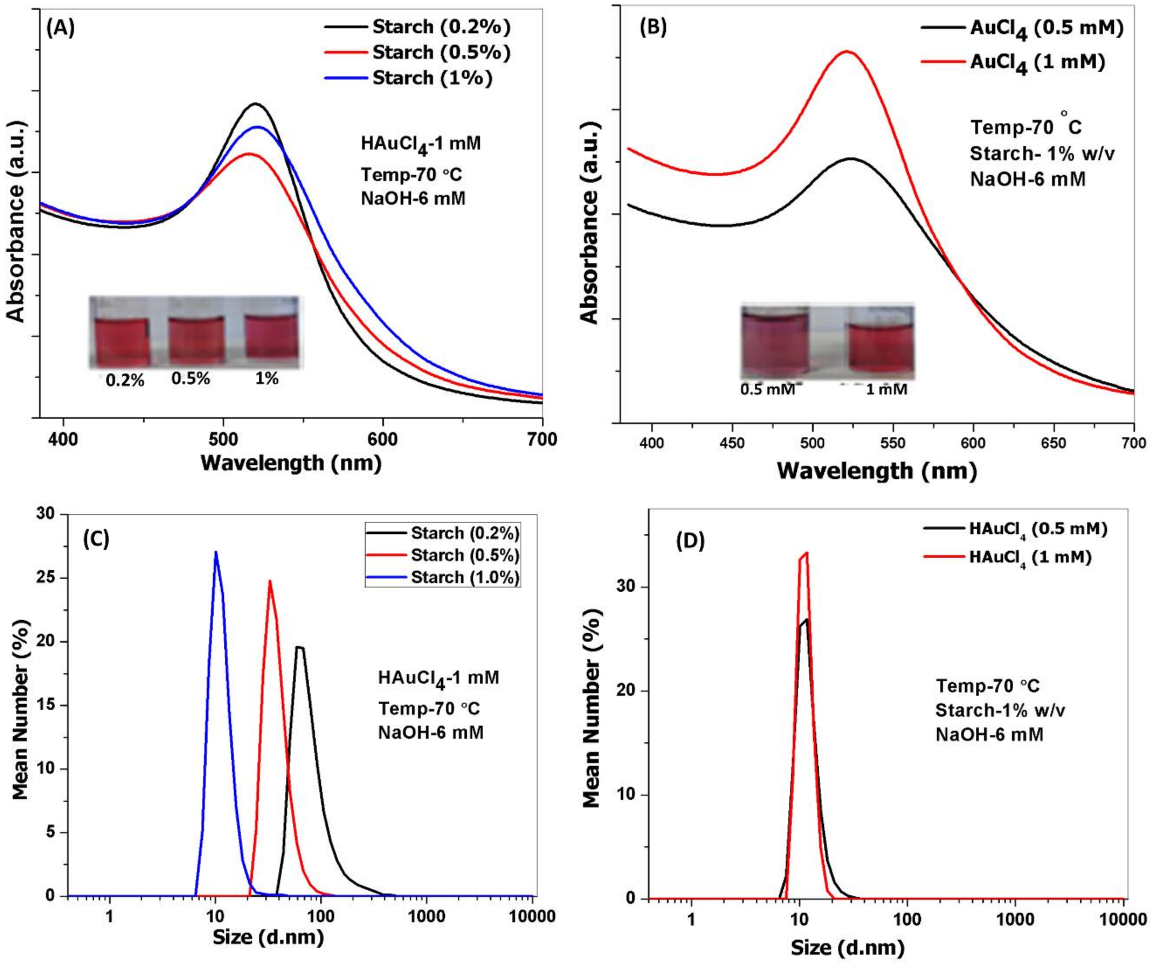

Figure 4.2 The effect of different concentration of starch (0.2-1%) and $AuCl_4$ analyzed. (A) SPR analysis of AuNP with different starch concentrations. (B) hydrodynamic size of AuNP with increasing temperature was analyzed by DLS analysis (C) The effect of various concentration of gold salt (0.5-1 mM) on the SPR. (D) DLS analysis of AuNP synthesized from 0.5 and 1.0 mM.

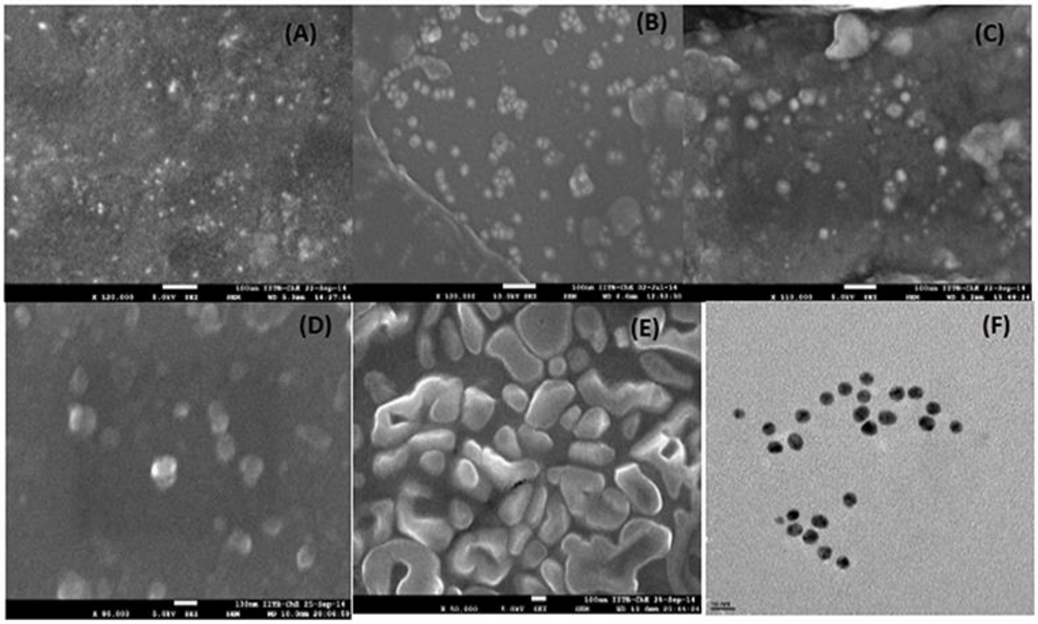

Figure 4.3 (A) & (B) AuNP synthesized from $HAuCl_4.3H_2O$ (0.5 mM and 1.0 mM), 1% starch and 6 mM NaOH at 70 ^{0}C (C) $HAuCl_4.3H_2O$ (1.0 mM), 1% starch and NaOH (8 mM) at 70^{0}C (D) the sample with $HAuCl_4.3H_2O$ (1.0 mM), 1% starch and NaOH (6 mM) at 80 °C; (E) AuNP-starch precipitate was observed under FESEM (Jeol) for analyze the morphology of samples. (F) The purified AuNP ($HAuCl_4.3H_2O$ (1.0 mM), 1% starch and NaOH (6 mM) at 70 ^{0}C) sample prepared on a copper grid and observed under transmission electron microscope.

4.4.7 FTIR analysis of starch

To analyze the structural change in starch on the AuNP surface, we performed FTIR spectroscopy analysis. The structural changes and variation in bending of bonds due to heating and NaOH treatment were analyzed by FTIR spectroscopy in ATR mode. We found that short period of treatment of starch in microwave irradiation and further heating at 50 ^{0}C or above with different concentration of NaOH caused a structural modification in starch. FTIR analysis of native starch demonstrated no sharp peak, however, peaks between 907-1106 cm^{-1} showed crystalline nature of starch with water content and reduction in peak intensity indicate a reduction in crystalline nature (Figure 4.4). The peak between 1133-1158 cm^{-1} was of C-OH bond, 1347-1420 cm^{-1} of COO$^-$ group, 1425-1580 cm^{-1} of CH_2 in aliphatic and 1582-1700 cm^{-1} was the peak of water and free OH group. The peak between 2743-3000 cm^{-1} represented CHO and CH^{3-} a group with bending, 3515-3600 cm^{-1} of OH in alcohol . Starch with NaOH and heating resulted in reduced peak between 907-1106 cm^{-1} that indicated reduced crystalline nature of starch (Figure 4.4). The peak between 2500-3100 cm^{-1} was found narrow, and other peaks between 3200-3800 cm^{-1} either were less intense or missing (Figure 4.4) . Here, we conclude that treatment of starch with mild alkali and heating perhaps modified the structure of starch molecules, which were perhaps responsible for the active nature of starch in nanoparticles. Further, we also analyzed the effect of various conditions for starch solubility to heat and analyzed by FTIR spectroscopy.

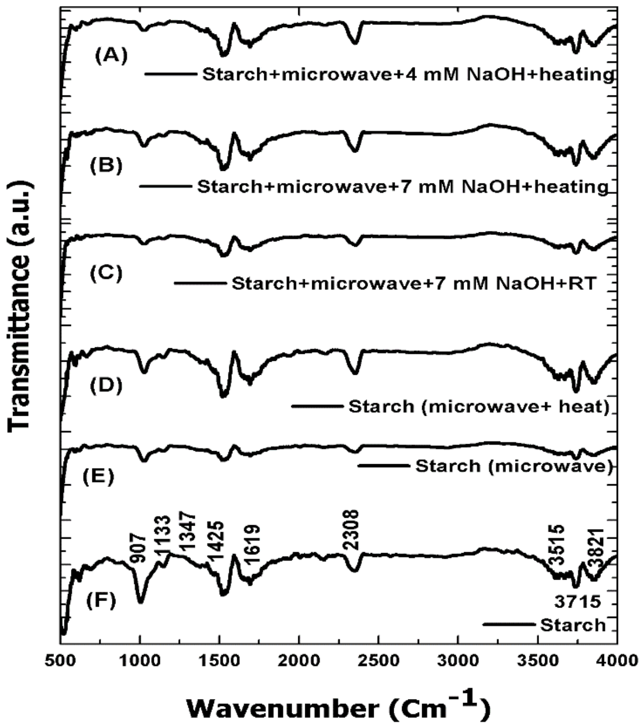

Figure 4.4 FTIR analysis of native starch and starch in different conditions after treatment with heat (microwave and hot plate heating) and NaOH.

4.4.8 X-Ray diffraction analysis

XRD analysis was performed to observe the characteristic crystallite size and the effect of various parameters on the growth of AuNP crystallite size (Figure 4.5). The peak broadening and peak shift of nanostructure signified the decrease in the particle size. The data were analyzed by background subtraction and fitting of peaks. From Figure 4.5, we observed that the lattice points were located at 111, 200, 220, and 311 positions with some peak shift and peak broadening. The lattice planes were matched with JCPDS card No 40784 [161], which confirmed the face centered cubic structure of the sample. The peak broadening at various positions indicated the formation of AuNP. The sample with a different concentration of NaOH (5, 6, 8 mM) showed peak broadening which varies with the concentration of NaOH (Figure 4.5 A, C, and H) and showed crystallite size of 13.76, 7.95, and 14.56 nm, respectively. Moreover, we also analyzed the effect of various temperatures (60, 70, and 80 ^{0}C) on the AuNP crystallite size (Figure 4.5 C, D, and E) that showed crystallite size of 8.68, 7.95, and 18.62 nm, respectively. We found that AuNP produced at higher temperature demonstrated narrow peaks, which signified the synthesis of larger particles.

Furthermore, we also analyzed the effect of various concentration of starch (0.5, 1, 2%) (Figure 4.5 C, F, and G) which showed AuNP crystallite of 6.84, 7.95, and 7.55 nm, respectively and gold salt (0.5, and 1 mM) (Figure 4.5 B and C) that showed AuNP crystallite size of 7.16, and 7.95, respectively. We observed that increase in the concentration of starch to 2% reduced the intensity of the peak at 200, while variation in gold salt concentration showed little shift in a peak at (200) and reduced intensity of the peak at (220), and (311). The crystallite size of AuNP samples were analyzed using Scherrer's formula: $\mathbf{D = 0.94\lambda /\beta\ (1/2\ Cos\theta)}$**;** where λ is the wavelength of X-ray (1.54 A), β is line broadening, θ is Bragg's angle. The peak at 38^{0}, 44^{0}, 64^{0}, and 77^{0} was used, and an average of crystallite size (nm) obtained by analysis of all four peaks was represented.

The effect of various parameters on the characteristic peak intensity and broadening was analyzed. Accordingly, we proposed a mechanism of AuNP synthesis involving heat-mediated modification of starch in the presence of NaOH. Initially, when starch was heated, it caused the starch structure to open (amylose and amylopectin) while the addition of NaOH by alkalization of hydroxyl group activated the starch molecule and produced reducing species. When gold salt was added to the activated starch solution, excess NaOH first reacted with gold salt to produce hydroxyl intermediate $Au(OH)_x$ which further reacted the reducing species of the starch molecule and produced AuNP nucleus. AuNP nucleus was grown further to produce AuNP. When excess NaOH was added with heating, it produced a higher order of $Au(OH)_x$ that caused rapid growth and production of large particles. At low temperature, the generation rate of the nucleus was slow and required a larger amount of NaOH for starch modification while heating with various concentration of NaOH (5-8 mM) rapidly produced the reducing species. Moreover, unreduced starch acted as a capping agent and prevented the production of larger particles due to heating.

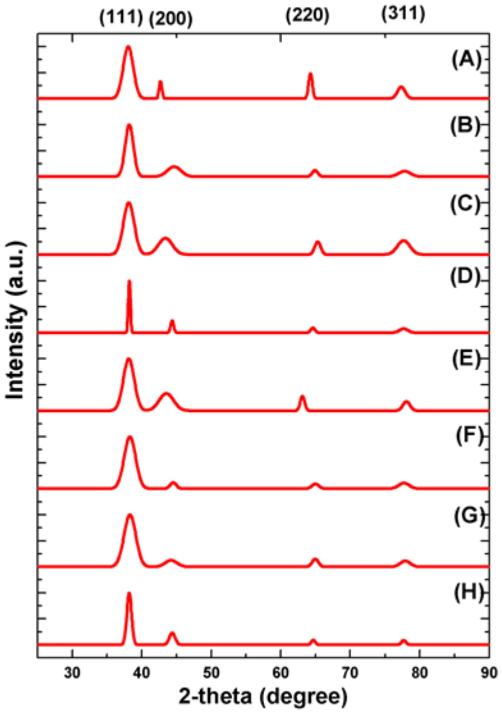

	AuCl$_4$ (mM) + Au-seed (µl)	NaOH (mM)	Starch (% w/v)	Temperature (^{0}C)
AuNP	1	7	1	70
AuNP	1+0	7	0	70
AuNP-ST	1+ 100	0	1	boiling
AuNP	1+0	7	1	80
AuNP	1+100	7	1	RT
AuNP	1+0	6	1	70
AuNP	1+0	5	1	70
AuNP	1+0	4	1	70

Figure 4.5 X-Ray diffraction spectra of various AuNP samples and crystallite size of respective samples.

However, heating with a higher concentration of NaOH reduced to a great extent and hence less amount of unreduced starch was present for capping. Ji et al. [156] and Zhang et al. [157] reported that reaction of NaOH with auric chloride produce intermediate gold hydroxide that causes conversion of yellow color to transparent and the order of hydroxide increased from 1.0 to 4.0 with increasing the NaOH concentration. Moreover, higher order of Au(OH)x was responsible for the different redox potential and reduction rate of gold [162, 163]. The plausible reaction mechanism of AuNP synthesis was represented below while detail of reaction with hydroxyl intermediate formation and higher order of gold chloride hydroxide was given in supplementary information (see appendix data Section 4):

$$HAuCl_4.3H_2O + NaOH \xrightarrow{50\text{-}80\ ^0C} Au(OH)_x + \text{Starch (reduced)} \xrightarrow{50\text{-}80\ ^0C} \text{Au-Nucleus}$$

$$\text{Au-Nucleus} + Au(OH)x + \text{Starch} \xrightarrow{50\text{-}80\ ^0C} \text{AuNP (starch capped)}$$

Furthermore, the TEM, SPR, DLS, Zeta potential of optimized AuNP capped with starch and polyethylene glycol (PEG-400) shown below (Figure 4.6 A & B). The results showed the formation of 7-10 nm average size of both the NP with SPR peak at 521 nm and 526 nm (Figure 4.6 C), respectively. Zeta potential analysis showed -26 mV and -16.5 mV, respectively (Figure 4.7 D). The XRD analysis showed a characteristic peaks corresponding (111), (200), (220), and (311) with peak broadening signifies the formation of the nanoparticle. The crystallite size analysis by Scherr's equation showed 6.8 and 6.6 nm for $AuNP_{ST}$ and $AuNP_{PEG}$, respectively (Figure 4.7 A & B).

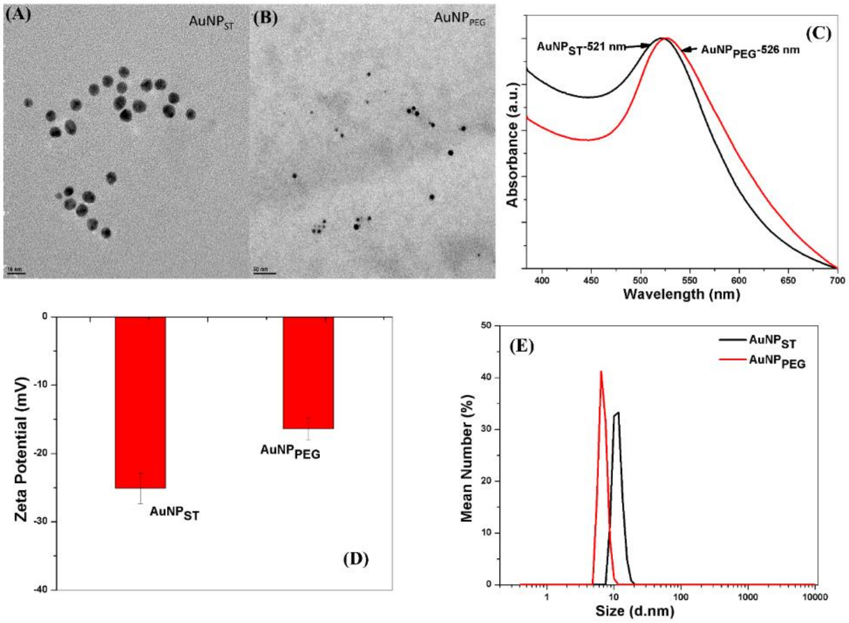

Figure 4.6 Electron microscopy images of (A) $AuNP_{ST}$ and (B) $AuNP_{PEG}$. (C) Surface plasmon resonance analysis of AuNP. (D) Zeta potential; (E) Hydrodynamic size distribution of $AuNP_{ST}$ (15 nm) and $AuNP_{PEG}$ (10 nm).

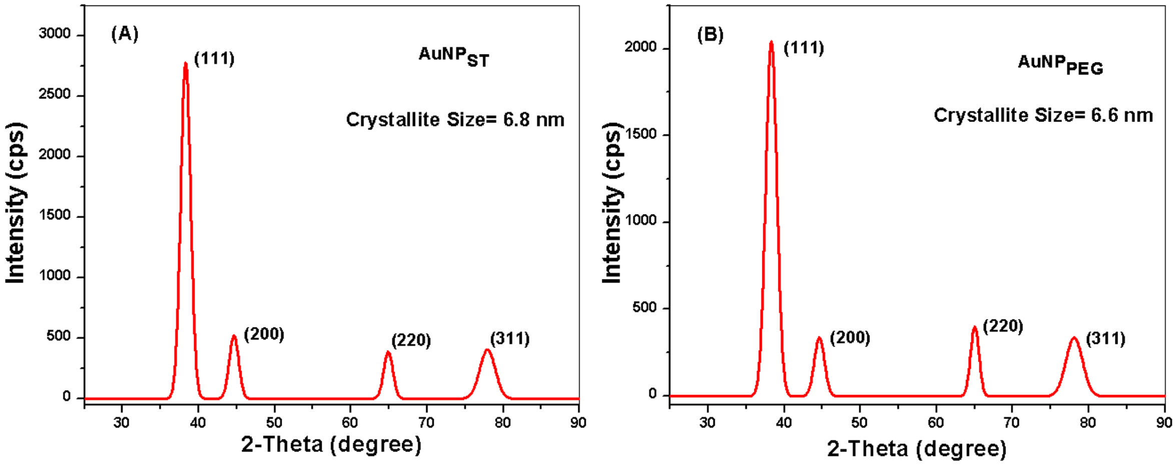

Figure 4.7 XRD analysis of (A) AuNP$_{ST}$ and (B) AuNP$_{PEG}$ in the range of 25-90^0. The data were processed, and Gaussian peak fitting was performed.

4.5 Synthesis and characterization of AgNP

The various parameters were optimized to synthesize the AgNP with least polydispersity, high stability, and size below 20 nm. The parameter such as the concentration of the reactant (i.e. starch, NaOH, and $AgNO_3$), and temperature (RT, 60, 70, and 90 ^{0}C) vary to produce AgNP.

4.5.1 Effect of NaOH concentration

The different concentration of NaOH (3.0, 4.0, 5.0, 6.0, and 7.0 mM) with 1% starch (w/v) was used in the synthesis of AgNP when 0.5 mM of silver nitrate ($AgNO_3$) was used as initial precursor concentration and reaction temperature 90 ^{0}C (Figure 4.8). We found that increasing NaOH concentration from 3.0 to 5.0 mM causes a gradual change in color from brownish to pale yellow. The appearance of brown color indicates the formation of silver oxide, which we observed by the formation of the brown color solution when the reaction was performed with (0.5 mM) $AgNO_3$ and (5 mM) NaOH of without starch. However, when 6.0 mM NaOH was used, the solution color initially turned dark brown and finally changed to yellow. Further increasing of NaOH concentration to 7.0 mM revealed dark yellow color. This indicates that the use of NaOH above 4 mM showed the ability to completely convert silver nitrate to silver hydroxide to silver oxide, which was further converted to Ag in the presence of starch at 90 ^{0}C. Moreover, more AgNP was producing when we used NaOH concentration of 6, and 7 mM, which was shown by dark yellow color. However, when higher NaOH concentration was used dark yellow color was converted to dark brown that showed the synthesis of larger particle.

The SPR analysis also showed a shift from 401 nm to 400 nm with enhancing absorption peak indicates forming of the smaller size of the particle in higher concentration (Figure 4.8 A). However, further increasing of NaOH concentration to 7 mM causes a red shift in SPR peak to 402 nm, indicates the formation of larger size particles. Moreover, SPR peak broadening was also found when we increase the NaOH concentration above 5 mM, indicates the increase in a polydispersity of AgNP. Below 3 mM of NaOH either brown color was found indicates the formation of silver oxide or insufficient conversion, because it was possible that NaOH was not sufficient to modify the starch with the conversion of $AgNO_3$ to Ag(OH) to produce AgNP.

This fact collectively indicated that NaOH has a crucial role in starch modification and formation of a silver intermediate compound that converted to silver and finally AgNP. Moreover, the lower concentration was insufficient to proceed reaction while a higher concentration of NaOH causes an uncontrolled reaction and larger particle synthesis, which signifies by the color change from yellow to brown.

The dynamic light scattering (DLS) analysis and zeta potential analysis of AgNP was performed. The volume percent of the different size of AgNP in suspension with respect to hydrodynamic size was plotted. The intensity of mean number percent with respect to hydrodynamic size and peak width was analyzed (Figure 4.8 B). The results revealed that NaOH concentration was critical for the synthesis of a higher population of AgNP with less than 20 nm and low polydispersity. When NaOH concentration was below a critical value (i.e. less than 5 mM), the larger particles were produced. However, increasing NaOH concentration from 5 to 6 mM, it produced AgNP with a smaller size (10-20 nm). To monitor the stability of the suspension, when zeta potential was measured, we found that the stability was highest at NaOH concentration of 5 and 6 mM (-25 to -20 mV) (Figure 4.8 C). Therefore, the overall experimental results indicated that for obtaining reduced size with high stability, the critical concentration of NaOH was required. Nisimura et al. [164] reported that increasing NaOH play crucial role in nucleation ionization rate of silver nanoparticle. In our study, we also observed that increasing NaOH increased the rate of AgNP synthesis.

4.5.2 The effect of starch concentration

Further, we wanted to know the role of starch in controlling AgNP size when other parameters were kept constant (1.0 mM $AgNO_3$, 5 mM NaOH, and reaction temperature at 90 ^{0}C). Figure 4.9 showed that the variation in starch concentration also affects SPR and subsequently the size of NP, which was further confirmed by color variation and DLS data (Figure 4.9 A & B). The SPR analysis also revealed that at a lower concentration, larger particles was synthesized (shown by brown color for 0.2% starch concentration). With the increase of starch concentration i.e., from 0.2 to 3%, AgNP solution turned pale yellow from dark brown color, indicates the synthesis of AgNP. When SPR was analyzed between starch concentrations of 0.2 to 2%, it showed a red shift in SPR for both lower (0.2%) and higher (2%) concentration of starch (Figure 4.9. A), However, SPR shift remained constant for 0.5, and 1% of starch (Figure 4.9. A).

Further, we also analyzed the hydrodynamic size distribution of AgNP samples with different starch concentration (0.2-2%). The results showed that variation in starch concentration of 1.0, and 2% decreased the hydrodynamic size of AgNP while 0.2% and 0.5% starch produced larger particles (Figure 4.9 B). However, we also found that increasing starch concentration from 0.2% to 0.5% increased the zeta potential of AgNP from -12 mV to -26 mV, indicated higher stability while increasing the starch concentration to 1% and 2% decreased the zeta potential to -19 mV and -17 mV (Figure 4.9 C).

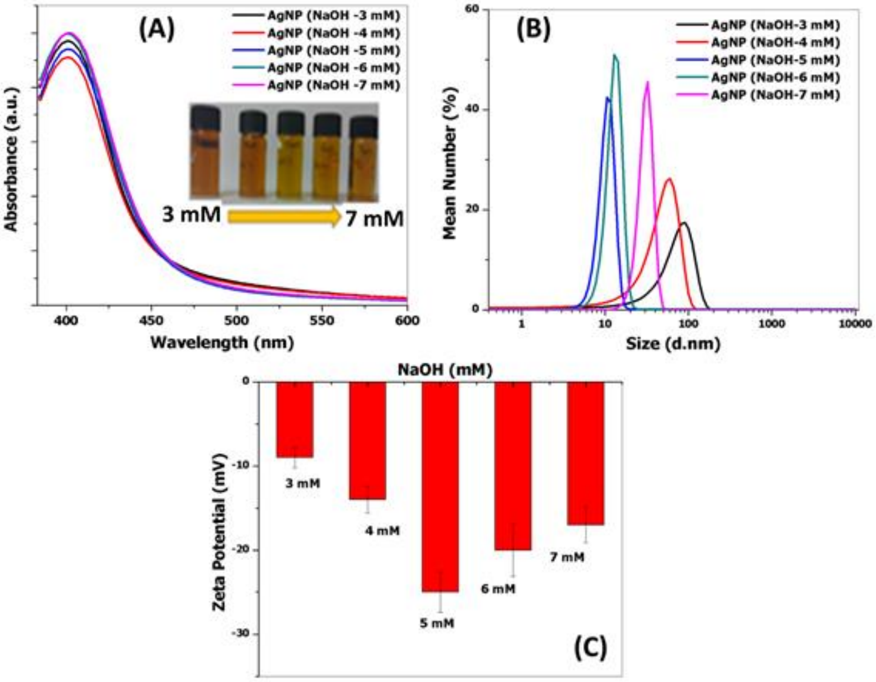

Figure 4.8 The effect of NaOH concentration (3, 4, 5, 6, and 7 mM) on AgNP synthesis. (A) SPR shift (B) hydrodynamic size of AgNP, (C) zeta potential analysis of AgNP.

We found that both lower concentration (below 0.5% w/v) and higher concentration (above 1% w/v) of starch was unable to stabilize the AgNP. Vigneshwar et al. [165] used starch as a reducing as well as capping agent in synthesis of AgNP in autoclave. Sharma et al. [166] in a review on green synthesis of AgNP also reported the role of starch as a capping agent. From these reports and our finding, it was observed that starch can be use as capping agent while modification of starch by chemical and physical method convert inert starch into active reducing agent.

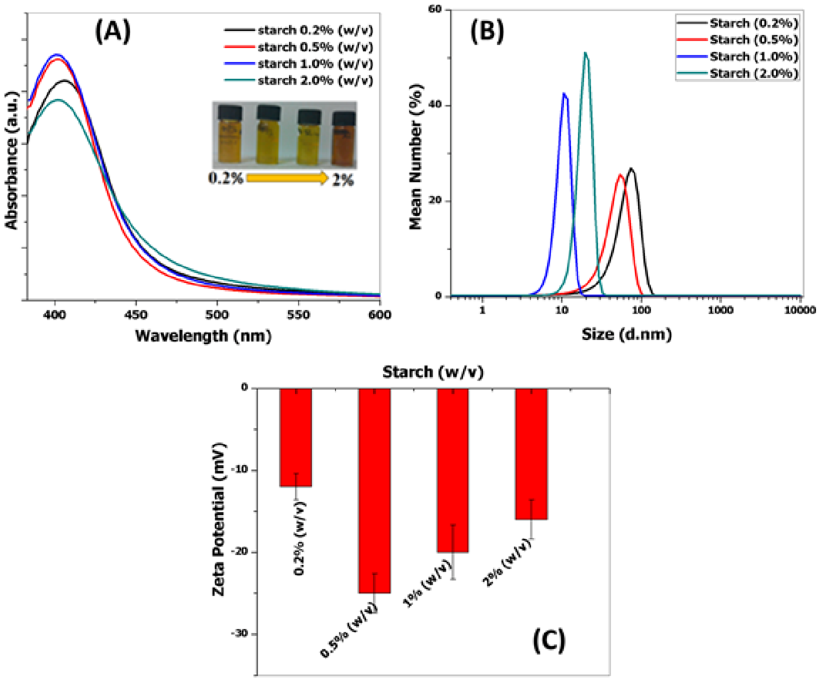

Figure 4.9 The effect of starch concentration (0.2, 0.5, 1, 2% w/v) on AgNP synthesis. (A) SPR shift (B) hydrodynamic size of AgNP, (C) zeta potential analysis of AgNP.

4.5.3 The effect of silver nitrate concentration

The effect of various concentration of gold salts was also analyzed when other parameters were unchanged (1% starch, 5 mM NaOH, and reaction temperature at 90 ^{0}C). The results showed that SPR of various AgNP solutions varied with $AgNO_3$ concentration. It was observed that increasing silver salt concentration from 0.2 to 1 mM also enhanced the SPR peak significantly while at 0.2 mM concentration showed broad peak that signifies formation of polydispersed particles while higher concentration produced more amount of NP (Figure 4.10 A). Further, DLS analysis showed that 0.5 mM silver salt produced AgNP of the equivalent hydrodynamic size of 12-18 nm (Figure 4.10 B) with narrow peak while for 0.2 and 1 mM silver salt produced larger NP. The zeta potential analysis also showed the stability of AgNP was highest for following precursor composition and reaction temperature: 0. 5 mM $AgNO_3$ with 1% starch, 5 mM NaOH and 90 ^{0}C. AgNP sample produces by using 0.5 mM silver salt showed zeta potential approximately of -24 mV (Figure 4.10 C).

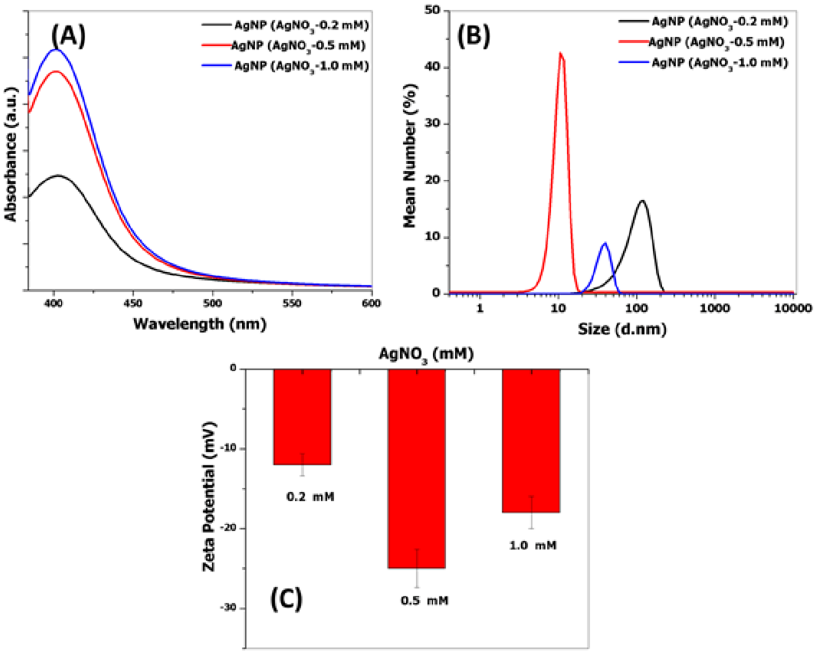

Figure 4.10 The effect of $AgNO_3$ concentration (0.2, 0.5, 1 mM) on AgNP synthesis. (A) SPR shift (B) hydrodynamic size of AgNP, (C) zeta potential analysis of AgNP.

4.5.4 Effect of reaction temperature

To understand the role of reaction temperature, we also performed the reaction at room temperature (RT i.e. 25 ^{0}C), 60 ^{0}C, 70 ^{0}C, and 90 ^{0}C (Figure 4.11 A, B, and C), when other parameters were constant (1.0 mM auric chloride, 1% starch, and 6 mM NaOH). When we performed the reaction at RT and below 50 ^{0}C for more than 1.0 h, we found that the solution became transparent after addition of NaOH (5 mM), and become dark brown after 24 h of incubation. However, when the reaction was performed at 60 ^{0}C, and 70 ^{0}C, the solution was initially found transparent, however, turned light brown thereafter, indicated the synthesis of silver oxide (AgO_2) (Figure 4.11. A).When we plotted the SPR, we found that at RT and below 90 ^{0}C , the SPR analysis showed broad peak and redshift in SPR (see appendix Figure 4.11 A) while reaction at 90-100 ^{0}C showed the disappearance of brown color and formation of pale yellow color. The SPR analysis showed a narrow peak at 401 nm (Figure 4.11 A). DLS analysis showed a larger particle of more than 100 nm average size (Figure 4.11 B) with high polydispersity index.

From here, it was observed that reaction below 90 ^{0}C produced polydispersed NP, which contains both AgNP and AgO_2 mixture. Therefore, it is essential to perform the reaction between 90-100 ^{0}C to get smaller AgNP with less polydispersity. Moreover, zeta potential measurement of AgNP suspension showed that reaction at a higher temperature (i.e. 90-100 ^{0}C) produced more stable AgNP (-24 mV) while reaction at lower temperature formed a larger particle with less stability and more AgO_2 (Figure 4.11 C). Jiang et al. [167] also reported that reaction temperature play crucial role in particle growth, shape, and size. The variation in reaction temperature influence the rate of the reaction and the particle size. Kasture et al. [168] reported that AgNP synthesis at lower temperature produce highly polydispersed nanoparticles while at higher temperature smaller nanoparticle with narrow size distribution. Therefore, these reports further verify our finding on AgNP synthesis.

4.5.5 Electron microscopic analysis

FESEM analysis of AgNP under various conditions and TEM imaging of the AgNP sample with the various condition was performed (Figure 4.12 A-F). We observed that AgNP synthesized using 0.5 % starch (other parameter remain constant e.g. $AgNO_3$ (0.5 mM), temperature 90 ^{0}C, 5 mM NaOH), produced larger particles with polydispersity (Figure 4.12 A). The results showed that AgNP synthesized from 0.5 mM of $AgNO_3$ contains smaller particles (Figure 4.12 B). However, when NaOH concentration was increased from 5 to 7.0 mM, the AgNP image revealed the formation of large particles with high polydispersity and irregulars shape (Figure 4.12 C). When AgNP was prepared at lower temperature like RT (Figure 4.12 G), and 60 ^{0}C (Figure 4.12 H), it produced larger particles while at reaction at 80 ^{0}C produced more amount of small particles than larger aggregates (Figure 4.12 I).

4.5.6 X-Ray diffraction analysis

XRD analysis was performed to observe the characteristic crystallite size and the effect of various parameters on the growth of AgNP crystallite size (Figure 4.13). The peak broadening and peak shift of AgNP signified the decrease in the particle size to the nanoscale. The data were analyzed by background subtraction and fitting of peaks. From Figure 4.13, we observed that the lattice plane were located at (111), (200), (220), (311) lattice positions with some peak shift and peak broadening.

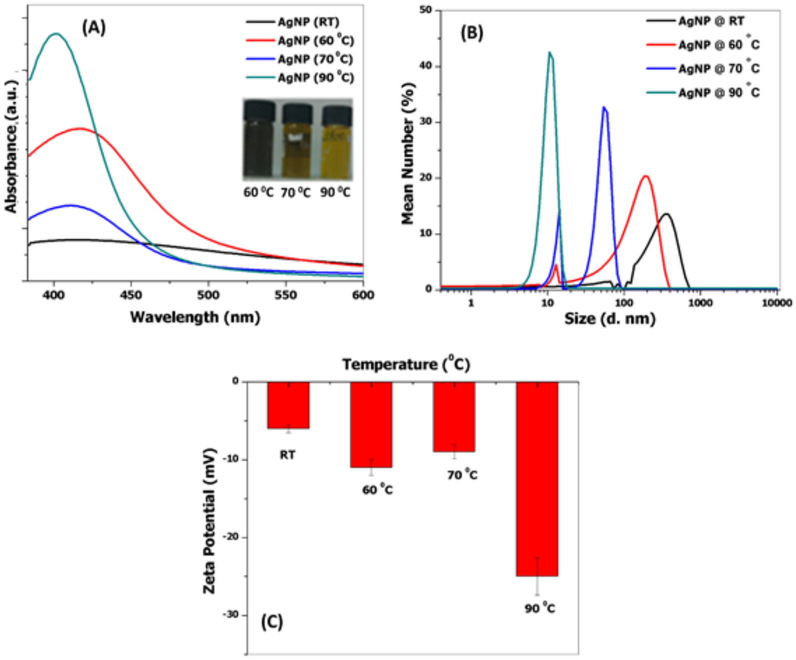

Figure 4.11 The effect of reaction temperature (room temperature (RT), 60, 70, and 90 ^{0}C) on AgNP synthesis. (A) SPR shift (B) hydrodynamic size distribution, (C) zeta potential analysis of AgNP.

These lattices were matched with JCPDS card No 40784, which confirmed the face centered cubic structure of the sample. The peak broadening at various positions indicated the formation of nanosize AgNP. The sample with a different concentration of NaOH (4, 5, and 7 mM) showed peak broadening which varies with the concentration of NaOH (Figure 4.13 A, D, & G) and showed crystallite size of 12.7, 9.3, and 15.67 nm, respectively. Moreover, we also analyzed the effect of various temperatures (70, 80, and 100 ^{0}C) on the AgNP crystallite size (Figure 4.13 D, E, & F) that showed crystallite size of 13.17, 14.91, 9.3 nm, respectively. We found that AgNP produced at higher temperature demonstrated broad peaks, which signified the synthesis of smaller particles.

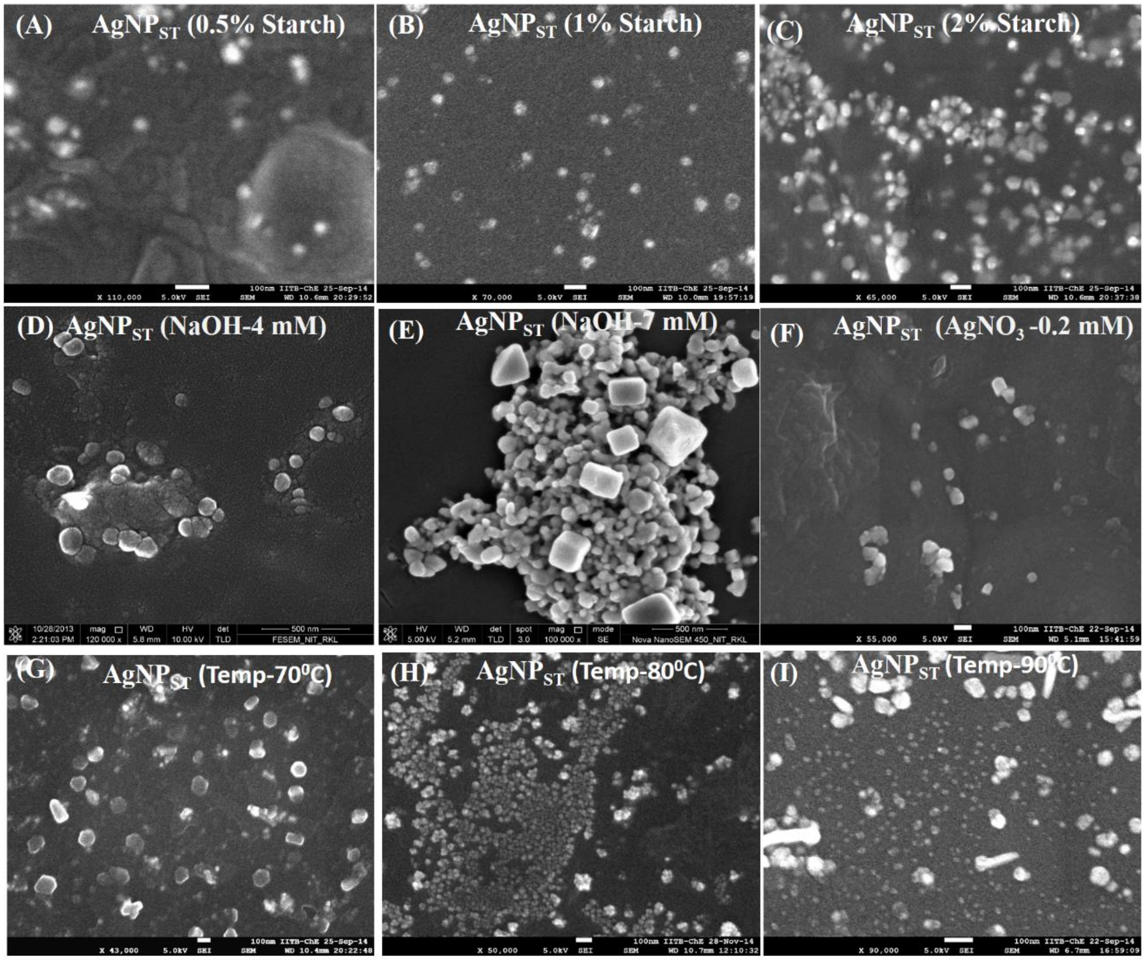

Figure 4.12 FE-SEM images of AgNP. Image (A) and (B) showed effect of NaOH (5, & 7 mM) concentration on AgNP. (C) and (D) showed effect of 0.5% and 2% starch, (A) and (E) showed 0.5, and 0.2 mM $AgNO_3$. The effect of temperature on AgNP ((G) at 70 ^{0}C, (H) 80 ^{0}C, (I) 90 ^{0}C showed the effect of temperature.

Furthermore, we also analyzed the effect of various concentration of starch (0.5, and 1 %) (Figure 4.13 C & D) which showed AgNP crystallite size of 10.28, 9.3 nm, respectively and silver salt (Figure.4.13 B & D) (0.5, and 1 mM) that showed AgNP crystallite size of 10.66, and 9.3, respectively. The crystallite size of AgNP samples were analyzed using Scherrer's formula: $D = 0.94\lambda /\beta$ (1/2 Cosθ); where λ is the wavelength of X-ray (1.54 A), β is line broadening, θ is Bragg's angle.

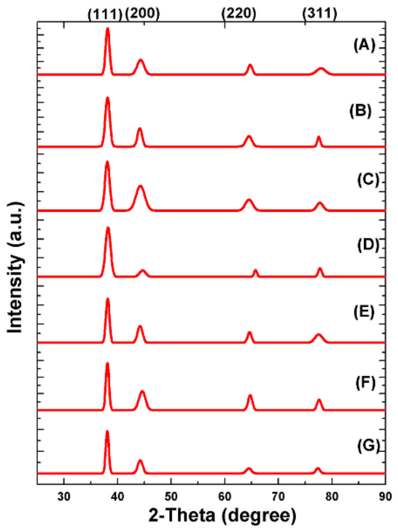

$AgNO_3$ (mM)	NaOH (mM)	Starch% (w/v)	Temperature °C	Crystallite size (nm)
0.5	4	1	100	12.7
1.0 mM	5	1	100	10.66
0.5	5	0.5	100	10.28
0.5	5	1	100	9.3
0.5	5	1	70	13.17
0.5	5	1	80	14.91
0.5	7	1	100	15.65

Figure 4.13 XRD analysis of $AgNP_{ST}$ samples XRD scanning was performed in the range of 25-90^0. We proposed a plausible mechanism of AgNP synthesis involving heat-mediated modification of starch in the presence of NaOH.

$$AgNO_3 + NaOH \xrightarrow{60\text{-}100\ ^0C} Ag\,(OH) \longrightarrow Ag_2O + \text{Starch (reduced)} \xrightarrow{60\text{-}100\ ^0C} \text{Ag-Nucleus}$$

$$\text{Ag-Nucleus} + Ag + \text{Starch} \xrightarrow{60\text{-}100\ ^0C} \text{AgNP (starch capped)}$$

Further, we also synthesized PEG capped AgNP of equivalent size by using 0.5% v/v PEG and by maintaining same reaction condition. The synthesized starch capped AgNP ($AgNP_{ST}$), and PEG capped AgNP ($AgNP_{PEG}$) were observed by TEM imaging (Figure 4.14 A and B). SPR analysis showed that $AgNP_{ST}$ and $AgNP_{PEG}$ showed SPR peak at 402 and 417 nm, respectably (Figure 4.14 C).

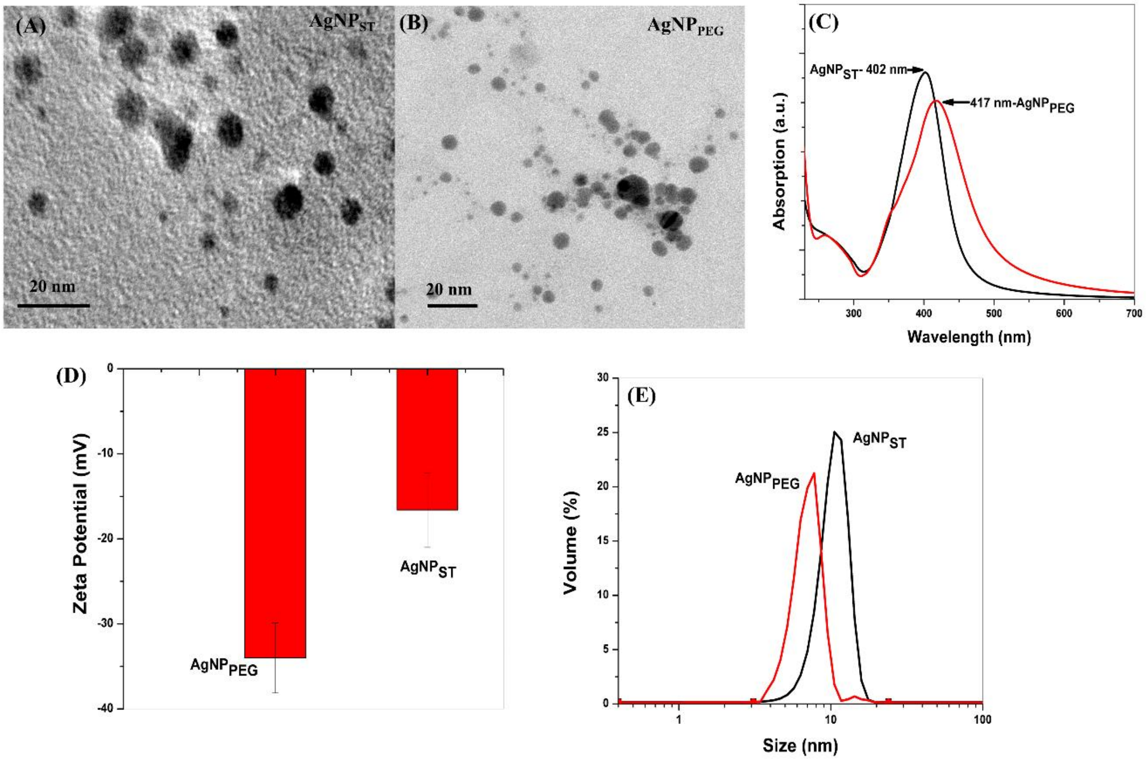

Figure 4.14 TEM images of (A) AgNP$_{ST}$ and (B) AgNP$_{PEG}$. (C) Surface plasmon resonance analysis of NP. (D) Zeta potential; (E) Hydrodynamic size distribution of AgNP$_{PEG}$ (10 nm) and AgNP$_{ST}$ (15 nm).

The Zeta potential analysis showed that PEG capping increased the solution stability of AgNP (-34 mV) compared to starch capped AgNP (-24 mV) (Figure 4.14 D), while hydrodynamic size analysis showed the AgNP$_{ST}$ size of 15 nm and AgNP$_{PEG}$ of 10 nm (Figure 4.14 E). XRD analysis of both the NP sample showed the peak broadening and crystallite size of 13.7 nm and 9.09 nm, respectively (Figure 4.15 A & B), which also matched with the results of TEM and DLS

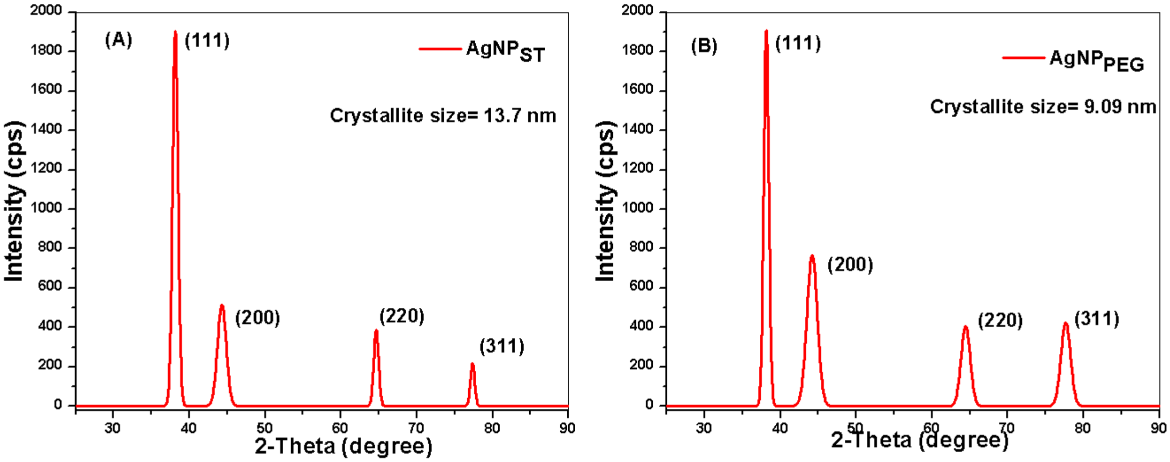

Figure 4.15 XRD analysis of AgNP$_{ST}$ and AgNP$_{PEG}$ in the range of 25-90^0. The data were processed, and Gaussian peak fitting was performed. (A) AgNP$_{ST}$ sample, (B) AgNP$_{ST}$ sample.

4.7 Characterization of ZnONP

The initial reaction was carried out at room temperature so that Zn $(NO_3)_2.6H_2O$ and NaOH reaction can be performed at a slow rate and resulted in the formation of Zn $(OH)_2$. The heating of starch (amylose and amylopectin) at 60-65 ^{0}C increase their solubility in water and expands the structure of amylopectin. Hence, we proposed here that the NP could assemble with expanded form of amylopectin of starch. We also used calcination temperature of 60, 70, and 80 ^{0}C for overnight with an aim to achieve a complete conversion of $Zn(OH)_2$ to ZnO.

4.6.1 UV-VIS spectroscopic analysis

UV-VIS spectroscopy analysis of different ZnONP samples showed absorbance peak shift with varying starch concentration, calcination temperature, and $Zn(NO_3)_2.6H_2O$ concentration. ZnONP [10 mM $Zn(NO_3)_2.6H_2O$] prepared with 0.5, 1, 2, and 3 % (w/v) starch showed absorbance peak at 384, 349, 358, and 360 nm, respectively (Figure 4.16 C). It showed that at low concentration of starch (0.5%), the amount of absorbed light was more compared to other samples (1%, 2%, and 3%). We also found that absorption peak of ZnONP prepared with 0.5% starch was broader compared to other samples. This fact indicated that varying starch concentration also affect the amount and wavelength of light absorbed by ZnONP. This may be due to more exposed surface of ZnONP than other samples.

Furthermore, when we analyzed the effect of calcination (Figure 4.16 B) temperature on the absorption spectra of ZnONP prepared with (50 mM) $Zn(NO_3)_2.6H_2O$, it was found that calcination temperature of various sample also affects the amount and wavelength of light absorption and consequently the morphology and size of ZnONP. Goh et. al. [169] reported that UV absorption by ZnONP depends on the size of ZnONP. They observed that UV absorption of ZnONP increased with NP size, but larger NP showed a decrease in absorption. It was also observed that ZnONP prepared at a calcination temperature of 60 ^{0}C showed no sharp absorbance peak while calcination at 70 ^{0}C showed a peak at 359 nm. However, calcination at 80 ^{0}C showed a blunt absorbance peak with maxima at 328 nm. Furthermore, the different concentration of Zn $(NO_3)_2.6H_2O$ like 5, 10, 20, and 50 mM was used with 1% starch, and the calcination process was performed at 70 ^{0}C. These samples showed the absorbance at 352 nm, 349 nm, 358 nm, and 359 nm, respectively. Figure.4.16 A showed that the amount and wavelength of light absorbed by ZnONP also vary with zinc nitrate concentration. It indicated that size and surface of nanoparticle also vary with zinc nitrate used in the reaction, when other parameters were constant (i.e. 1% starch, and calcination at 70 ^{0}C).

The shift in the absorption peak signifies the change in particle size with varying concentration of starch (0.5-3%), zinc salt (5-50 mM) and calcination temperature [169]. It showed that low concentration of starch like 0.5 % (w/v) was unable to stop the growth of the particle and caused self-aggregation, but higher concentration caused absorption of excess starch on ZnONP surface and increased particle size (Figure 4.16 C). The reason may be the separation of the boundary between assembled particle and some shrinkage of starch at a higher temperature as well as evaporation of water that vary the size and surface morphology of the particles. The sample produced by calcination at 60 ^{0}C showed no sharp peak, which may be due to the lower conversion rate of Zn $(OH)_2$ to ZnONP and structural variations in ZnONP. Moreover, we have also calculated the energy of the absorption peak using equation $E=hc/\lambda$ (Table.4.1).

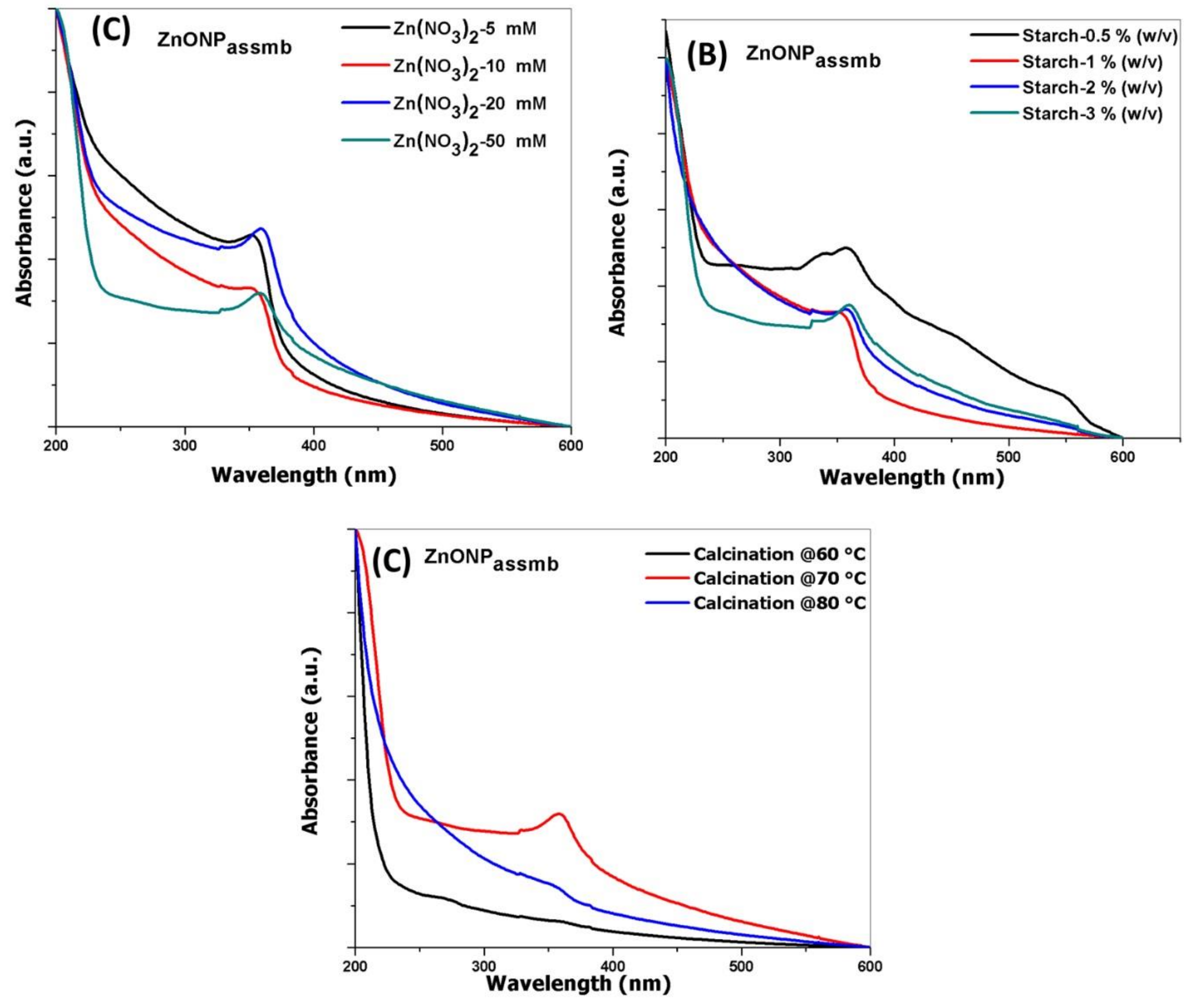

Figure 4.16 UV/VIS spectra of ZnONP; (A) UV/VIS spectroscopic analysis of ZnONP synthesized with 1% (w/v) starch using 5-50 mM of $Zn(NO_3)_2.6H_2O$ and at a calcination temperature of 70 ^{0}C; (B) UV/VIS spectra of ZnONP prepared with 1% (w/v) starch by using 50 mM of $Zn(NO_3)_2.6H_2O$ and calcination temperature of 60, 70, and 80 ^{0}C. (C) UV/VIS spectra of ZnONP prepared with 0.5-3% (w/v) starch, 10 mM of $Zn(NO_3)_2.6H_2O$ and a calcination temperature of 70 ^{0}C.

4.6.2 Hydrodynamic size and stability analysis of ZnONP

The hydrodynamic size and stability analysis of ZnONP suspension in water was studied using Malvern zeta sizer (ZS-Nano) (Figure 4.17). The effect of zinc salt, starch concentration, and calcination temperature on particle size was studied. When zinc nitrate concentration was increased from 5 mM to 10 mM with a starch concentration of 1% w/v and calcination temperature 70 ^{0}C, hydrodynamic average size measured was 230 nm and 153 nm, respectively. When ZnONP sample was prepared using 50 mM zinc nitrate at a calcination temperature of 80 ^{0}C caused a reduction in the hydrodynamic size of the particle up to 143 nm with the broadening of peak and polydispersity. Moreover, the increasing starch concentration from 1%-3% (w/v) caused reduction of particle size with increased in the polydispersity. The result was further confirmed by the UV spectroscopic measurement.

Table 4.1 The energy for respective wavelength of absorption maxima ($E=hc/\lambda$; h is plank constant, c is velocity of light, λ is wavelength of absorption maxima in nm) and crystallite size calculated by Scherrer method [($D_p=K\lambda / \beta½ \cos\theta$), K= 0.94, λ is X-ray wavelength (1.54 nm), β is linear broadening in degree, θ is Bragg angle].

$Zn(NO_3)_2.6H_2O$ (mM)	**Calcination (^{0}C)**	**Starch (w/v)%**	**Absorption maxima, nm (energy, eV)**	**Crystallite size (nm)**
5	70	1.0	352 (3.52 eV)	9.4
10	70	1.0	349 (3.55 eV)	8.3
20	70	1.0	358 (3.46 eV)	8.6
50	70	1.0	359 (3.45 eV)	8.9
10	70	**0.5**	384 (3.23 eV)	7.3
10	70	**2.0**	358 (3.46 eV)	7.8
10	70	**3.0**	360 (3.44 eV)	10.1
50	**60**	1.0	358 (3.46 eV)	7.8
50	**80**	1.0	328 (3.78 eV)	9.5

When we analyzed the effect of size on the stability of particle by measuring zeta potential, ZnONP showed approximately -12 mV zeta potential value when prepared with 5 mM and 10 mM zinc nitrate concentration. The sample calcinated at 80 ^{0}C and with 3% starch showed -10 mV zeta potential. The fact indicated that excess starch reduced the charge on the surface of the particle and hence, sample stability. Moreover, the results revealed that hydrodynamic size, polydispersity, and zeta potential were dependent on starch and zinc nitrate concentration. Further, it also showed a low level of polydispersity and high zeta potential for ZnONP, prepared with 10 mM zinc nitrate, 1% of starch and calcination temperature of 70 ^{0}C. Such fact indicated that for a particular stoichiometry ratio of primary ZnONP and starch, ZnONP assembly was more homogenous and showed high stability. The reason may be the limited number of available sites in starch to accommodate the nanoparticles, which was synthesized due to the heating starch molecule. This fact also triggers the opening of amylopectin as flower or branch and interact using its own hydroxyl group with ZnONP during calcination and the reaction induces the self-assembly.

Furthermore, the zeta potential of various samples were plotted with respect to starch and $Zn(NO_3)_2$ concentration and calcination temperature (see appendix, Figure S8. A). It was observed that zeta potential of ZnONP was decreased from -12.5 mV to -8.0 mV when $Zn(NO_3)_2$ concentration was increased from 5 mM to 20 mM, however, further increasing of $Zn(NO_3)_2$ concentration to 50 mM showed zeta potential of -12.1 mV (see appendix Figure S8. B). Here, it was possible that when other parameters (starch 1%, and calcination 70 ^{0}C) were constant the increasing concentration of $Zn(NO_3)_2$ also produced larger ZnONP while synthesis of a polydispersed particle in the case of 50 mM sample provide zeta potential of -12.1 mV. When we have analyzed the effect of starch concentration on the zeta potential of ZnONP it was clearly shown that increasing starch concentration also decrease the zeta potential of the particle (see appendix Figure S8. C). It confirmed that starch act as a passivizing agent on the surface of ZnONP. Zeta potential of ZnONP (50 mM) samples prepared by calcination at 60, 70, and 80 ^{0}C were also performed (see appendix Figure S8. D). The results showed calcination at 60 and 80 ^{0}C causes a reduction in zeta potential of the nanoparticle. The reason may be variation in structure and surface morphology of ZnONP while NP prepared by calcination at 70 ^{0}C showed zeta potential of 12.1 mV.

4.6.3 X-ray diffraction analysis

X-Ray diffraction analysis revealed peak position of ZnONP crystal with a broadening in peak and intensity of different peak under varying parameter (Figure 4.18). Full width of half maxima (FWHM) value of each peak was calculated, and crystallite size of the nanostructure was determined using Scherrer equation (Table.4.1).

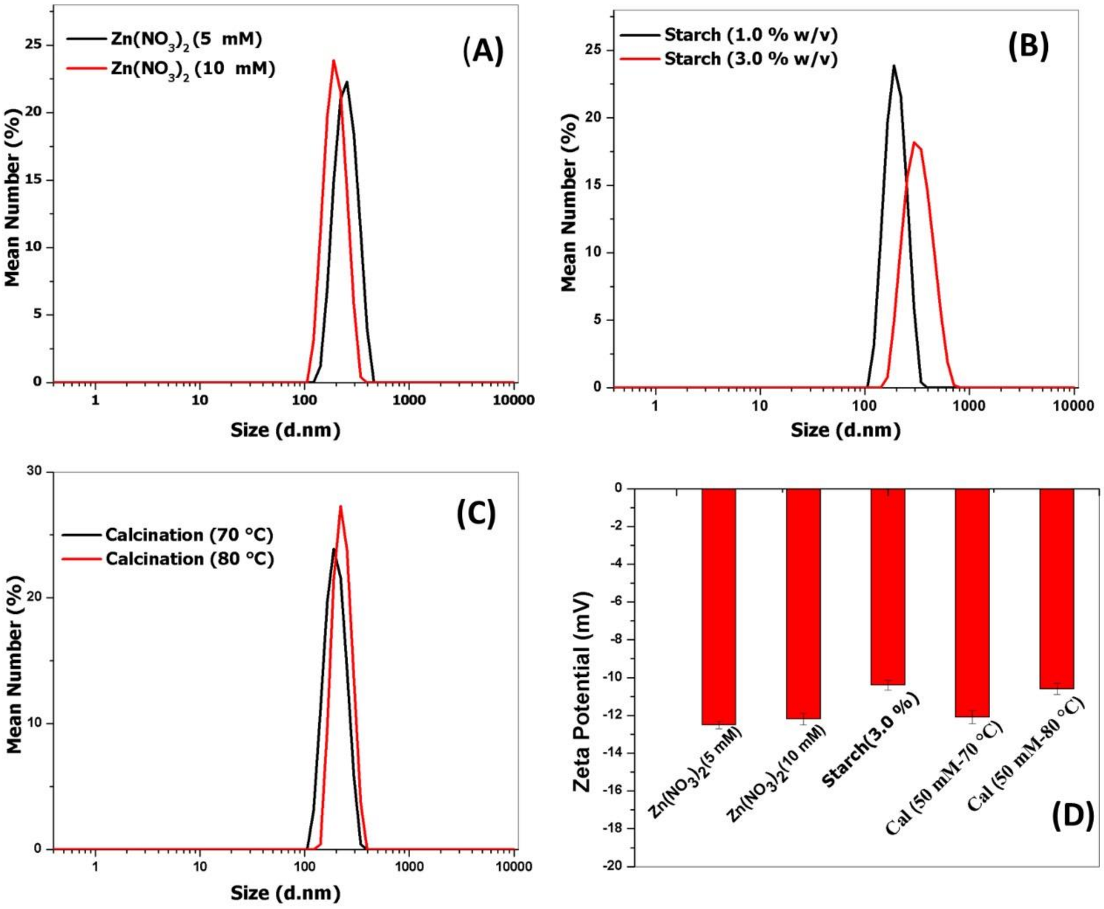

Figure 4.17 DLS and zeta potential of a different aqueous solution of ZnONP. The size and stability of ZnONP under varying $Zn(NO_3)_2.6H_2O$, starch concentration, and calcination temperature were analyzed. DLS analysis showed that the average hydrodynamic size of particles was more than 100 nm for all the cases.

The peak position of each crystal was compared with JCPDS database. Here, we found that increasing starch concentration (0.5-3 %) caused narrowing the peaks, which signifies the fact that the increase of starch concentration could increase the size of ZnONP from 7.3 nm to 10 nm. However, the increase of $Zn(NO_3)_2.6H_2O$ concentration (10 mM) showed the formation of smaller crystallite size (8.3 nm) in comparison to other samples with different concentration (5, 20, 50 mM) of Zn $(NO_3)_2.6H_2O$ (Table.1). Here, we found that the use 10 mM of Zn $(NO_3)_2$ showed smaller crystallite size than others. The lattice planes (100), (002), (101), (102), (110), (103), and (200) of all spectra matched with ZnO of JCPDS card NO 361451. Moreover, increased calcination temperature showed an increase of crystallite size from 7.8 to 9.5 nm. This fact further indicated the role of temperature and starch concentration on the growth of the particles. It was also found that the sample produced by using 5 mM and 20 mM of Zn $(NO_3)_2.6H_2O$ concentration and 0.5 and 3% starch concentration and with a calcination temperature of 80 ^{0}C showed less intensity for (002)-lattice plane. The reduction of the aspect ratio of (002) to 101 in comparison to bulk form indicated the exposed surface of the crystallite [17]. It signifies that (002)-lattice plane exposed the surface of ZnO.

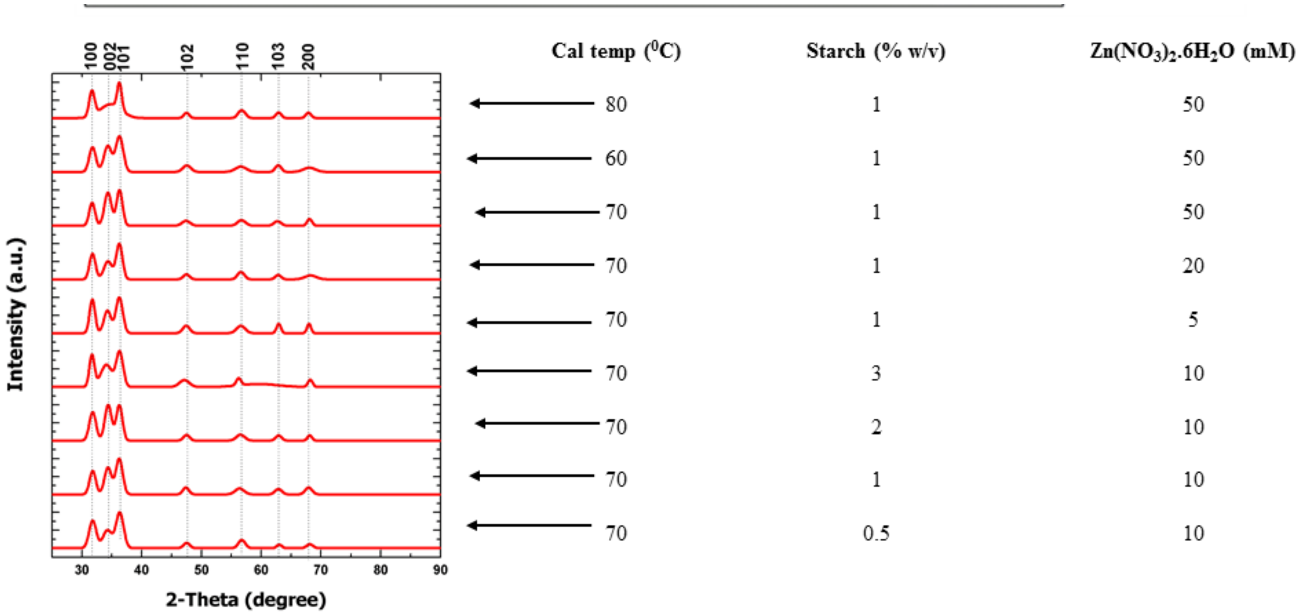

Figure 4.18 XRD analysis of all ZnONP samples performed in the range of 25-90^0. Baseline correction of obtained data was done and compared with ZnO crystal structure.

4.6.4 Electron microscopy analysis

The FESEM analysis of samples was prepared to observe the shape and size of the nanostructures. It revealed that the sample prepared with 10 mM $Zn(NO_3)_2.6H_2O$ showed mono-dispersed self-assembled nanostructure with an average size of 100 nm, but other samples also showed larger size or nanostructure with less homogenous nature. The samples prepared with 5 mM of $Zn(NO_3)_2$ and 0.5% starch showed agglomeration of two assemblies. However, the samples prepared with 50 mM $Zn(NO_3)_2$ or 2%, or 3% starch showed heterogeneous population. From Figure 4.19, we found that the sample calcinated at 60 ^{0}C showed cubic and random shape particles while both the samples calcinated at 80 ^{0}C and 70 ^{0}C showed particle population of small. However, the calcination at 80 ^{0}C caused heterogeneous size distribution. FESEM analysis also supports the polydispersity and particle size results obtained by DLS analysis for both the ZnONP samples prepared using 3% starch and higher calcination temperature. Furthermore, we analyzed the primary particle of ZnONP that participate in self-assembly using TEM, which confirmed that the average size of the nanoparticle was 7 nm and shape of the particle was spherical in nature.

Furthermore, the growth mechanism of ZnONP assembly was analyzed by collecting the sample at the interval of 0 h, 1 h (at Room temperature), 1h (at 60 ^{0}C), 2h (at 60 ^{0}C), and after calcination at 70 ^{0}C. All the sample were deposited on silica wafer and analyzed by FESEM. The FESEM observation showed that at 0 h there were random large structures were deposited (Fig. 4.20 I), which was modified to a small particle-like structure after 1h of reaction at RT (Figure 4.20 II). When the reaction was further performed at 60 ^{0}C (after 1 h), the randomly oriented branched structure was observed (Figure 4.20 III). Furthermore, the observation of sample after 2 h, the branched structures were showed now in spherical orientation (Figure 4.20 IV). After completion of the reaction, the sample was centrifuged to obtain the precipitate, and the sample was calcinated at 70 ^{0}C and observed by FESEM. The calcinated sample showed starched assembled ZnONP structure (Figure 4.20 V).

From here, we can propose a growth mechanism of how ZnONP assembly was made. Starch is made up of amylose (20-30%, linear chain) and amylopectin (70-80%, branch chain). The chemical formula of amylopectin is $C_{30}H_{52}O_{26}$ [linear bonding $\alpha(1\rightarrow4)$ glycosidic bonds and Branching with $\alpha(1\rightarrow6)$ bonds) and amylose is $(C_6H_{10}O_5)_n$ [$\alpha(1\rightarrow4)$ glycosidic bonds]. During the reaction $Zn(NO_3)_2$ was reduced to $Zn(OH)_2$ particles. Further, the reaction temperature was increased to 60 ^{0}C that causes the branched amylopectin to open like flower, which then interacted with Zn(OH)$_2$ particles. After completion of the reaction, the white gel was separated and calcinated at 70 ^{0}C. The calcination process completely converts the Zn(OH)$_2$ to ZnO and produces the self-assembled ZnONP structure.

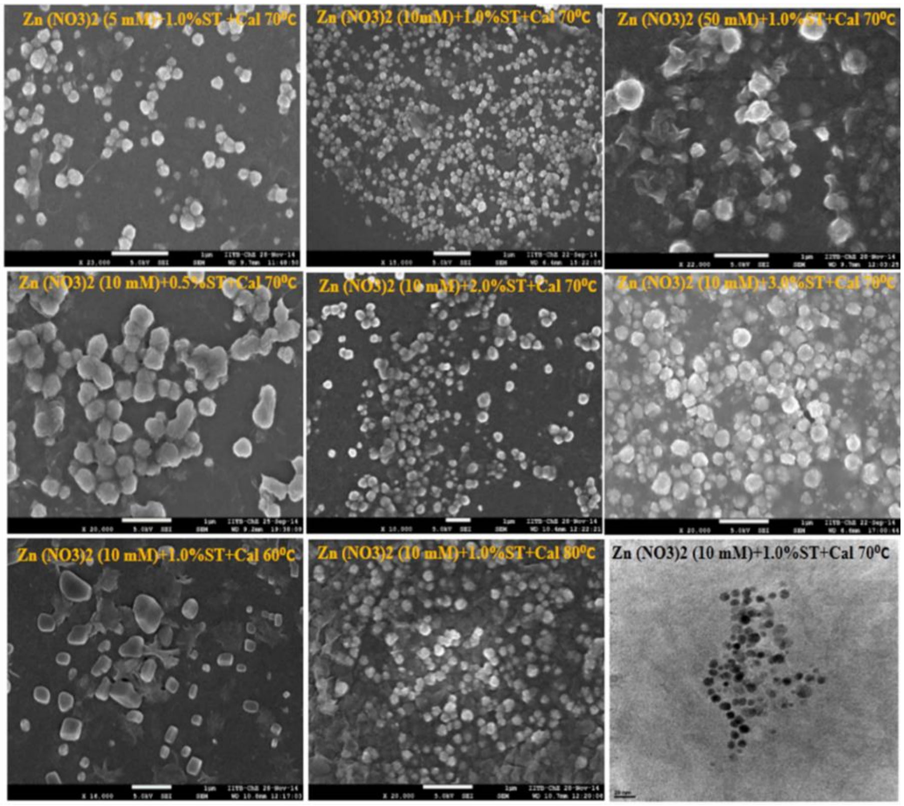

Figure 4.19 FESEM analysis of different samples. (A)-(C) ZnONP prepared with different concentration of Zn(NO$_3$)$_2$.6H$_2$O like 5 mM, 10 mM, 50 mM with 1% (w/v) starch. (D)- (F) Sample prepared with 10 mM Zn(NO$_3$)$_2$.6H$_2$O prepared with 0.5, 2, 3% (w/v) of starch and calcinated temperature of 70 ^{0}C for overnight. (G)-(H) Samples prepared with 10 mM Zn(NO$_3$)$_2$.6H$_2$O and 1% starch and calcination at 60 ^{0}C, 80 ^{0}C were shown. (I) Primary ZnONP of average size 7.0 nm analyzed by TEM analysis.

Further, we also synthesized the starch capped ZnONP (ZnONP$_{\mathrm{ST}}$) at room temperature using 10 mM Zn(NO$_3$)$_2$.6H$_2$O and 1% w/v starch. After 2 h of reaction, the sample was centrifuged at 8000 rpm for 10 min and washed three times. Similarly, uncapped ZnONP was also synthesized without starch in similar condition. All the ZnONP samples were calcinated at 70 ^{0}C for overnight to convert Zn(OH)$_2$ to ZnO. The electron microscopic study showed that ZnONP$_{\mathrm{uncap}}$, ZnONP$_{\mathrm{ST,}}$ and ZnONP$_{\mathrm{assmb}}$ were spherical in shape (Figure 4.21 A, B, & C).

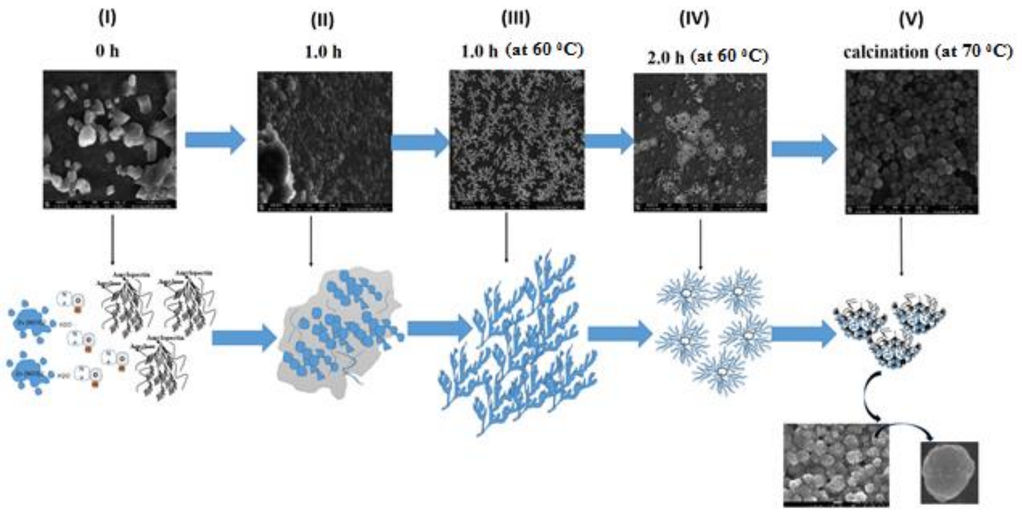

Figure 4.20 Time-dependent growth mechanism of ZnONP was analyzed using FESEM by collecting sample after 0 h, 1.0 h (RT), 1.0 h (at 60 ^{0}C), and 2.0 h (at 60 ^{0}C) and after calcination. (I) random structure of precursor molecules during 0 h. (II) embedded small particle on the starch surface after 1 h reaction at RT. (III) showed branched amorphous structure randomly oriented after 1 h of reaction at 60 ^{0}C. (IV) Annular arrangement of branched structure after 2 h of reaction at 60 ^{0}C. (V) Self-assembly of ZnONP after overnight calcination of the sample at 70 ^{0}C. (see Appendix Figure S7).

Further, the DLS analysis showed that hydrodynamic size of ZnONP$_{uncap}$ was 12 nm, ZnONP$_{ST}$ was 30 nm, and ZnONP$_{assmb}$ was 163 nm (Figure 4.21 D, E, and F). The zeta potential analysis showed ZnONP$_{uncap}$ value is -19 mV, ZnONP$_{ST}$ is -29.8 mV, and ZnONP$_{assmb}$ is -15.2 mV (Figure 4.21 G). Therefore, it was revealed that starch-based capping increased the stability of ZnONP while the formation of larger assembly reduced the stability. Zamiri et al. [170] and Becheri et al. [171] reported the starch capped ZnONP synthesis. The results showed that variation in starch concentration influence the size and stability of ZnONP. Therefore, starch play crucial role in size control synthesis of ZnONP.

XRD analysis of these samples showed the characteristic peak for wurtzite crystal structure for ZnO. The crystallite size analysis by Scherr's equation showed the crystallite size of 10.2 nm for ZnONP$_{ST}$, 13 nm for ZnONP$_{uncap}$, and 7.10 nm for ZnONP$_{assmb}$ (Figure 4.22 A, B, & C).

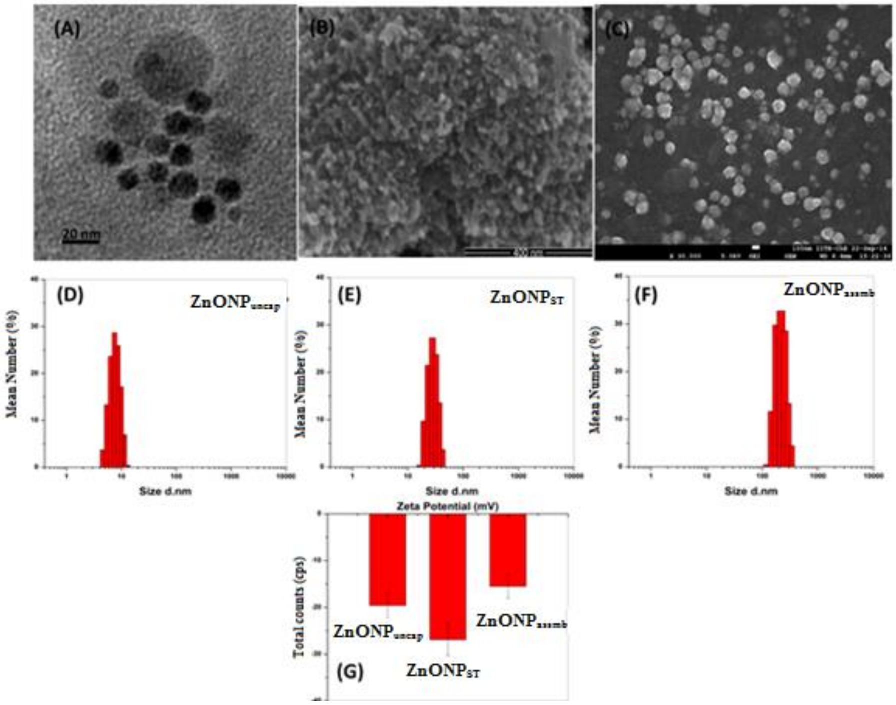

Figure 4.21 Electron microscopy images of (A) ZnONP$_{uncap}$, (B) ZnONP$_{ST}$ and (C) ZnONP$_{assmb}$. Hydrodynamic size distribution of (D) ZnONP$_{uncap}$ (15 nm), (E) ZnONP$_{ST}$ (30 nm), and (F) ZnONP$_{assmb}$ (163 nm). (G) Zeta potential of ZnONP$_{uncap}$, ZnONP$_{ST}$, and ZnONP$_{assmb}$.

The characterization of ZnONP showed that starch capped ZnONP produced less polydispersed NP of 30 nm size with higher stability, while NP produced by the formation of a larger assembly and without capping, were less stable in solution.

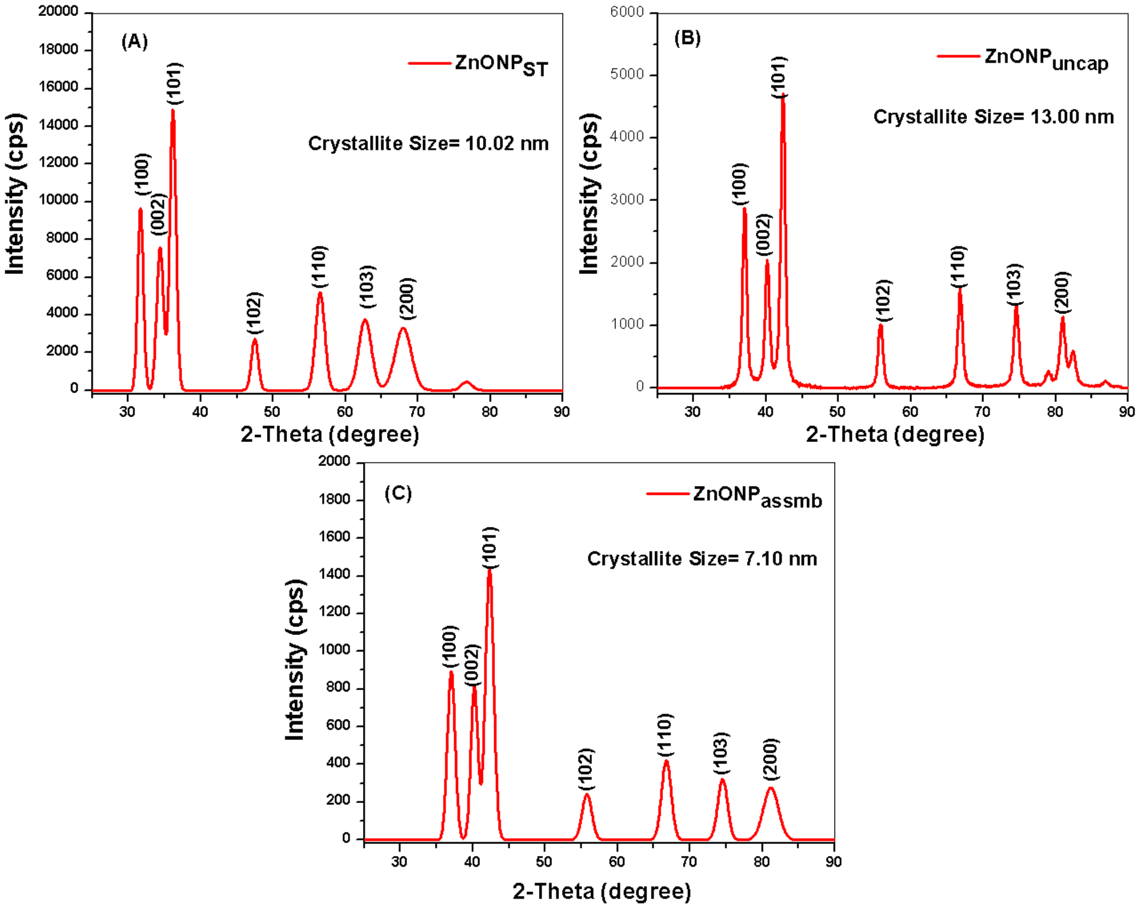

Figure 4.22 XRD analysis of (A) ZnONP$_{ST}$, (B) ZnONP$_{uncap}$, and (C) ZnONP$_{assmb}$ in the range of 25-90^0 was performed. The data were processed, and Gaussian peak was fitted.

4.6.5 Analyzing the surface activity of NP

4.6.5.1 Heavy metal sensing

The order to study surface the interaction of NP with proteins, it is required to conform the active surface properties of our synthesized NP. Hence, we wanted to evaluate the surface activity of our synthesized AuNP$_{ST}$ and AgNP$_{ST}$ (size 7-10 nm, Figure 3F) in the sensing of six heavy metals using optical properties (colorimetric and SPR). Colorimetric sensing and SPR analysis with 50 ppm of Cu^{2+}, Ni^{2+}, Zn^{2+}, Pb^{2+}, Hg^{2+}, and As^{2+} revealed that starch capped AuNP$_{ST}$ (100 µM) was most sensitive with Pb^{2+} and Cu^{2+} (Figure 4.23 7 A and B) and less or insensitive to other four metals. However, AgNP$_{ST}$ showed highest sensitivity to Hg^{2+} (Figure

4.24 A & B) and less/ no sensitivity to other heavy metals. When different concentration of Pb^{2+} (1-20 ppm), Cu^{2+} (10-50 ppm), and Hg^{2+} (1-10 ppm) were mixed with 100 µM of $AuNP_{ST}$ and $AgNP_{ST}$ solution and incubated for 10 min, the change in color from pink to dark ruby red for Pb^{2+}, violet color for Cu^{2+}, and color yellow color of $AgNP_{ST}$ become colorless for Hg^{2+}. Further, the SPR shift and peak broadening was also observed for all tested heavy metals with $AuNP_{ST}$ and $AgNP_{ST}$, which signified the formation of larger particles (Figure 4.23 A and B, and Figure 4.24 A and B). Therefore, in this study, we found that our $AuNP_{ST}$ and AgNP demonstrated sensitivity to heavy metal ions Cu^{2+} , Pb^{2+}, and Hg^{2+}. Moreover, $AgNP_{ST}$ also showed H_2O_2 sensing ability.

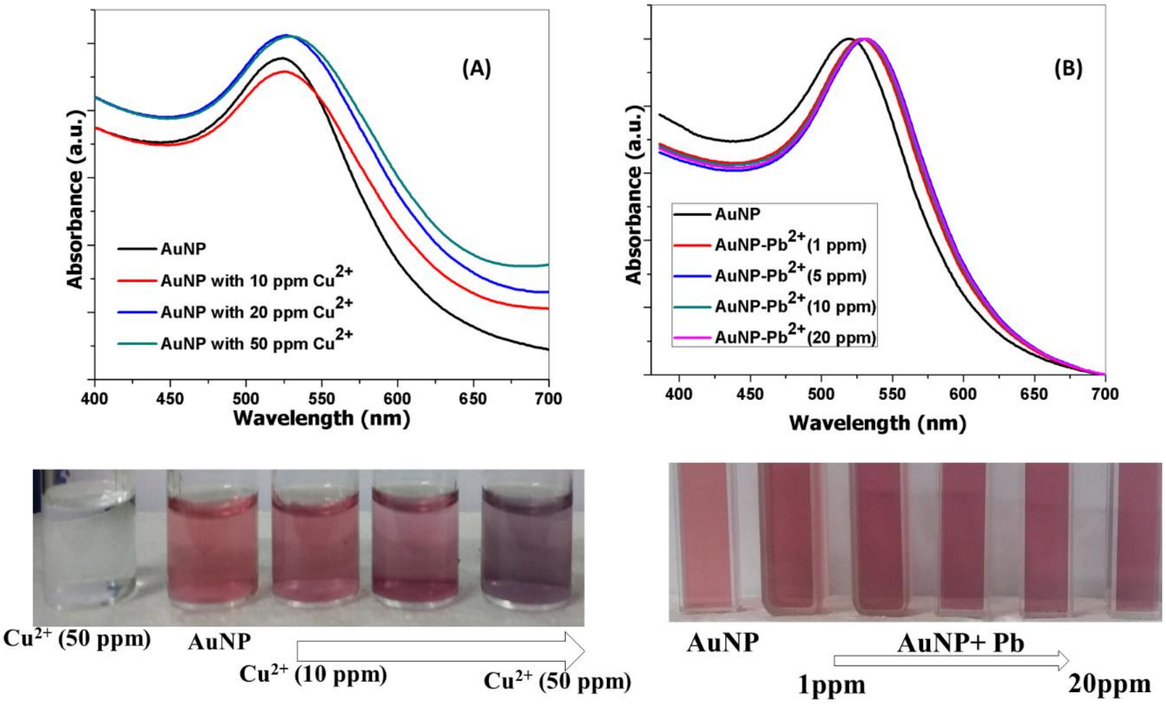

Figure 4.23 The effect of $AuNP_{ST}$ with different concentration of heavy metal in ppm level was analyzed. (A) The effect of $AuNP_{ST}$ with Cu^{2+}. (B) with Pb^{2+}.

4.6.5.2 Photocatalytic degradation of methyl green and rhodamin-B

The photocatalytic degradation ability of ZnONP self-assembly was tested with methyl green (MG) and rhodamine-B (Rho-B) dye. The absorption spectra of dye were measured in the range of between 450 to 700 nm with a 2 h time interval. The photocatalytic degradation of methyl green (Figure.7 A and C) in UV-C showed that the primary absorption peak height for MG dye decreased, and the new secondary peak emerged. It indicated the degradation of MG dye was decreased with time. Moreover, a similar experiment with RhoB was performed, and absorption data was collected with 2 h interval up to 12 h by incubating the sample in UV-C. The decrease in the absorption peak with time obtained that indicated the photo-degradation of Rho-B dye (Figure 4.25 B and D).

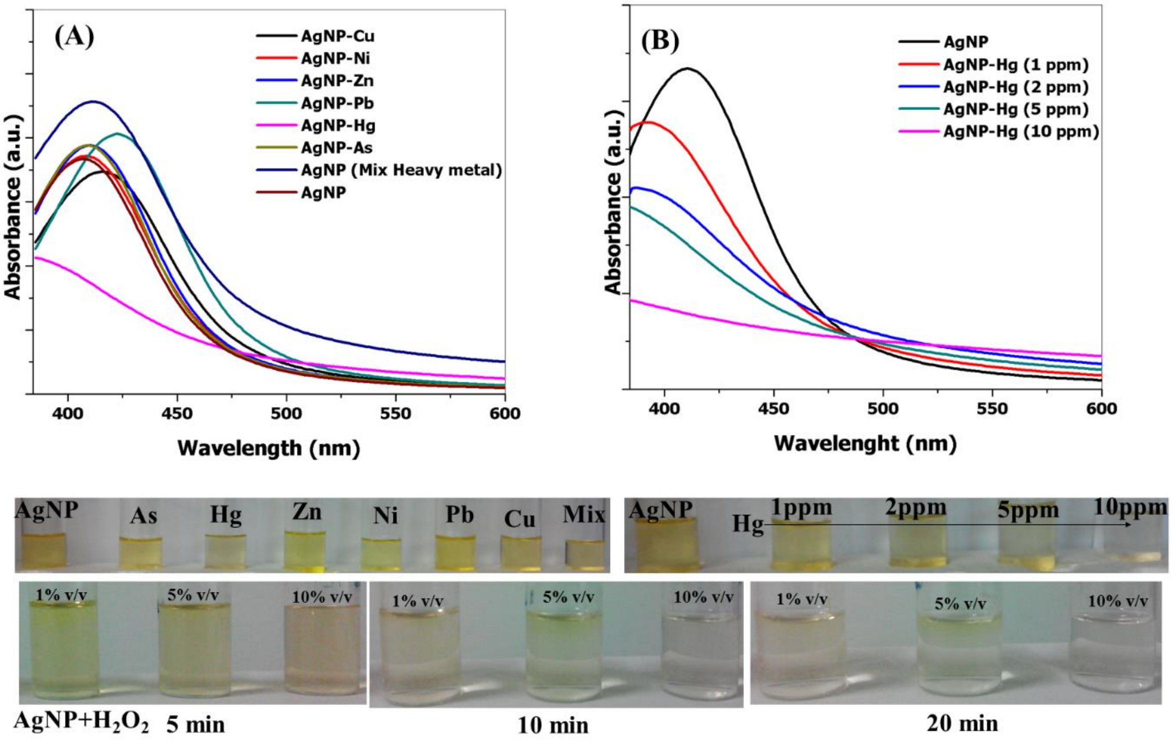

Figure 4.24 The effect of AgNP$_{ST}$ with different concentration of heavy metal in ppm level was analyzed. (A) The effect of AgNP$_{ST}$ with 50 ppm of all metals. (B) with Hg^{2+} (1-10 ppm)

From, surface activity analysis of AuNP, AgNP by analysis of heavy metal sensing and photo-catalytically degradation of dye by ZnONP clearly indicated that the surface of our synthesized NPs was highly active.

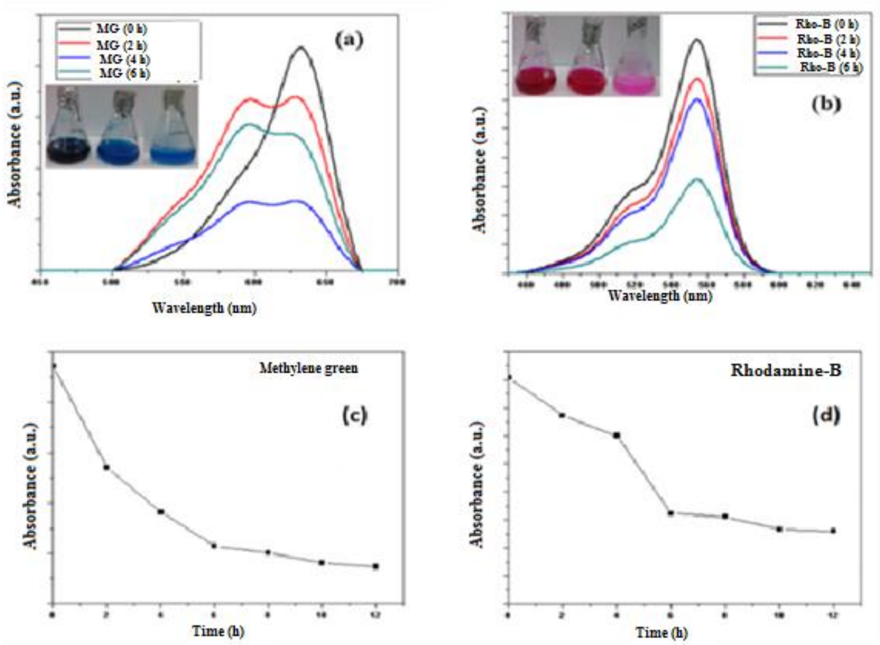

Figure 4.25 Photolytic degradation of dye by ZnONP analyzed by absorption spectroscopy. (A) and (C) Methylene green (MG); (B) and (D) Rhodamine-B

CHAPTER 5

STUDY OF THE INTERACTION BETWEEN NANOPARTICLES AND PROTEINS

5.1 Materials and methods

The detail of nanoparticle synthesis and characterization was described in chapter-4.

5.2 Characterization of NP-protein conjugate

All the NP and protein were mixed in different molar ratios (1:20, 1:10, 1:5, 1:2, 1: 1.5, and 1:1) and were incubate at room temperature for 2 h (to get equilibrium). The formation of NP-protein conjugate was monitored by UV-Vis and tryptophan (Trp) fluorescence spectroscopy of protein (λ_{ex} 280 nm) while stability and hydrodynamic size analysis of conjugate was also observed using DLS analyzer attached with a zeta sizer (ZS-nano series, Malvern Pvt. Ltd).

5.2.1 Fluorescence spectroscopy

The conformational change of protein due to interaction with nanoparticles was analyzed by exciting 7 μM of protein at 295 nm and recording variation in intrinsic fluorescence emission in the range of 300 to 400 nm. Fluorescence spectroscopic analysis was performed by using Cary eclipse fluorescence spectrometer (Agilent Pvt. Ltd.) when emission and excitation slit width was fixed at 5 and 10 nm, respectively. The baseline correction was performed with respect to buffer and nanoparticle concentration.

5.2.2 Circular dichroism spectroscopy measurement

The secondary structural contents of BLA and HEWL were measured using circular dichroism (CD) spectroscopy (Jasco 815) under constant N2 purging. Protein concentration of 14 μM was used in sodium phosphate buffer (pH 7.4, 20 mM) with different molar ratio of NP to protein (1:1, 1:2, 1:4, 1:8, and 1:10). The effect of different concentration of NP was analyzed in the range of 200-260 nm. The PMT voltage of below 600 V during analysis. The data obtained was average of three scans of data collected with 1 nm interval. The obtained data was converted to molar residual ellipticity using following equation:

$$\boldsymbol{MRE} = \frac{\boldsymbol{Observed}\,[\boldsymbol{\theta}]\cdot\ \mathbf{10^6}}{\boldsymbol{n}\cdot\ \boldsymbol{c}\cdot\ \boldsymbol{l}} - - - - - - - - (\mathbf{1})$$

Here, n is a number of amino acids, ‘c’ is the concentration of protein in µM, ‘l’ is path length in mm.

5.2.3 Lysozyme activity assay

The lysozyme activity was analyzed by the method as suggested by Shugar [172] with some modification. The decrease in turbidity of 0.01 per minute was a measurement at 450 nm, at 25 ^{0}C and pH 7.4, as one unit of enzyme activity. For analysis of enzyme activity, *Micrococcus lysodeikticus* cells of 18 mg were prepared in phosphate buffer, and volume was made up to 30 ml. For 3 ml enzyme assay, 2.9 ml of *lysodeikticus* solution was prepared by adding 1.5 ml from stock and 100 µl of protein was added from 3 mg/ml lysozyme solution. The variation in turbidity at 450 nm was measured up to 10 min with 1 min interval and the activity of lysozyme was calculated by using following equation:

$$\boldsymbol{Unit/mg} = \frac{\boldsymbol{\Delta A_{450\,nm}}\cdot\ \mathbf{1000}}{\boldsymbol{mg\ enzyme}} - - - - - - - - (\mathbf{2})$$

Here, ΔA is OD difference of sample between two times intervals, enzyme activity expressed in unit/mg.

5.2.4 Effect of guanidine hydrochloride:

Guanidine hydrochloride (GdnHCl) is strong denaturant used to study protein unfolding. The change of protein conformation was analyzed by tryptophan fluorescence analysis and circular dichroism (CD) spectroscopy analysis. For the unfolding study, 10 µM of protein was incubated at room temperature for 2 h in different concentrations of GdnHCl (0, 1, 2, 4, 6 M). For the refolding study, the 700 µM protein sample was incubated in 8 M GdnHCl for 2 h. The solution was further diluted by 70 fold and incubated for 2 h in similar condition and refolding was measured. The samples were analyzed using Trp fluorescence, and CD spectra.

5.2.5 Analyzing the thermal stability of protein

Thermal stability of protein was analyzed by incubating the protein and NP (complex) at different temperature (25-60 ^{o}C) with a step size of 5 ^{o}C during heating and cooling with stabilization time 10 min after each step. The variation in Trp fluorescence and CD spectra was analyzed by fluorescence and CD spectroscopy, as described above.

5.2.6 Surface hydrophobicity analysis

The surface hydrophobicity of NP-protein complex was analyzed by 8-anilino naphthalene sulfonic acid (ANS) binding assay. The protein samples (10 µM) (both free and NP-protein complex) (1:2 molar ratio) and 300 µM of ANS were incubated in sodium phosphate buffer (pH 7.4) for 30 min and samples were analyzed by exciting at 350 nm. The emission was recorded between 400-650 nm with excitation and emission slit width of 5 and 10 nm, respectively.

5.2.7 Proteinase-K digestion assay

To study the effect of proteinase K (PK) digestion of BLA and HEWL in NP conjugate (NP: 5 µM; BLA: 1.6 mg/ml), we incubated the conjugate solution with a various concentration of PK (0, 1, 3, 5, 7 µM). All the samples were incubated at RT for 10 min, and the reaction was stopped by adding 20 µM of PMSF. The samples were loaded onto 15% SDS-PAGE gel. The Biorad electrophoretic mini-gel apparatus was used, while the image was collected by Biorad gel doc instrument. All experiments were independently performed, and an equal amount of protein (20-40 µg) was loaded in each well.

Further, test tube base ANS assay was also performed with BLA and HEWL with NP. All the samples were incubated at RT for 10 min, and the reaction was stopped by using 20 µM of phenylmethane sulfonyl fluoride (PMSF). The samples were further diluted so that final protein concentration becomes 10 µM and incubated with 400 µM ANS for 20 min. The sample was excited at 350 nm and emission was collected in the range of 400-600 nm with fixed slit width of 10 nm. To, analyze the susceptibility of protein towards PK, we calculated the final ANS fluorescence using following equation:

$$\mathbf{F_{net} = F_{PNK} - (F_P - F_K - F_N) - - - - - - - - (3)}$$

Here, F_{net} is ANS fluorescence due to exposure of new hydrophobic sites. F_{PNK} is ANS fluorescence of test sample, F_P is ANS fluorescence of control sample without proteinase-K, F_K is ANS fluorescence of PK, F_N is ANS fluorescence of NP. The F_{net} fluorescence was plotted with respect to proteinase-K (PK) concentration. The hypothesis was digestion of protein by PK exposed the new hydrophobic sites of proteins, which will increase/decrease with variation in protein susceptibility with various concentration of PK.

5.3 Results and discussion

5.3.1 Analyzing the interaction of protein with nanoparticles

5.3.1.1 UV-Vis spectroscopic analysis

Surface plasmon analysis (SPR) is a very sensitive method to study the interaction of metal nanoparticles with biomolecules because SPR depends on the surface properties of the metal NP, and surface properties of NP vary with the change in size, shape, local environment and dielectric properties of NP [2]. We incubated different concentration of BLA and HEWL (10, 20, and 40 μM) with fixed concentration of both the NP (20 μM) in sodium phosphate buffer at RT for 2 h to reach equilibrium, which was shown by no further shift in SPR after 2 h.

The starch capped gold nanoparticle ($AuNP_{ST}$) was scanned in the range of 400-700 nm, while starch capped silver NP ($AgNP_{ST}$) was scanned between 300-700 nm. The results showed that the interaction of $AuNP_{ST}$ and BLA causes a red shift in surface plasmon resonance (SPR) (1-3 nm) (Figure 5.1 A) while the interaction of BLA with $AgNP_{ST}$ showed the SPR shift of 5-8 nm (Figure 5.1 B).

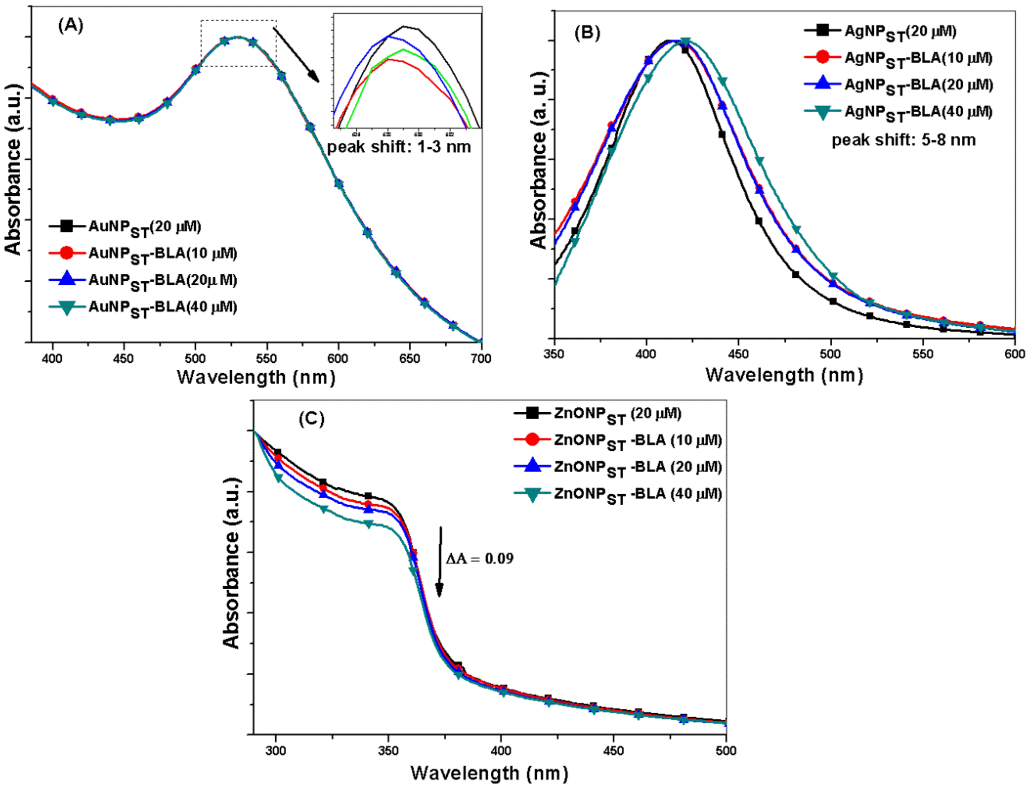

Figure 5.1 BLA and NP interaction monitored by Spectroscopy. The shift in UV-Vis absorption peak due to BLA interaction was monitored. (A) AuNP$_{ST}$-BLA, (B) AgNP$_{ST}$-BLA, (C) ZnONP$_{ST}$-BLA.

A shift in absorption maxima of NP indicates the molecules induced alteration over NP [3]. Further, it was observed that the interaction of AuNP$_{ST}$ and AgNP$_{ST}$ with HEWL in similar condition causes 10-15 nm (Figure 5.2. A) and 8-10 nm shift (Figure 5.2. B), respectively. This fact clearly confirmed the interaction of AuNP$_{ST}$ and AgNP$_{ST}$ with BLA and HEWL.

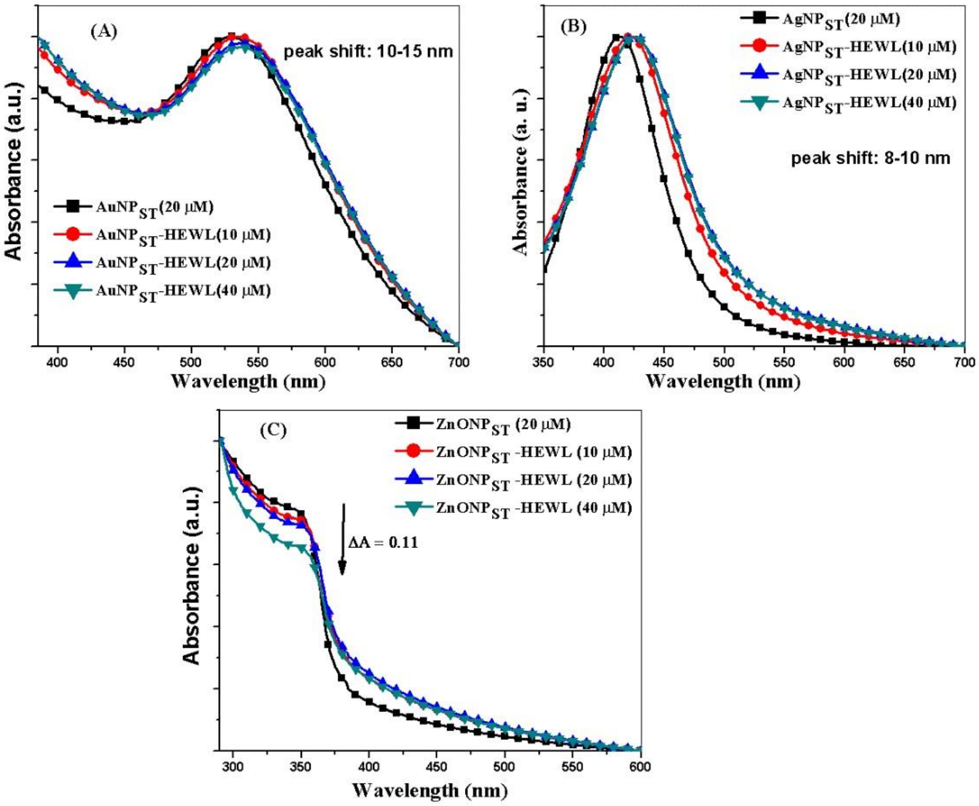

Figure 5.2 Interaction of HEWL was analyzed with various NP (AuNP$_{ST}$, AgNP$_{ST}$, and ZnONP$_{ST}$). The shift in UV-Vis absorption peak due to HEWL interaction was monitored. (A) AuNP$_{ST}$-HEWL, (B) AgNP$_{ST}$-HEWL, (C) ZnONP$_{ST}$-HEWL.

The band gap analysis of starch capped zinc oxide nanoparticle (ZnONP$_{ST}$) with different concentrations (10, 20, and 40 µM) of BLA and HEWL was performed in sodium phosphate buffer. We found that interaction of BLA causes a reduction in UV absorption of ZnONP$_{ST}$ while interaction with a similar amount of HEWL reduces the UV absorption in greater extent (Figure 5.2 C). The UV-Vis spectra of ZnONP$_{ST}$ with different concentration of BLA and HEWL showed quenching in UV absorption perhaps due to the formation of protein corona over NP.

From SPR shift and band gap analysis of tested NP, when surface capping agent was same, indicated that SPR of AuNP$_{ST}$ was more sensitive to interaction, and SPR shift clearly varies with the type of protein at the interface of NP. It showed higher SPR shift when a protein with opposite zeta potential (i.e. HEWL) interact with AuNP$_{ST}$ (Figure 5.1 A and Figure 5.2 A). Band gap analysis of ZnONP$_{ST}$ also showed that the UV absorption was affected to a greater extent by the interaction of opposite net charge of protein (Figure 5.1C and Figure.5.2 C). However, $AgNP_{ST}$ showed a slight difference in SPR with two proteins and only showed a shift of 5-8 nm with BLA, and 8-10 nm with HEWL, respectively. Metal nanoparticle showed highly sensitive surface plasmon resonance (SPR), which can be utilize for biomolecule detection such as protein, and nucleic acid. You et al. [173] synthesized the fluorescence AuNP for detection of protein. Nath and Chilkoti utilized colorimetric sensing and SPR of gold nanoparticle for biomolecular detection [6]. Nam et al. [174] used antibody capped gold nanoparticle for identification of various proteins. Lee and El-Sayed also reported the effect of size, shape, and metal composition of gold and silver nanoparticle in sensing and imaging [4]. Therefore, SPR shift due to biomolecular interaction confirm the interaction of protein with nanoparticle. The variation in SPR shift and band gap due to interaction with BLA and HEWL also indicated that UV-Vis spectra shift also vary with protein on the nanoparticle surface.

5.3.1.2 Hydrodynamic size analysis

DLS size analysis was performed to analyze the hydrodynamic size distribution of NP, pure protein (BLA, and HEWL) and NP-protein (BLA, and HEWL) complex. Hydrodynamic size analysis showed that major population of BLA and HEWL were 2.2 nm and 1.5 nm size. Further, analyzing the hydrodynamic size of NP and protein conjugates showed that $AuNP_{ST}$ and $AgNP_{ST}$ formed highly poly-dispersed protein-NP conjugate (Figure 5.3 A & B, and Figure 5.4 A & B) while $ZnONP_{ST}$ showed less poly-dispersed conjugate with the size of below 100 nm (Figure 5.3. C and Figure 5.4. C).

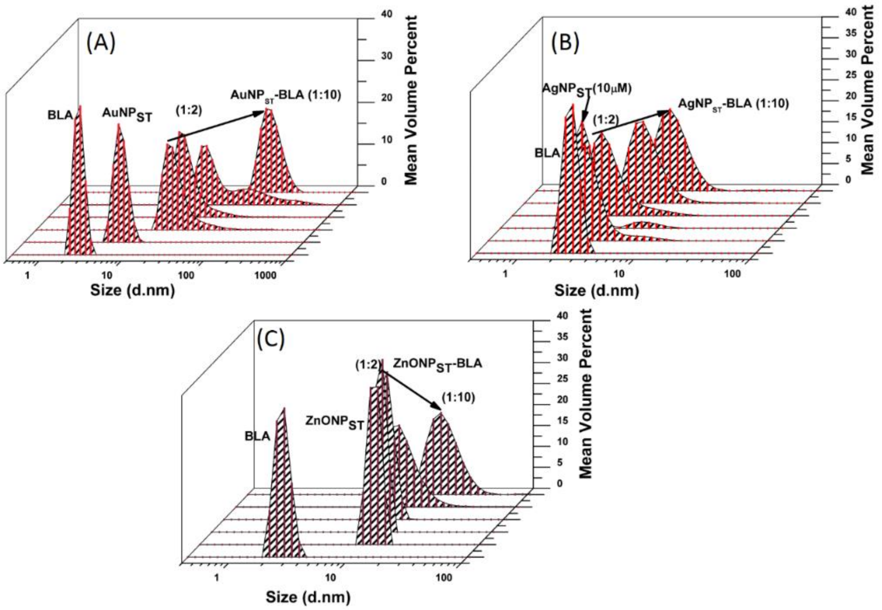

Figure 5.3 Hydrodynamic size distribution of NP-protein conjugates. (A) AuNP$_{ST}$-BLA, (B) AgNP$_{ST}$-BLA, (C) ZnONP$_{ST}$-BLA

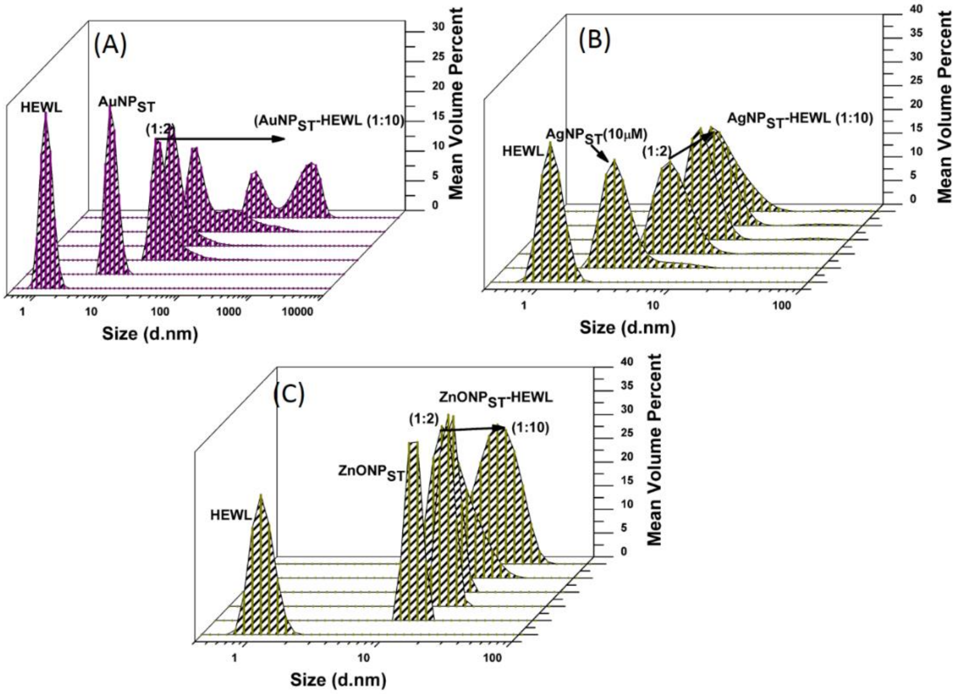

Figure 5.4 Hydrodynamic size analysis of AuNP$_{ST}$, AgNP$_{ST}$, and ZnONP$_{ST}$ and their conjugates with HEWL. Hydrodynamic size distribution of (A) AuNP$_{ST}$-HEWL (B) AgNP$_{ST}$-HEWL, (C) ZnONP$_{ST}$-HEWL conjugates.

The results showed that $ZnONP_{ST}$ of 30 nm produces larger conjugates of NP-HEWL. The DLS analysis of conjugates showed that the size of NP-HEWL conjugate varies with the variation of NP core material and protein. BLA formed smaller NP-protein conjugate with higher polydispersity while HEWL having a net positive surface charge trigger to form larger NP-protein conjugates (Figure 5.4). However, $AuNP_{ST}$ showed polydispersed conjugates with both the proteins (Figure 5.3 A and Figure 5.4 A).

5.3.1.3 FESEM analysis of conjugates

The field emission scanning electron microscopy (FESEM) was performed in cryo-mode to visualize the morphology, shape, and size of conjugates. The results revealed the presence of both small and larger aggregate of the random shape of BLA (Figure 5.5 A). The FESEM analysis also showed that $AuNP_{ST}$-BLA conjugate produced the very small size of conjugates with only a few larger aggregates (Figure 5.5 B) indicated a thick layer of BLA over $AuNP_{ST}$. The $AgNP_{ST}$-BLA and $ZnONP_{ST}$-BLA conjugates showed both larger and smaller aggregates of spheroidal and random shape (Figure 5.5 C & D). It was observed that $ZnONP_{ST}$ formed a more spherical shaped particle of larger size (Figure 5.5 D).

FESEM analysis of HEWL showed uniformly distributed spheroidal shape particles with some larger aggregates (Figure 5.6 A). The $AuNP_{ST}$ and $ZnONP_{ST}$ with HEWL revealed random shape conjugates (Figure 5.6 B & D) while $AgNP_{ST}$-HEWL conjugates showed both larger and smaller spherical particles with some aggregates (Figure 5.6 C).

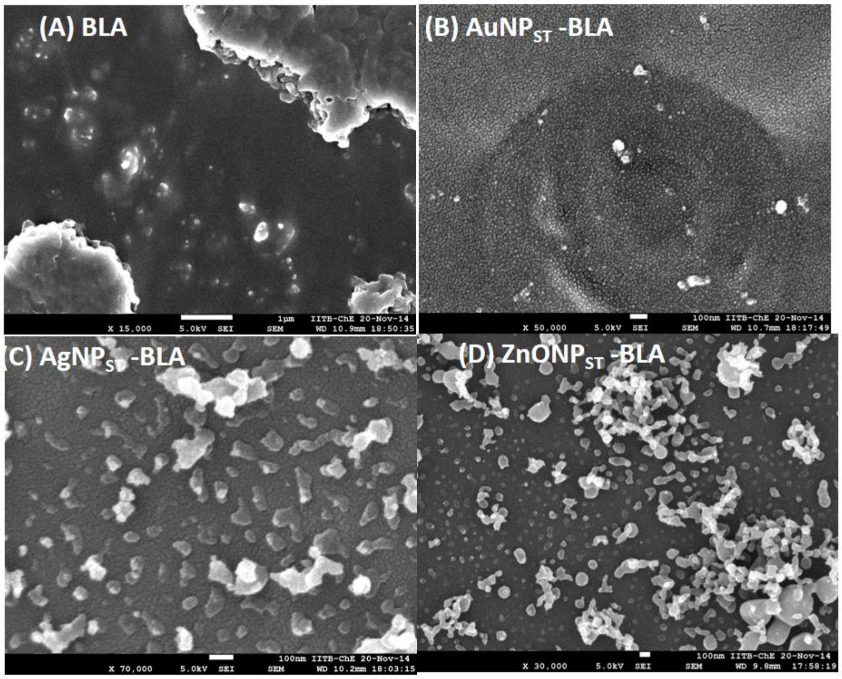

Figure 5.5 FESEM analysis of BLA and its conjugate with different NP (Au, Ag, ZnO). (A) BLA (random aggregates), (B) AuNP$_{ST}$-BLA, (C) AgNP$_{ST}$-BLA, (D) ZnONP$_{ST}$-BLA conjugate.

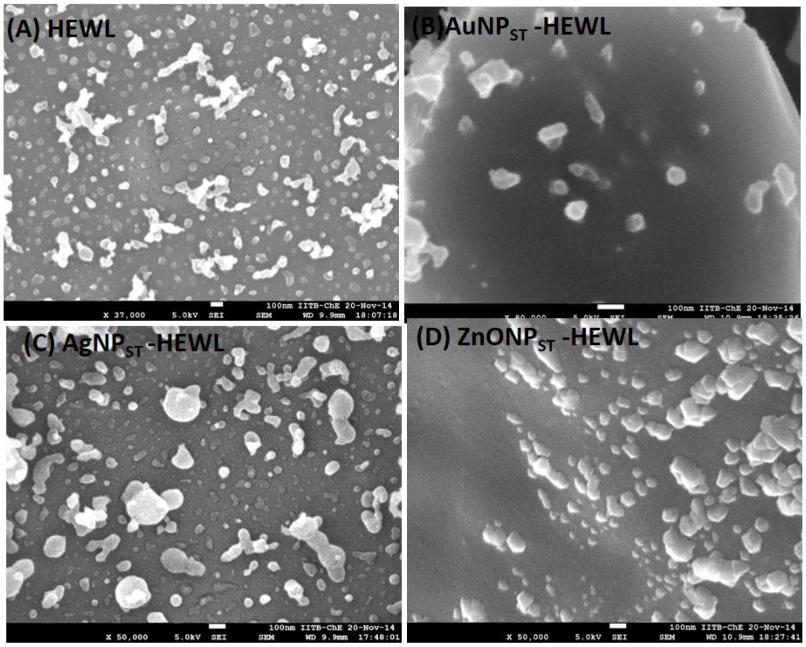

Figure 5.6 FESEM analysis of HEWL and its conjugate with different NP (Au, Ag, ZnO). (A) HEWL, (B) AuNP$_{ST}$-HEWL, (C) AgNP$_{ST}$-HEWL, (D) ZnONP$_{ST}$-HEWL.

From FESEM image of conjugates, it was clear that HEWL interaction with all three NP formed larger particles, which indicates the formation of a multilayer of protein over NP surface. However, BLA formed smaller conjugates but showed more poly-dispersity. The shape of conjugate also varies with NP and protein as HEWL with $AgNP_{ST}$ formed spherical particle while HEWL formed random shape structure with other two NP. It was also revealed that $AuNP_{ST}$ forms the smallest conjugate with BLA. Therefore, our DLS and FESEM analysis confirmed the formation of NP-protein conjugates with different size, shape, and polydispersity. The amount of protein adsorbed on the surface of NP depends on the core material of NP and type of protein interacting with NP.

5.3.1.4 Surface zeta potential of conjugate

Further, we wanted to analyze the stability of different NP-protein conjugates in the sodium phosphate buffer. Therefore, the zeta potential of NP-protein conjugates was analyzed. Surface zeta potential of BLA (-15.1 mV) with $AuNP_{ST}$ (-20.6 mV), $AgNP_{ST}$ (-24.2 mV), and $ZnONP_{ST}$ (-26.9 mV) showed zeta potential of -16.4 mV, -11.6 mV, and -14.04 mV (Figure 5.7) while conjugate with HEWL (+6.09 mV) showed zeta potential of -14.6 mV, -6.37 mV, and -16.7 mV (Figure 5.8), respectively. The zeta potential analysis of NP, proteins, and NP-protein conjugates showed that stability of conjugate decreased with respect to NP and protein, but it varies with the core material of NP and protein. From zeta potential analysis, it was revealed that $AgNP_{ST}$ produced conjugates with the low stability of both the proteins while $AuNP_{ST}$-BLA and $ZnONP_{ST}$-HEWL produced conjugates with the high stability.

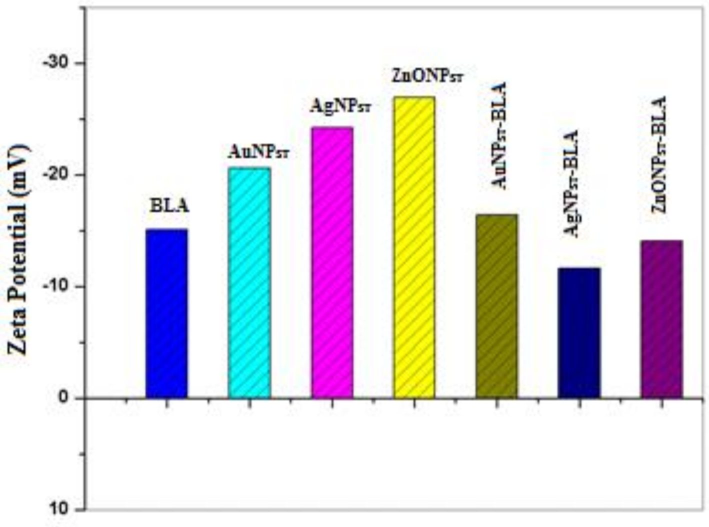

Figure 5.7 Effect of AuNP$_{ST}$, AgNP$_{ST}$, and ZnONP$_{ST}$ on the colloidal stability of NP-protein conjugates. Zeta potential analysis of various NP-BLA conjugates.

The solution stability of NP-protein conjugate decreased in biological solution; therefore, there were higher chances of larger particle formation. Another important point is the stability of conjugate depends on the core material of NP. The decrease in zeta potential also indicated that interaction of NP and protein is electrostatic in nature because BLA has both negative and positively charged patches, which showed a decrease in zeta potential. Similarly, HEWL showed net negative zeta potential due to electrostatic interaction of positively charged patches of HEWL and negatively charged NP surface. Therefore, HEWL conjugate with all NP showed negative zeta potential. Surface zeta potential play crucial role in stability of colloidal solution, and protein in aqueous environment. Jiang et al. [175] higher surface charge help to prevent aggregation of nanoparticle. Patil et al. [176] reported that protein adsorption and cellular uptake of nanoparticle depends on the surface zeta potential. Moreover, Zhang et al. [177] reported that surface zeta potential play crucial role in cellular uptake. Therefore, higher zeta potential of colloidal solution not stabilize the conjugate but also play important role in biological uptake and disease cell killing.

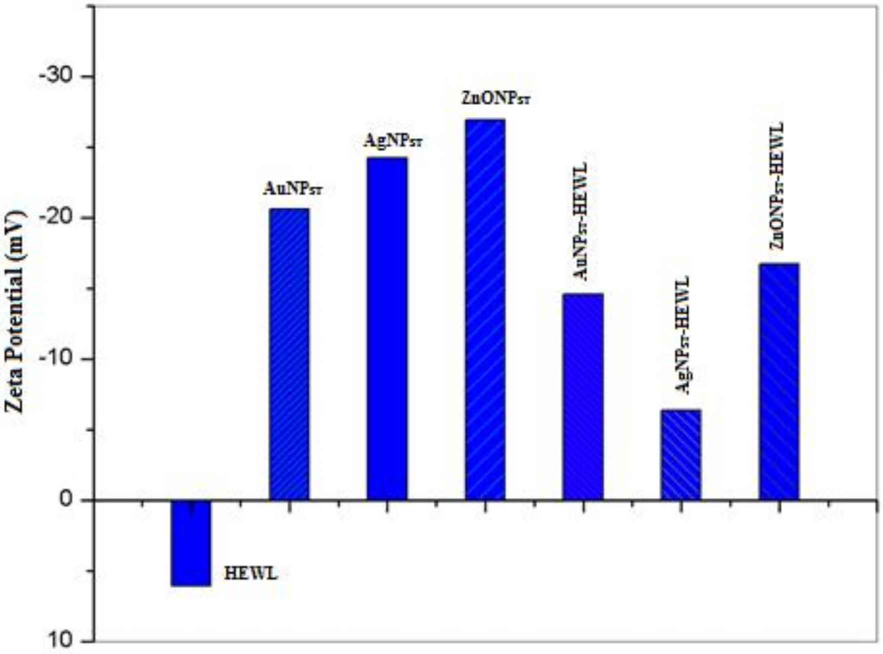

Figure 5.8 Effect of AuNP$_{ST}$, AgNP$_{ST}$, and ZnONP$_{ST}$ on the colloidal stability of NP-protein conjugate. Zeta potential analysis of different NP-HEWL conjugates.

5.3.1.5 Surface hydrophobicity analysis

The surface hydrophobicity of protein plays an important role in the stability of protein in solution [178, 179]. It interaction of NP with protein altered the protein structure and might expose or protect the hydrophobic surfaces in protein; hence, it affects the stability of proteins. For surface hydrophobicity, analysis of 10 µM of BLA and HEWL was used. The surface hydrophobicity analysis of BLA showed that interaction of AgNP$_{ST}$ and ZnONP$_{ST}$ (NP: protein, 1:2 molar ratio) decrease the surface hydrophobicity of BLA while AuNP$_{ST}$ interaction with BLA increased the surface hydrophobicity of protein (Figure 5.9 A). ANS binding assay showed that interaction of AgNP$_{ST}$ and ZnONP$_{ST}$ with BLA protect the hydrophobic surface of protein, therefore, reduces the chances of hydrophobic interaction while AuNP$_{ST}$ causes exposure of the hydrophobic surface of BLA; which increased the chance of hydrophobic interaction leading to protein aggregation.

Moreover, a similar study was performed with HEWL and NP showed that AuNP$_{ST}$ and ZnONP$_{ST}$ increased the surface hydrophobicity of protein while AgNP$_{ST}$ reduced the surface hydrophobicity of protein. Therefore, $AuNP_{ST}$ and $ZnONP_{ST}$ interaction with HEWL increased the chance of hydrophobic interaction and formation of larger particles while $AgNP_{ST}$ prevents such kind of interactions (Figure 5.9 B). For this analysis, the effect of NP and ANS binding and ANS (without NP) were also analyzed (Figure S14). The result showed that the emission spectra of ANS with and without NP showed insignificant difference.

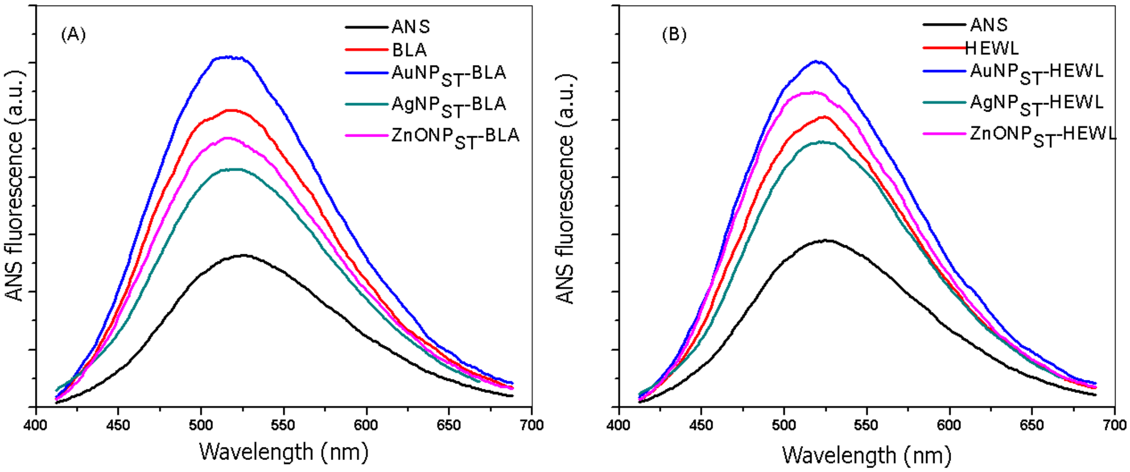

Figure 5.9 Effect of $AuNP_{ST}$, $AgNP_{ST}$ and $ZnONP_{ST}$ on the surface hydrophobicity of NP-protein conjugate. (A) BLA with NP, (B) HEWL with NP.

Zeta potential and surface hydrophobicity analysis showed that interaction of NP with protein vary with the change in nanoparticle material and type of protein interacting with NP, which is responsible for the colloidal stability of NP-protein complex in solution. The protein surface hydrophobicity plays important role in stability and protein-protein interaction and ultimately aggregation. The interaction of protein hydrophobic site at the interface prevent hydrophobic interaction while exposed of hydrophobic surface reduces the protein stability in aqueous environment. Vegenede et al. [180] glycerol interact with the large patches of protein hydrophobic surface; therefore, prevent aggregation of protein in solution. Chi et al. [181] reported the various factors such as pH, salt, and surfactant concentration in stability of protein structure. The salt and pH help to maintain surface charge while variation in surface hydrophobicity also paly crucial role in aggregation of proteins.

5.3.1.6 Fluorescence spectroscopy of protein

Tryptophan fluorescence spectra were recorded to get the information regarding protein conformational changes. Trp fluorescence is highly sensitive to its microenvironment and other weak interactions. The exposure of Trp towards polar environment causes a red shift in emission intensity; similarly, movement toward non-polar environment exhibit blue shift in Trp fluorescence [182-184]. BLA contain four tryptophan buried in protein [185] and HEWL has six tryptophan (three buried and three in active site of protein) [186]. Therefore, analyzing the Trp fluorescence intensity provides valuable information about interaction and conformational changes in protein.

Therefore, the effect of different concentration of $AuNP_{ST}$, $AgNP_{ST}$, and $ZnONP_{ST}$ on intrinsic fluorescence of BLA and HEWL was analyzed. The NP were mixed with fixed amount of protein (7 μM) in different molar ratio such as 1:20, 1:10, 1:5, 1:2, 1: 1.5, and 1:1 and the samples were incubated for 2 h to get the equilibrium at room temperature (25 ^{0}C) (See Figure S8-S13 and Figure 5.10). Further, all the samples were analyzed by the exciting sample at 295 nm when excitation and emission slit width was fixed at 5 nm and 10 nm, respectively. The result showed the quenching of overall emission spectra of both the proteins, which indicates the interaction of NP_{ST} with proteins in different extent with shift in emission spectra.

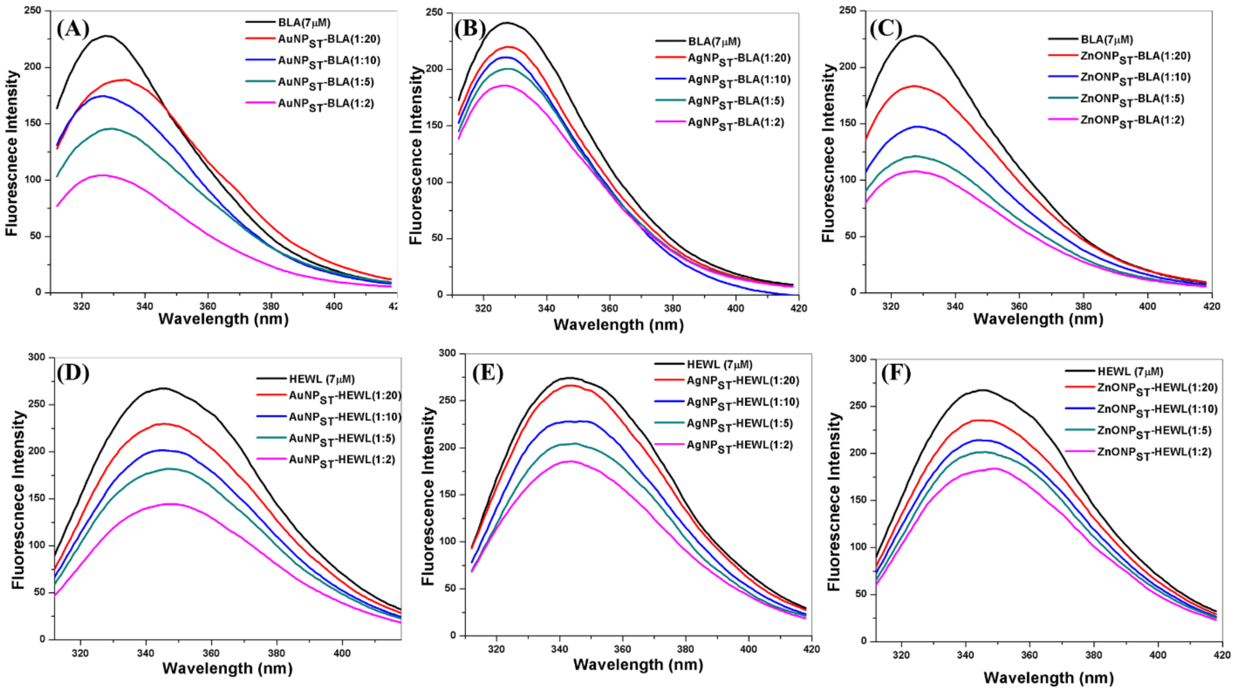

Figure 5.10 Trp fluorescence quenching of BLA and HEWL with different concentration of NP (AuNP$_{ST}$, AgNP$_{ST}$ and ZnONP$_{ST}$). (A), (B), and (C) Trp fluorescence quenching of BLA, (D), (E), and (F) Trp fluorescence quenching of HEWL was plotted in the range of 300-420 nm. The result showed the different extent of fluorescence quenching due to interaction with NP.

BLA interaction with AuNP$_{ST}$ and ZnONP$_{ST}$ causes quenching of Trp fluorescence to a greater extent (Figure 5.10 A and C). Moreover, BLA with AuNP$_{ST}$ showed a red shift in Trp emission peak (328 nm to 333 nm); however, ZnONP$_{ST}$ showed a blue shift in Trp fluorescence. Therefore, the fluorescence quenching in AuNP$_{ST}$-BLA might be due to the exposure as well as the interaction of BLA with NP. However, blue shift (328-326 nm) with greater extent of quenching of Trp with ZnONP$_{ST}$ might be due to movement of Trp towards the non-polar environment and interaction of ZnONP$_{ST}$ (Figure 5.10 C). BLA interaction with AgNP$_{ST}$ also exhibit Trp fluorescence quenching (less quenching than AuNP$_{ST}$, ZnONP$_{ST}$) with a blue shift in emission (328-324 nm) indicated the alteration in BLA structure that might cause movement of Trp to the non-polar environment (Figure 5.10 B).

Further, we also performed a similar experiment with another protein hen egg white lysozyme (HEWL), which is homologous to BLA protein but have net positive surface charge. It was observed that interaction of AgNP$_{ST}$ with HEWL causes quenching and blue shift (3 nm) in

Trp fluorescence (i.e. 344 to 342 nm) (Figure 5.10 E) while $ZnONP_{ST}$ showed quenching with red shift (344 to 349 nm) in Trp fluorescence (Figure 5.10 F). Trp fluorescence analysis indicated that interaction of $AgNP_{ST}$ shifts the Trp towards the non-polar environment, which might be due to $AgNP_{ST}$-HEWL interaction but simultaneous quenching in Trp fluorescence (Figure 5.10 E) was also observed. However, it was observed from Trp fluorescence analysis with different concentration of $AuNP_{ST}$ that the NP quenched the Trp fluorescence in a higher extent than $AgNP_{ST}$ and $ZnONP_{ST}$ but also showed the red shift in Trp fluorescence (344 to 347) (Figure 5.10 D). The red shift and quenching in Trp fluorescence indicated the movement of Trp towards the polar environment. Some previous reports earlier demonstrated the fluorescence quenching of ZnONP (uncapped) and AuNP (citrate-capped) by interacting with BSA, HEWL, and BLA [187-189]. Therefore, we concluded that interaction of $AuNP_{ST}$ and $ZnONP_{ST}$ might alter the BLA structure and Trp fluorescence quenching might be due to both exposures of the Trp to polar environment and interaction with NP. However, $AgNP_{ST}$ interaction with BLA might shift the Trp toward non-polar environment or interact near Trp to protect it from the polar environment.

5.3.1.7 Circular dichroism of proteins

Further, we also analyzed the secondary structure variation by circular dichroism spectroscopy. The obtained data converted to molar residual ellipticity (MRE) by using equation given in “method” section. MRE value at 222 nm represents variation in the α-helix content of protein [190] while at 218 nm indicates β-sheet content [191]. The interaction study with BLA and all three NP showed that increasing concentration of NP causes an increment of the α-helix content of BLA (Figure 5.11 A-C), and the highest effect is shown by $AuNP_{ST}$. Analyzing the circular dichroism (CD) data using online server CAPITO [192] showed the gain of α-helix (32% to become 53%) and loss of β-sheet (22% to 9%) in BLA (Figure 5.11 A). The gain of α-helix and simultaneous drop in of β-sheet made the protein structure highly flexible due to NP-protein interaction.

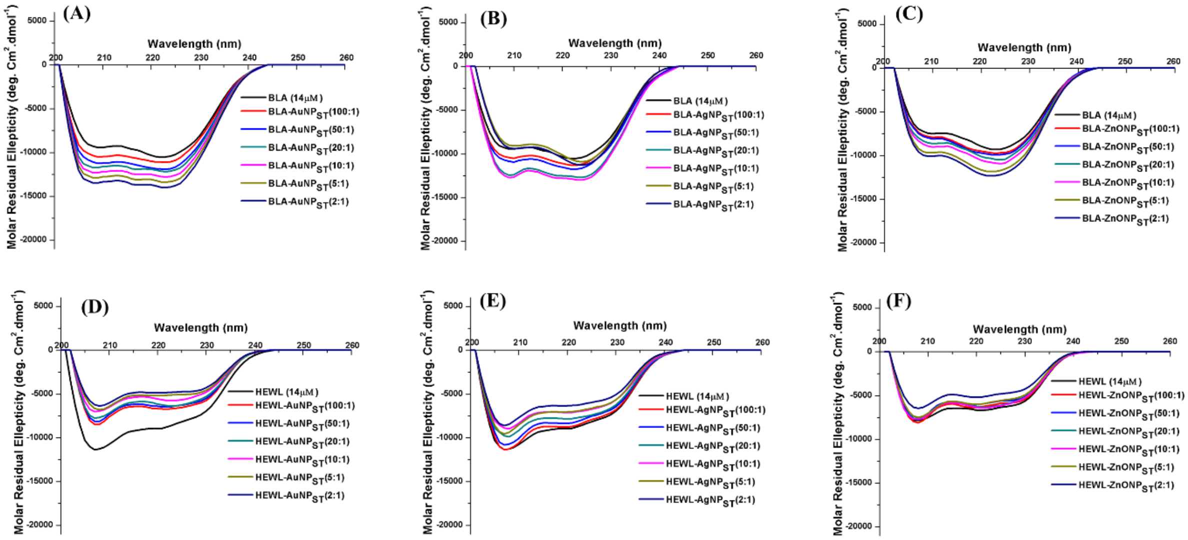

Figure 5.11 CD spectra of BLA with different concentration of (A) AuNP$_{ST}$, (B) AgNP$_{ST}$, and (C) ZnONP$_{ST}$; CD spectra of HEWL with (D) AuNP$_{ST}$, (E) AgNP$_{ST}$, (F) ZnONP$_{ST}$.

When, we analyzed the effect of various concentrations of AuNP$_{ST}$, AgNP$_{ST,}$ and ZnONP$_{ST}$ on HEWL secondary structure, it was observed that interaction of these NP (AuNP$_{ST}$ and AgNP$_{ST}$) with HEWL causes a substantial increase of β-sheet content with increasing NP concentration. (Figure 5.11 D-F). However, HEWL showed increment in α-helix content (41% to 54%) with ZnONP$_{ST}$ at the expense of β-sheet. The interaction between HEWL and all three NP revealed that the β-sheet content was increased by almost to two folds when the concentration of metal NP such as AuNP$_{ST}$ and AgNP$_{ST}$ were increased, perhaps at the expense of α-helix content (Figure 5.11 D-F), However, the ZnONP$_{ST}$ causes increase in α-helix content of both BLA and HEWL. Therefore, it was observed that interaction of AuNP$_{ST}$ and AgNP$_{ST}$ increased the flexibility in BLA by increasing α-helix content while increasing the rigidity in HEWL by increasing β-sheet content. However, it clearly indicated that ZnONP$_{ST}$ tends to increase the α-helix content of both BLA and HEWL (Figure 5.11 A -F). Further, we observed that increasing NP concentration initially altered the protein secondary structure; however, after approaching certain concentration ratio (10:1 to onward) there was no change in CD spectra shape, which indicated that nanoparticle-protein interaction depends on the availability of free protein in the solution. However, in absence of free protein for interaction, NP not able to alter the structure but either quench or enhance the CD spectra (Figure 5.11 A-F).

5.3.1.8 Effect of NP interaction on HEWL activity

From activity assay, it was observed that interaction of NP causes loss of enzyme activity of lysozyme. It clearly showed that $AgNP_{ST}$ causes the highest loss in enzyme activity (~30%) of HEWL (Figure 5.12) while $ZnONP_{ST}$ causes least. This fact also indicated that the structural change also altered the catalytic site of HEWL, which must be due to overall conformational changes of the protein.

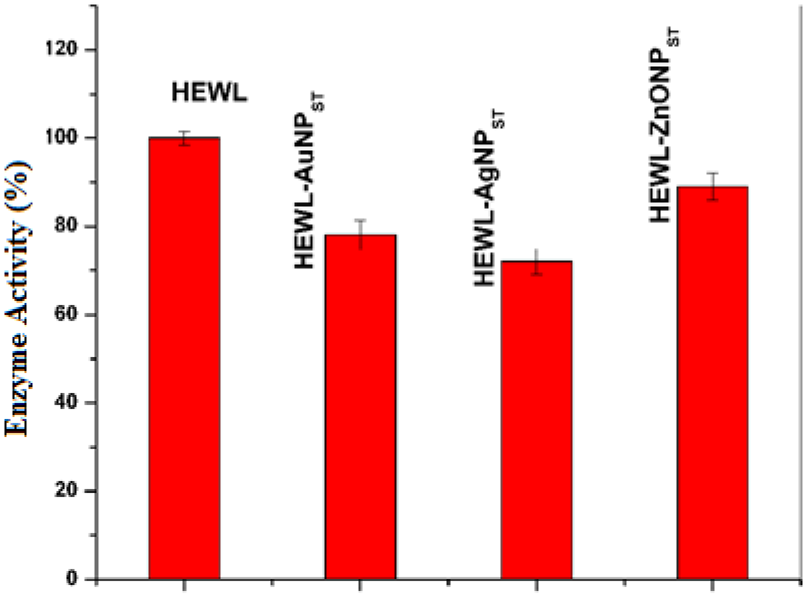

Figure 5.12 The enzyme activity analysis of HEWL after the interaction with different NPs.

5.3.1.9 Effect of NP on unfolding and refolding of proteins

The guanidine hydrochloride (GdnHCl) is a strong denaturant used to analyze the unfolding of various model proteins. Here, we analyzed the unfolding and refolding of both the proteins (10 µM). To analyze the unfolding of BLA and HEWL, different concentration of guanidine hydrochloride (0-6 M) was used. All the protein samples were incubated at 25 ^{0}C for 2 h to attain unfolding equilibrium. In an another experiment, protein stock solution (700 µM) was incubated in 8 M guanidine hydrochloride solution for 2 h and followed by dilution (70 folds) with buffer to make 10 µM in 6-1 M guanidine hydrochloride solution. Refolding solution was further incubated for 2 h before analysis (See Appendix Figure S15-S18 for BLA and Figure S21-S22 and S24-S25 for HEWL).

To analyze the effect of GdnHCl on protein tertiary and secondary structure, the protein solution was analyzed using tryptophan fluorescence spectroscopy, and circular dichroism (CD) spectroscopy, respectively. The fluorescence spectroscopy showed that free BLA showed Trp fluorescence drop during refolding with a red shift in emission wavelength but at 1 M of GdnHCl, both unfolding and refolding states were reached to an identical state (Figure 5.13 A). However, BLA complex with AuNP$_{ST}$ (2:1 molar ratio) showed a large gap in unfolding and refolding state of protein at all GdnHCl concentration (0-6 M) (Figure 5.13 B). It was also observed that BLA in refolding clearly showed a visible shift in a fluorescence spectrum in the presence of different concentration of GdnHCl (Figure 5. 13 C & D).

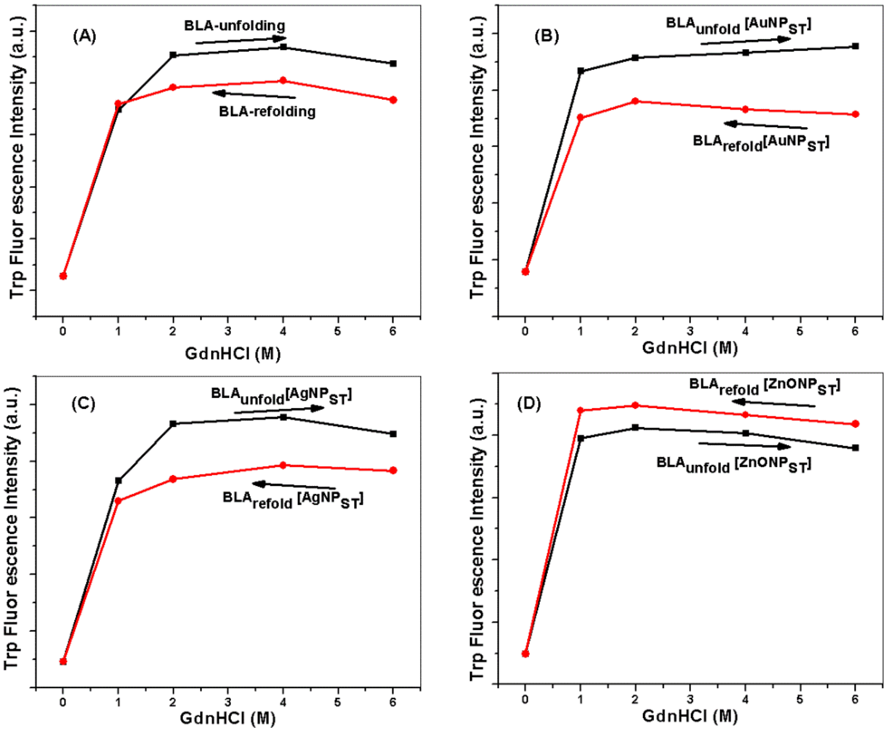

Figure 5.13 Effect of Guanidine hydrochloride (0-6 M) on BLA refolding. Unfolding and refolding of BLA with (A) none (B) AuNP$_{ST}$, (C) AgNP$_{ST}$, (D) ZnONP$_{ST}$. (See Trp fluorescence spectra in Appendix Figure S16-S19, Figure S25).

CD spectroscopy is an important tool to analyze the secondary structure of protein. Moreover, molar residual ellipticity (MRE) at 222 nm indicated the α-helix content of protein while absorption at 218 nm represents β-sheet content. Analyzing the CD peak of free BLA at 222 nm and 218 nm showed that with increasing GdnHCl concentration causes a loss in α-helix and β-sheet but during refolding it formed more β-sheet (Figure 5.14 A). When we analyzed refolded BLA in the presence of NP, it was observed that BLA contain a lower percentage of α-helix and β-sheet than free BLA in similar condition. This indicated that $AuNP_{ST}$ resists the regain of secondary structure, therefore compromise structural flexibility and rigidity (Table 5.3). We observed that $AgNP_{ST}$ showed less effect on the secondary structure of refolded BLA compared to $AuNP_{ST}$. Therefore, both in unfolding and refolding condition there was very lower loss in α-helix and β-sheet contents compared to free BLA (Table 5.1). Further, it was observed that BLA with $ZnONP_{ST}$ protects the content during refolding while contains more amounts of β-sheet (Table 5.1). Further, we have analyzed the variation in secondary structure during unfolding and refolding by utilizing CD spectra at 222 nm and fitting normalized absorption peak at 222 nm (Figure 5.14 A-D). the result showed that BLA without NP (Figure 5.14 A) showed similar unfolding and refolding pathway while administration of NP in BLA altered the folding pathway (Figure 5.14 B-D). The administration of $AuNP_{ST}$ and $AgNP_{ST}$ resist the unfolding while altered the refolding facilitate folding (Figure 5.14 B-C). Moreover, the $ZnONP_{ST}$ showed less effect on the folding pathway of BLA (Figure 5.14 D)

The fluorescence spectroscopy analysis showed that $AgNP_{ST}$ and $ZnONP_{ST}$ cause less effect on the protein tertiary structure during refolding process. However, $AuNP_{ST}$ showed drastic change the refolding state of HEWL. It was found that during refolding process, Trp fluorescence of HEWL showed a drop of fluorescence with $AgNP_{ST}$, and $ZnONP_{ST}$ (Figure 5.15 A, B, D), indicated some larger extent of unfolding and exposure of Trp to polar environment. However, Trp fluorescence was enhanced when similar experiment performed with $AuNP_{ST}$, the enhancement in fluorescence intensity the movement of Trp toward the non-polar environment probably the core of protein that causes enhancement of fluorescence (Figure 5.15 C).

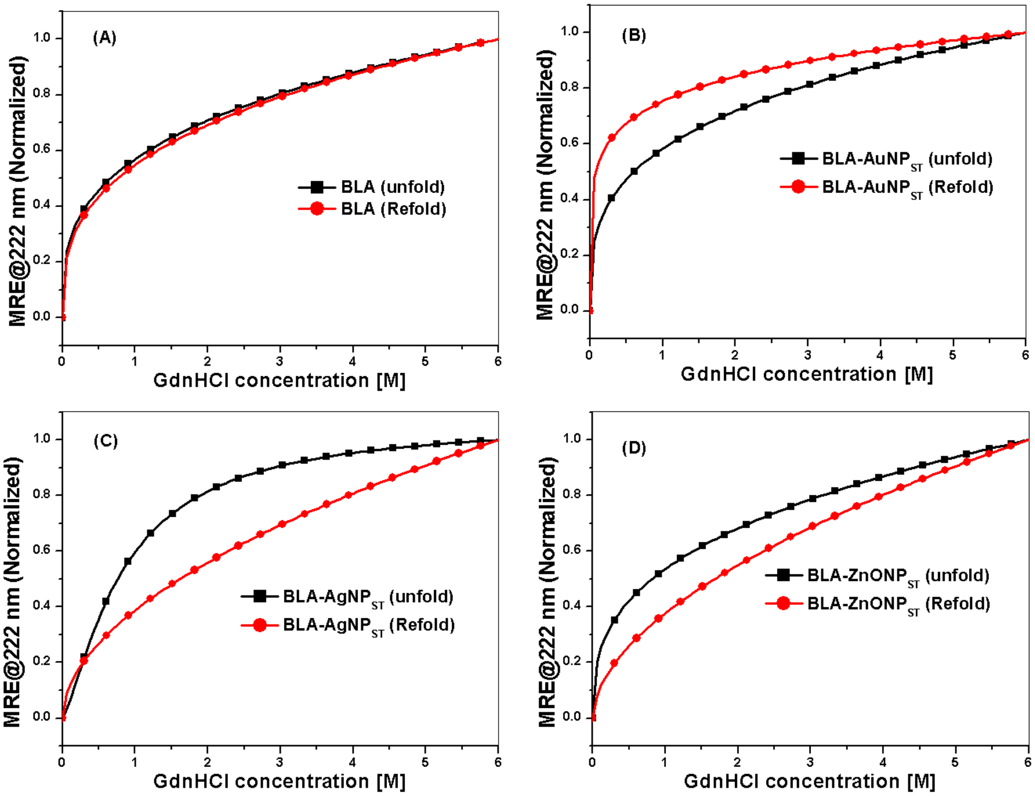

Figure 5.14 BLA chemical denaturation in different concentration of guanidine hydrochloride (GdnHCl) (0-6 M). CD spectra of 222 nm were normalized and fitted by non-linear curve fitting (R^2 value range 0.98-0.99). BLA with (A) none, (B) AuNP$_{ST}$, (C) AgNP$_{ST}$, (D) ZnONP$_{ST}$.

The analysis of secondary structure of HEWL sample showed that free protein regains its secondary structure during the refolding process with a certain difference in secondary structure (Table 5.2). From CD spectroscopic data, it was clear that AuNP$_{ST}$ and AgNP$_{ST}$ cause a little gain of HEWL secondary structure during the refolding process (Table 5.4). However, ZnONP$_{ST}$ protected the changes in HEWL secondary structure and showed less variation in absorption peak at 222 nm and 218 nm (Table 5.2). Therefore, it was clear that ZnONP$_{ST}$ protects the HEWL structure at the tertiary structure and secondary structural level while AuNP$_{ST}$ causes drastic changes in HEWL structure during refolding process.

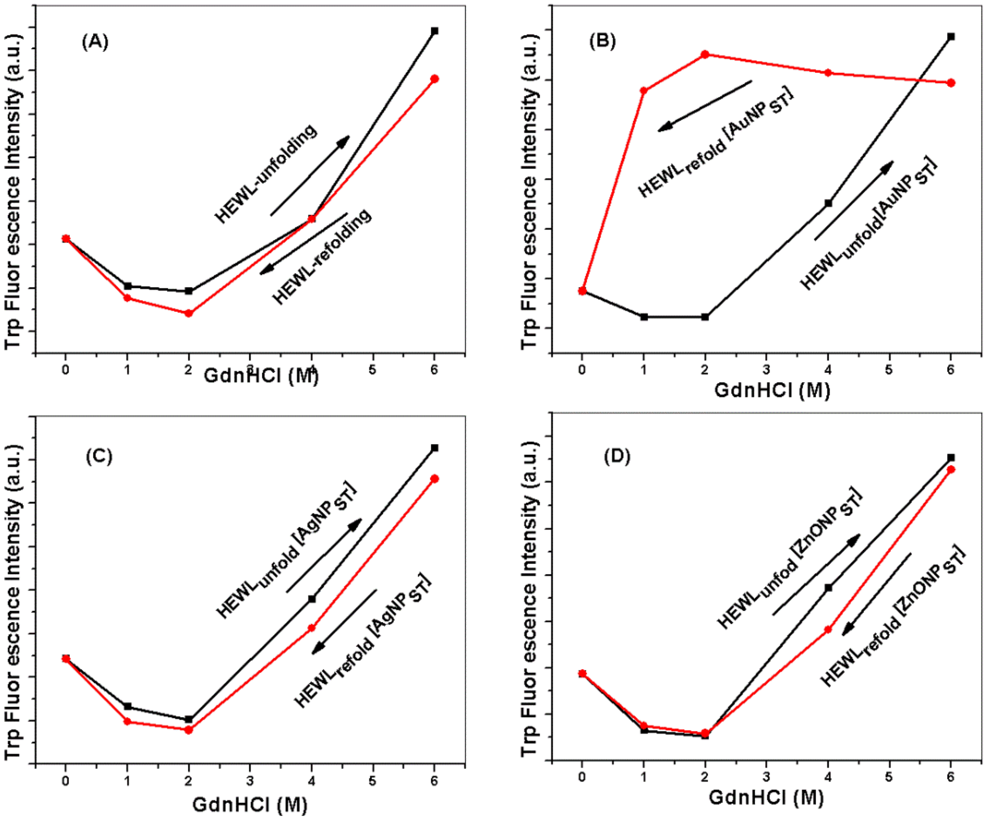

Figure 5.15 Unfolding and refolding of HEWL with (A) None, (B) AuNP$_{ST}$, (C) AgNP$_{ST}$, (D) ZnONP$_{ST}$. (See Trp fluorescence spectra in Appendix Figure S21, Figure S23, Figure S25).

Further, we have analyzed the variation in secondary structure of HEWL during unfolding and refolding by utilizing CD spectra at 222 nm and fitting normalized absorption peak at 222 nm (Figure 5.16 A-D). the result showed that BLA without NP (Figure 5.16 A) showed almost identical two step unfolding and refolding pathway while administration of NP in BLA altered the folding pathway (Figure 5.16 B-D). The administration of AuNP$_{ST}$ showed less effect on the unfolding and refolding of HEWL (Figure 5.16 B). However, AgNP$_{ST}$ and ZnONP$_{ST}$ resist the unfolding while altered the refolding pathway drastically and facilitate folding (Figure 5.16 C-D). The Fluorescence spectroscopy and CD spectra analysis showed that AuNP$_{ST}$ altered the tertiary structure of protein more drastically but has less effect on the secondary structure during unfolding and refolding. While AgNP$_{ST}$ and ZnONP$_{ST}$ showed less effect on the tertiary structure but showed high impact on the protein secondary structure during chemical denaturation. Chakroborti et al.[187, 188] investigated the effect of ZnONP on the structure and unfolding of BLA and HEWL. It was reported that ZnONP stabilize the folded form of HEWL while BLA retain tertiary structure but secondary structure showed significant changes.

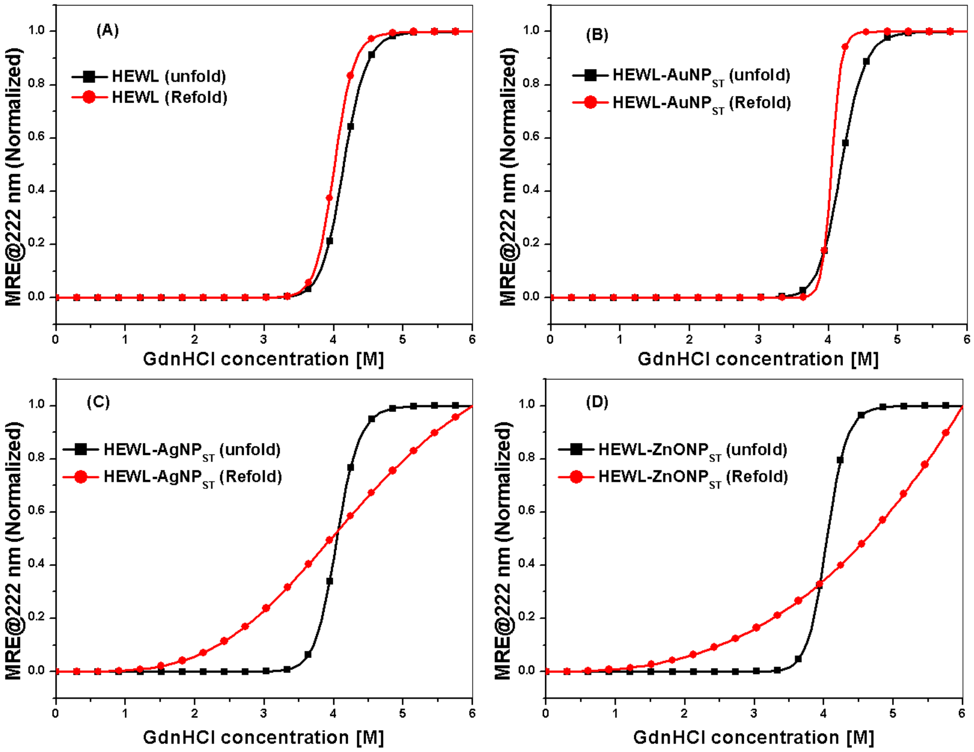

Figure 5.16 HEWL chemical denaturation in different concentration of guanidine hydrochloride (GdnHCl) (0-6 M). CD spectra of 222 nm were normalized and fitted by non-linear curve fitting (R^2 value range 0.98-0.99). HEWL with (A) none, (B) AuNP$_{ST}$, (C) AgNP$_{ST}$, (D) ZnONP$_{ST}$.

5.3.1.10 Effect of NP on heat-induced unfolding and refolding of proteins

Thermal unfolding and refolding were observed by incubating both the protein between 25-60 ^{0}C with an increment of 5 ^{0}C. Protein samples were incubated for 20 min at each temperature, and Trp fluorescence spectra and MRE of protein was measured. Analyzing the Trp fluorescence and CD spectra of BLA (Figure 5.17 and Figure 5.18) showed that thermal unfolding and refolding in the presence of all three NPs drastically changed the BLA tertiary and secondary structure. It was observed that Trp fluorescence of BLA over AuNP$_{ST}$-BLA and ZnONP$_{ST}$-BLA complex initially decreased up to 40 ^{0}C temperature and afterward showed enhancement and red shift (Figure 5.17 B & D). This indicated initial unfolding of BLA protein and exposure of Trp to polar environment, however, increasing the temperature causes movement of Trp toward the non-polar environment and showed enhancement.

Table 5.1 Effect of Guanidine hydrochloride (0-6 M) on BLA secondary structure. The data was measured and percentage secondary structure contents were analyzed by CAPITO online server. (See CD spectra in Appendix Figure S20-S21, Figure S24, and Figure S27)

GdnHCl (M)	**β-Sheet (%)**							
	BLA		**BLA -AuNP$_{ST}$**		**BLA -AgNP$_{ST}$**		**BLA -ZnONP$_{ST}$**	
	Unfolding	**Refolding**	**Unfolding**	**Refolding**	**Unfolding**	**Refolding**	**Unfolding**	**Refolding**
0	22.5	22.5	9	9	9	9	9	9
1	42	44.5	40.5	44.5	39	40.5	43	40.5
2	52	49	39	39.5	33	33	39.5	33
4	39.5	39.5	39.5	37.5	37	39	39.5	39.5
6	39.5	38	39.5	40	36	36	38	39.5

Table 5.2 Effect of Guanidine hydrochloride (0-6 M) on HEWL secondary structure. The data was measured, and Percentage secondary structure contents were analyzed by CAPITO online server. (See CD spectra in Appendix Figure S20-S21, Figure S24, and Figure S27)

GdnHCl (M)	**β-Sheet (%)**							
	HEWL		**HEWL -AuNP$_{ST}$**		**HEWL -AgNP$_{ST}$**		**HEWL -ZnONP$_{ST}$**	
	Unfolding	**Refolding**	**Unfolding**	**Refolding**	**Unfolding**	**Refolding**	**Unfolding**	**Refolding**
0	11.5	11.5	21.5	21.5	21.5	21.5	20.5	20.5
1	24	27.5	24	23.5	24	24	24	23.5
2	24	24	42.5	36.5	31	26	31	29
4	36	36	39.5	38	39.5	39.5	39.5	39.5
6	46	46	46	46	46	46	42	41

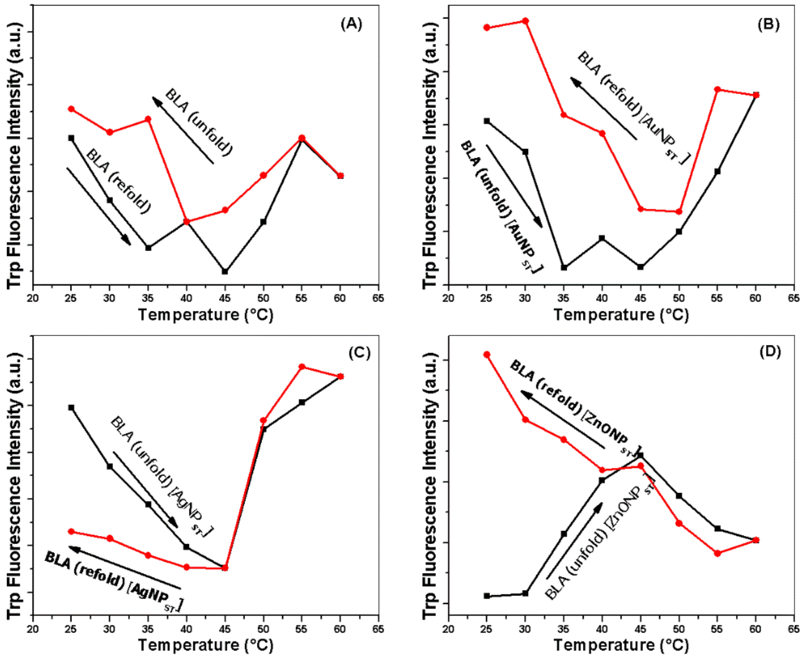

Figure 5.17 Thermal unfolding and refolding on BLA. (A) Trp fluorescence of BLA during thermal unfolding and refolding, (B) AuNP$_{ST}$-BLA, (C) AgNP$_{ST}$-BLA, (D) ZnONP$_{ST}$-BLA. (See Trp fluorescence in Appendix Figure S28-S30).

Moreover, AgNP$_{ST}$ causes exposure of Trp to the more polar environment (Figure 5.17 C). Therefore, Trp fluorescence analysis showed that AuNP$_{ST}$ and ZnONP$_{ST}$ cause a shift of hydrophobic Trp to the core of protein while AgNP$_{ST}$ exposed it to the polar environment indicated the unfolded state of BLA. However, CD spectroscopy analysis of BLA showed that NP effect is at tertiary structure level while secondary structure analysis showed at 222 nm there was an equivalent amount of secondary content in BLA during thermal refolding (except AuNP$_{ST}$) (Figure 5.15 A-D) but showed alteration secondary structure between 35-50 ^{0}C.

Further, the HEWL structural changes at tertiary and secondary structure level by analyzing variation in Trp fluorescence and MRE variation at 222 nm showed that all three NP causes drastic changes in HEWL tertiary structure (Figure 5.16 B-D). Free HEWL showed good refolding ability during thermal unfolding and refolded process (Figure 5.16 A). It was observed that Trp fluorescence during refolding was higher than the unfolding fluorescence with emission wavelength shift for HEWL conjugated with NP. Therefore, the interaction of

HEWL with NP decreased the stability of its tertiary structure and protein was unable to regain its native tertiary structure in the presence of all three NP.

Moreover, secondary structure analysis of HEWL showed variation during refolding (Figure 5.17 A). Moreover, it was also observed that all the tested NP altered the unfolding and refolding pathway of the HEWL secondary structure and showed fewer amounts of α-helix and β-sheet after refolding (Figure 5.17 B). However, it was cleared that AgNP$_{ST}$ and ZnONP$_{ST}$ showed protection in the HEWL secondary structure during thermal refolding, which was shown by less shift in absorption peak at 222 nm and 218 nm during refolding of HEWL at different temperature (Figure 5.17 C & D).

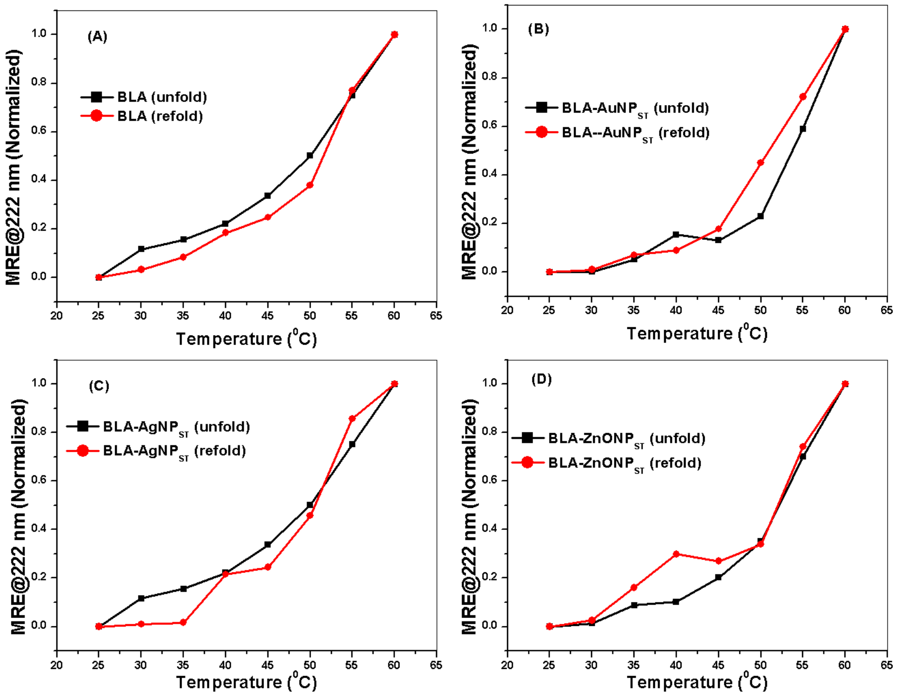

Figure 5.18 Thermal denaturation of BLA at different temperature (25-60 ^{0}C). BLA with (A) none, (B) AuNP$_{ST}$, (C) AgNP$_{ST}$, (D) ZnONP$_{ST}$.

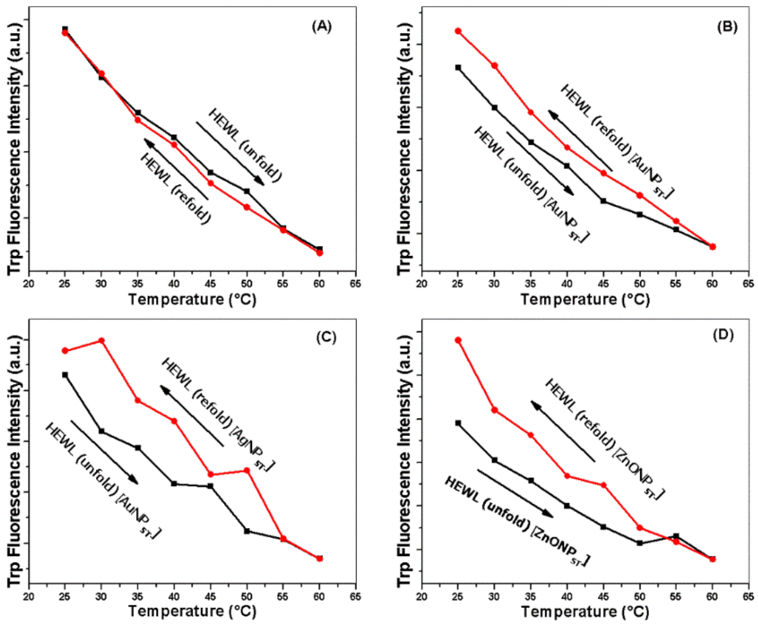

Figure 5.19 Analyzing the thermal unfolding and refolding on HEWL. (A) Trp fluorescence of HEWL during thermal unfolding and refolding, (B) AuNPST-HEWL, (C) AgNPST-HEWL, (D) ZnONPST-HEWL. (See Trp fluorescence spectra in Appendix Figure S35-S37).

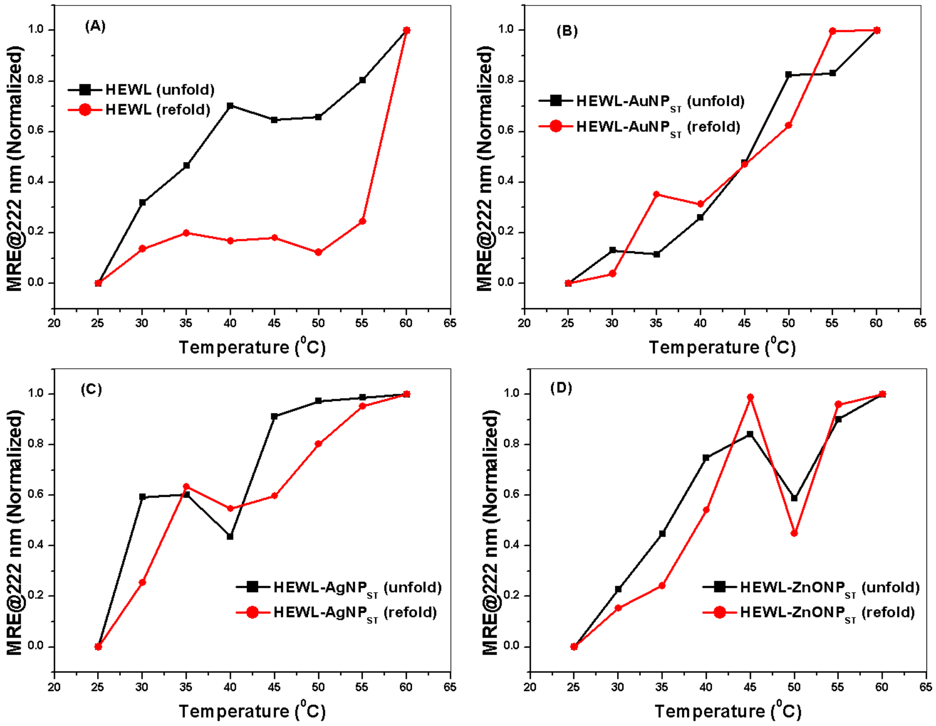

Figure 5.20 Thermal denaturation of HEWL at different temperature (25-60 ˚C). HEWL with (A) none, (B) AuNPST, (C) AgNPST, (D) ZnONPST.

This fact clearly indicated that interaction of $AgNP_{ST}$ and $ZnONP_{ST}$ protect the HEWL secondary structure during thermal denaturation and help to regain it structure during their folding process while a similar amount of $AuNP_{ST}$ unable to do so.

The BLA has high degree of homology with HEWL, four disulphide bond occupied same position. However, BLA and HEWL showed opposite net surface charge in physiological pH [193]. The chemical and thermal unfolding with AuNP, AgNP, ZnONP showed that the effect of NP on the protein vary with nature of interaction complex. The secondary structure as well as tertiary structure variation and denaturation of protein also vary with interaction of different NP.

5.3.1.11 Analyze the folding Model and Free energy of folding

Further, we analyzed the chemical and thermal denaturation data for calculation of folding fraction of both the proteins (i.e. BLA and HEWL) and calculated the free energy of folding using method reported by Fersht [194] and Greenfield [195]. The understanding the energetics by calculation of free energy will help to understand the energetics of protein folding and the effect of tested NP during chemical and thermal denaturation and renaturation. Bovine α-lactalbumin (BLA) and hen egg white lysozyme (HEWL) are monomeric proteins. Therefore, thermal denaturation study using circular dichroism spectroscopy will be done by using following equations:

$$K = [F]/[U] \text{---} (5.1)$$

Here, K is equilibrium constant for folding. If, the fraction folded at given temperature is α.

$$K = \alpha/(1- \alpha) \text{ --} (5.2)$$

$$\alpha = K/(1+K) \text{ --} (5.3)$$

The free energy of folding will be calculated using following equation:

$$\Delta G = -nRT\ln K \text{-------------------------------------- } (5.4)$$

ΔG is free energy of folding and R is gas constant (1.98 cal/mol)

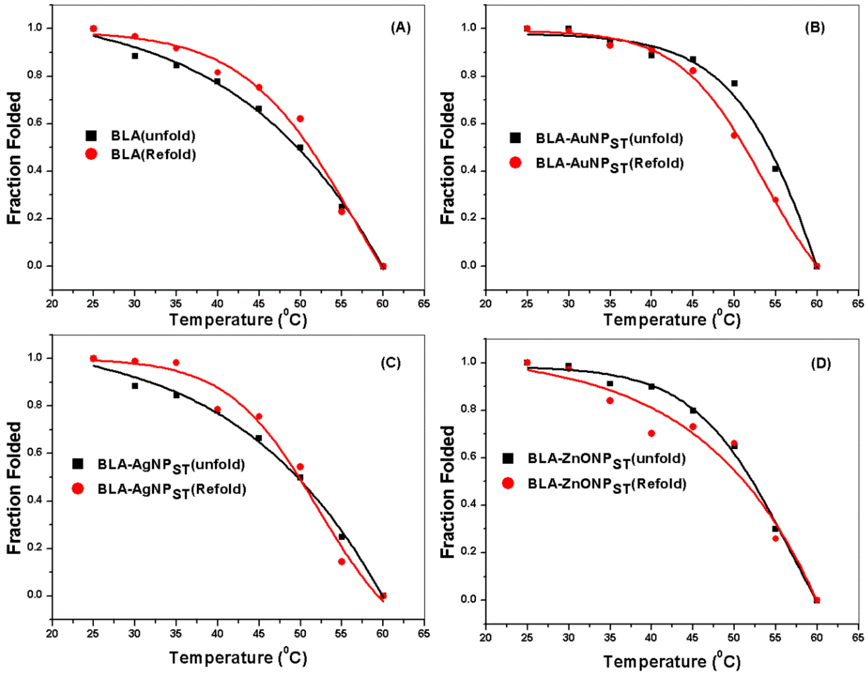

Figure 5.21 Thermal denaturation (25-60 ˚C) and renaturation (60-25 ^{0}C) of BLA was performed and fraction of protein in the folding state was calculated with (A) none, (B) AuNP$_{ST}$, (C) AgNP$_{ST}$, (D) ZnONP$_{ST}$. The non-linear curve fitting was performed using originPro2016. The R^2 value for the fitted curve in the range of 0.94-0.988.

The folding fraction of BLA (without and with NP) (Figure 5.21 A-D) showed that BLA interaction with all the tested NP shift the T$_M$ (temperature when half of the protein in folded state) toward higher temperature (i.e.50 ^{0}C <). However, AgNP$_{ST}$ showed lower amount of folding fraction compared to AuNP$_{ST}$ and ZnONP$_{ST}$ (Figure 5.21 C and D). Moreover, it was observed that BLA- AgNP$_{ST}$ and BLA alone showed higher amount of folding fraction up to the T$_M$ however, below T$_M$ AgNP$_{ST}$ showed less amount of folded state compared to BLA-AuNP$_{ST}$ while BLA-ZnONP$_{ST}$ showed lower amount of folding fraction throughout the thermal denaturation and renaturation (Figure 5.21 D). Hiraoka and Suqai [196] reported the thermal denaturation of BLA is two state folding and energetic of apo and holo form of BLA and observed that both the proteins follow similar pattern. Vanderheeren and Hanssens [197] performed the thermal denaturation of apo-BLA and reported that thermal denaturation exposes the hydrophobic sites while calcium binding in apo-BLA make it stable.

Table 5.3 Calculation of folding constant (K), Free energy of folding (ΔG Kcal/mol) during thermal denaturation and renaturation of BLA, BLA-AuNP$_{ST}$, BLA-AgNP$_{ST}$, and BLA-ZnONP$_{ST}$.

Temperature (˚C)	**BLA (unfold/refold)**		**BLA-AuNP$_{ST}$ (unfold/refold)**		**BLA-AgNP$_{ST}$ (unfold/refold))**		**BLA-ZnONP$_{ST}$ (unfold/refold)**	
	K	**ΔG**	**K**	**ΔG**	**K**	**ΔG**	**K**	**ΔG**
30	7.6/ 30.2	-1.2/ -2.0	$2.0x10^{3}$/ $0.1x10^{3}$	-4.6/ -2.8	7.6/ 93.4	-1.2/ -2.7	72.1/ 37.5	-2.6/ -2.2
35	5.4/ 10.9	-1.0/ -1.4	18.2/ 13.1	-1.8/ -1.6	5.4/ 58.8	-1.0/ -25	10.3/ 5.2	-1.4/ -1.0
40	3.5/ 4.4	-0.8/ -0.9	5.5/ 10.2	-1.1/ -1.4	3.5/ 3.7	-0.8/ -0.8	8.8/ 2.4	-1.3/ -0.5
45	1.9/ 3.0	-0.4/ -0.7	6.7/ 4.6	-1.2/ -1.0	1.9/ 3.1	-0.4/ -0.7	3.9/ 2.7	-0.9/ -0.6
50	1.0/ 1.6	0.003/ -0.3	3.3/ 1.2	-0.8/ -0.1	1.0/ 1.2	0.003/ -0.1	1.9/ 1.9	-0.4/ -0.4
55	0.3/ 0.3	0.7/ 0.8	0.7/ 0.4	0.2/ 0.6	0.3/ 0.2	0.7/ 1.1	0.4/ 0.4	0.5/ 0.7

Further calculating the free energy of folding using equation 5.1 to 5.4 showed thermal unfolding/refolding free energy become negative to positive, which indicated that increasing temperature causes unfolding of protein and formation folded state become difficult. Therefore, folding is unfavorable at higher temperature while at lower temperature folding is favorable, which was shown by negative free energy (Table 5.3). We analyzed folding of BLA with AuNP$_{ST}$, AgNP$_{ST}$, and ZnONP$_{ST}$ at different temperature and calculated the free energy of folding. The result clearly showed that BLA-AuNP$_{ST}$ sample higher amount of negative folding free energy compared to AgNP$_{ST}$ and ZnONP$_{ST}$ (Table 5.3). The thermal folding analysis of BLA and free energy calculation showed that although AuNP$_{ST}$ showed higher amount of alteration in tertiary structure but favored the folding of BLA compared to AgNP$_{ST}$ and ZnONP$_{ST}$.

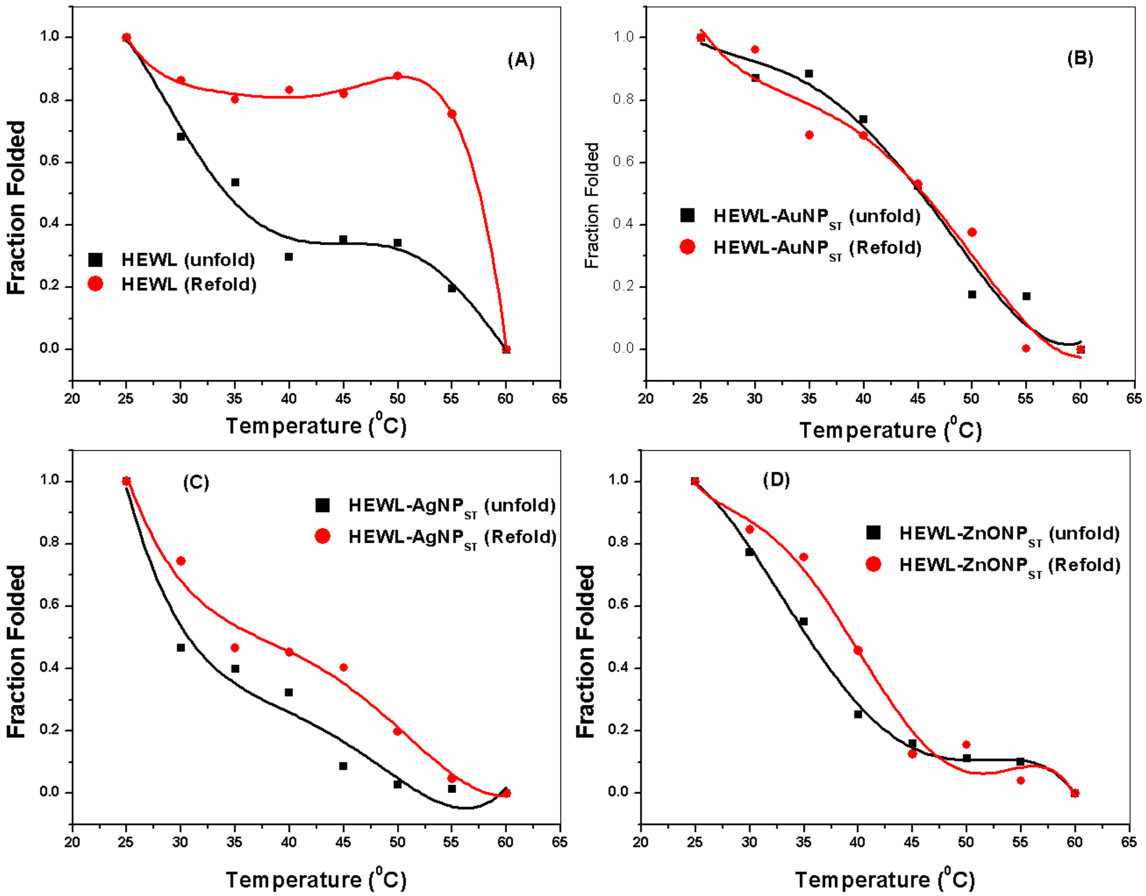

Figure 5.22 Thermal denaturation (25-60 ^{0}C) and renaturation (60-25 ^{0}C) of HEWL was performed and fraction of protein in the folding state was calculated with (A) none, (B) AuNP$_{ST}$, (C) AgNP$_{ST}$, (D) ZnONP$_{ST}$. The non-linear curve fitting was performed using polynomial-4 function. The R^2 value for the fitted curve in the range of 0.95-0.96.

Further, we also analyzed the thermal unfolding of HEWL wth and without NP and folding fraction as well as free energy of folding were calculated. Analyzing the thermal unfolding and refolding showed that HEWL has high efficiency of refolding (Figure 5.22 A). When, we analyzed the folding fraction of HEWL with AuNP$_{ST}$, it was revealed that interaction of HEWL altered the refolding fraction of HEWL (Figure 5.22 B). The results showed that T_M value for HEWL was reduced to below 45 ˚C with all the tested NP. The folding fraction analysis also showed that HEWL showed negligible difference in folding fraction during thermal unfolding and refolding with AuNP$_{ST}$ (Figure 5.22 B).

Table 5.4 Calculation of folding constant (K), Free energy of folding (ΔG Kcal/mol) during thermal denaturation and renaturation of HEWL, HEWL-AuNP$_{ST}$, HEWL-AgNP$_{ST,}$ and HEWL-ZnONP$_{ST}$.

Temperature (^{0}C)	**HEWL (unfold/refold)**		**HEWL-AuNP$_{ST}$ (unfold/refold)**		**HEWL-AgNP$_{ST}$ (unfold/refold))**		**HEWL-ZnONP$_{ST}$ (unfold/refold)**	
	K	**ΔG**	**K**	**ΔG**	**K**	**ΔG**	**K**	**ΔG**
30	2.1/6.3	-0.5/-1.1	6.7/25.7	-1.1/-19.5	0.8/2.9	0.2/-0.6	3.4/5.5	-0.7/-1.0
35	1.2/4.0	-0.1/-0.8	7.7/1.8	-1.3/-0.4	0.7/0.6	0.3/0.3	1.2/3.1	-0.1/-0.7
40	0.4/4.9	0.5/-0.9	2.8/2.2	-0.6/-0.5	1.3/0.8	-0.2/0.1	0.3/0.8	0.7/0.1
45	0.5/4.5	0.4/-0.9	1.1/1.1	-0.6/-0.8	0.1/0.7	1.5/0.2	0.2/0.01	1.1/2.7
50	0.5/7.2	0.4/-1.3	0.2/0.6	0.9/0.3	0.02/0.2	2.3/0.9	0.7/1.2	0.2/-0.1
55	0.2/3.1	0.9/-0.7	0.2/0.002	1.0/3.8	0.01/0.5	2.8/1.9	0.1/0.04	1.4/2.1

Blumlein and McManus [198] reported that thermal denaturation of HEWL reversible and irreversible denaturation in low ionic pH solution. The results showed that increase in T_M was not correlated with reversibility of folding. Chang and Li [199] reported that HEWL is highly thermostable and showed stability up to 55 ^{0}C. Therefore, variation in thermal stability during denaturation is altered by tested NP.

When we analyzed the free energy of folding using folding constant obtained utilizing equation 5.1 to 5.3 and free energy was calculated using equation 5.4. The results showed that AuNP$_{ST}$ highest amount of negative free energy (ΔG = -19 kcal/mol) while AgNP$_{ST}$ showed least amount of negative free energy of folding. When increased the temperature it was observed that all the tested NP not favored the folding of HEWL at higher temperature compared to free HEWL (Table 5.4). form free energy analysis it is cleared that NP favored the HEWL folding at lower temperature but inhibit the folding at higher temperature.

Further, we analyzed the unfolding and refolding of BLA and HEWL using different concentration of guanidine hydrochloride (0-6 M). The CD absorption peak at 222 nm was utilized for calculation of folding fraction of BLA and HEWL using following equation:

fraction folded α is calculated by using following equation:

$$\alpha= (\Theta_{ob} - \Theta_{U})/ (\Theta_{F} - \Theta_{U})\text{---------------------------------}(5.5)$$

Here, Θ_{ob} is molar residual ellipticity at given temperature; Θ_{U} unfolded protein; Θ_{F} folded protein.

The curve is plotted between α and GdnHCl concentration and fitted,

Thermodynamics of protein folding using denaturants:

$$K= \alpha/ (n*[C]^{n-1}) * (1- \alpha)^{n}\text{----------------------------------}(5.6)$$

[C] is a concentration of monomeric protein; n is 1, 2, 3, and 4.

$$\Delta G = -nRTlnK\text{--}(5.7)$$

ΔG value is the free energy of folding in the presence of chemical denaturant

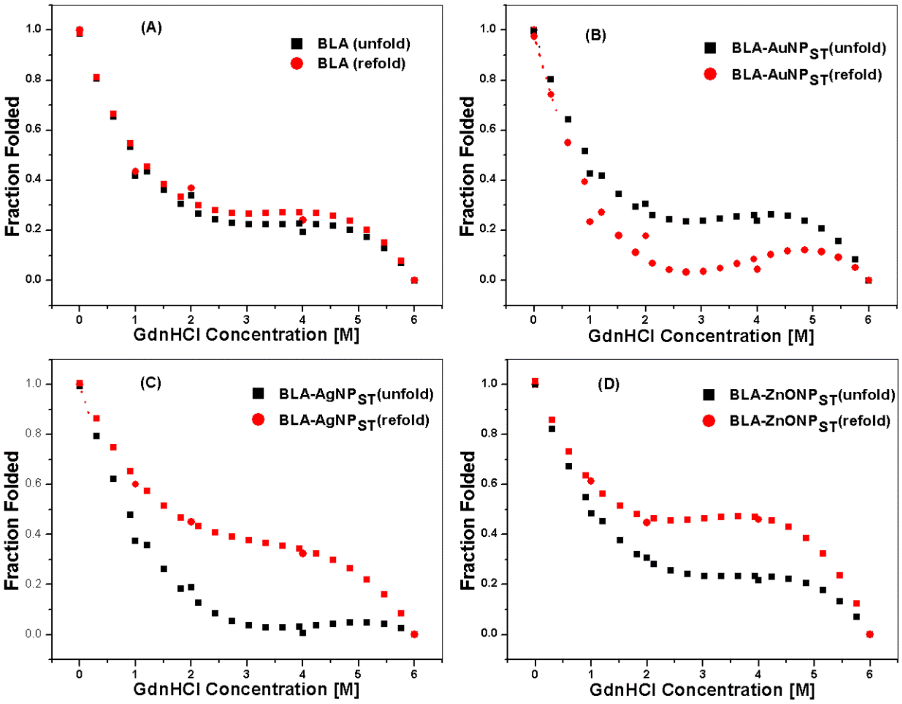

Figure 5.23 Chemical denaturation of BLA in the presence of guanidine hydrochloride (0-6 M) and folding was calculated with (A) none, (B) AuNP$_{ST}$, (C) AgNP$_{ST}$, (D) ZnONP$_{ST}$. The non-linear curve fitting was performed using originPro2016. The R^2 value for the fitted curve in the range of 0.96-0.99.

The Chemical denaturation of BLA and BLA-NP showed that folding fraction of BLA reduced with $AuNP_{ST}$. It was revealed that C_M (concentration of GdnHCl when half protein in folded state) value increased for refolding of BLA-$AgNP_{ST}$ and BLA-$ZnONP_{ST}$ while C_M value reduced for BLA-$AuNP_{ST}$. Therefore, folding fraction analysis revealed that $AuNP_{ST}$ unable to protect folding fraction of BLA while $AgNP_{ST}$ and $ZnONP_{ST}$ protect against chemical denaturant efficiently. Ikeguchi et al.[200] reported that BLA and lysozyme showed two state chemical denaturation and found that similar folding intermediate observed in both the proteins. Kuwajima et al. [201] reported that both the proteins showed similar folding fraction at early stage of folding and intermediate has similar structure during folding.

Table 5.5 Calculation of folding constant (K), Free energy of unfolding (ΔG Kcal/mol) during Chemical denaturation and renaturation of BLA, BLA-$AuNP_{ST}$, BLA-$AgNP_{ST,}$ and BLA-$ZnONP_{ST}$.

GdnHCl [M]	**BLA (unfold/refold)**		**BLA-$AuNP_{ST}$ (unfold/refold)**		**BLA-$AgNP_{ST}$ (unfold/refold)**		**BLA-$ZnONP_{ST}$ (unfold/refold)**	
	K	**ΔG**	**K**	**ΔG**	**K**	**ΔG**	**K**	**ΔG**
1	0.7/ 0.7	0.2/ 0.2	0.7/ 0.3	0.2/ 0.7	0.6/ 1.5	0.3/ -0.2	0.9/ 1.6	0.03/ -0.3
2	$2.8x10^4$/ $1.3x10^5$	-6.0/ -7.0	$22.6x10^3$ / $9.4x10^3$	-5.9/ -5.4	$10.2x10^3$/ $53.1x10^3$	-5.4/ -6.4	$22.8x10^3$/ $52.4x10^3$	-5.9/ -6.4
4	$4.2x10^{13}$/ $6.7 x10^{13}$	-18.5/ -18.7	$6.4x10^{13}$/ $4.8x10^{12}$	-18.7/ -17.2	$4.7x10^{11}$/ $1.4x10^{14}$	-15.9/ -19.2	$5.3x10^{13}$/ $4.9x10^{14}$	-18.6/ -19.9

When, we calculate the free energy of folding in presence of various concentration of GdnHCl; it was revealed that all the tested NP with BLA showed higher amount of negative free energy of folding (Table 5.5). This revealed that folding favored in terms of free energy with all tested NP while folding fraction vary with different NP with BLA. Therefore, protein folding fraction analysis, free energy calculation, and fluorescence spectroscopy clearly indicated that interaction of BLA with NP altered the tertiary and secondary structure of BLA to different extent. It was further revealed that $AuNP_{ST}$ was unable to protect BLA structure in presence of GdnHCl while facilitate the folding of protein while $AgNP_{ST}$ and $ZnONP_{ST}$ significantly protected the BLA structure in presence of GdnHCl and favored the folding state of BLA.

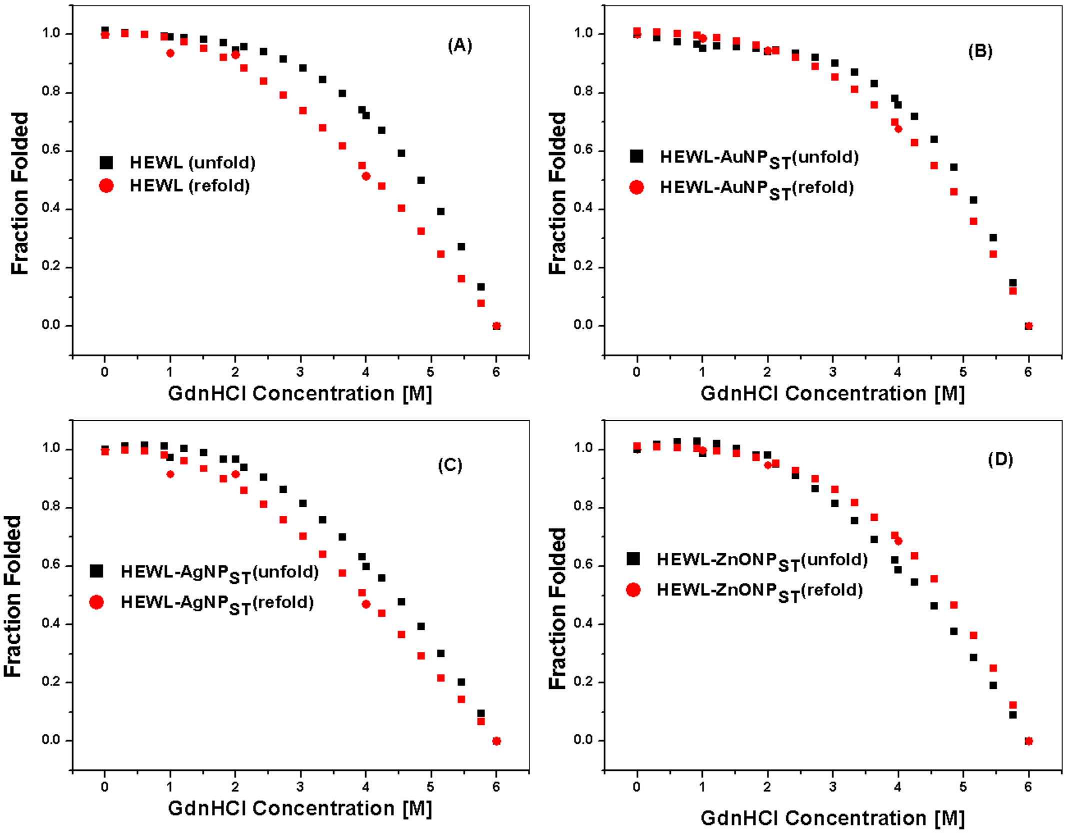

Figure 5.24 Chemical denaturation of HEWL in the presence of guanidine hydrochloride (0-6 M) and folding was calculated with (A) none, (B) $AuNP_{ST}$, (C) $AgNP_{ST}$, (D) $ZnONP_{ST}$. The non-linear curve fitting was performed using originPro2016. The R^2 value for the fitted curve in the range of 0.96-0.99.

HEWL denaturation and renaturation in presence of GdnHCl was performed (Figure 5.24 A-D). the analysis of folding fraction showed that there is very less alteration in folding fraction of HEWL by tested NP during unfolding and refolding analysis. Moreover, free energy calculation also showed that interaction of $AuNP_{ST}$, $AgNP_{ST}$, and $ZnONP_{ST}$ unable to drastically altered the unfolding and refolding of HEWL in the presence of different concentration of GdnHCl (Table 5.6). The CD spectra, and fluorescence spectra analysis with free energy calculation clearly indicated that all the tested NP altered the tertiary as well as secondary structure of HEWL protein to different extent; however, neither of tested NP able to drastically facilitated or inhibited the HEWL unfolding and refolding in the presence of GdnHCl. Ahmad and Bigelow [202] reported that free energy of folding of HEWL for guanidine hydrochloride is 1.25 to 4.22 Kcal/mol*M while with urea it is 0.88 to 2.08 kcal/mol*M. The free energy of chemical denaturation also depends on the pH, ionic strength and temperature of solution. Moreover, interaction of protein with NP also affect folding of HEWL and variation in free energy.

Table 5.6 Calculation of folding constant (K), Free energy of folding (ΔG Kcal/mol) during chemical denaturation and renaturation of HEWL, HEWL-AuNP$_{ST}$, HEWL-AgNP$_{ST,}$ and HEWL-ZnONP$_{ST}$.

GdnHCl [M]	HEWL (unfold/refold)		HEWL-AuNPST (unfold/refold)		HEWL-AgNPST (unfold/refold)		HEWL-ZnONPST (unfold/refold)	
	K	**ΔG**	**K**	**ΔG)**	**K**	**ΔG**	**K**	**ΔG**
1	$1.4x10^2$/ 14.3	-2.9/ -1.6	19.7/ 66.4	-1.8/ -2.5	35.7/ 10.8	-2.1/ -1.4	71.8/ $3.6x10^2$	-2.5/ -3.5
2	$1.1x10^7$/ $6.6x10^6$	-9.6/ -9.3	$9.7x10^6$ /10.3 $x10^6$	-9.5/ -9.5	$3.4x10^7$/ $4.6x10^6$	-10.2/ -9.0	$11.0x10^7$/ $11.5x10^6$	-10.9 -9.6
4	$1.0x10^{16}$/ $8.3x10^{14}$	-21.8/ -20.3	$2.1x10^{16}$/ $5.6x10^{15}$	-22.2/ -21.4	$2.1x10^{15}$/ $5.4x10^{14}$	-20.8/ -20.0	$1.8x10^{15}$/ $6.3x10^{15}$	-20.7/ -21.5

5.3.1.12 Proteinase-K digestion assay

To understand the vulnerability of NP-bound protein to PK, we performed PK digestion assay of BLA and HEWL with AuNPST, AgNP$_{ST}$, and ZnONP$_{ST}$ complex. Proteinase K (PK) is a broad-spectrum serine protease whose activity is greatly increased by the addition of denaturing agents that expose the PK digestion sites [105-106, 172, [203]], indicating that the unfolding of the substrates helps PK to degrade them. Protein interaction with NP causes perturbation in protein structure that was already demonstrated by fluorescence and CD spectra measurement.

Hence, it was anticipated that the interaction should make the non-native protein more susceptible to PK. Here we performed 15% SDS-PAGE analysis and ANS hydrophobicity analysis experiment with both the proteins (BLA and HEWL). The samples were incubated with different concentration of PK (0, 1, 3, 5, 7 μM) and the reaction was stopped using PMSF. For ANS assay, 500 μM of ANS was added and incubated for 10 min. PMSF of 50 μM was added in the solution to stop the reaction and further incubated for 20 min. The digestion produced new fragments that reduced the band size. Moreover, for ANS assay, our hypothesis was that the digestion of protein by PK produced more amounts of hydrophobic fragments and this fragment when interacted with ANS causes enhancement of fluorescence. All samples were baseline corrected, and final data were plotted by subtracting the ANS fluorescence of native protein and respective fluorescence of PK.

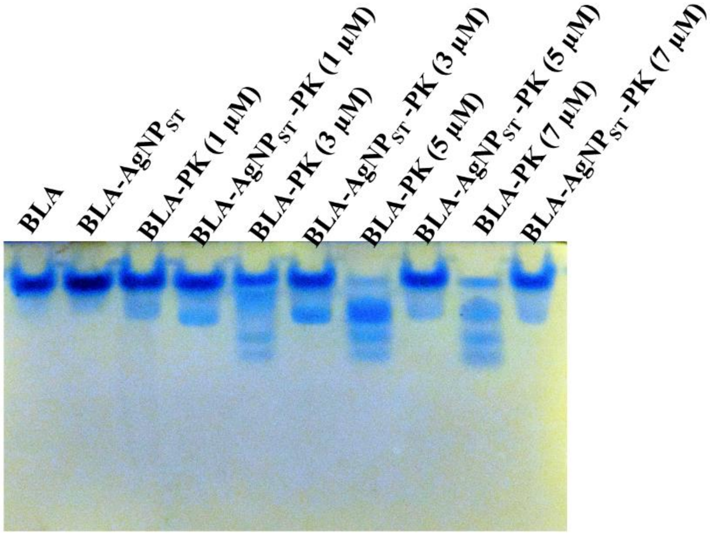

Figure 5.25 Proteinase-K digestion assay of various AgNP$_{ST}$-BLA conjugates, 20 μl of all loading sample contains 20 μg of BLA.

The result clearly revealed that BLA and HEWL when in pure form, were highly susceptible to PK (above 3 μM of concentration completely digested fragments by PK-treatment) (Figure 5.25, Figure 5.26) while BLA in AgNP$_{ST}$-BLA (Figure 5.25, and Figure 5.26 A) showed protection against PK digestion to higher extent but protein complex with other NP (AuNP and ZnONP) showed (Figure S41.A & C, Figure 5. 26 B) susceptibility under the same condition. Such PK-resistance of protein molecules in the protein corona over AgNP has utter significance. The use of NP in the biological system thus might trigger the protein into highly PK-resistant, which could prevent its normal degradation process in cells and resulted in the accumulation of non-functional proteins in cells.

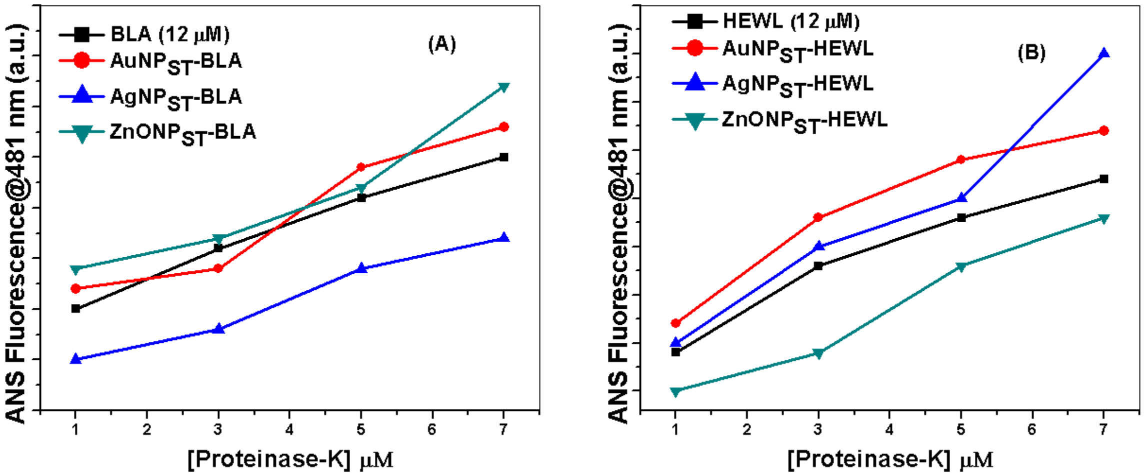

Figure 5.26 Proteinase-K digestion assay was performed by ANS based fluorescence spectroscopy method. (A) PK digestion assay with different concentration of PK (1, 3, 5, 7 μM) with 0.2 mg/ml BLA; (B) PK digestion assay with different concentration of PK (1, 3, 5, 7 μM) with 0.2 mg/mL HEWL.

5.3.1.13 Effect of surface capping

Further, we also analyzed the effect of starch capping on the NP by variation in surface capping agent. For analysis, polyethylene glycol capped AuNP and AgNP of equivalent size were prepared and uncapped and starch self-assembled ZnONP was synthesized. The protein and NP were mixed in sodium phosphate buffer in 10:1 molar ratio and incubated for 2 h. The variation in Trp fluorescence and circular dichroism (CD) spectra was analyzed to analyze the effect of NP on protein structure (Figure 5.27 and Figure 5.28). The Trp fluorescence spectroscopy analysis showed that PEGylation of AuNP and AgNP weaken the NP-based quenching of BLA and HEWL indicated that interaction of both the NP was weaker than starch capped NP (Figure 5.27 A-D). Moreover, the interaction of uncapped and assembly of ZnONP with BLA showed that uncapped ZnONP weakly interacts with BLA while ZnONP assembly showed higher quenching, signifies stronger interaction than ZnONP$_{ST}$ (Figure 5.27 E). However, the interaction of HEWL with uncapped and assembly ZnONP showed no significant difference in Trp fluorescence quenching and equivalent amount Trp fluorescence quenching as with ZnONP$_{ST}$ and HEWL interaction (Figure 5.27 F).

The secondary structure analysis of these BLA and HEWL were also performed to analyze the effect of variation of capping on the secondary structure of both the proteins. The results were analyzed with respect to variation in absorption peak at 222 nm (indicate α-helix) and at 218 nm (indicate β-sheet) (Figure 5.28). NP and protein were mixed in 1:2 molar ratios and incubated for 2 h at room temperature. The absorption peak analysis at 222 nm and 218 nm for various BLA-NP samples showed that PEGylation showed less effect on the secondary structure of BLA while starch capped AuNP and AgNP showed higher extent of secondary structure alteration, which was shown by higher amount of circular dichroic light absorption at 222 nm, therefore more amount of α-helix formation (Figure 5.28 A & C). Moreover, uncapped ZnONP ($\mathrm{ZnONP}_{\mathrm{uncap}}$) and self-assembly of ZnONP ($\mathrm{ZnONP}_{\mathrm{assmb}}$) also showed less effect on the secondary structure of BLA due to interaction (Figure 5.21 E).

The CD spectra at 222 nm and 218 nm showed that the interaction of HEWL with $\mathrm{AuNP}_{\mathrm{ST}}$ over $\mathrm{AuNP}_{\mathrm{PEG}}$ showed no significant difference in peaks. Therefore, PEGylation of AuNP showed the similar effect as shown by $\mathrm{AuNP}_{\mathrm{ST}}$ (Figure 5.28 B), which indicated that the effect of AuNP on HEWL secondary structure was due to the core material of NP. Moreover, a similar analysis with PEGylated AgNP ($\mathrm{AgNP}_{\mathrm{PEG}}$) also showed a similar effect in CD spectra, but fluorescence spectra showed that PEGylation reduced the conformational changes in HEWL by AgNP (Figure.5.28 D). Moreover, uncapped ZnONP ($\mathrm{ZnONP}_{\mathrm{uncap}}$) and self-assembly of ZnONP ($\mathrm{ZnONP}_{\mathrm{assmb}}$) showed higher amount circular dichroic light absorption at 222 nm and 218 nm than $\mathrm{ZnONP}_{\mathrm{ST}}$ indicated a higher amount of secondary structure alteration and reduction in α-helix and β-sheet content Figure 5.28 F). Therefore, Trp fluorescence and CD spectroscopy analysis showed that variation of surface properties by capping agent and alteration surface structure of NP (e.g. formation of assembly) altered the interaction strength and different extent of secondary structure, which depends on the type of protein and NP.

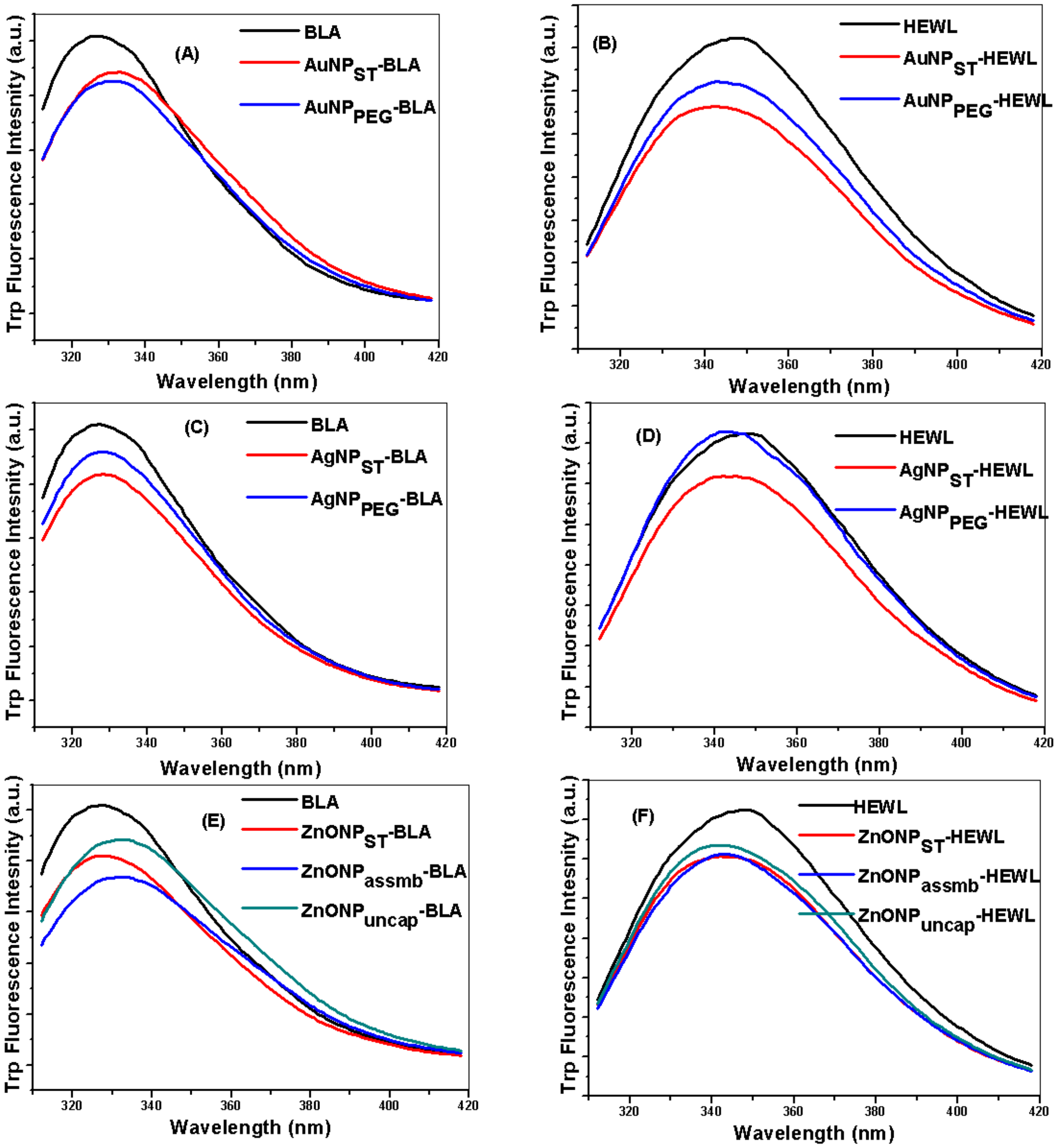

Figure 5. 27 Trp fluorescence analysis of different BLA and HEWL sample (A) AuNP-HEWL (starch and PEG capped), (B) AuNP-HEWL (starch and PEG capped), (C) AgNP-BLA (starch and PEG capped), (D) AgNP-HEWL (starch and PEG capped), (E) ZnONP-BLA (starch, assembly and uncapped), (B) ZnONP-HEWL (starch, assembly and uncapped).

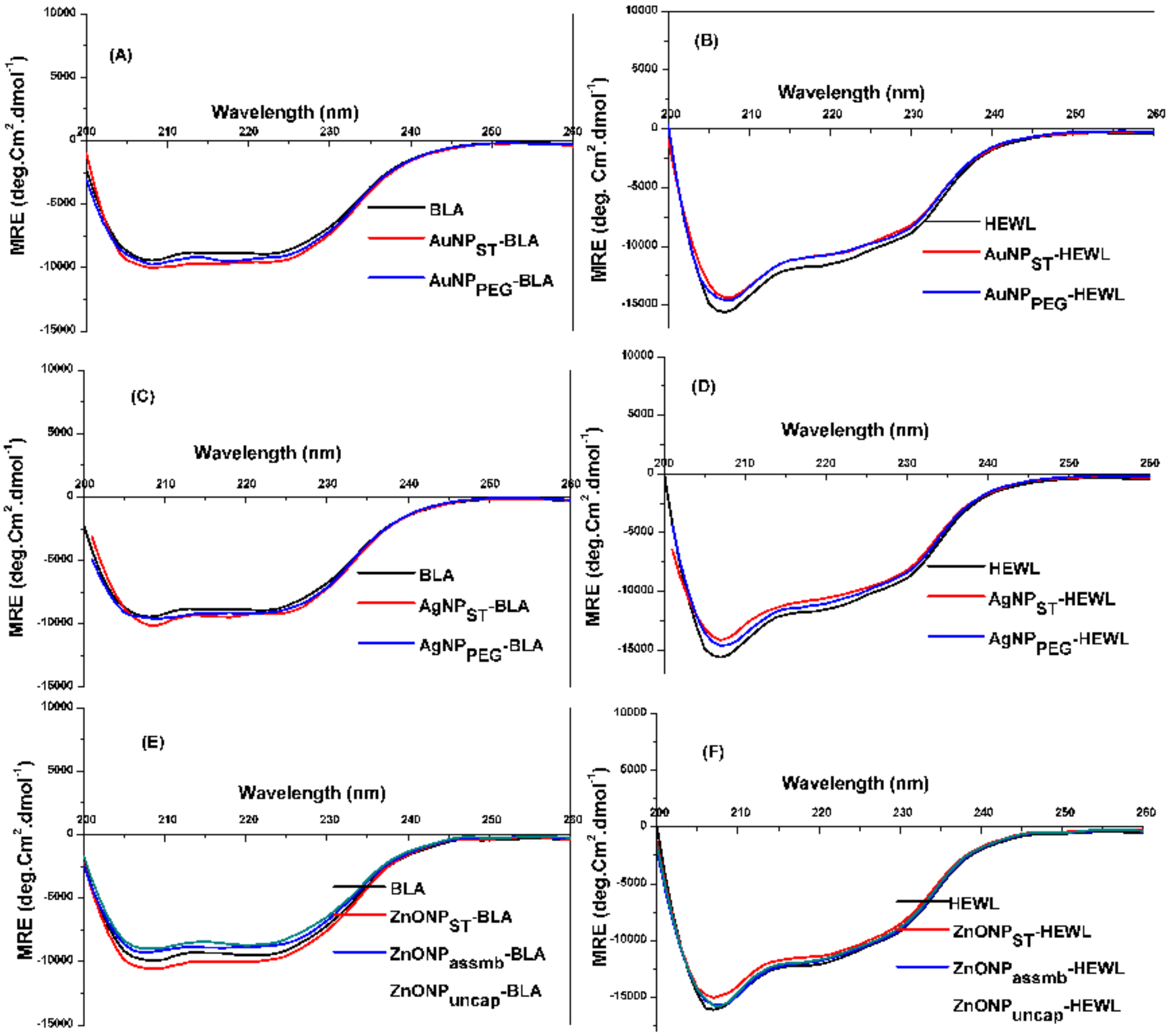

Figure 5.28 CD spectroscopic analysis of different conjugate of NP with BLA and HEWL sample (A) AuNP-HEWL (starch and PEG capped), (B) AuNP-HEWL (starch and PEG capped), (C) AgNP-BLA (starch and PEG capped), (D) AgNP-HEWL (starch and PEG capped), (E) ZnONP-BLA (starch, assembly and uncapped), (B) ZnONP-HEWL (starch, assembly and uncapped).

5.3.1.14 Lysozyme activity

The enzyme assay of various NP-protein complexes showed that starch and PEG capped AuNP and AgNP were unable to retain the free HEWL enzyme activity. The enzyme activity analysis showed that AuNP$_{ST}$ and AuNP$_{PEG}$ cause loss in activity of 40% and 33%, respectively. Moreover, AgNP$_{ST}$ and AgNP$_{PEG}$ showed 39% and 33.9% loss, respectively. This indicated that PEGylation of AuNP and AgNP showed reduced the loss in enzyme activity compared starch capped NP.

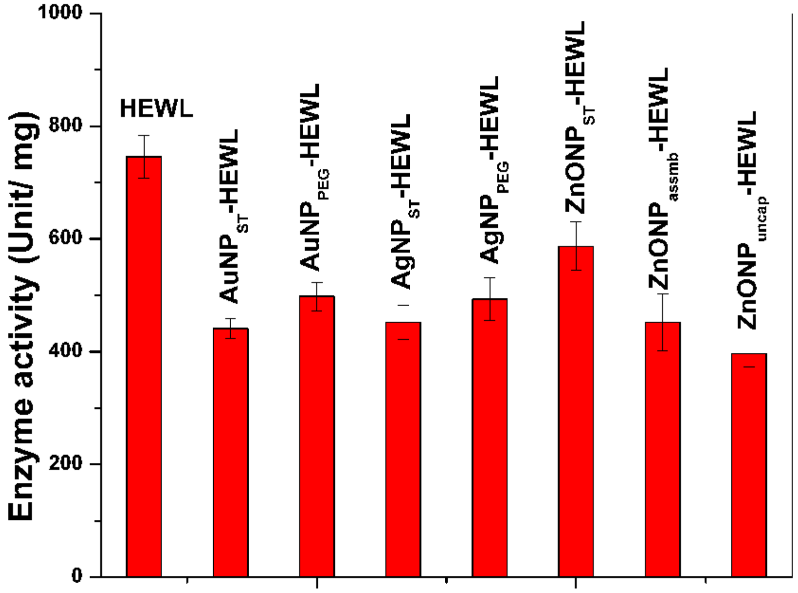

Figure 5.29 Enzyme activity of different HEWL (0.1 mg/ml) sample with HEWL-AuNP (starch and PEG capped), HEWL-AgNP (starch and PEG capped), BLA-ZnONP (starch capped, assembly and uncapped).

When we analyzed the effect of starch-capped (ZnONP_{ST}), uncapped ($\text{ZnONP}_{\text{uncap}}$), and self-assembly ($\text{ZnONP}_{\text{assmb}}$) of ZnONP on HEWL activity, the result indicated the structural changes in protein due to interaction causes a loss in enzyme activity. The results showed that ZnONPST causes 21% loss in enzyme activity while $\text{ZnONP}_{\text{uncap}}$ and $\text{ZnONP}_{\text{assmb}}$ showed 46.9% and 39.4% loss in enzyme activity. Therefore, the enzyme activity analysis showed that self-assembly and uncapped ZnONP reduced the enzyme activity of protein (Figure 5.29) by altering the HEWL structure more severally than ZnONP_{ST}. Therefore, it is confirmed that variation in surface capping and its effect also vary the function of NP. However, the variation is mostly governing by core material because variation in surface is capping unable to protect the loss but can reduce the effect.

CHAPTER 6

EFFECT OF GOLD AND SILVER NANOPARTICLE ON THE INHIBITION OF HEN EGG LYSOZYME AMYLOID FIBRILLATION AND ITS CELLULAR TOXICITY

6.1 Materials and methods

6.1.1 Materials

Hen egg white lysozyme (HEWL) (EC 3.2.1.17), DMEM media, and Fetal bovine serum (FBS) were obtained from Sigma-Aldrich (Germany). Hydrochloric acid (HCl), potassium dihydrogen phosphate (KH_2PO_4), sodium chloride (NaCl), thioflavin-T (ThT), and potassium chloride (KCl) were purchased from Himedia (India). Mice neuroblastoma cell line, N2a and human keratinocyte cell line, HaCaT were procured from NCCS, Pune, India. All glassware was rinsed by aqua regia and washed using double distilled water and dried in hot air oven before use. All the experiments were performed using Milli-Q water.

6.2 Methods

6.2.1 Synthesis of gold and silver nanoparticle

For this study, starch and polyethylene glycol (PEG) capped gold and silver nanoparticles (AuNP and AgNP) were synthesized by the wet chemical method and characterized by standard techniques for size, shape, and stability analysis. Detail protocol was already described in chapter-4.

6.2.2 Preparation of amyloid

Hen egg white lysozyme (HEWL) solution was prepared as described by Liu and Wang with slight modification [118]. Protein (70 μM) samples were prepared in hydrochloric acid (pH 2.0), which contain 2.7 mM KCl, 137 mM NaCl, and 0.01% (w/v) NaN_3. The solutions (20 mL) were incubated in a shaker incubator at 58 ^{0}C temperature and at a shaking speed of 100 rpm. Further, amyloid samples were analyzed by various standard methods such as thioflavin-T fluorescence assay and electron microscopy.

6.2.3 Electron microscopic imaging of amyloid samples

The amyloid growth was observed by atomic force microscopy (AFM) (Agilent 5500) and field emission scanning electron microscopy (FESEM) (Nova Nano-SEM) at 5 kV voltage, and TEM (CM 200, Phillips). For AFM analysis, samples were deposited by drop casting method, dried under vacuum and analyzed in tapping mode. For FESEM analysis, the sample was drop cast on silica wafer and dried under vacuum for overnight and gold coated for 1 min using sputtering of the sample. For TEM analysis, the sample was deposited on a copper grid of 300 meshes, negatively stained with uranyl acetate and dried in a vacuum drier for overnight before analysis.

6.2.4 Analyzing the effect of AuNP and AgNP

The effect of ZnONP (uncapped, starch capped, and self-assembly) on the HEWL amyloid growth was analyzed. A fixed concentration of three types of NP (10 μM) was administered to 70 μM protein samples at 0 h and incubated at 58 ^{0}C for 72 h, and amyloid growth kinetics was monitored by Thioflavin-T fluorescence assay performed at an interval of 12 h up to 120 h. Moreover, the effect of different concentration of $AuNP_{ST}$ and $AgNP_{ST}$ (0.1, 0.2, 0.5, 1, 2, 5, 10, and 20 μM) on the growth and structure of amyloid was also analyzed after 72 h of incubation. The effect of NP on the different phases of growth such as lag, log phase, and stationary phase was also monitored by adding optimized NP sample. Moreover, the surface hydrophobicity was studied by protein-bound ANS fluorescence assay. The ζ-potential and hydrodynamic size distribution were analyzed by a zeta sizer (Nano-ZS, Malvern Pvt.). The structural change of amyloid was monitored by measuring Tryptophan (Trp) fluorescence spectra (Cary Eclipse, Agilent Pvt.) and secondary structural analysis was performed by Circular dichroism (CD) (Jasco-815) spectroscopy. The surface morphology and assembly of amyloid was observed by electron as well as atomic force microscopy using TEM (Jeol), AFM (Agilent), and FESEM.

6.2.5 Thioflavin-T (ThT) fluorescence measurement

The amyloid samples were diluted to 7 μM concentration and ThT was added such that the final concentration of ThT was 20 µM in sodium phosphate buffer, pH 7.4. The solutions were incubated for 20 min before spectrofluorometric (Cary eclipse, Agilent) analysis. The excitation was set at 440 nm and emission was recorded between 460-600 nm. The excitation and emission slit width were set at 5.0 and 10 nm, respectively. The growth of amyloid fibers was analyzed by ThT fluorescence at a different time interval (0, 24, 36, 48, 60, 72, 84, 96, 108, 120 h), and emission was recorded. The amyloid growth curve was plotted with time (h), using the area under the curve of ThT emission spectra. The contribution of free ThT was subtracted before analysis.

6.2.6 1-Anilinonaphthalene-8-sulfonic (ANS) assay

The protein-bound ANS fluorescence assay was performed in 3 mL sodium phosphate buffer (20 mM). The amyloid sample was diluted to make the final concentration of protein and ANS of 7 µM and 150 µM, respectively. The solution was incubated for 30 min before measuring ANS fluorescence. The samples were excited at 350 nm and emission spectra were recorded between 400 and 600 nm by a Cary eclipse fluorescence spectrophotometer (Agilent Pvt. Ltd.). The excitation and emission slit width were adjusted at 5 and 10 nm, respectively

6.2.7 Dynamic light scattering and ζ-potential analysis

The hydrodynamic size distribution of amyloid samples was analyzed by a zeta sizer (Malvern Nano-ZS series). Moreover, Aggregation index (AI) was also calculated to monitor the larger aggregate formation by protein. The size of protein aggregates was also monitored using DLS particle size analysis in dual angle mode. Aggregation index (AI) was calculated using the following equation:

$$\boldsymbol{AI = \frac{(Z_{average\,forward})}{(Z_{average\,backward})} - 1 - - - - - - - - (1)}$$

$Z_{\text{average forward}}$ is hydrodynamic size analyzed at a forward angle, and $Z_{\text{average backward}}$ is hydrodynamic size at a backward angle.

The ζ-potential of amyloid samples was analyzed by the zeta sizer (Malvern Nano-ZS series) connected with a DLS particle size analyzer. The samples were diluted five times with distilled water, and ζ-potential of samples was estimated in a disposable cuvette.

6.2.8 Circular Dichroism (CD) analysis

CD spectra of lysozyme amyloid samples (14 µM) were analyzed in the range of 200-260 nm. The baseline correction of the sample was performed. The mean residual ellipticity was plotted, and percentage β-sheet was estimated by using CAPITO online server [192]. All the data were converted to molar residue ellipticity (MRE) by using following equation:

$$\boldsymbol{MRE = \frac{Observed\,[\theta] \cdot 10^6}{n \cdot c \cdot l}} \text{ --------- } \mathbf{(2)}$$

Here, n is a number of amino acids, c is the concentration of protein in µM, ‘l’ is path length in mm.

6.2.9 Intrinsic fluorescence analysis

Tryptophan (Trp) fluorescence of protein samples was also measured by exciting the sample at 295 nm and recording emission in the range of 300-400 nm, with an excitation and emission slit width of 5 and 10 nm, respectively.

6.2.10 Effect of surface capping

We have also used the polyethylene glycol (PEG-400) capped AuNP and AgNP of equivalent size of different concentration (0.1, 0.2, 0.5, 1 µM) in amyloid formation condition. The Th-T binding assay, surface hydrophobicity and zeta potential, secondary structure analysis, hydrodynamic size, morphology, and intrinsic fluorescence were analyzed and compared with starch capped AuNP of equivalent concentration.

6.2.11 Analyzing cytotoxicity of amyloid

The cytotoxicity of amyloid produced with all NP was also analyzed, in mice neuroblastoma N2a cells and normal skin HaCaT cells. The cell lines were procured from the repository in NCCS, Pune. The obtained cells were cultured in Dulbecco's modified Eagle's medium (DMEM) with 10% fetal bovine serum. The obtained cells were counted using cell counter and 2000 cells/ well were inoculated in each well of 96 well plate at 37 ^{0}C and 5% of CO_2 humidity maintained for 24 h. Both the NP, amyloid and amyloid with NP was first washed using sterile water then resuspended in culture media. The 5, 10, 50 μM of the sample were inoculated, and highest concentration (50 μM) was reported. The cells were treated with MTT (0.5 mg/ml) after 24 h of administration of samples and after 2 h of incubation; the undissolved MTT was solubilized by using DMSO. Further, the cells were analyzed at 595 nm, and cell viability was calculated by dividing the absorbance of treated cells with control cells, Mean±SD, n. =3.

$$\textbf{Cell viability (\%)} = (\textbf{OD}_{\textbf{treated}} / \textbf{OD}_{\textbf{control}}) \times 100$$

Here, $OD_{treated}$ is OD 595 of amyloid treated cell; $OD_{control}$ is OD 595 of untreated cells.

6.3 Results and discussion

The synthesis and characterization of nanoparticles were described in chapter-4.

6.3.1 Monitoring the amyloid growth

The *in vitro* monitoring of amyloid formation was performed using enhancement of thioflavin-T (ThT) fluorescence emission due to specific binding of ThT with cross β-sheet [204, 205]. The ThT assay was performed to quantify the amyloid growth at every 12 h of time interval up to 120 h. Further, the variation in surface zeta potential, hydrophobicity, intrinsic fluorescence (tryptophan, and tyrosine), and secondary structure were also monitored.

$AuNP_{ST}$ and $AgNP_{ST}$ (10 μM) were administered at 0 h of amyloid formation, and ThT binding assay was performed by the exciting sample at 440 nm, when excitation and emission slit width was 5 and 10 nm, respectively. The ThT area under the curve was plotted with regard to time

(Figure 6.1 A). The ThT binding assay showed that administration of $AuNP_{ST}$ and $AgNP_{ST}$ caused the inhibition of amyloid growth. Here, we analyzed that addition of NP slowed down the growth of amyloid compared to control (amyloid formed without NP). When an equal amount of NP at 0 h of growth was administered, $AuNP_{ST}$ showed higher amyloid inhibition potential than $AgNP_{ST.}$ Further, we also analyzed the time-dependent variation in surface properties by zeta potential, and surface hydrophobicity measurement of both control and test samples of amyloid with NP.

6.3.2 Surface zeta potential

Change of surface zeta potential with time was analyzed using Malvern zeta sizer. The HEWL (1 mg/ml) was incubated in acidic buffer (pH 2.2), and high temperature (58 ^{0}C) for 120 h and zeta potential of samples were analyzed at every 12 h of the interval. It was observed that the zeta potential of native HEWL in phosphate buffer (pH 7.4) was +6.14 mV, which was reduced to +1.89 mV for amyloid (with none) after 2 h, while amyloid with $AuNP_{ST}$ showed -0.679 mV and +1.66 mV with $AgNP_{ST.}$ From here, it was cleared that initially, all three protein samples (i.e. amyloid, amyloid-$AuNP_{ST}$, and amyloid-$AgNP_{ST}$) lost the solution stability due to reducing surface charge. However, after 36 h of incubation, amyloid samples showed enhanced zeta potential of +29.8 mV, +33.6 mV, +33 mV for amyloid, amyloid-$AuNP_{ST}$, and amyloid-$AgNP_{ST}$, respectively.

6.3.3 Surface hydrophobicity

Surface hydrophobicity of a protein plays an important role in the kinetics of amyloid growth. The formation of a higher amount of hydrophobic surface also promotes the assembly of protein during aggregation and amyloid formation [206]. Therefore, the presence of higher amount of hydrophobic amino acid on the protein surface enhances the assembly of protein by hydrophobic interactions. Here, we observed that amyloid sample (without NP) showed higher surface hydrophobicity up to 48 h of incubation; however, hydrophobicity start decreasing thereafter. Moreover, amyloid samples treated with both NP showed lower surface hydrophobicity than amyloid without NP (Figure 6.1 C) throughout the growth analysis. However, it was observed that during maturation phase of growth surface hydrophobicity of pure amyloid start decreasing; the reason might be the interaction of hydrophobic surfaces and amyloid assembly (Figure 6.1 C).

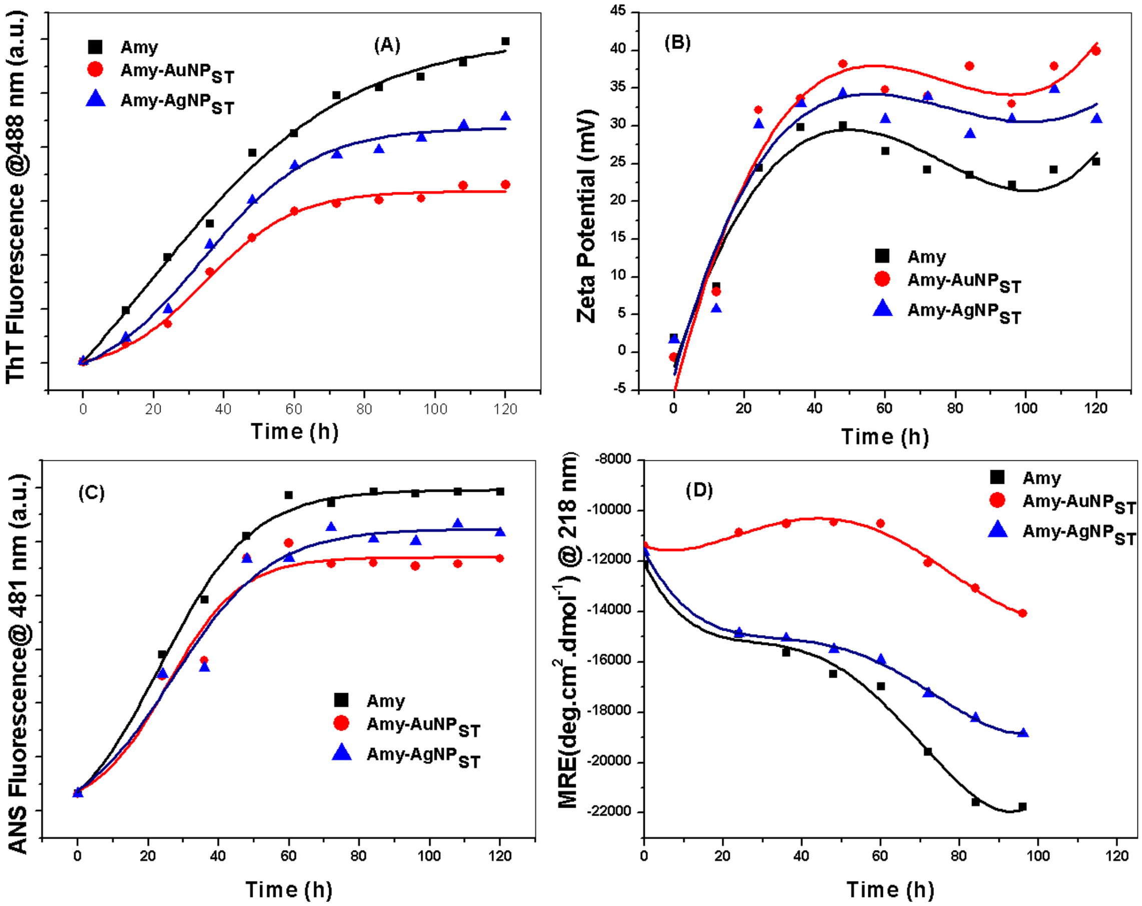

Figure 6.1 The growth profile of amyloid in the presence of AuNP$_{ST}$ and AgNP$_{ST}$. The amyloid growth monitored by (A) ThT binding fluorescence (B) surface zeta potential, (C) surface hydrophobicity (ANS fluorescence) (D) MRE value at 218 nm (correspond to β-sheet).

The time-dependent surface hydrophobicity, zeta potential, ThT analysis showed that amyloid assembly depends on the hydrophobicity and charge of the amyloid surface. The Higher positive charge might inhibit the assembly process due to repulsion force between similar charges while higher surface hydrophobicity facilitates the same and subsequently formation of amyloid fibers. Marshell et al. [207] , reported that hydrophobic, aromatic, and electrostatic interactions play an important role in amyloid fibril formation as well as stability. Moreover, Raman et al. [208] reported that the amyloid fibril growth and stability highly depends on the critical balance of electrostatic and hydrophobic interactions. The hydrophobicity and charge analysis showed that NP, which reduced the surface hydrophobicity but increases the surface zeta potential of proteins showed inhibition of amyloid fibers assembly.

6.3.4 Atomic force microscopic analysis of amyloid morphology

We applied atomic force microscopy (AFM) to analyze the morphology of amyloid formed after 120 h of incubation under different conditions. AFM analysis showed that HEWL formed thin and long fibers by the assembly of protofibrils (Figure 6.2. A); However, administration of $\mathrm{AuNP_{ST}}$ and $\mathrm{AgNP_{ST}}$ (20 µM each), inhibited the fibrillar growth. It was further observed that $\mathrm{AuNP_{ST}}$ was able to completely inhibit the amyloid fibril assembly and formed the amorphous protein aggregates of smaller size (Figure 6.2 B).

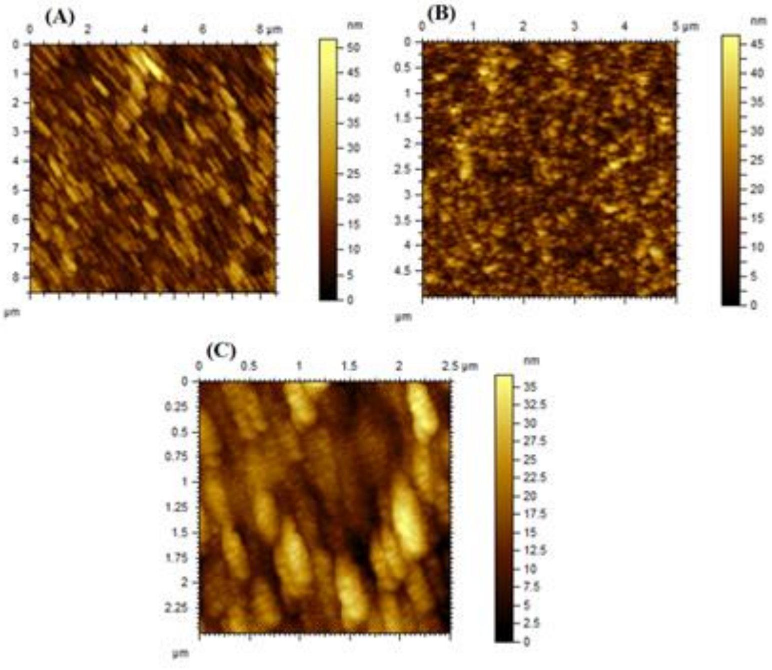

Figure 6.2 AFM analysis of amyloid fibrils in different conditions. Amyloid prepared with (A) none, (B) $\mathrm{AuNP_{ST}}$, (C) $\mathrm{AgNP_{ST}}$

Moreover, AFM analysis of amyloid with $\mathrm{AgNP_{ST}}$ showed that $\mathrm{AgNP_{ST}}$ was able to form larger aggregates of proteins (Figure 6.2. C). From AFM analysis, it was clear that different metal nanoparticles of equivalent size and similar surface capping agent could affect the growth of amyloid fiber assembly and structure and prevent the amyloid formation to a different extent and developed the different morphology of protein aggregates.

6.3.5 CD measurement

The secondary structure analysis of HEWL samples (without and with NP) using CD measurement showed that administration of $AuNP_{ST}$ (10 μM) causes reduction of β-sheet production of HEWL. The results showed that after 72 h of incubation pure amyloid showed 68% of β-sheet formation (Figure 6.1 D), but HEWL produced with $AuNP_{ST}$ (Figure 6.3 D), and $AgNP_{ST}$ (Figure 6.1 D) showed much-reduced amount of β-sheet i.e. 39% and 47%, respectively. Such drastic reduction of β-sheet was perhaps associated with the inhibition of amyloid fiber formation.

6.3.6 Intrinsic fluorescence

The variation in intrinsic fluorescence is an important tool to analyze the conformational changes in the protein. It was observed that fluorescence quenching and a shift in emission wavelength indicate the variation in the microenvironment of the protein [182-184]. Therefore, variation in protein tryptophan fluorescence with time was analyzed by exciting samples at 295 nm and emission was recorded between 300-400 nm using fixed excitation and emission slit width of 5 and 10 nm, respectively. Both the amyloid sample (with none, and $AuNP_{ST}$) showed equivalent fluorescence quenching, but amyloid prepared with $AgNP_{ST}$ showed a higher amount of quenching up to 48 h of incubation (Figure 6.3). However, at 60 h of growth of amyloid (produced with $AuNP_{ST}$ and $AgNP_{ST}$) showed less amount of quenching than pure amyloid. Moreover, after 72 h, amyloid prepared with both NP showed less fluorescence quenching than pure amyloid (Figure 6.3). The time-dependent Trp fluorescence analysis showed the continuous tertiary structure transition in during amyloid growth. The pure amyloid sample showed quenching in Trp fluorescence with a red shift in emission peak this fact indicated that during amyloid formation Trp and hydrophobic core of protein exposed to the polar environment. However, the later state of growth, assembly of fibrils showed the movement of Trp toward non-polar environment with some blue shift in emission.

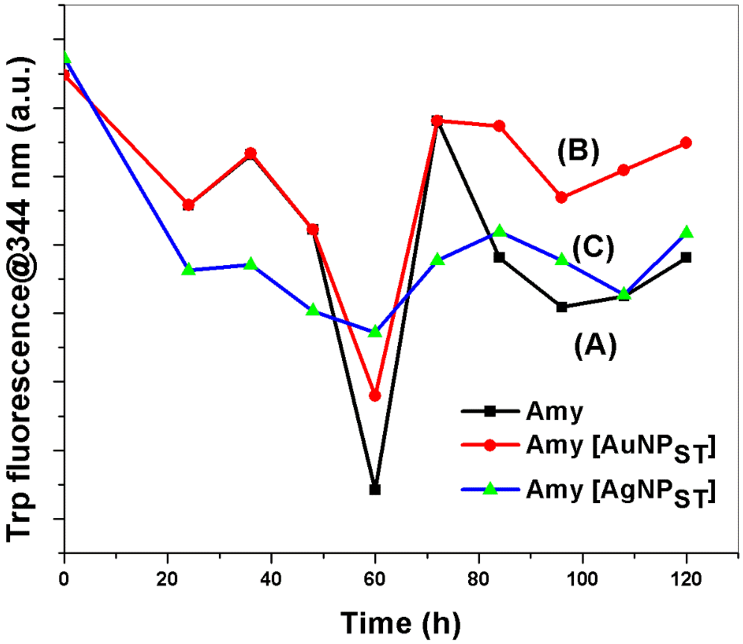

Figure 6. 3 Tryptophan fluorescence spectra of amyloid prepared with (A) none, (B) AuNP$_{ST}$, (C) AgNP$_{ST}$.

Moreover, Trp fluorescence analysis of an amyloid sample prepared with NP showed fluorescence quenching with a blue shift in emission indicated that fluorescence quenching was related with the interaction of amyloid with NP. It was also revealed that intrinsic fluorescence and conformational changes vary with the type of NP administered in amyloid solution, which causes variation in exposure of Trp residue to polar environment and subsequently the amyloid growth.

6.3.7 Effect of NP dose

To analyze the effect of different doses of AuNP$_{ST}$ and AgNP$_{ST}$ in amyloid formation, we used a wide range of NP concentration i.e. 0.1, 0.2, 0.5, 1, 5, 10, and 20 µM with 1 mg/ml of HEWL protein and incubated up to 120 h. Further, ThT binding assay, surface hydrophobicity analysis by ANS binding, zeta potential analysis, aggregation index (AI) analysis, Trp fluorescence analysis, and TEM analysis were performed.

The ThT analysis showed that binding of ThT with amyloid cross β-sheet structure continuously decreased with an increment of both the NP concentration up to the 20 μM (Figure 6.4 A and Figure 6.5 A). However, it was observed that increment of $AuNP_{ST}$ showed higher effect than $AgNP_{ST}$ of similar concentration. The ThT emission analysis clearly indicated that $AuNP_{ST}$ was more effective to inhibit the amyloid fibrillar assembly than $AgNP_{ST}$ of similar concentration.

Further, we analyzed the effect of different concentration of NP in the structure of HEWL amyloid by circular dichroism (CD) and fluorescence spectroscopic analysis. The CD analysis of different amyloid sample showed that addition of both NP causes inhibition of β-sheet formation with $AuNP_{ST}$ showed the highest effect. The pure amyloid sample showed 68% of β-sheet formation from 19% of native HEWL. However, incubation of HEWL with different concentration of $AuNP_{ST}$ and $AgNP_{ST}$ causes the formation of 57 to 40% of beta-sheet content with $AuNP_{ST}$ (Figure 6.4 B), however, $AgNP_{ST}$ showed 62- 51% beta- sheet for the same concentration of NP (Figure 6.6 B). Further, we have analyzed the effect of NP concentration on the surface hydrophobicity of amyloid protein (Figure 6.4 C and Figure 6.5 C). Here, we observed that increment of $AuNP_{ST}$ concentration causes a reduction in surface hydrophobicity compared to amyloid without NP (Figure.6.4 A). However, we also observed that similar amount of $AgNP_{ST}$ showed the insignificant effect on the surface hydrophobicity of amyloid (Figure 6.5 C).

Moreover, analyzing the zeta potential of NP treated amyloid sample showed that increasing the $AuNP_{ST}$ concentration up to 20 μM causes increment of zeta potential from 30 mV to 40 mV (Figure 6.4 D). When we have analyzed the zeta potential of $AgNP_{ST}$ treated sample, the results showed that increment of $AgNP_{ST}$ concentration up to 10 μM causes an increment of zeta potential to 38 mV but further increment causes saturation of zeta potential to 39 mV (Figure 6.5 D). Zeta potential analysis showed that stability of amyloid and its assembly vary with the type of NP and concentration added in solution. Here, we observed that $AuNP_{ST}$ showed higher potential to inhibit amyloid growth, which was shown by reduced ThT fluorescence, and CD spectroscopy.

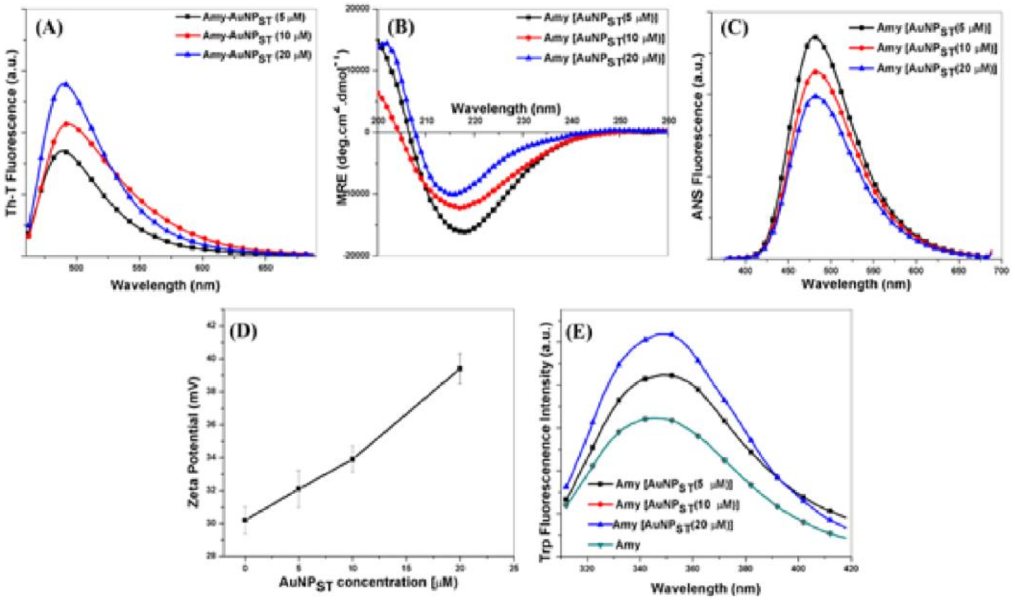

Figure 6.4 The effect of different concentration of AuNP$_{ST}$ (5, 10, 20 μM) in amyloid fibrils formation. (A) ThT binding assay, (B) CD analysis, (C) surface hydrophobicity analysis by ANS binding fluorescence, (D) zeta potential analysis, (E) Trp fluorescence variation.

Further, we analyzed the surface properties of amyloid samples by surface hydrophobicity analysis and net surface charge by zeta potential analysis. The surface hydrophobicity analysis was performed using ANS, samples were excited at 350 nm, and emission was recorded at 481 nm (Figure 6.4 C & D and Figure 6.5 C & D). The results showed that amyloid sample with AuNP$_{ST}$ and AgNP$_{ST}$ showed decreased in surface hydrophobicity and enhanced positive zeta potential with increasing NP concentrations. From ANS binding fluorescence and zeta, the potential analysis showed that administration of different concentrations of NP enhanced the solution stability of protein-NP conjugates and reduced the amyloid formation.

Here, we observed that AuNP$_{ST}$ cause a reduction in surface hydrophobicity (Figure 6.4 C) while AgNP$_{ST}$ was unable to change the surface hydrophobicity significantly (Figure 6.5 C); however, both NPs increase the zeta potential.

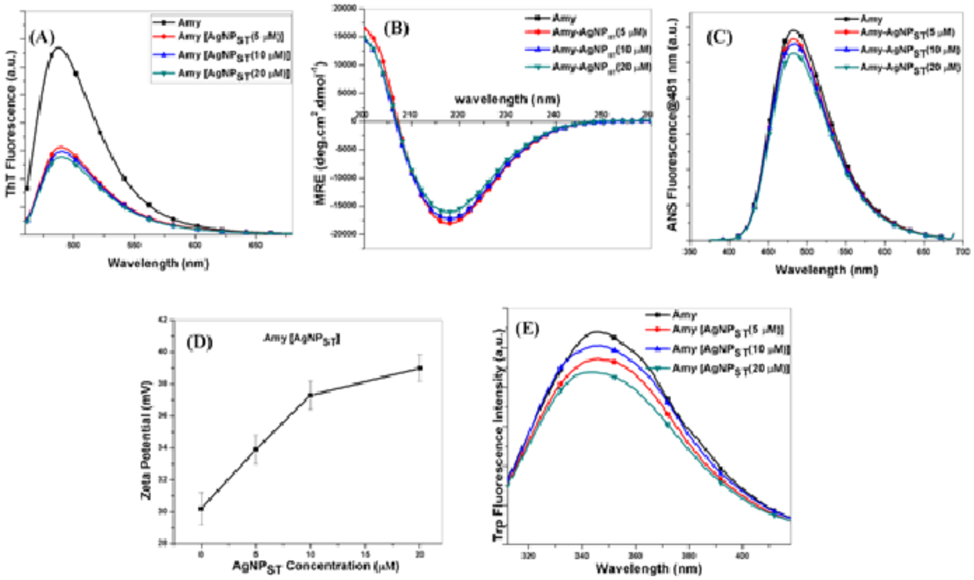

Figure 6.5 The effect of different concentration of AgNP$_{ST}$ (5, 10, 20 μM) on amyloid fibril formation. (A) ThT binding assay, (B) CD analysis, (C) surface hydrophobicity analysis by ANS binding fluorescence, (D) zeta potential analysis, (E) Trp fluorescence variation.

This indicated that although AgNP$_{ST}$ increased the surface zeta potential but simultaneously it was less efficient to protect the hydrophobic patches evolved during amyloid formation. Moreover, AuNP$_{ST}$ not only reduced the surface hydrophobicity but also increased the surface zeta potential at higher concentrations. Analyzing the dose-dependent effect of NP on amyloid formation clearly indicated that amyloid formation and assembly depends on both zeta potential and surface hydrophobicity of protein and the NP that were able to reduce the hydrophobicity and increased zeta potential, which indicates higher inhibition potential.

Further, we analyzed the Trp fluorescence by exciting protein sample at 295 nm. The administration of different doses of AuNP$_{ST}$ and AgNP$_{ST}$ (5, 10, 20 μM) and analyzing the variation in Trp fluorescence to study the variation in tertiary structure (Figure 6.4 E) and (Figure 6.5 E). Here, we observed that administration of different dose of AuNP$_{ST}$ enhanced the Trp fluorescence to a greater extent than amyloid produce with none (i.e. 10 μM) (Figure 6.4 E); this indicated the movement of Trp toward the non-polar environment. However, amyloid with AgNP$_{ST}$ showed a gradual decrease in Trp fluorescence with increasing NP concentration (Figure 6.5 E), which indicated that during interaction Trp was expose to the more polar environment and causes quenching in fluorescence. It was also observed that amyloid sample prepared with $AuNP_{ST}$ showed the different extent of blue shift (2-10 nm) in Trp fluorescence, while redshift (5-10 nm) was observed in the case of $AgNP_{ST}$. Trp fluorescence analysis indicated structural changes in amyloid also depends on the concentration of administered NP. Moreover, some other reports also observed the similar type of phenomenon. Medina et al. [209] reported that adsorption of protein on NP surface and aggregation of NP-protein complex highly depends on the NP to protein molar ratio. Radic et al. [210] in their simulation study reported that the effect of NP on amyloid growth varies with the variation of NP to protein molar ratio and strength of interaction. Therefore, our observation also supports this observation and revealed that variation in NP to protein ratio causes variation in amyloid structure.

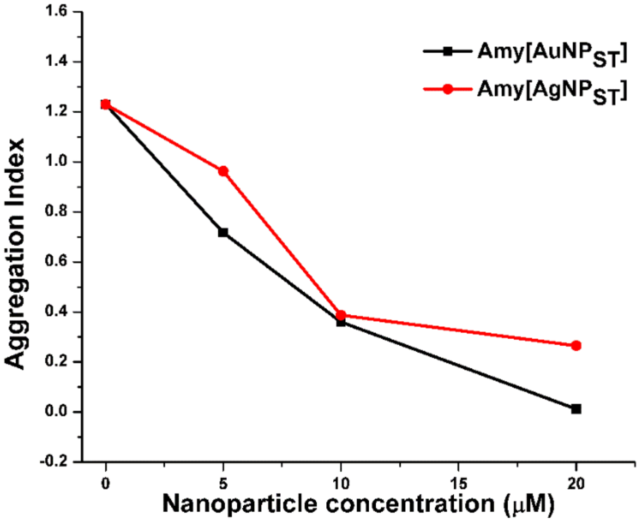

Figure 6.6 Analysis of amyloid Aggregation index (AI) of amyloid samples produced with different concentration of $AuNP_{ST}$ and $AgNP_{ST}$ of 0-20 μM.(The calculation of AI value was given in "Method section 6.1.7" of this chapter.)

TEM and aggregation index (AI) analysis of amyloid sample showed that increasing the NP concentration inhibited the assembly of fibrils assembly and subsequently inhibited the formation of long fibers (Figure 6.6, and Figure 6.7). Therefore, both the results confirmed that administration of starch capped AuNP and AgNP not only inhibited the amyloid β-sheet formation to a different extent but also prevented the assembly of formed amyloid fibrils and produced fragmented amyloid fibers with small aggregates (Figure 6.6, Figure 6.7 B & C and Figure 6.7 D &E), respectively. The Figure 6.7 (A) and (D) are amyloid sample without NP.

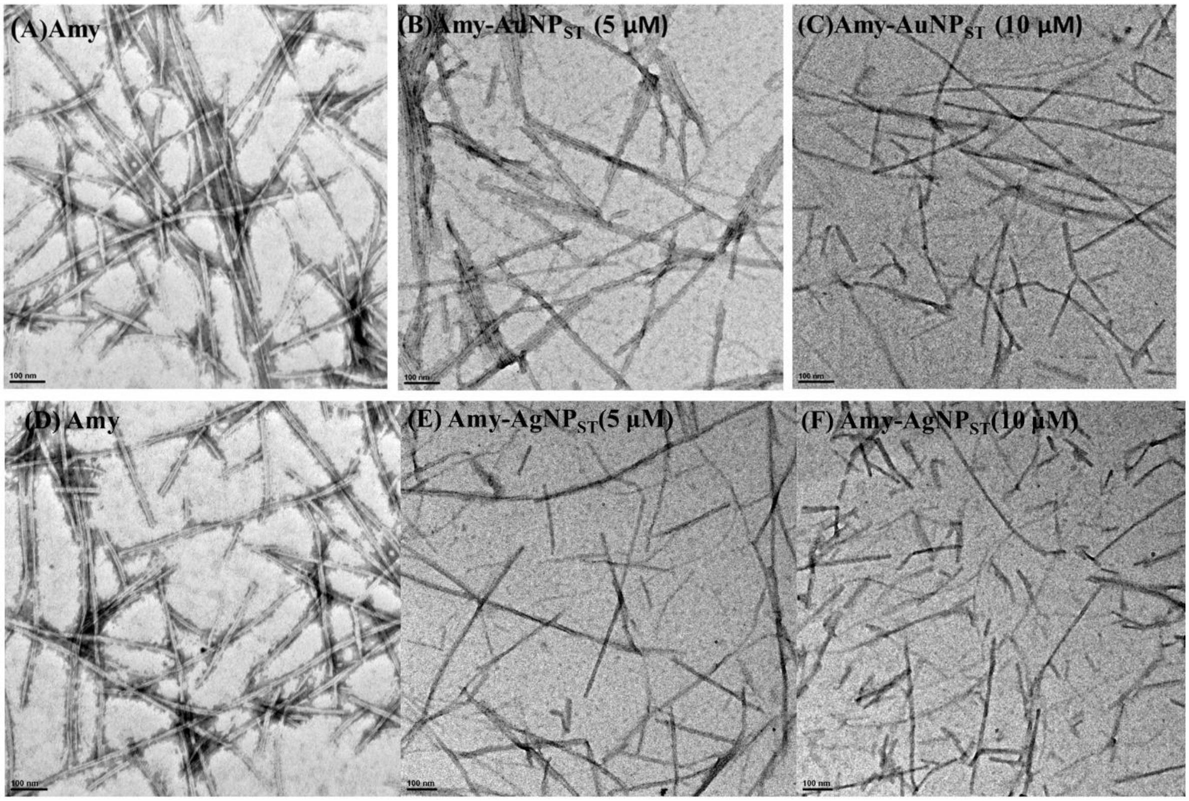

Figure 6.7 TEM analysis of amyloid samples formed with different concentration of AuNP$_{ST}$ and AgNP$_{ST}$. amyloid formed with (A) with none, (B) 5 μM (C) 10 μM of AuNP$_{ST}$; (D) with none, (E) 5 μM and (F) 10 μM of AgNP$_{ST}$.

6.3.8 Effect of administration time

Most of the reports on the effect of NP on amyloid growth ignored that variation in efficacy of NP on a different state of amyloid growth. Therefore, it is essential to observe the effect of NP on the different states of amyloid growth. Here, we used AuNP$_{ST}$, and AgNP$_{ST}$ of 10 μM to observe the role of the NP administration time on amyloid growth. Therefore, we administered both the NP at the beginning of the amyloid growth (0 h), the intermediate state of growth (36 h) and a later phase of growth (48 h). The amyloid growth was analyzed by ThT binding assay and CD spectroscopy by quantifying the β-sheet contents.

The ThT binding analysis showed that administration of both the NP was most effective when we administered the NP at the beginning of amyloid growth (0 h) (Figure 6.8 A & B). The reason might be the interference of NP in amyloid nucleation during growth while administration of NP during later phase might inhibit the assembly of precursor molecule, secondary nucleation, and growth. However, we also observed that administration of both the NP showed less effect on the amyloid growth when administered in the intermediate phase (36 and 48 h), which is a well-known fact for the formation of small fibrils by the assembly of the nucleus. The reason might be the bulk amount of nucleus formed during initial phase and interaction of NP with nucleus might act as a solid support for amyloid nucleus and unavailability free NP for further interaction during intermediate phase might promote fibril formation and secondary growth. However, the addition of NP after the initial state of growth might inhibit the assembly of nucleus and protofibril to form long fibrils due to the availability of free NP to interact.

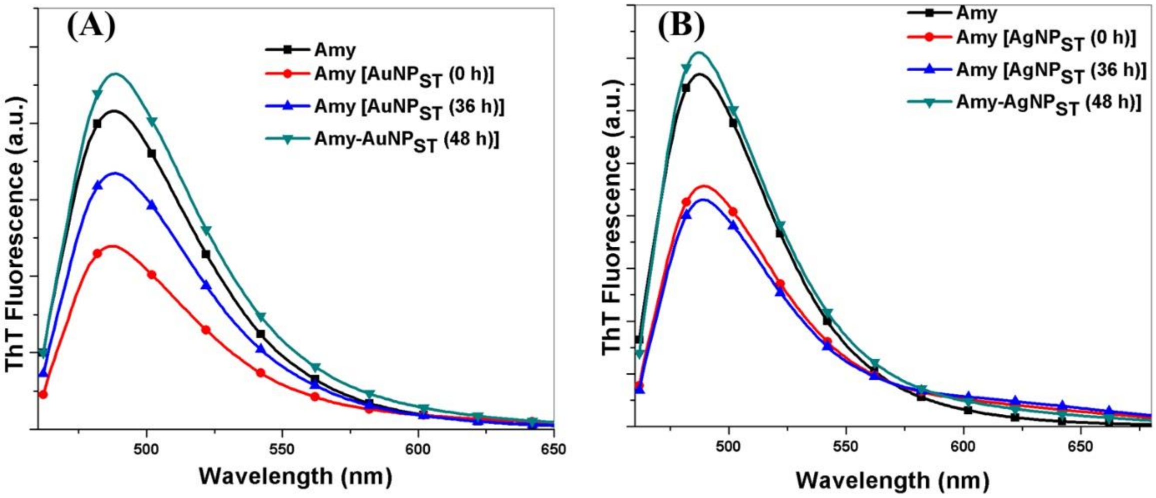

Figure 6.8 ThT analysis of amyloid produced with AuNP$_{ST}$ and AgNP$_{ST}$ administered at 0, 36, 48 h. Amyloid prepared with (A) AuNP$_{ST}$ (B) AgNP$_{ST}$.

Further, the effect of both the NP administration time on Trp fluorescence of amyloid (Figure 6.8 A & B) was analyzed. The result showed that administration of AuNP$_{ST}$ during intermediated and final phase of growth causes quenching of intrinsic fluorescence (Figure 6.8 A). However, the addition of AuNP$_{ST}$ during the early phase of growth showed the lower extent of quenching of fluorescence compared to amyloid with none. Different extent of Trp fluorescence quenching due to the administration of NP in different time indicated the different conformational state of amyloid. Moreover, AgNP$_{ST}$ administration during a different phase of amyloid growth showed quenching in Trp fluorescence in all cases but the different extent of red shift. This fact indicated that AgNP$_{ST}$ administration causes exposure of Trp to the polar environment due to different extent of conformational changes (Figure 6.9 B).

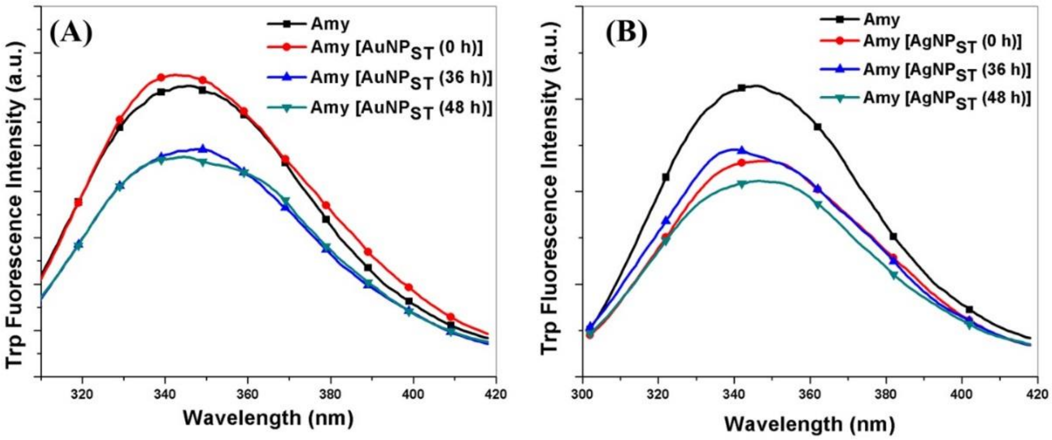

Figure 6.9 Trp fluorescence spectra of various amyloid samples when NP administered at different time (0, 36, 48 h) (A) amyloid with AuNP$_{ST}$ (B) amyloid with AgNP$_{ST}$.

Further, it was observed that the addition of NP during 0 h showed highest zeta potential of 45 mV while administration at 36 h and 48 h reduce the zeta potential to 33 mV and 27 mV (Figure 6.10 A), respectively. Moreover, AgNP$_{ST}$ administration at 0 h and 36 h showed higher zeta potential of 40 and 34 mV indicated the higher stability of amyloid solution (Figure 6.10 B). Therefore, it was observed that administration time also affect the stability of amyloid solution and subsequently the assembly of fibrils.

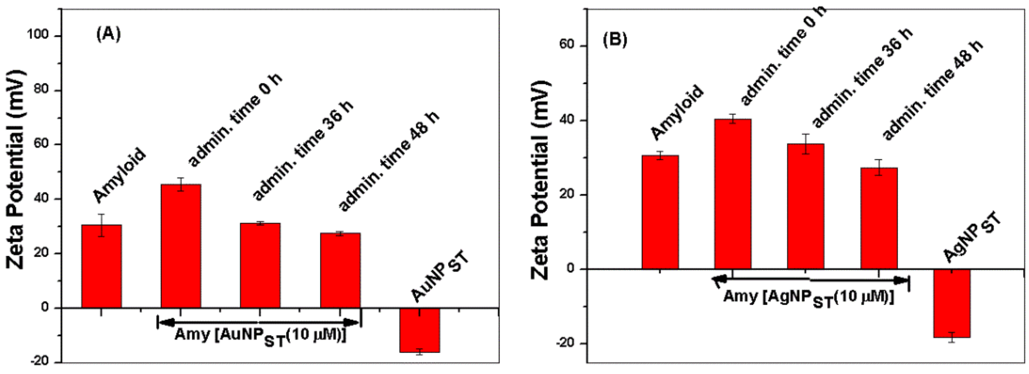

Figure 6.10 Stability of various amyloid samples when NP administered at different time (0, 36, 48 h) (A) amyloid with AuNP$_{ST}$ (B) amyloid with AgNP$_{ST}$.

The ANS fluorescence measurement of amyloid samples showed that the administration time of NP also affects the exposure of hydrophobic surface (Figure 6.11). The $AuNP_{ST}$ administration at 0, 36, and 48 h showed the lower amount of exposure of hydrophobic surface compared to amyloid samples. When NP was administered at 48 h (Figure 6.11 A), showed more amount of hydrophobic surface compared to 0 and 36 h amyloid samples but lower than amyloid with none during amyloid formation. Moreover, the addition of $AgNP_{ST}$ at 48 h also showed the exposure of more hydrophobic surfaces compared to an amyloid sample formed by the addition of $AgNP_{ST}$ (administered at 0 h and 36 h) (Figure 6.11 B). Therefore, ANS analysis also revealed that administration time also could affect the surface hydrophobicity and subsequently the stability of amyloid samples, which is essential for amyloid β-sheet formation and assembly of amyloid precursor to form long fibers.

However, it was observed that higher surface potential might prevent the amyloid formation and assembly even for a sample having higher surface hydrophobicity, which was cleared by ThT assay.

Further, CD spectroscopy analysis was performed to analyze the effect of NP administration time on the secondary structure of amyloid (Figure 6.12 A & B). The obtained data were analyzed using CAPITO server [192] for CD data analysis. The CD analysis showed that administration of both NP at 0 h and 36 h drastically reduced the formation of β-sheet; however, administration of NP at 48 h showed the least effect on the amyloid growth. It was observed that administration of 10 μM of $AuNP_{ST}$ and $AgNP_{ST}$ at 0 h produces 40% and 46% of β-sheet compared to pure amyloid (68%).

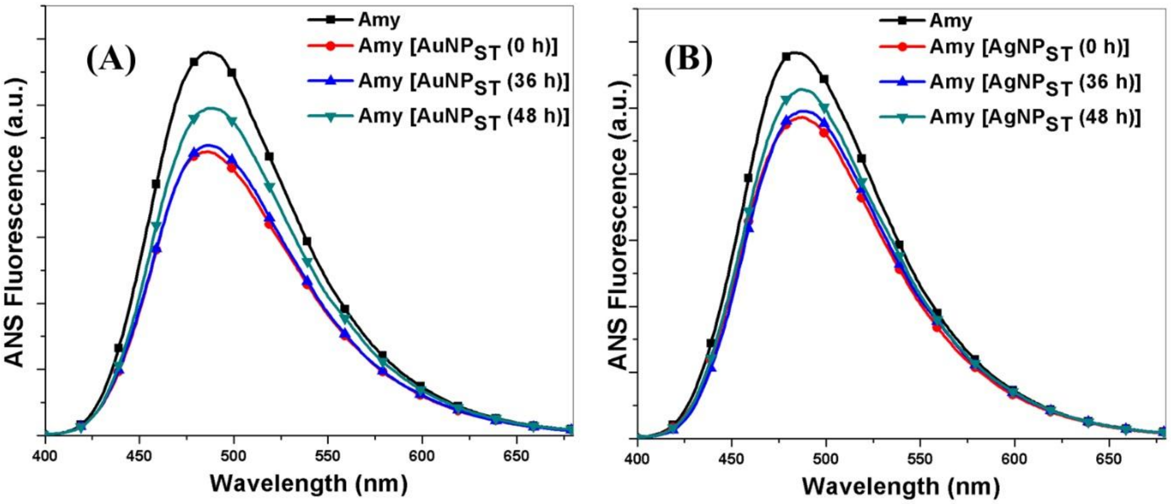

Figure 6.11 ANS fluorescence of amyloid samples produced with AuNP$_{ST}$ and AgNP$_{ST}$ when administered at 0, 36, and 48 h (A) AuNP$_{ST}$ (B) AgNP$_{ST}$.

Moreover, administration of NP at 48 h showed the least effect and produced the 57% and 59% of β-sheet. However, administration of NP at 36 h showed 48% and 52% of β-sheet for AuNP$_{ST}$ and AgNP$_{ST}$. Here, we concluded that reduced amyloid growth due to the administration of NP might be due to the inhibition of amyloid protofibrils assembly and further nucleus formation and subsequent growth of amyloid fibers. However, a higher amount of amyloid formation due to the administration of NP at 48 h compared to 0 and 36 h might be due to the availability of nucleus and protofibrils and subsequently amyloid assembly. Therefore, we concluded that our NP was unable to effectively inhibit or slow down the protofibrils and assembly formation but affect the nucleation amyloid. Various reports on the effect of NPs and active surfaces on amyloid growth also reported the various effects of tested surface on a different state of amyloid growth. Lines et al. [37] reported that co-polymer NP, cerium oxide NP, quantum dots, and carbon nanotubes promote the nucleus formation of β2-microglobulin. Moores et al. [211] reported that variation in surface charge and hydrophobicity of surfaces also vary the amyloid formation. Moreover, Zhu et al. [212] reported that mica surface enhances the protofibril formation and subsequent amyloid assembly compared to free protein.

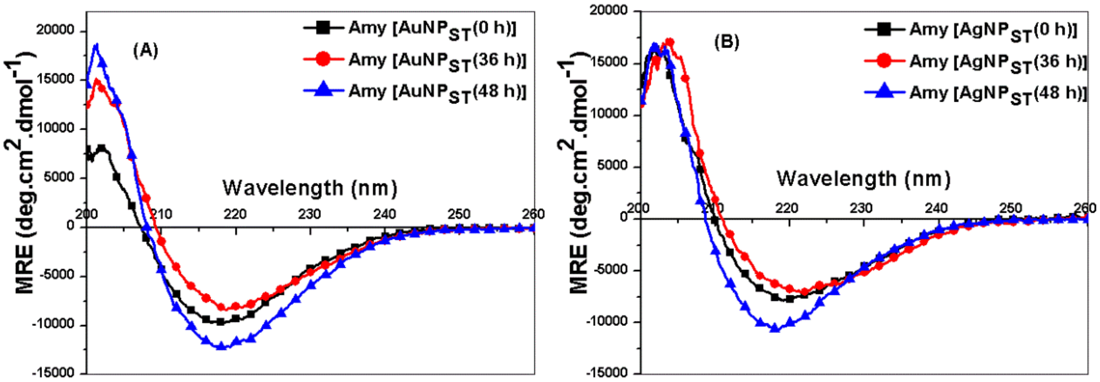

Figure 6.12 CD spectroscopy of amyloid produced with AuNP$_{ST}$ and AgNP$_{ST}$ when administered at 0, 36, 48 h (A) AuNP$_{ST}$ (B) AgNP$_{ST}$.

6.3.9 Effect of capping

Further, we analyzed the effect of the capping agent on amyloid growth. Since polyethylene glycol-400 (PEG-400) has been reported as non-toxic and used as a capping agent to reduce the protein absorption on the NP surface [213] and to develop NP with stealth properties against immune system [56, 214]. We also used different concentrations (0.1-1 µM) of PEG capped AuNP and AgNP of equivalent size in HEWL amyloid forming condition. The ThT assay results showed that PEG capped NP showed a lesser amount of amyloid than starch capped NP (Figure 6.13. A & B) and (Figure 6.14 A & B), which is demonstrated by reduced ThT binding fluorescence. According to previous reports on PEGylated NP and protein interaction, PEGylation reduced the protein adsorption on NP surface. Therefore chances of formation of hard corona on NP surface is less with PEGylated NP. Hence, the interaction of PEGylated nanoparticles might have disturbed the equilibrium of amyloid growth in solution by dynamic interaction on NP surfaces. Radic et al. [210] showed by their analysis that dynamic interaction disturbed the amyloid growth by continued depletion of the precursor from solution. It was also revealed these type of NP amyloid interaction showed inhibition in amyloid at a lower concentration of NP to protein ratio. This fact clearly indicated that reducing the protein absorption on the NP surface using PEG as a capping agent might facilitate the other type of interactions with NP and showed the enhanced potential of amyloid inhibition by PEGylated NP.

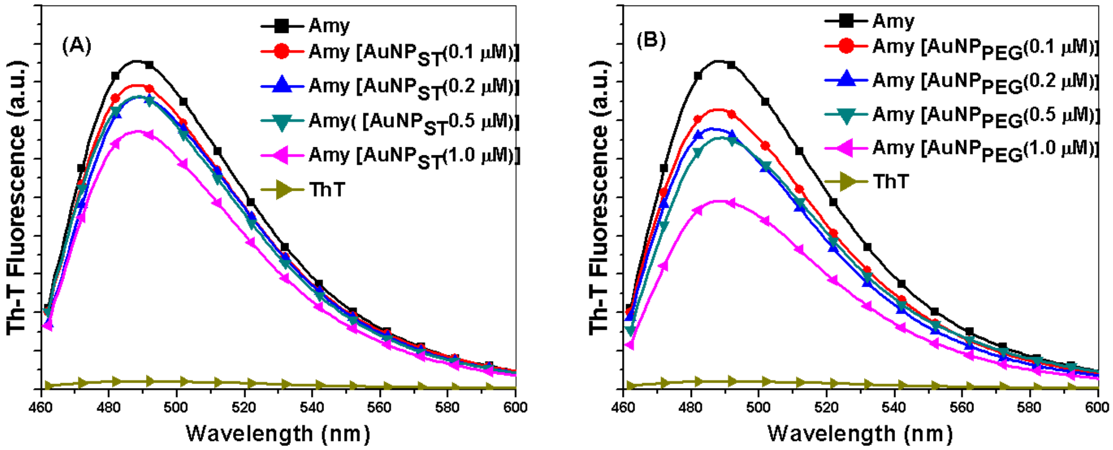

Figure 6.13 Effect of different concentrations (0.1-1 μM) of (A) starch and (B) PEG capped gold nanoparticles on the amyloid formation by the thioflavin-T binding assay.

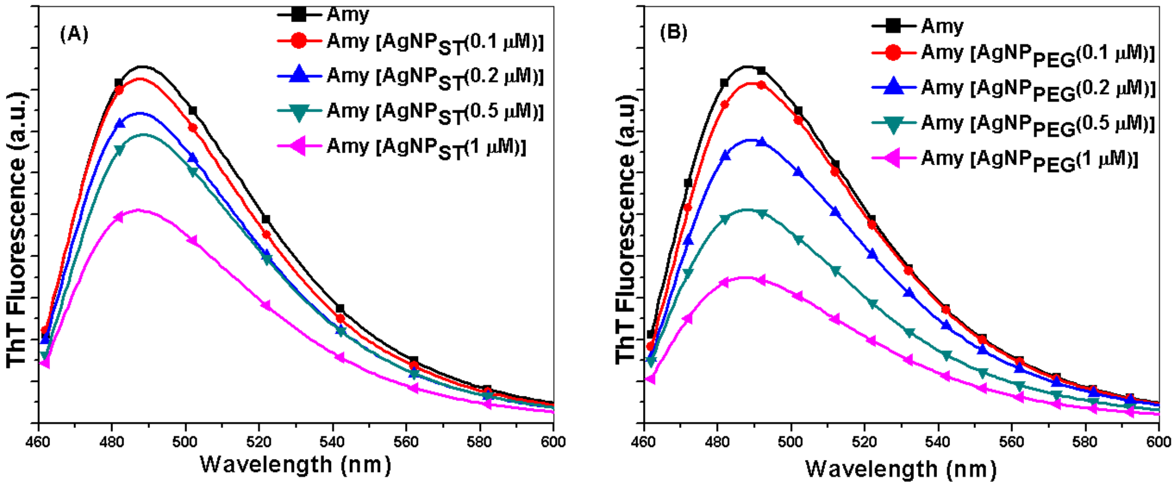

Figure 6.14 Effect of different concentrations (0.1-1 μM) of (A) starch and (B) PEG capped silver nanoparticles on the amyloid formation was analyzed by the thioflavin-T binding assay.

The Trp fluorescence analysis of amyloid produced with starch and PEGylated AuNP and AgNP at various concentration (Figure 6.15 A & B for AuNP), (Figure 6.16 A & B for AgNP) was studied. It was observed that PEGylated AuNP$_{ST}$ showed concentration-dependent quenching of Trp fluorescence while AuNP$_{ST}$ did not show such effect (Figure 6.15). This fact indicated that at lower concentration (0.1-1 μM) of starch capped AuNP showed a lesser effect in Trp fluorescence (Figure 6.15 A) while the similar concentration of PEGylated AuNP showed concentration-dependent quenching of Trp fluorescence (Figure 6.15 B). However, a higher amount of $AuNP_{ST}$ (5-20 µM) showed significant variation in Trp fluorescence (Figure 6.5 E).

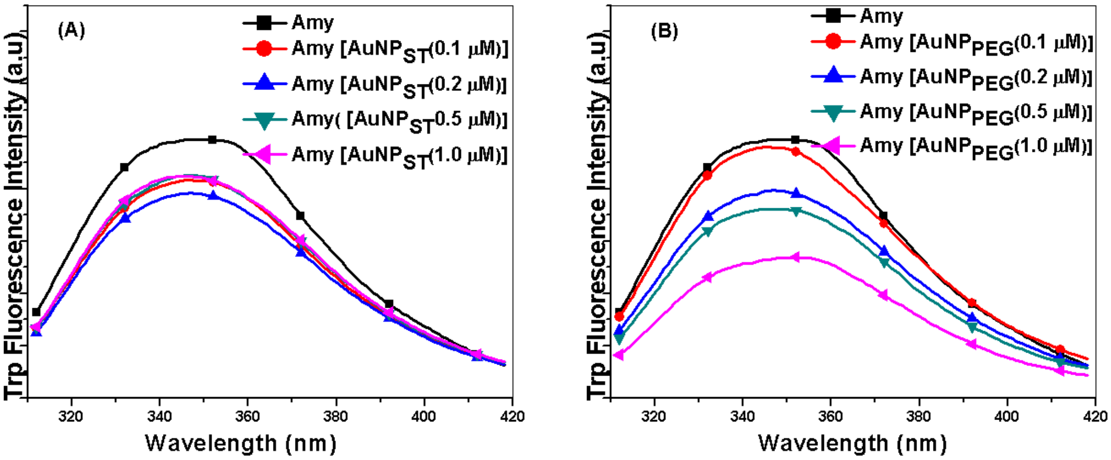

Figure 6.15 Effect of different concentrations (0.1-1 µM) of (A) starch and (B) PEG capped gold nanoparticles on the amyloid samples monitored by Trp fluorescence spectroscopy.

Further, analyzing the effect of PEGylated AgNP on Trp fluorescence showed that variation in Trp fluorescence is less compared to pure amyloid sample, while administration of similar amount of $AgNP_{ST}$ (0.1-1 µM) showed significant variation in Trp fluorescence. This fact indicated that the lower concentration quenched the Trp fluorescence to different extent while showed less shift (blue or red shift) Trp fluorescence compared to pure amyloid (Figure 6.16 A); however, PEGylated AgNP showed less quenching of Trp fluorescence but showed simultaneous blue shift in emission, indicated the movement of Trp toward non-polar environment (Figure 6.16 B). Therefore, PEGylated $AgNP_{ST}$ affects the tertiary structure more drastically than $AgNP_{ST}$.

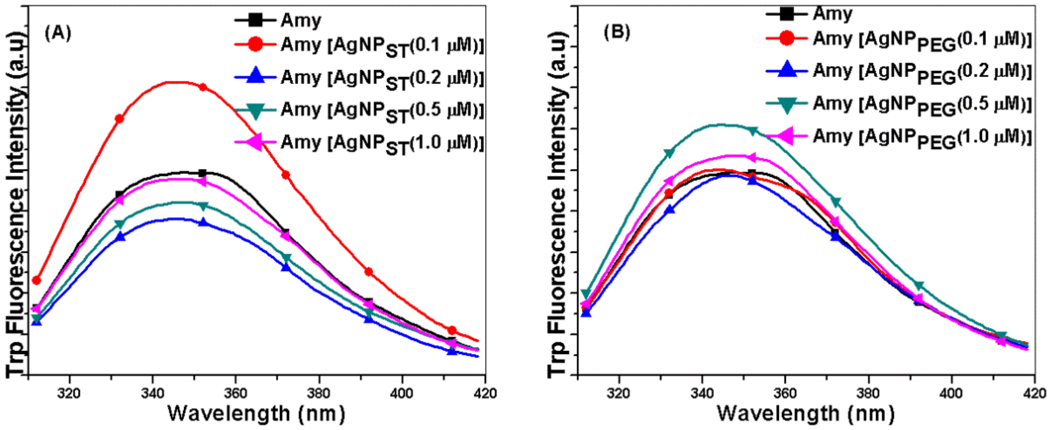

Figure 6.16 Effect of different concentrations (0.1-1 μM) of (A) starch and (B) PEG capped AgNP on the amyloid samples monitored by Trp fluorescence spectroscopy.

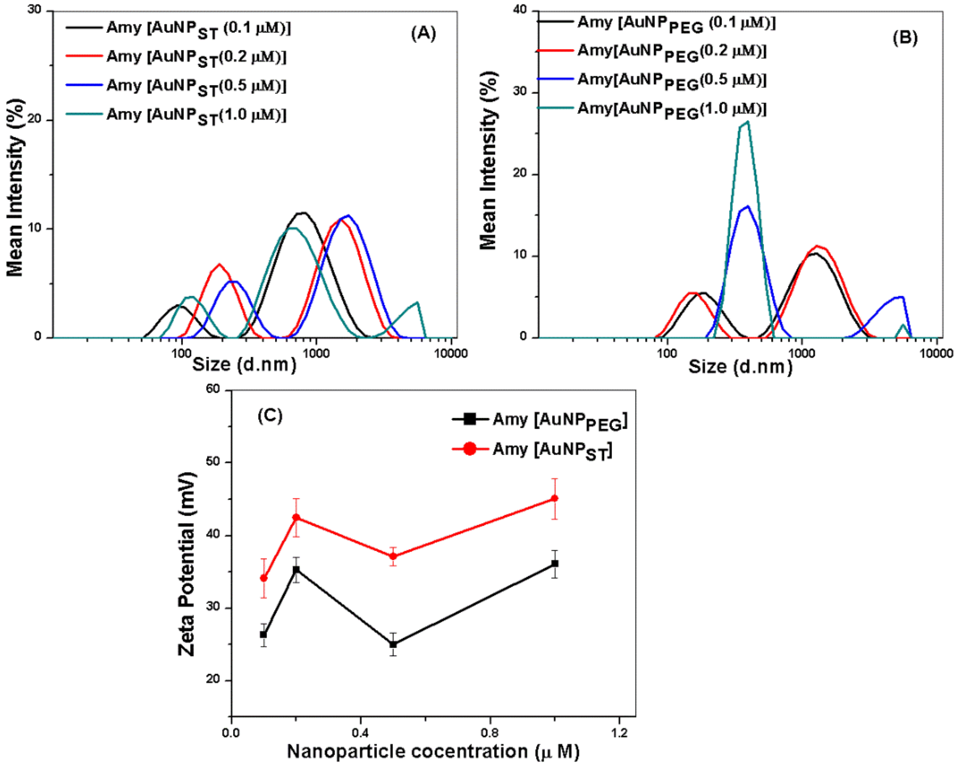

Figure 6.17 Effect of different concentrations (0.1-1 μM) of (A) starch and (B) PEG capped AuNP on hydrodynamic size variation. (C) Amyloid surface zeta potential same sample.

Further, we analyzed the hydrodynamic size and surface zeta potential of amyloid samples treated with starch and PEGylated AuNP and AgNP (Figure 6.17) and (Figure 6.18). The DLS analysis showed that addition of PEGylated NP produced smaller fibers while starch capped AuNP showed multiple peaks; indicates the formation of poly-dispersed NP-protein aggregates (Figure 6.16 A & B). Zeta potential analysis showed that increasing the $AuNP_{ST}$ concentration also increase the zeta potential of amyloid (46 mV) while $AuNP_{PEG}$ of same concentration showed less effect on the amyloid zeta potential (39 mV) (Figure 6.17 C). Therefore, starch capped and PEG capped AuNP produced highly stable amyloid suspension.

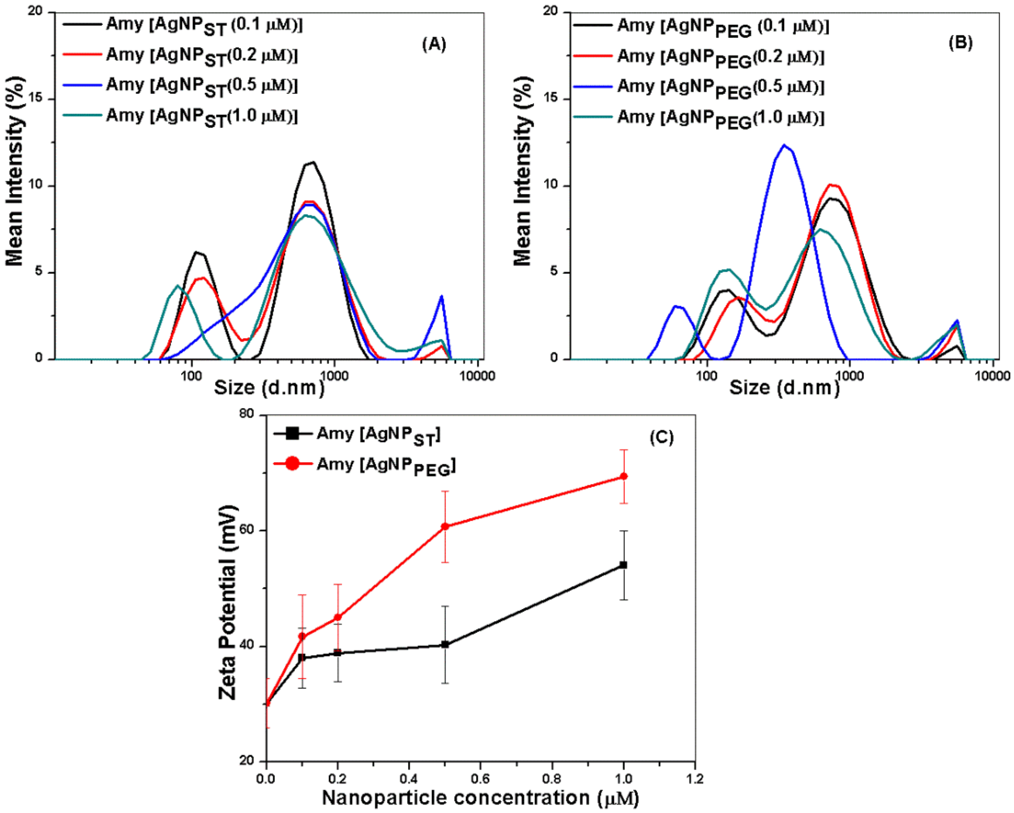

Figure 6.18 Hydrodynamic size and surface zeta potential of amyloid, when the different concentration of (A) starch AgNP (B) PEG capped AgNP on hydrodynamic size variation. (C) surface zeta potential amyloid with $AgNP_{ST}$ and $AgNP_{PEG}$.

We analyzed hydrodynamic size distribution and zeta potential of the amyloid samples prepared with the different concentration of $AgNP_{ST}$ and $AgNP_{PEG}$ (Figure 6.17). The DLS analysis showed that AgNP (starch and PEGylated) produced highly poly-dispersed protein aggregates (Figure 6.18 A & B). Moreover, the result showed that although AgNP increased the zeta potential of the amyloid solution and above 0.2 µM causes drastic enhancement of zeta potential in case of both starch capping and PEGylated AgNP and both samples showed zeta potential more than > 40 mV. Hydrodynamic size and zeta potential analysis showed that even PEGylation produced a more stable amyloid solution and therefore, reduced the chance of assembly of amyloid protein precursors.

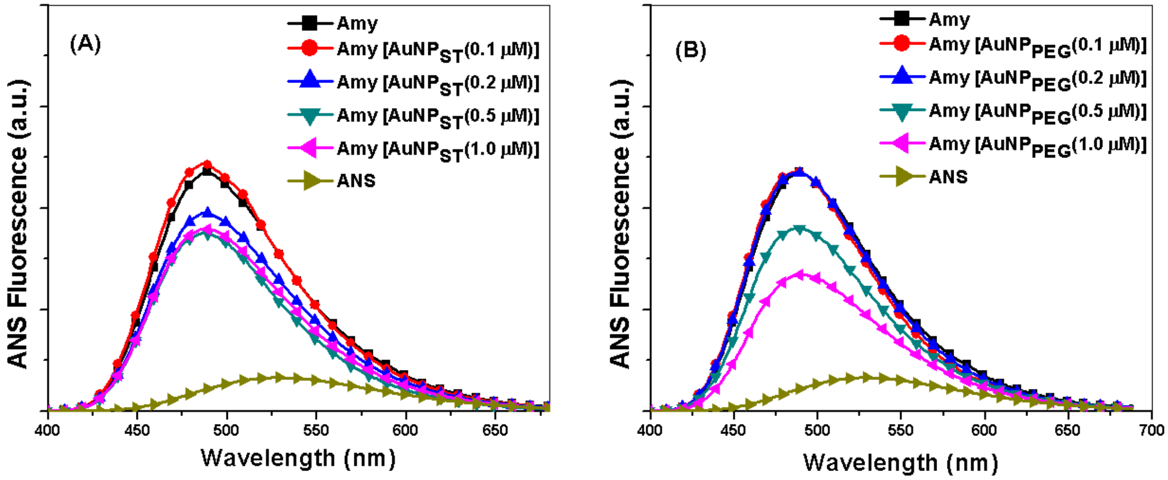

Figure 6.19 Effect of different concentrations (0.1-1 µM) of starch and PEG capped gold nanoparticles on the amyloid surface hydrophobicity.

Further, we analyzed the effect of capping agent on the surface hydrophobicity of amyloid samples (Figure 6.19 and Figure.6.20). The results showed that addition of different concentration of PEGylated AuNP reduced the surface hydrophobicity of amyloid solution while starch capped AuNP showed less effect at lower concentrations (Figure 6.19 A & B) and found that increasing the concentration of AuNP$_{PEG}$ from 0.5 µM to 1 µM causes drastic reduction in surface hydrophobicity (Figure 6.19 B); however, similar concentration of AuNP$_{ST}$ showed less effect. Further, analyzing the effect of PEGylated AgNP showed the similar kind of effect (Figure 6.20). AgNP$_{PEG}$ showed a reduction in surface hydrophobicity more drastically than amyloid samples with AgNP$_{ST}$ of similar concentrations.

Therefore, surface hydrophobicity analysis indicated that PEGylation of AuNP and AgNP reduced the exposer of hydrophobic patches and subsequent hydrophobic interaction of proteins while higher zeta potential of amyloid samples prepared with PEGylated NP; further, inhibit the assembly of amyloid by similar charge repulsion force, therefore, inhibit the amyloid formation and assembly.

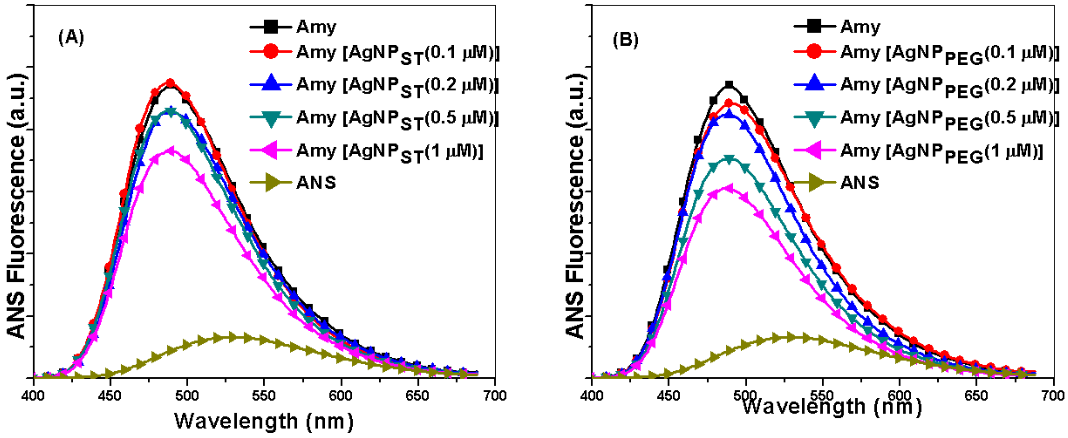

Figure 6.20 Effect of different concentrations (0.1-1 μM) of starch and PEG capped silver nanoparticles on the amyloid surface hydrophobicity.

Further, CD spectroscopy analysis of amyloid samples showed that the reduced ThT fluorescence was closely correlated with decreased in β-sheet formation. It was observed that increasing the AuNP$_{PEG}$ and AuNP$_{ST}$ concentration from 0.1 to 1 μM also reduced the β-sheet content of amyloid sample; however, PEGylation of AuNP causes higher amount of reduction in β-sheet from 68%- 38% (Figure 6.21 A, Tab 6.1) while similar amount of AuNP$_{ST}$ produced 49% of β-sheet (Figure 6.22 A). The result showed that AgNP$_{ST}$ and AgNP$_{PEG}$ inhibit beta-sheet content of 17%, and 30%, respectively (Figure 6.22 A & B, and Table-6.2). The results clearly indicated that PEGylation of AgNP enhance inhibition of cross-beta-sheet formation in HEWL during amyloid growth even at a lower concentration of AgNP than starch capped NP.

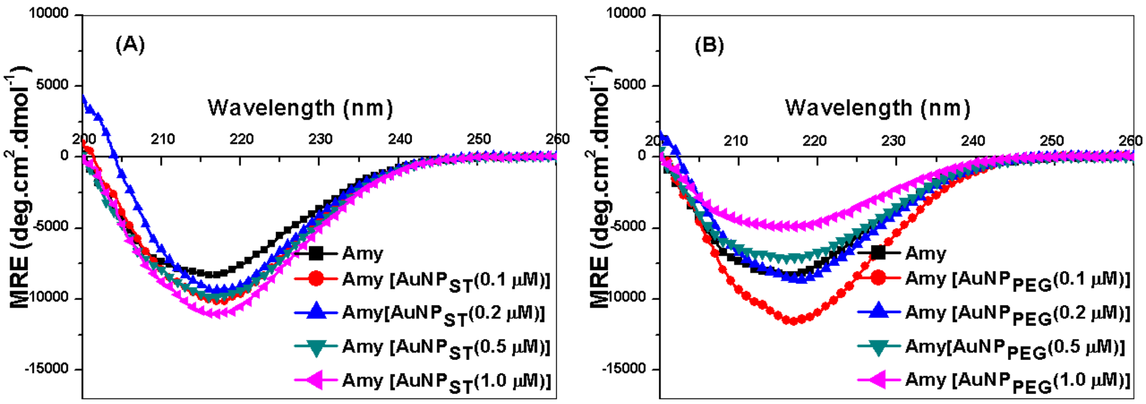

Figure 6.21 Effect of different concentrations (0.1-1 μM) of starch and PEG capped gold nanoparticles on the amyloid secondary structure.

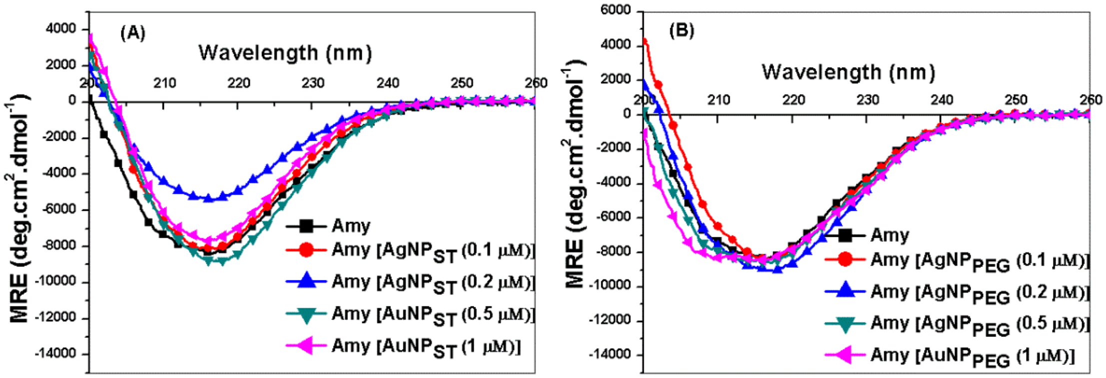

Figure 6.22 Effect of different concentrations (0.1-1 μM) of starch and PEG capped silver nanoparticles on the amyloid secondary structure. CD spectra were performed, and MRE was measured.

TEM analysis of AuNP$_{PEG}$ and AgNP$_{PEG}$ was analyzed and compared the effect of similar amount AuNP$_{ST}$ and AgNP$_{ST}$ (Figure 5.23 A & B and Figure 5.24 A & B). The results showed close correlation with our ThT analysis. We observed that both AuNP$_{PEG}$ and AgNP$_{PEG}$ produced less amount of amyloid fibers than respective starch capped NP. Therefore, TEM analysis further validated that PEGylation of metal NP enhanced the amyloid inhibition potential and showed high impact even at a lower concentration.

Table 6.1 The effect of different concentrations (0.1-1 μM) of AuNP (PEG and starch capped) on the secondary structure of amyloid samples

Sample	α-helix%	β-strand%
Amy	10	68
$AuNP_{PEG}$-Amy (0.1 μM)	11.6	58
$AuNP_{PEG}$-Amy (0.2 μM)	12	39
$AuNP_{PEG}$-Amy (0.5 μM)	13	38
$AuNP_{PEG}$-Amy (1 μM)	13	38
$AuNP_{ST}$-Amy (0.1 μM)	7	62
$AuNP_{ST}$-Amy (0.2 μM)	7	41
$AuNP_{ST}$-Amy (0.5 μM)	6	40
$AuNP_{ST}$-Amy (1 μM)	6	49

Table 6.2 The effect of different concentrations (0.1-1 μM) of AuNP (PEG and starch capped) on the secondary structure of amyloid samples

Sample	%α-helix	%β-strand
Amy	10	68
$AgNP_{PEG}$-Amy (0.1 μM)	11	48
$AgNP_{PEG}$-Amy (0.2 μM)	12	39
$AgNP_{PEG}$-Amy (0.5 μM)	13	38
$AgNP_{PEG}$-Amy (1 μM)	13	30
$AgNP_{ST}$-Amy (0.1 μM)	7	58
$AgNP_{ST}$-Amy (0.2 μM)	7	54
$AgNP_{ST}$-Amy (0.5 μM)	6	51
$AgNP_{ST}$-Amy (1 μM)	6	51

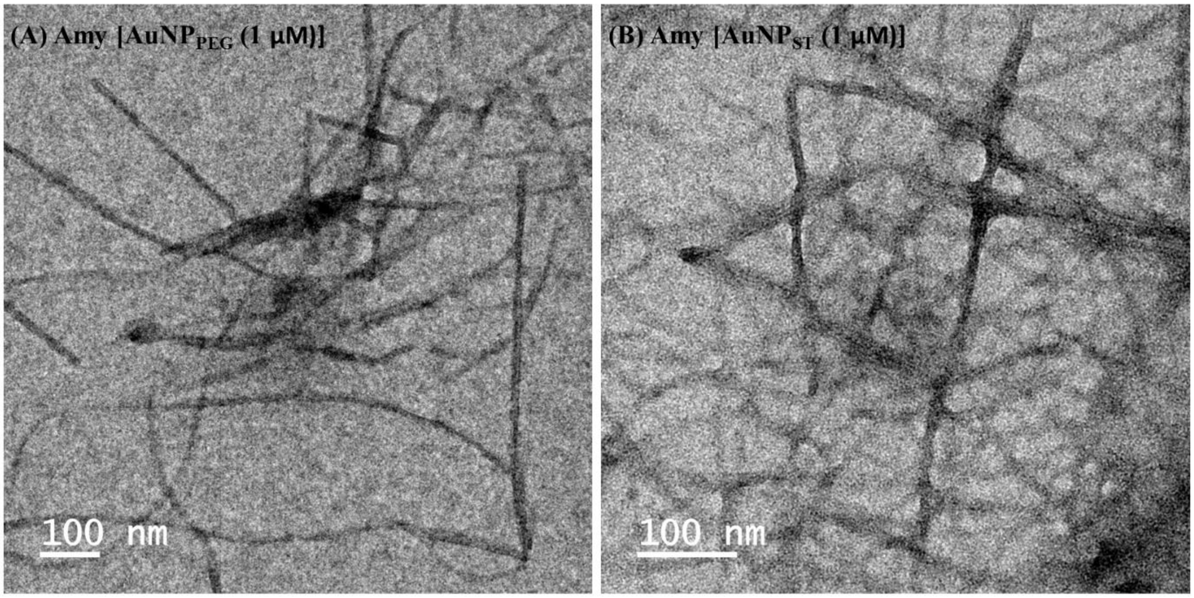

Figure 6.23 Effect of different concentrations (1 μM) of starch and PEG capped AuNP on the amyloid growth.

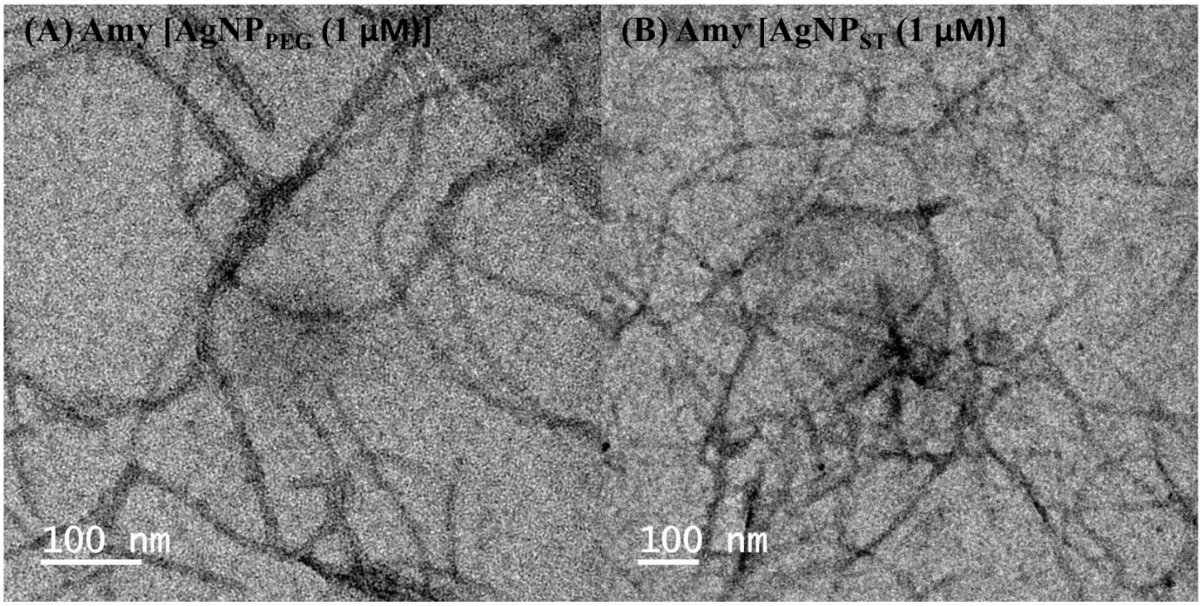

Figure 6.24 Effect of different concentrations (1 μM) of starch and PEG capped AgNP on the amyloid growth.

Therefore, the results showed that AuNP and AgNP both have the potential to inhibit the amyloid growth to a different extent while amyloid growth inhibition potential can be enhanced by variation in nanoparticle material, surface properties using a various capping agent, dose, and administration time.

6.3.10 Effect of amyloid in cellular toxicity

It was already reported that amyloids cause ROS generation that might be the reason behind high toxicity to cells [117, 215, 216]. To analyze the toxicity of amyloid prepared with NP, we measured the cellular toxicity of amyloid samples in N2a (mice neural cell line) and HaCaT (human keratinocyte) cells. The cell viability assay was performed by standard MTT assay after 24 h post administration and expressed as percentage cell viability. We observed that pure amyloid caused 78% and ~80% cell death in HaCaT and N2a cells, respectively, while amyloid formed with different AuNP (starch and PEG capped) showed a cell death of 21 %, and 19%, respectively in N2a cells (Figure 6.25 A) and 19%, 18%, respectively in HaCaT cells (Figure 6.26 A). A similar assay was also performed with 50 μM (optimized concentration) of $AgNP_{ST}$ and $AgNP_{PEG}$, which showed cellular death in both the cells of 28% and 18% in N2a cells and 16 % and 18% in HaCaT (Figure 6.26. A and Figure 6.27. A) respectively. Therefore, it was clearly proved that AuNP and AgNP not only reduced the quantity and changed the structure of amyloid but also reduced their cytotoxicity. The results also supported our previous observation that protein aggregates produced with NP results lower amount of cross β-sheet and fragmented fibrillar bodies, which were perhaps the reasons of causing reduced level of toxicity.

The above results also support our earlier observations of reduced cross β-sheet amount and fibrillar bodies of protein amyloids produced with both AuNP and AgNP, which were perhaps the reasons of causing reduced level of toxicity. Bieschke et al.[217] reported that mature α-synuclein and its fibrils are toxic to the PC12 cells while polyphenol (-)-epi-gallocatechine gallate (EGCG) treatment reduces the cellular toxicity by remodeling of fibrils and reducing β-sheet formation. Therefore, here perhaps lack of formation of mature fibrils reduced cellular toxicity. Moreover, capping of AuNP and AgNP with PEG showed a reduced cellular toxicity for HaCaT and N2a cells, respectively. The reason was perhaps having the biocompatibility of PEG capped NP, which enhanced the anti-amyloid potential and reduced cellular toxicity and hence, amyloid-mediated cellular toxicity.

Moreover, we already observed that amyloid sample possessed high surface hydrophobicity. The reason is the misfolding of the protein which exposes hydrophobic residues on its surface that further trigger aggregation through hydrophobic interaction. Here, in our present study, we observed that samples are having a lower amount of surface hydrophobicity showed a reduced ROS generation and cellular death. In fact, Mannini et al.[218] recently reported that cellular toxicity of amyloid sample varies with surface hydrophobicity of protein oligomers .

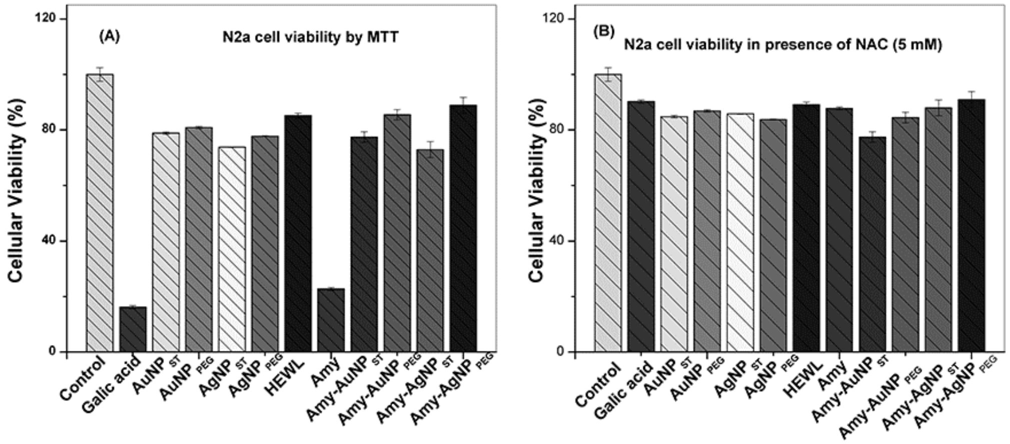

Figure 6.25 Cellular viability analysis of amyloid samples in (A) N2a cells (B) N2a in the presence of 5 mM NAC, amyloid samples were prepared in the presence of different AuNP (starch and PEG capped), AgNP (starch and PEG capped). Gallic acid was used as positive control for analysis of ROS based death. Percentage error was within 5%.

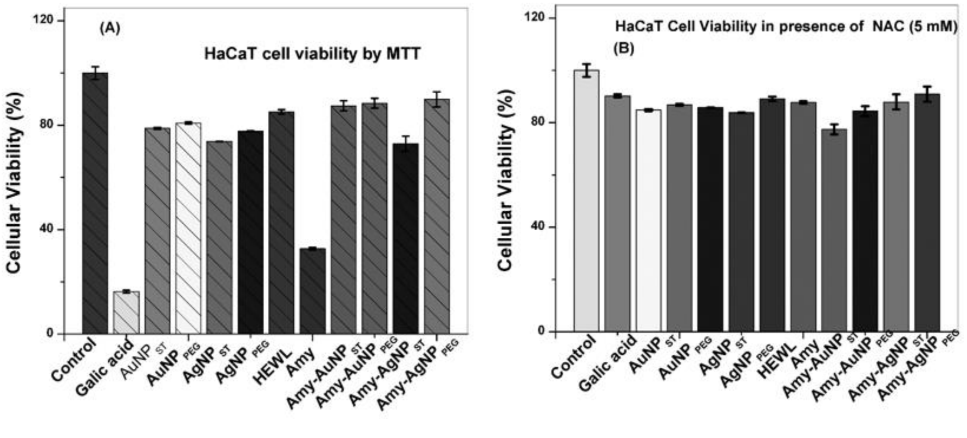

Figure 6.26 Cellular viability analysis of amyloid samples in (A) HaCaT cells (B) HaCaT in the presence of 5 mM NAC, amyloid samples were prepared in the presence of different AuNP (starch and PEG capped), AgNP (starch and PEG capped). Gallic acid was used as positive control for analysis of ROS-based death. Data were produced in triplicate and error is within 5%.

Further, to estimate ROS generation by cells, we administered N-acetyl cysteine (NAC), an ROS inhibitor and gallic acid (ROS-mediated apoptosis inducing agent) a positive control in cell culture. When, we administered NAC (5 mM) at 0 h in cells, and cell viability assay was performed after 24 h, the MTT assay demonstrated a cell death within 10% in both cells for pure amyloid while gallic acid showed only 16% cell death (Figure 6.25 B for N2a and Figure 6.26 B for HaCaT) after 24 h post administration. These results indicated that amyloid and gallic acid predominantly caused ROS-mediated apoptotic cell death. However, when NAC was administered, all the NP samples showed the ignorable level of cellular toxicity in both cells indicated that the cell death by pure NPs was caused by ROS generation. Rest 10-12% cell death, was perhaps due to other kinds of cell death mechanism. Therefore, from our cell viability assay, we demonstrated that HEWL amyloid was highly toxic to both N2a cells and HaCaT cells and such toxicity was predominantly caused by ROS generation. However, when amyloid was produced in the presence of $AuNP_{ST}$ and $AgNP_{ST}$, such toxicity was reduced significantly, while $AuNP_{PEG}$ and $AgNP_{PEG}$ demonstrated minimum cell death (10%) (Figure 6.26 A, & C). Such drop of toxicity was perhaps associated with the interaction of both the NP with amyloid forming HEWL molecules (probably through hydrophobic interaction), which further produced higher amount of thin, shorter fibers and loose aggregates rather than long and thick (toxic) fibers, which also reduced the ROS-dependent toxicity of both NP and amyloid.

CHAPTER 7

NANO ZINC OXIDE EFFECT ON FIBRILLAR GROWTH OF LYSOZYME AMYLOID AND ITS CELLULAR TOXICITY

7.1 Methods

7.1.1 ZnONP synthesis and characterization

For this study, uncapped zinc oxide nanoparticles (ZnONP) was synthesized and characterization method described in detail in chapter 4 (section 4.3 & 4.4).

7.1.2 Preparation of amyloid and Characterization

Described in detail in chapter 6 (section 6.1.2-7.1.10).

7.1.3 Cytotoxicity assay

To study the cytotoxicity of HEWL amyloid samples prepared under different conditions, we applied them to two different cell lines; mice neuroblastoma (N2a) cells and human keratinocyte (HaCaT) cells. Cells were cultured in Dulbecco's modified Eagle's medium (DMEM) supplemented with 10% fetal bovine serum. The cells (2000 cells/well) were inoculated in a 96-well plate at 37 ^{0}C for 24 h. Various amyloid samples prepared with ZnONP$_{uncap}$, ZnONP$_{ST}$, and ZnONP$_{assmb}$ (50 µM), were applied in triplicates and cytotoxicity was estimated after 24 h of administration. After incubation, MTT (3-(4,5-dimethylthiazol-2-yl)-2,5-diphenyl-2*H*-tetrazolium bromide) assay was performed as described by Risset et al. [219] using MTT kit (Himedia). MTT was added to a final concentration of 0.5 mg/ml and cells were incubated for 2 h. The excess formazan was dissolved in DMSO, and the absorbance was measured at 570 nm within 1 h and viability percentage was calculated by dividing the absorbance of treated cells with control cells. To analyze the ROS-dependent cell death, we administered 5 mM of N-acetyl cysteine (NAC) at 0 h in the cell culture, and cell viability was analyzed. Gallic acid (50 µM) was also used as positive control after 24 h post-administration.

7.2 Results and Discussion

7.2.1 ZnONP synthesis and characterization

ZnONPs were synthesized as per the protocol described in the ‘Materials and methods’ section. The synthesized NPs were found to be spherical in shape (Figure S1. A, B, and C) as revealed by electron microscopy and average hydrodynamic size of ZnONP$_{uncap}$, ZnONP$_{ST}$, and ZnONP$_{assmb}$ were estimated to be 15, 30, and 163 nm, respectively. Zeta potential values were also estimated to be -19.6 (ZnONP$_{uncap}$), -26.9 (ZnONP$_{ST}$) and -15.5 mV (ZnONP$_{assmb}$), which concluded that ZnONP$_{ST}$ possessed the highest stability among all (see Figure 4.17 and 4.21 in chapter-4).

7.2.2 Amyloid formation with ZnONP

In order to obtain the size distribution of amyloid samples, we performed DLS analysis of all the samples. It showed two independent peaks; one was around 100 nm, and another broad peak was at 600 nm (See Appendix Figure S42). It signified the presence of both small as well as large aggregates (See Appendix Figure S42). Further, we analyze the effect of all three forms of ZnONP on the amyloid formation using various biophysical techniques. When samples were analyzed by tryptophan (Trp) fluorescence spectroscopy, we observed that the fluorescence intensity of amyloid was quenched drastically for all the samples. Further, the fluorescence spectra showed red shift for ZnONP$_{ST}$ and ZnONP$_{assmb}$ while amyloid formed with ZnONP$_{uncap}$ and none showed a slight blue shift of λ_{max} (Figure 7.1 A). All these results indicated the drastic change of environment around Trp residue due to the interaction with NP, which might also be associated with fluorescence quenching by ZnONP.

The amyloid formation of all HEWL (7 μM) samples was monitored using Thioflavin-T (ThT) (10 μM) fluorescence. The protein samples were excited at 440 nm and emission was analyzed at 488 nm. We also observed that HEWL amyloid (formed with none) exhibited highest fluorescence intensity; however, amyloid formed with all ZnONP showed reduced fluorescence intensity while ZnONP$_{ST}$ showed maximum fluorescence drop (Figure 7.1 B). The protein bound ThT fluorescence is normally considered an indicative of cross β-sheet contents in amyloid, hence, the results revealed that the administration of ZnONP caused the inhibition of forming cross β-sheet structure. The secondary structure of amyloid samples was also analyzed by CD spectroscopy to quantify the β-sheet formation (original spectra in Figure S3). Amyloid samples prepared with $ZnONP_{uncap}$ and $ZnONP_{assmb}$ showed 57% and 54% β-sheet structure, while the amount of β-sheet in amyloid formed with $ZnONP_{ST}$ was estimated only 44% and the value was indeed lowest among all amyloid samples (Figure 7.1 C) (see CD spectra in Appendix Figure S43). Moreover, when we measured the surface charge of amyloid samples, we found that zeta (ζ)-potential of amyloid formed with ZnONP showed much higher (>30 mV) values than pure amyloid while $ZnONP_{ST}$ showed the highest stability (see Figure 7.1 D). It is assumed that the ζ-potential with a value of more than 30 shows high stability; hence, the sample showed the strong stability of amyloid sample when to interact with $ZnONP_{ST}$. The results also indicated a lower chance of further reaction of fiber formation in the presence of ZnONP due to higher charge repulsion.

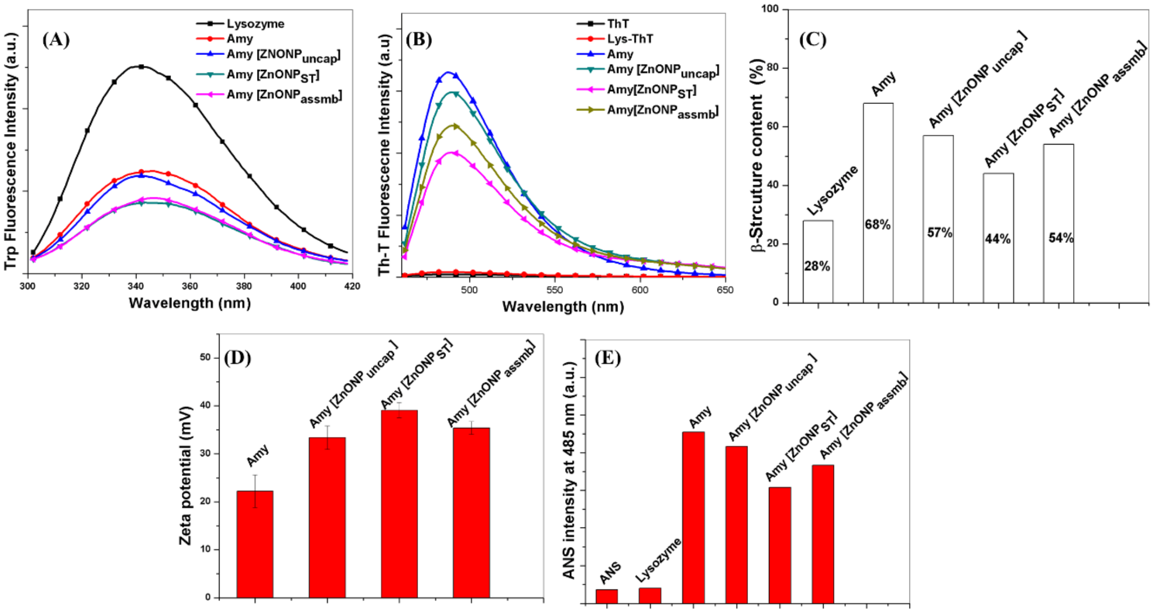

Figure 7.1 The effect of $ZnONP_{uncap}$, $ZnONP_{ST}$, and $ZnONP_{assmb}$ on the HEWL amyloid formed after 72 h. The ZnONP was administered at t=0 h. (A) Tryptophan fluorescence, (B) Thioflavin-T fluorescence, (C) % β-sheet contents of various samples estimated from Circular dichroism spectra, (D) zeta (ζ)-potential, (E) ANS fluorescence, of various amyloid samples.

Further, we analyzed the effect of three different forms of ZnONP on the stability of amyloid by analyzing the surface hydrophobicity. We found that amyloid formed without NP showed the highest hydrophobicity, while amyloid samples formed with all three ZnONP showed lower hydrophobicity (Figure 7.1 E) (ZnONP$_{ST}$ showed the lowest hydrophobicity). Vetri et al. [120] reported that during the amyloid formation process, new hydrophobic regions are spontaneously formed for fast interaction. Therefore, here ZnONP perhaps interacted with hydrophobic sites of proteins and subsequently inhibits the amyloid growth.

7.2.3 Microscopic analysis of amyloid formation

The AFM images showed the formation of amyloid fibers under different conditions (Figure 7.2 A-D). It showed that amyloid formed with ZnONP$_{uncap}$ and ZnONP$_{assmb}$ consists of loose aggregates with a small fraction of fiber production (Figure 7.2 B & D) while amyloid sample formed with ZnONP$_{ST}$ demonstrated reduced amount of protein aggregates and almost no fiber formation (Figure 7.2 C). The overall result proved that ZnONP prevented the formation of fibrillar structure/amyloid to a different extent. Moreover, the growth of amyloid depends on the surface property of ZnONP used (ZnONP$_{uncap}$, ZnONP$_{ST}$, and ZnONP$_{assmb}$) that interact with the protein under the same conditions.

7.2.4 Effect of nanoparticle doses on amyloid formation

Further, we analyzed the effect of different concentrations of ZnONP on amyloid formation. We administered 1.0, 2.0, 5.0, 10, and 20 μM of NP with 70 μM of protein and incubated for 72 h at 58 ^{0}C. We found that with the increase of NP concentration, the ThT fluorescence intensity was decreased (Figure 7.3 A-C) with ZnONP$_{ST}$ caused the maximum effect. Further, secondary structural components were estimated using CD spectroscopy, which revealed a reduction in β-sheet of all samples while amyloid formed with ZnONP$_{ST}$ showed the maximum drop (68% to 39%) (Figure 7.3 D-F).

This finding further generated curiosity that why ZnONP$_{uncap}$ and ZnONP$_{assmb}$ demonstrated lower potential to prevent amyloid formation compared to ZnONP$_{ST}$ under same concentration. Since NP and protein interaction is an interfacial phenomenon and can change the surface properties of protein, it is essential to know the factors that are responsible for the concentration-based effect on amyloid growth. Hence, we further analyzed the surface hydrophobicity, zeta (ζ)-potential and aggregation index of amyloid samples for all the concentration of NP.

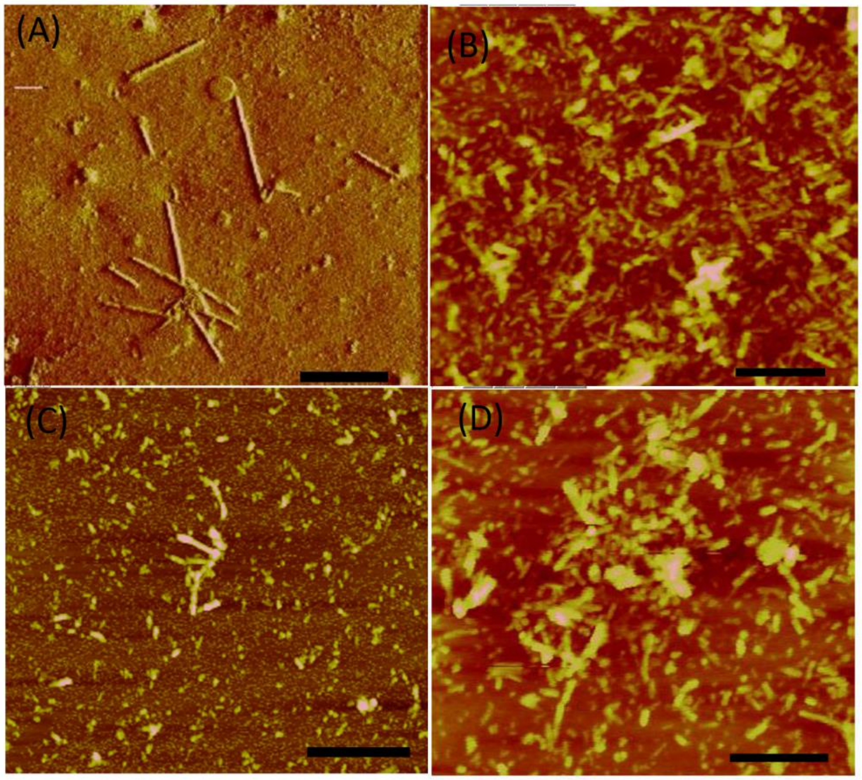

Figure 7.2 The effect of ZnONP$_{uncap}$, ZnONP$_{ST}$, and ZnONP$_{assmb}$ on the HEWL amyloid growth until 72 h. The ZnONP was administered at t=0 h. Amyloid formed in the presence of (A) none (B) ZnONP$_{uncap}$, (C) ZnONP$_{ST}$, and (D) ZnONP$_{assmb}$. Scale bar is equal to 0.5 µm.

Figure 3G showed that increase of ZnONP (uncap/assembly) concentration caused an initial increase in positive ζ-potential of amyloid but decrease at higher concentrations (> 10 µM) except ZnONP$_{ST}$ that showed an increase of ζ-potential with increasing NP concentration. However, when we increase the concentration of ZnONP$_{uncap}$ and ZNONP$_{assmb}$, it demonstrated reduction of surface hydrophobicity (Figure 3H) and such decrease was highest for an amyloid sample formed with ZnONP$_{ST}$. A similar effect was also observed when we measured aggregation index (AI) by dual angle analysis of dynamic light scattering (DLS) and calculated the AI. Here ZnONP$_{ST}$ also demonstrated maximum reduction of AI compared to other amyloid samples formed with ZnONP$_{\text{uncap}}$ and ZnONP$_{\text{assmb}}$ (Figure 7.3 I), collectively, indicates strong inhibition potential of amyloid formation.

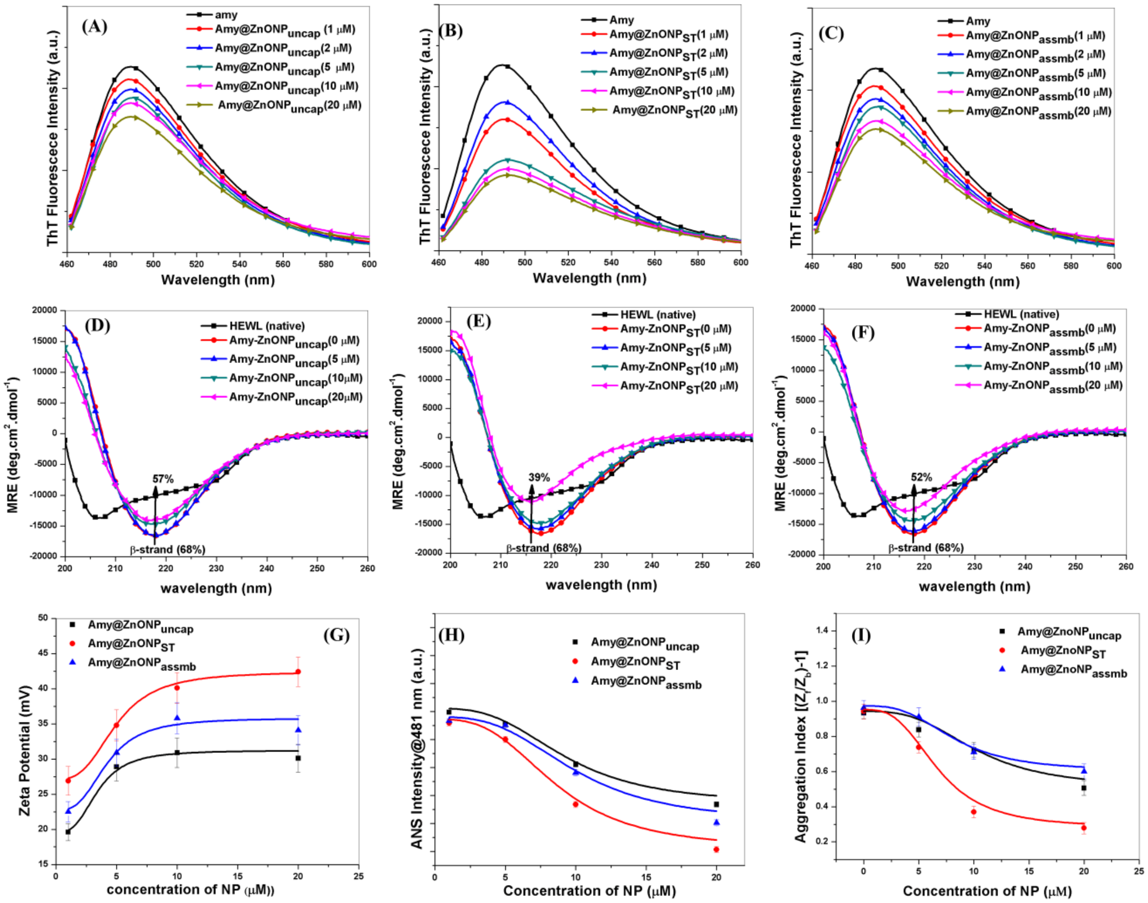

Figure 7.3 Thioflavin-T fluorescence assay of amyloid samples produced in the presence of different concentrations (1-20 μM) of ZnONP: (A) ZnONP$_{\text{uncap}}$, (B) ZnONP$_{\text{ST}}$, and (C) ZnONP$_{\text{assmb}}$. (D)-(F) showed CD spectra of the same samples. The change in β-sheet contents was also reported in the plot. (G) ζ-potential analysis of amyloid samples with different concentration of ZnONP (uncap, capped, and assembly). (H) Surface hydrophobicity analysis of amyloid samples using ANS. (I) Aggregation index of amyloid samples with different concentration of NP.

Galvagnion et al. [179] and Radic et al. [187] already reported that NP and protein interaction reduced the free protein concentration in solution [210, 220] Therefore, when the interaction between NP and protein is strong, NP inhibits the amyloid growth both in solution and on NP surface at all NP concentrations. However, when interaction is relatively weak, amyloid formation depends on the concentration of NP administrated in the solution. Here, we observed a concentration-dependent inhibition of amyloid growth by all ZnONP; however, highest amyloid inhibition was observed by $ZnONP_{ST}$.

In order to observe the amyloid fibrillar structure under three different concentrations of ZnONP (5, 10 and 20 µM), we analyzed TEM images of different amyloid samples (Figure 7.4). Amyloid formed with $ZnONP_{uncap}$ and $ZnONP_{assmb}$ showed less number of thicker and shorter fibers when NP concentration was increased from 5 to 20 µM (Figure 7.4 A-A2 & C-C2). However, the amyloid formed in the presence of $ZnONP_{ST}$ revealed thin fibers at 5 µM, however predominantly non-fibrillar aggregates at 10 and 20 µM (Figure 7.4 B, B1 & B2). All above results collectively established that the administration of $ZnONP_{ST}$ inhibited the formation amyloid fiber most efficiently.

7.2.5 Growth kinetics of amyloids

Further, we also analyzed the growth kinetics of amyloid by ThT, ANS fluorescence, ζ-potential and CD spectroscopy analysis. The amyloid formation in the presence of NP ($ZnONP_{uncap}$, $ZnONP_{ST,}$ and $ZnONP_{assmb}$) was analyzed at the interval of 12 h until 120 h. The area under the curve in ThT spectra (original ThT spectra in Appendix Figure S44) was plotted with respect to growth time up to 120 h. The results showed that amyloid formed with $ZnONP_{uncap}$ and $ZnONP_{assmb}$ demonstrated shorter lag phase and longer log phase (Figure 7.5 A) than amyloid formed with $ZnONP_{ST;}$ however, all ZnONP showed longer lag phase than amyloid formed without NP (Figure 7.5 A), which was observed by lower protein bound ThT fluorescence intensity. Here, it was also found that all ZnONP were able to reduce the amyloid formation with maximum effect demonstrated by $ZnONP_{ST}$ (Figure 7.5 A), which indeed also supported our previous results

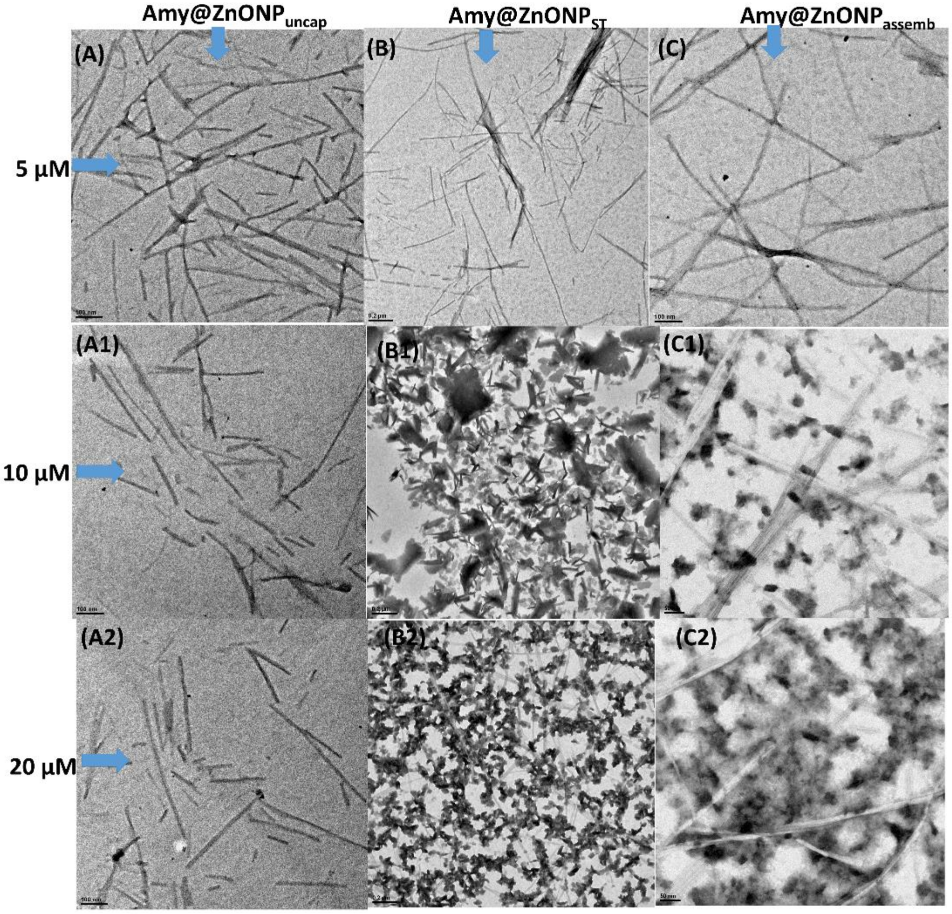

Figure 7.4 TEM image showed the effect of three different concentrations (5, 10 and 20 µM) of ZnONP on amyloid formation. (A)-(A2) $ZnONP_{uncap}$; (B)-(B2) $ZnONP_{ST}$; (C)-(C2) $ZnONP_{assmb.}$

When we analyzed the time dependent surface ζ-potential at an interval of 12 h, we found that the surface charge reached a maximum at 48 h, which was indeed matching with the end of amyloid growth phase. $ZnONP_{ST}$ demonstrated constant ζ-potential value after 48 h unlike other samples, indicates no further significant change of amyloid or its surface structure (Figure 7.5 B).

We further analyzed the quantity of β-sheet in different amyloid samples during the growth process. We found that the formation of β-sheet was rapid during nucleation phase; however, slowed down afterward (Figure 7.5 C). Amyloid sample formed with $ZnONP_{ST}$ was found to have lower percentage β-sheet contents (47%) and containing more irregular secondary structural components compared to other amyloid samples (β-sheet contents are 63% & 56%

for amyloid formed with ZnONP$_{uncap}$ and ZnONP$_{assmb}$) (Figure 7.5 C) while amyloid produced without NP showed 68% of β-sheet. Therefore, it was also concluded that inhibition of amyloid formation also associated with the drop of the β-sheet formation.

Further analysis of FESEM also demonstrated that after 2 h of amyloid growth both amyloid formed without NP and with ZnONP$_{ST}$ had shown smaller aggregates (Figure 7.6 A and C) but amyloid samples formed with ZnONP$_{uncap}$ and ZnONP$_{assmb}$ showed larger and more poly-dispersed aggregates (Figure 7.6 B& D). After 36 h of growth, we observed that all samples formed amorphous (unstructured/loose) aggregates (Figure 7.6 A1, B1, C1, & D1). However, at 48 h, samples in the presence of ZnONP$_{uncap}$ showed denser fibers while ZnONP$_{assmb}$ showed both fibers and amorphous (unstructured/loose) aggregates (Figure 7.6 A2, B2, C2, & D2). In contrary, pure amyloid showed long fiber formation (Figure 7.6 A2).

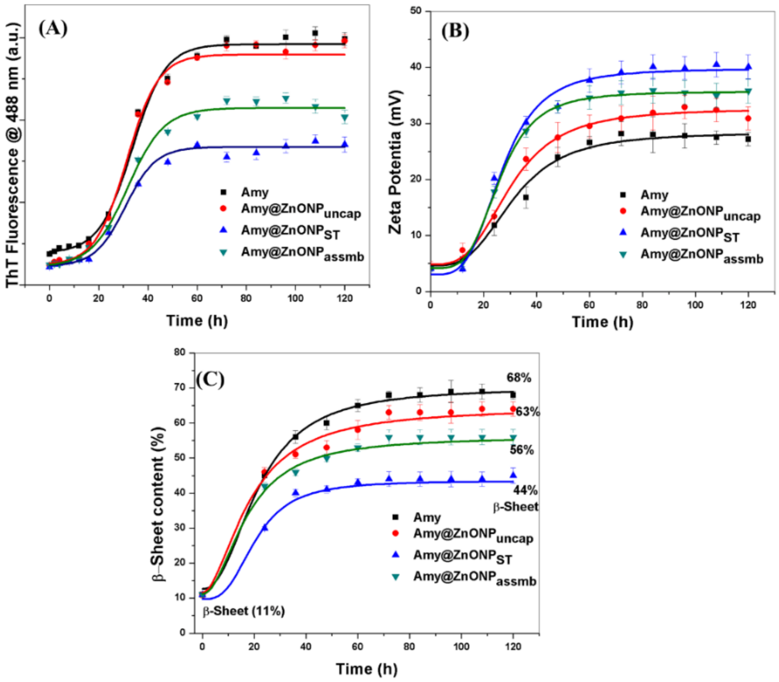

Figure 7. 5 Plot of (A) ThT fluorescence intensity at 488 nm. (B) zeta (ζ)-potential, (C) % β-sheet of amyloid samples with a time of amyloid growth. The measurement was taken after 72 h of amyloid growth. (See ThT and CD spectra in Appendix Figure S43 and Figure S44, respectively).

However, amyloid sample formed in the presence of ZnONP$_{ST}$ results in higher amount of loose aggregates and fewer fibers (Figure 7.6 A2). After 72 h of amyloid growth, we found that all samples except amyloid formed with ZnONP$_{ST}$ showed dense fibers but amyloid formed with ZnONP$_{ST}$ showed predominantly non-fibrillar (Figure 7.6 A3, B3, C3 & D3), which are also indicative of an inhibitory potential of ZnONP$_{ST}$ in amyloid growth of HEWL.

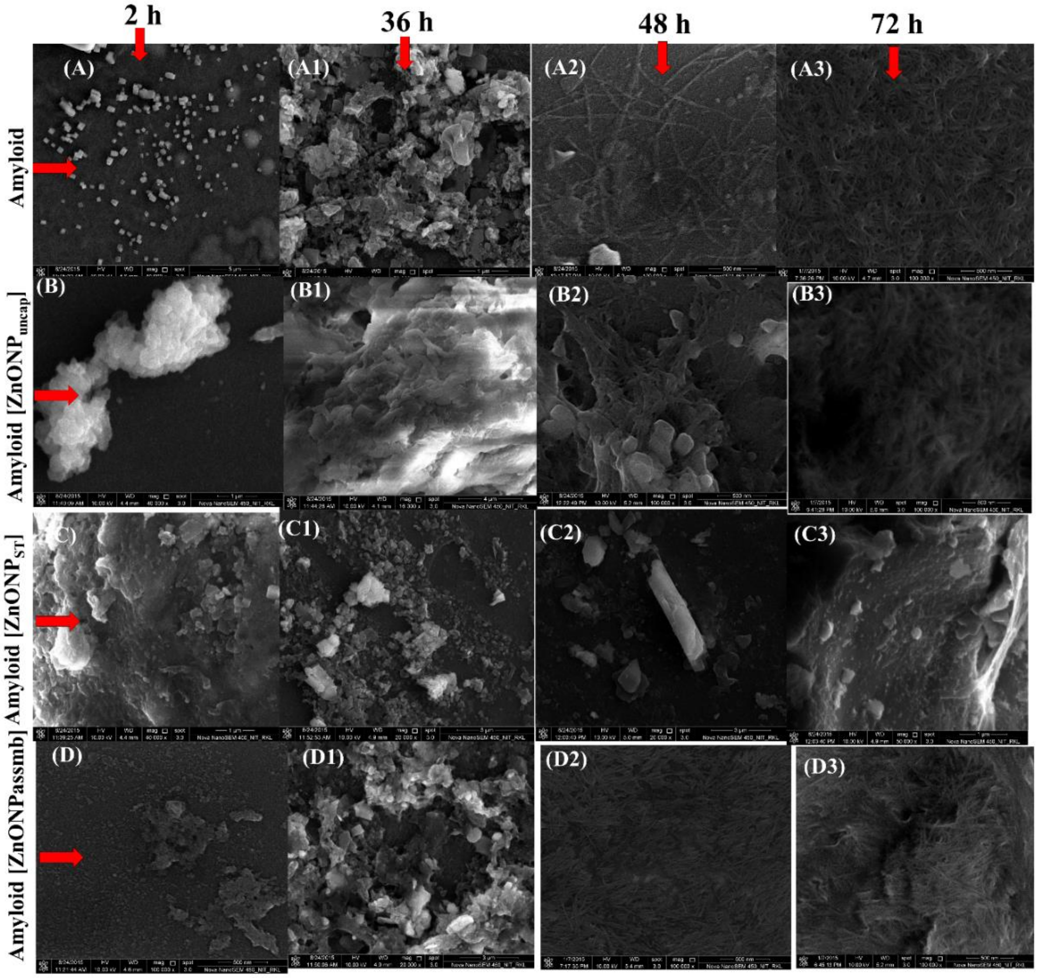

Figure 7.6 FESEM analysis of amyloid growth with time (2, 36, 48, and 72 h); (A-A3) without NP, (B-B3) with ZnONP$_{uncap}$ (C) with ZnONP$_{ST}$, (D) ZnONP$_{assmb}$. ZnONPwas administered at 0 h.

7.2.6 Effect of time of NP administration on amyloid structure

We further attempted to understand the effect of various ZnONP administration time on amyloid growth. We administered NP at 0, 36 and 48 h (Figure S46) in amyloid samples and samples were analyzed after 72 h. From FESEM imaging (Figure S47) we observed that inhibitory effect towards amyloid fibrillation of HEWL was still highest when NP was administered at 0 h. When administered at 36 and 48 h, from Figure S46, it was found that all three ZnONP produced HEWL amyloid fibers. Therefore, we concluded that administration at 0 h,i.e., in the lag phase produced highest inhibitory effect, and this fact indeed supports our hypothesis that prolonged lag phase and shorter elongation phase perhaps the key behind the inhibitory mechanism induced by $ZnONP_{ST}$.

Therefore, so far we observed that our ZnONP in three different forms could inhibit the HEWL amyloid fibrillation to various extents. Nanoparticle plays a multifaceted role, which depends on the properties of nanoparticle surface as well as a protein of interest. The variations of these factors also vary the effect of nanoparticle on amyloid formation. The three different form of ZnONP, which was made up of core size of 10-15 nm and having varying size due to surface capping and formation of self-assembly of ZnONP of 10-15 nm core size. Moreover, self-assembly of NP by starch altered the effect of NP on cellular toxicity and amyloid growth. In fact, Linse et al. and Cabaleiro-Lago et al. reported that the effect of nanoparticle on the amyloid growth depends on the various factors such as binding strength, NP to protein ratio on the surface, intrinsic stability and aggregation propensity of protein, surface hydrophobicity of NP [37, 153]. The catalytic and inhibitory effects of NPs were most pronounced with the least hydrophobic nanoparticles. Therefore, nanoparticles show dual role, catalyzing and inhibition, which depends on the inherent stability of protein, nanoparticle surface properties, protein to nanoparticle ratio, and strength of interaction. The variations of these factors also change the effect of nanoparticles on amyloid formation.

7.2.7 Cellular toxicity assay

Amyloid has already been reported to be highly toxic to cells, which were mediated via ROS generation [117, 215, 216]. To analyze, the death mechanism, here we analyzed the cellular toxicity of amyloid samples (70 μM) (formed in the presence of three different ZnONP samples) in N2a (mice neural cell line) and HaCaT (human keratinocyte) cells. The cell viability assay was performed by standard MTT assay after 24 h post administration and expressed as percentage cell viability. We observed that pure amyloid caused 78% and ~80% cell death in HaCaT and N2a cells, respectively, while amyloid formed with different ZnONP ($ZnONP_{uncap}$, $ZnONP_{ST}$, and $ZnONP_{assmb}$) showed a cell death of 21%, 8%, and 29%, respectively in HaCaT cells and 24%, 12% and 22% respectively in N2a cells (Figure 7A & C). Similar assay was also performed with 50 μM (optimized concentration) of ZnONP$_{uncap}$, ZnONP$_{ST}$, and ZnONP$_{assmb}$, which showed toxicity in both the cells (Figure 7.7 A) while ZnONP$_{ST}$ showed minimum (~ 9% in HaCaT and 16% in N2a cell death) cellular toxicity. Therefore, it was clearly proved that all three ZnONP not only changed the quantity and structure of amyloid (see Figure 7.4, 7.5 and 7.6) but also reduced their cytotoxicity. The results also support our earlier observation that protein aggregates produced with ZnONP results lower amount of cross β-sheet (Figure 7.7 A-C) and thick fibrillar bodies, which were perhaps the reasons of causing reduced level of toxicity.

Further, to estimate ROS generation by cells, we administered N-acetyl cysteine (NAC), an ROS inhibitor and gallic acid (ROS mediated apoptosis-inducing agent, a positive control) in culture [221]. When, we administered NAC (5 mM) at 0 h in cells, and cell viability assay was performed, the MTT assay demonstrated a cell death within 10% in both cells for pure amyloid (Figure 7.7 B & D) while gallic acid showed only 5-6% cell death (Figure 7.7 B & D) after 24 h post administration. These results indicate that amyloid and gallic acid predominantly caused ROS mediated apoptotic cell death. However, when NAC was administered, all three ZnONP samples showed ignorable level of cellular toxicity in both cells indicated that the cell death by pure ZnONPs was caused by ROS generation (Figure 7.7 A, B, C, and D). Rest 12-15% cell death which still occurred was perhaps due to other kinds of cell death mechanism.

Therefore, from our cell viability assay, we proved that HEWL amyloid was highly toxic to both N2a cells and HaCaT cells and such toxicity was predominantly caused due to ROS generation. However, when amyloid was produced in the presence of ZnONP, such toxicity was reduced significantly while ZnONP$_{ST}$ demonstrated lowest cell death (10%) (Figure.7.7 A & C). Such drop of toxicity was perhaps associated with the interaction of ZnONP with amyloid forming HEWL molecules (probably through hydrophobic interaction), which further produced higher amount of thin, shorter fibers and loose aggregates rather than long and thick (toxic) fibers. Further, it was perhaps the interaction between HEWL with ZnONP (uncap, assembly) which also lessen the ROS dependent toxicity of both NP and amyloid.

From here, we proposed a mechanism to demonstrate how the interaction of three different forms of ZnONP with HEWL produced fibrillar amyloids and aggregates of different proportion (Figure 7.8). Although three forms of ZnONP caused the change of amyloid structure by altering fiber thickness and length, $ZnONP_{ST}$ was observed to reduce the β-sheet formation and toxicity in both cells (N2a, and HaCaT) maximally.

The above results also support our earlier observations of reduced cross β-sheet amount and fibrillar bodies of protein amyloids produced with ZnONP (see Fig. 7.4A-C), which were perhaps the reasons of causing reduced level of toxicity. Bieschke et al. [217] reported that mature α-synuclein and its fibrils are toxic to the PC12 cells while polyphenol (-)-epi-gallocatechine gallate (EGCG) treatment reduces the cellular toxicity by remodeling of fibrils and reducing β-sheet formation .Therefore, here perhaps lack of formation of mature fibrils reduced cellular toxicity. Moreover, capping of ZnONP with starch showed a cellular toxicity to 9% and 16% for HaCaT and N2a cells, respectively. However, formation of starch mediated self-assembly by ZnONP ($ZnONP_{assemb}$) could not mitigate the cellular toxicity below 26% for HaCaT and 24% for N2a. The reason was perhaps having the largest size (avg size is 163 nm) of all ZnONPs used in our study which reduces surface to volume ratio and hence, the surface activity towards amyloid inhibition as well as toxicity.

Moreover, we already observed that amyloid sample possessed high surface hydrophobicity. The reason is the misfolding of the protein which exposes hydrophobic residues on its surface that further trigger aggregation through hydrophobic interaction. Here, in our present study, we observed that samples having lower amount of surface hydrophobicity (amy@$ZnONP_{ST,}$ amy@$ZnONP_{uncap,}$ and amy@$ZnONP_{assmb}$) showed a reduced ROS generation and cellular death. In fact, Mannini et al. [218] recently reported that cellular toxicity of amyloid sample varies with surface hydrophobicity of protein oligomers .

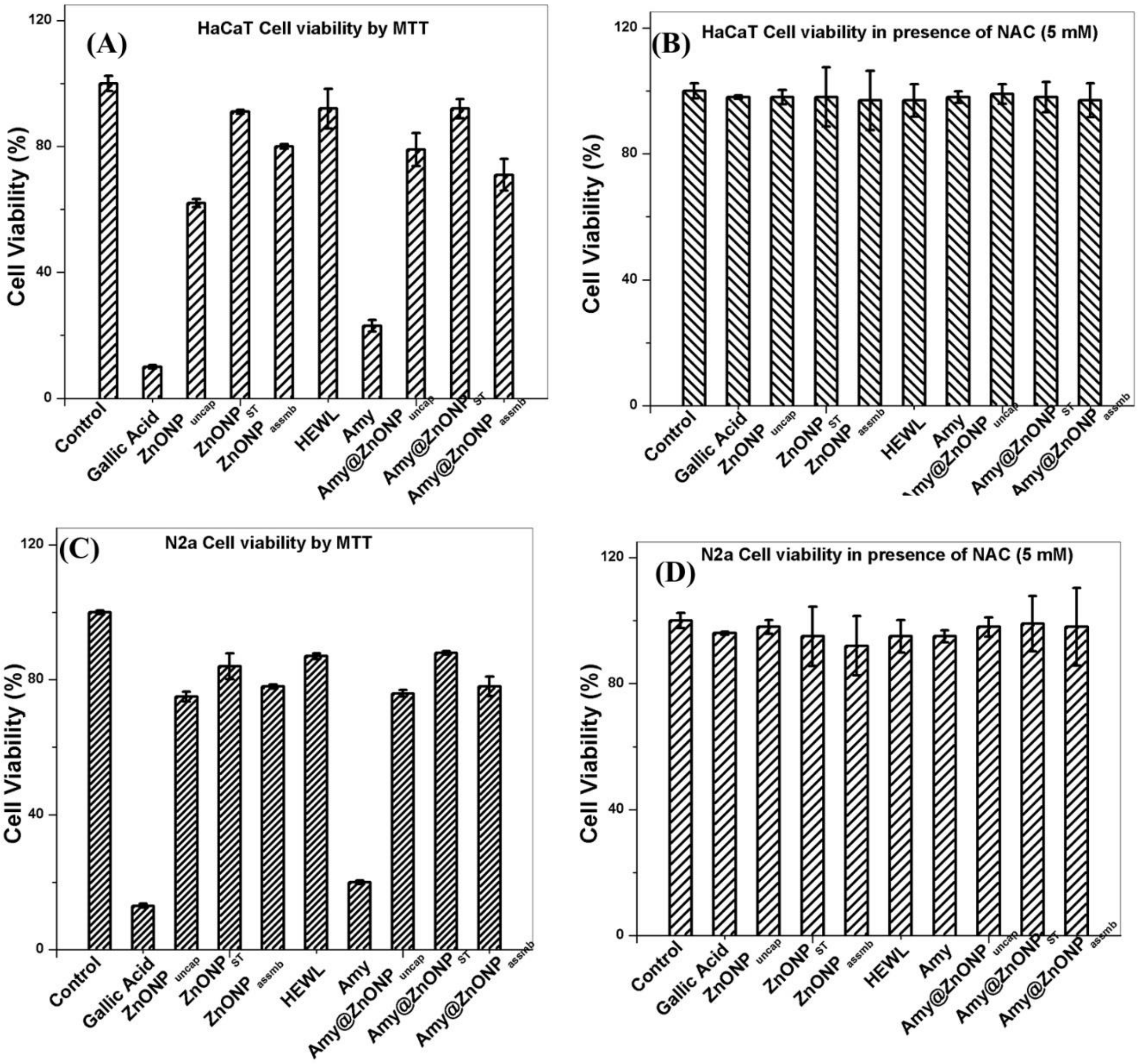

Figure 7.7 The effect of ZnONP (uncapped, starch capped, self-assembly), native lysozyme (HEWL), amyloid (Amy), amyloid formed in the presence of various ZnONP (50 μM) was analyzed on the cellular toxicity. Gallic acid was used as a positive control for ROS-based apoptotic death. Cell viability analysis was performed in (A) HaCaT cells (B) HaCaT cells in the presence of N-acetyl cysteine (5 mM), an ROS scavenger. (C) Mice neuroblastoma cell line (N2a) (D) N2a in the presence of N-acetyl cysteine.

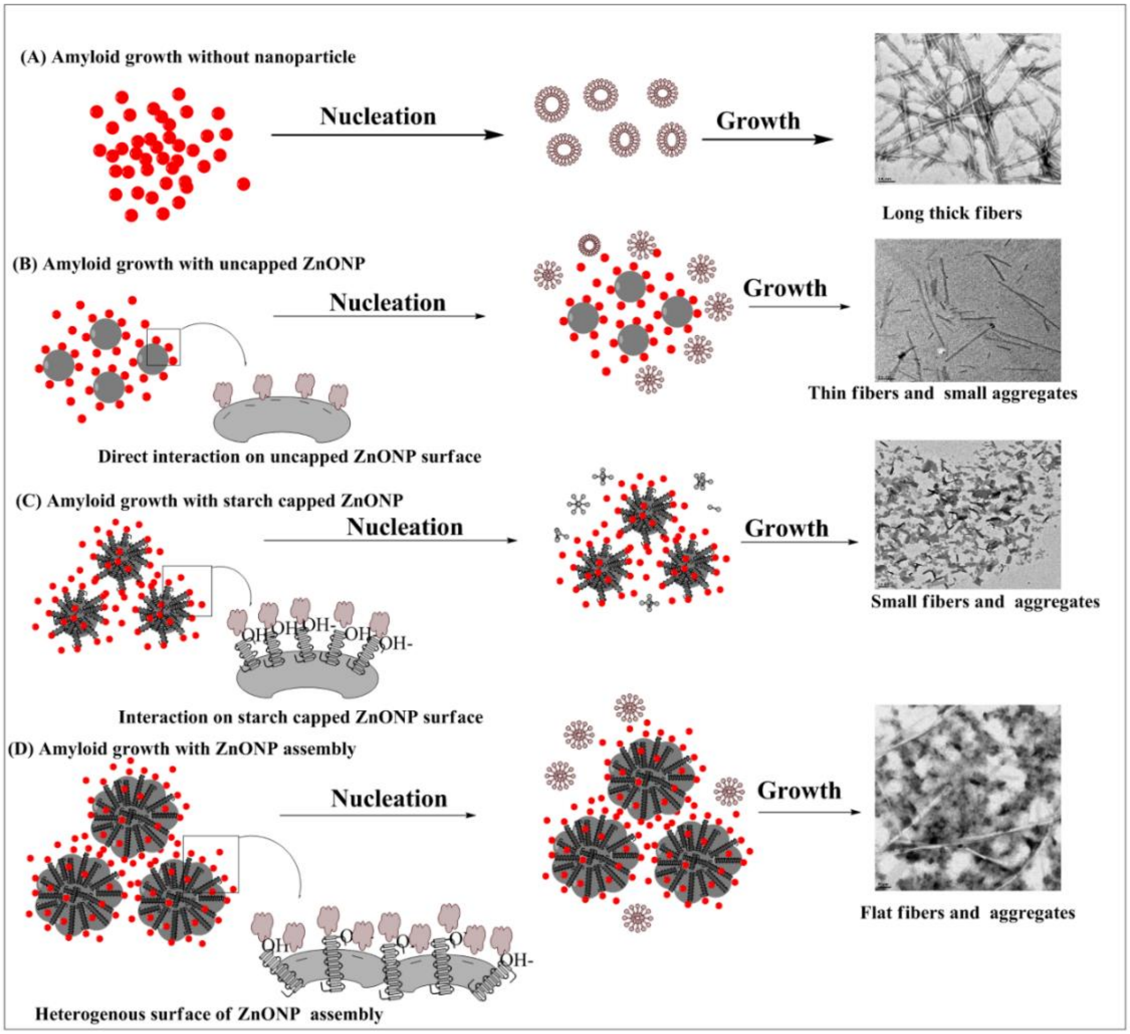

Figure 7.8 Schematic representation of HEWL amyloid formation in the presence of three different types of ZnO nanoparticles (NP). (A) Amyloid is formed without NP having long and thick fibers. (B) Amyloid produced in the presence of $ZnONP_{uncap}$ demonstrated thin and fragmented fibers of HEWL that indicated that direct interaction of HEWL with ZnONP surface reduced the secondary deposition over fibers that caused the formation of thin fibers. (C) When HEWL interacts with densely starch capped ZnONP, inhibit the amyloid growth and produced less toxic aggregates by increased ζ-potential. (D) The presence of heterogeneous surface on the $ZnONP_{assmb}$ caused the production of flat fibers with some aggregates. Overall, the variation in surface of ZnONP was found to produce different morphology of HEWL aggregates and prevent amyloid fiber to different extent with $ZnONP_{ST}$ having the highest effect.

CHAPTER 8

CONCLUSION AND FUTURE WORK

8.1 Conclusion

In the present thesis, we studied in detail the molecular interaction of two monomeric proteins bovine α-lactalbumin (BLA), and hen egg white lysozyme (HEWL) with three different nanoparticles (NPs) gold, silver, and zinc oxide under various conditions to understand structural and functional change of the proteins and their conjugate formation. All three NPs were successfully synthesized using starch as capping as well as reducing agent with NaOH as a reaction accelerator. Further, we also synthesized PEG (poly ethyl glycol) capped AuNP ($AuNP_{PEG}$) and AgNP ($AgNP_{PEG}$), uncapped ZnONP and self-assembly of ZnONP by varying reaction parameters. The results showed that starch capped ($AuNP_{ST,}$ $AgNP_{ST}$) and PEG capped ($AuNP_{PEG}$ and $AgNP_{PEG}$) NP have size in between 15-25 nm while starch capped, uncapped, self-assembly of ZnONP have 25 nm, 10 nm, and 163 nm, respectively. All NPs were successfully characterized using FESEM, TEM, XRD, UV-Vis spectroscopy, DLS particle size analyzer, and zeta potential analysis for shape, size, and stability. Further, the surface activity of synthesized AuNP and AgNP were analyzed by measuring their heavy metal sensing and ZnONP by photocatalytic dye degradation potential.

To, monitor the interaction of NPs with protein (BLA, and HEWL), we used various spectroscopic techniques such as fluorescence as well as circular dichroism spectroscopy for assessing structural changes of proteins. We concluded that both the proteins undergo substantial conformational change (tertiary as well as secondary) upon interactions. Further, it was revealed that the stability was also compromised in different stress conditions such as the presence of strong denaturant guanidine hydrochloride (0-6 M) and temperature. However, it was also observed that BLA in $AgNP_{ST}$-BLA and HEWL in $ZnONP_{ST}$-HEWL conjugates were become tolerant to proteinase-K while both the proteins did not demonstrate any resistance in other NP-proteins complex.

In the second phase, we also studied amyloid formation propensity of HEWL in the presence of NPs. The results showed that the presence $AuNP_{ST}$ and $AgNP_{ST}$ produced small fragments of amyloid fiber with aggregates while amyloid prepared with $ZnONP_{ST}$ showed more amorphous aggregates. From amyloid growth analysis, it was observed that dose of NP and administration time played crucial role in amyloid growth inhibition and such inhibition was found to be substantial during the NP dose in nucleation phase of amyloid. It was also observed by circular dichroism (CD) spectroscopic analysis that such suppression effect of amyloid formation was associated with reduced β-sheet contents. Further, our investigation showed that surface capping agent also affected the amyloid inhibition potential of NP. The PEGylated AuNP and AgNP showed higher potential to inhibit amyloid growth than starch capped NP of equivalent size; however, amyloid inhibition potential of uncapped and self-assembly of ZnONP was lower than $ZnONP_{ST}$. Our study also concluded that HEWL amyloid was highly toxic to both N2a and HaCaT cells, however, when formed in the presence of NP, demonstrated a substantial reduction in toxicity. We further concluded that such toxicity, which was associated with ROS generation, was perhaps caused due to amyloid fiber formation.

It was further observed that the effect of NP depends on the capping agent, dose of NP, and type of proteins. The inhibition potential of NP highly depends on the core material of NP; however, the amyloid growth inhibition potential of NP can be enhanced by varying the capping agent and administration time. From here, we concluded that although metal based NP altered the structure, function, and stability of proteins; their administration substantially inhibited the amyloid growth of HEWL and reduced the cellular toxicity caused by amyloid. Therefore, it was concluded that metal-based nanoparticles could be used in finding therapeutic approach in various neurodegeneration that are caused by protein amyloid deposition.

8.2 Future Work

The following may be proposed as future work.

1. Similar study should also be done with other key proteins such as blood proteins (e.g. albumin, globulin, and fibrinogen etc.) and other cellular proteins.

2. In vivo NP-protein interaction should be studied in detail and the results that obtained from in vitro may be validated with in vivo study.
3. Amyloid growth and subsequent NP-mediated effect on amyloid growth should be studied in disease carrying animal models for understanding the real impact of NPs.
4. Other metal-based nanoparticles should also be studied.

APPENDIX: SUPPLEMENTARY DATA

1. UV-VIS absorbance spectra of AuNP:

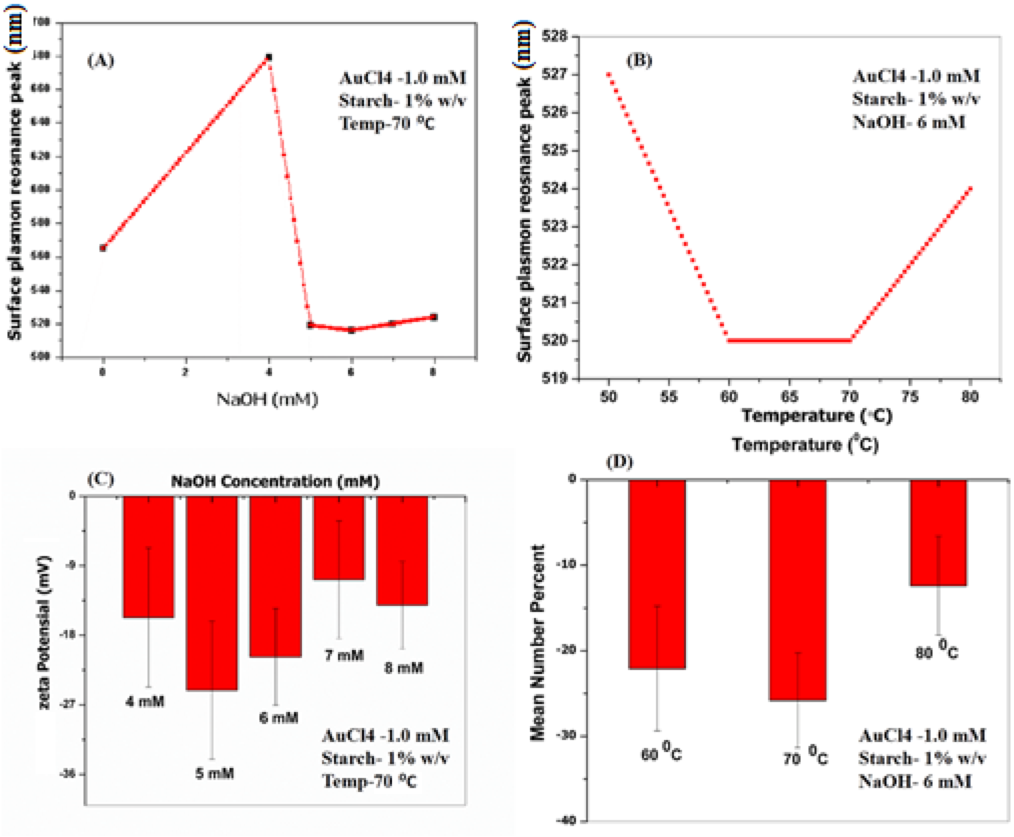

Figure S1 the results showed the SPR peak shift and zeta potential of AuNP; (A) & (C) the effect of NaOH concentrations (4-8 mM) on SPR and zeta potential; (B) & (D) the effect of reaction temperature (60-80 °C) on SPR and zeta potential

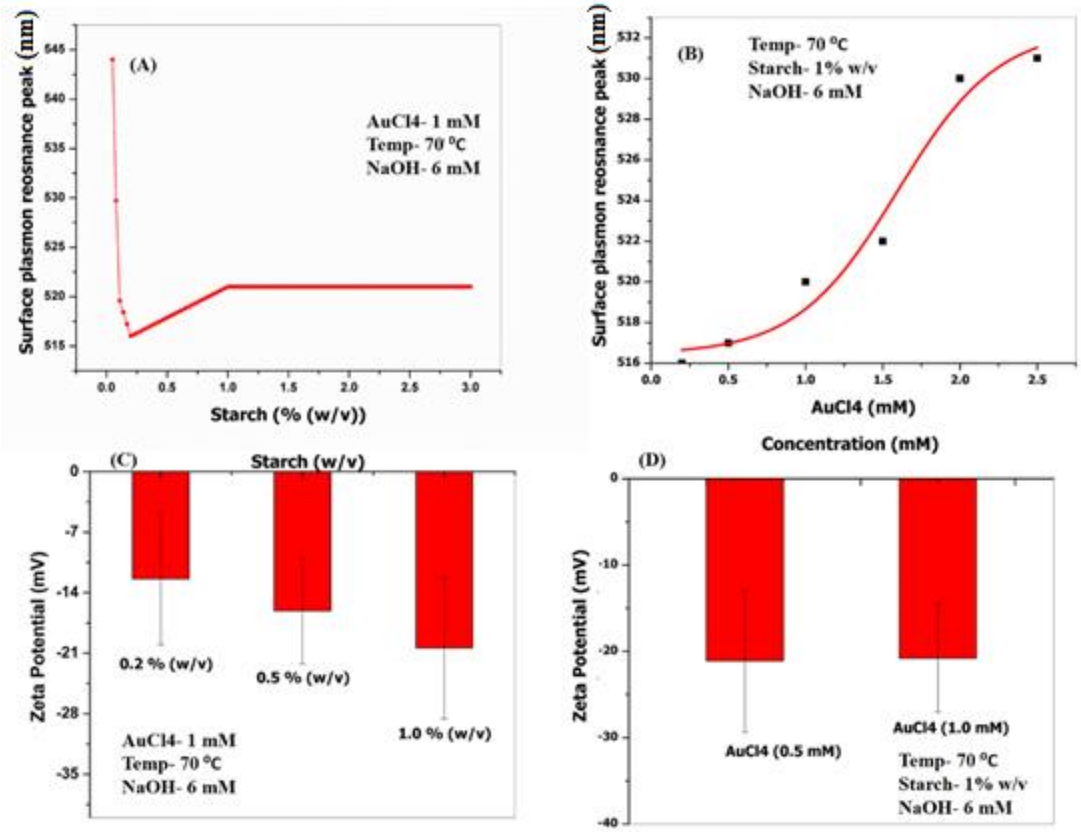

Figure S2 the results showed the SPR peak shift and zeta potential of AuNP; (A) & (C) the effect of various concentration of starch (0.2-1% w/v); (B) & (D) the effect of various concentration of $HAuCl_4$ (0.2-1% w/v).

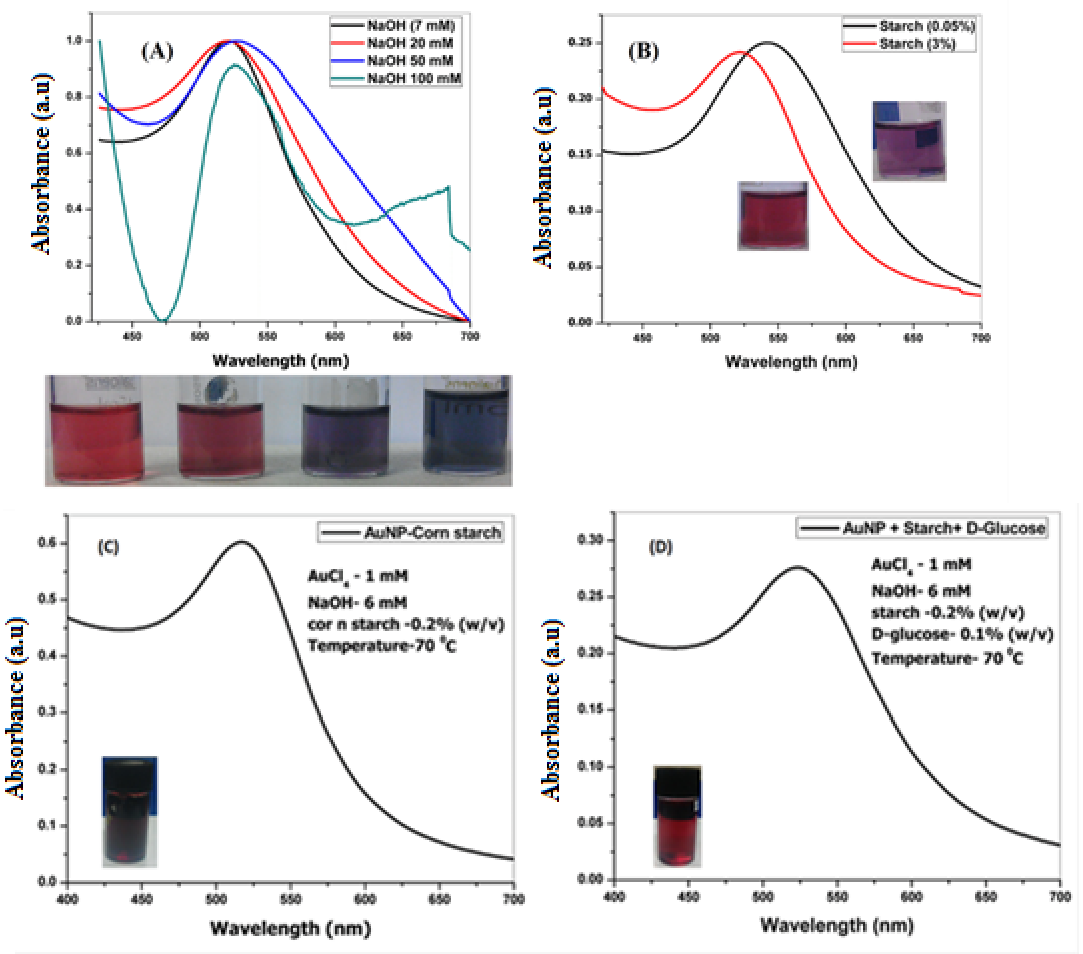

Figure S3 (A) The effect of higher concentration of NaOH (7, 20, 50, 100 mM) on the size and ultimately to the surface plasmon resonance of AuNP. At higher concentration (20-100 mM) SPR become broad and showed red shift in comparison to 7 mMNaOH and color change from ruby red to deep violet and blue showed the size variation. (B) at lower concentration of starch (0.05%) when NaOH concentration was 6 mM produce bright violet color, it showed formation of larger nanoparticles, while at 3% starch deep ruby red color. SPR analysis showed red shift for AuNP with 0.05% starch. AuNP synthesized using corn starch with (C) NaOH and (D) D-glucose and NaOH.

2. Semi-quantitative Benedict test for reducing sugar:

The 1% starch samples were dissolved in water by heating in microwave for 1 min. After cooling to room temperature, the sample was divided into three parts and added 2, 4, 7 mM NaOH solution and heated for 20 min. After cooling to room temperature, equal volume of benedict solution was added and incubates in boiling water for 5 min and observes the color variation. The color variation of samples indicates the presence of reducing sugar in solution. Such variation was compared with respect to known concentrations (0.5, 1, 2, 3, 4 % w/v) of reducing sugar (D-glucose) (Figure S5 showed only 0.5 and 4% images).

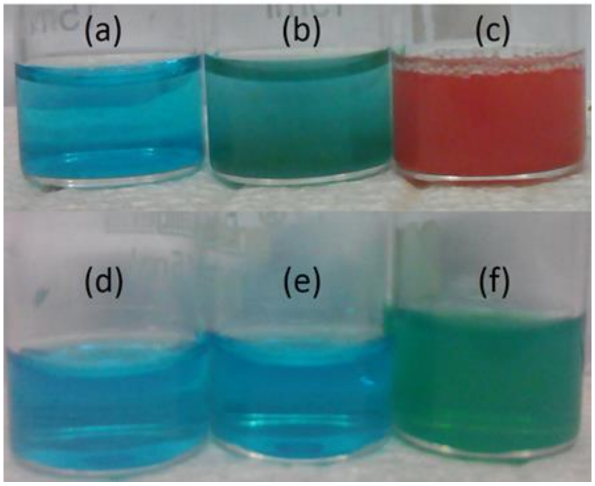

Figure S4 Benedict test for starch. (a) Benedict solution, (b) 0.5% D-glucose with Benedict solution (c) 3% D-glucose with benedict solution. Different concentration of NaOH mixed with 1% starch solution and heated for 20 min (d) 2 mM NaOH, (e) 4 mM NaOH, (f) 7 mM NaOH. The comparison of starch solution with known quantity of reducing sugar showed that 7 mM NaOH produced approximately 0.1-0.5% reducing species which act as reducing sugar in AuNP synthesis.

3. Reaction mechanism of AuNP synthesis:

Ji et al. (2007) and Zhang et al. (2008) reported that reaction of NaOH with auric chloride produce intermediate gold hydroxide that causes conversion of yellow color to transparent and the order of hydroxide increased from 1.0 to 4.0 with increasing the NaOH concentration. Moreover, higher order of Au(OH)x was responsible for the different redox potential and reduction rate of gold.

$$[\mathrm{AuCl}_4]^- + \mathrm{H}_2\mathrm{O} \rightleftharpoons \mathrm{AuCl}_3(\mathrm{H}_2\mathrm{O}) + \mathrm{Cl}^- \qquad (1)$$

$$\mathrm{AuCl}_3(\mathrm{H}_2\mathrm{O}) \rightleftharpoons [\mathrm{AuCl}_3(\mathrm{OH})]^- + \mathrm{H}^+ \qquad (2)$$

$$[\mathrm{AuCl}_3(\mathrm{OH})]^- + \mathrm{H}_2\mathrm{O} \rightleftharpoons \mathrm{AuCl}_2(\mathrm{H}_2\mathrm{O})(\mathrm{OH}) + \mathrm{Cl}^- \qquad (3)$$

$$\mathrm{AuCl}_2(\mathrm{H}_2\mathrm{O})(\mathrm{OH}) \rightleftharpoons [\mathrm{AuCl}_2(\mathrm{OH})_2]^- + \mathrm{H}^+ \qquad (4)$$

$$[\mathrm{AuCl}_2(\mathrm{OH})_2]^- + \mathrm{H}_2\mathrm{O} \rightleftharpoons [\mathrm{AuCl}(\mathrm{OH})_3]^- + \mathrm{H}^+ + \mathrm{Cl}^- \qquad (5)$$

$$[\mathrm{AuCl}(\mathrm{OH})_3]^- + \mathrm{H}_2\mathrm{O} \rightleftharpoons [\mathrm{Au}(\mathrm{OH})_4]- + \mathrm{H}^+ + \mathrm{Cl}^- \qquad (6)$$

4. Retrogrdation of starch:

Figure S5 Retro-gradation of starch by freezing thawing was shown. The bottom of the bottle showed retrograded starch (light pink color) with AuNP while dark ruby red color showed AuNP suspension

Zinc oxide nanoparticle

5. Zeta potential analysis

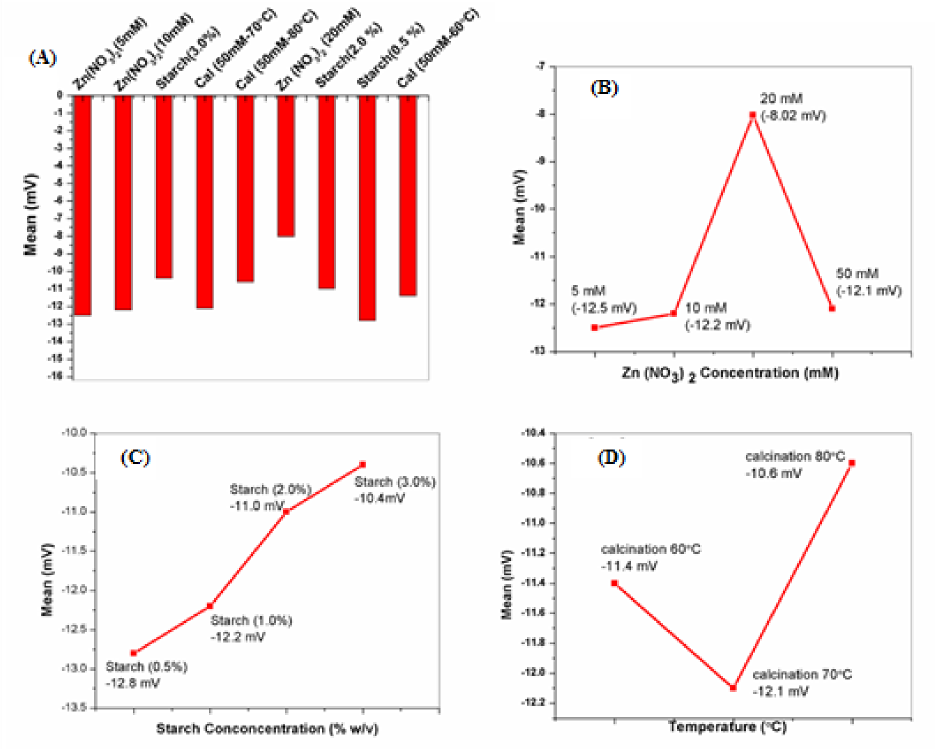

Figure S6 Zeta potential analysis of different samples. **(A)** Zeta potential of sample with different Zn $(NO_3)_2$ concentration (5, 10, 20, 50 mM), starch concentration (0.5, 1, 2, 3 % w/v), and calcination temperature (60, 70, 80 ^{0}C). **(B)** The effect different Zn $(NO_3)_2$ concentration (5, 10, 20, 50 mM). The zeta potential of ZnONP prepared using 5 and 10 mM of Zn $(NO_3)_2$. **(C)** The effect different starch concentration (0.5, 1, 2, 3 % w/v). **(D)** The effect of different calcination temperature (60, 70, 80 ^{0}C).

6. FESEM images of different stages of ZnONP synthesis:

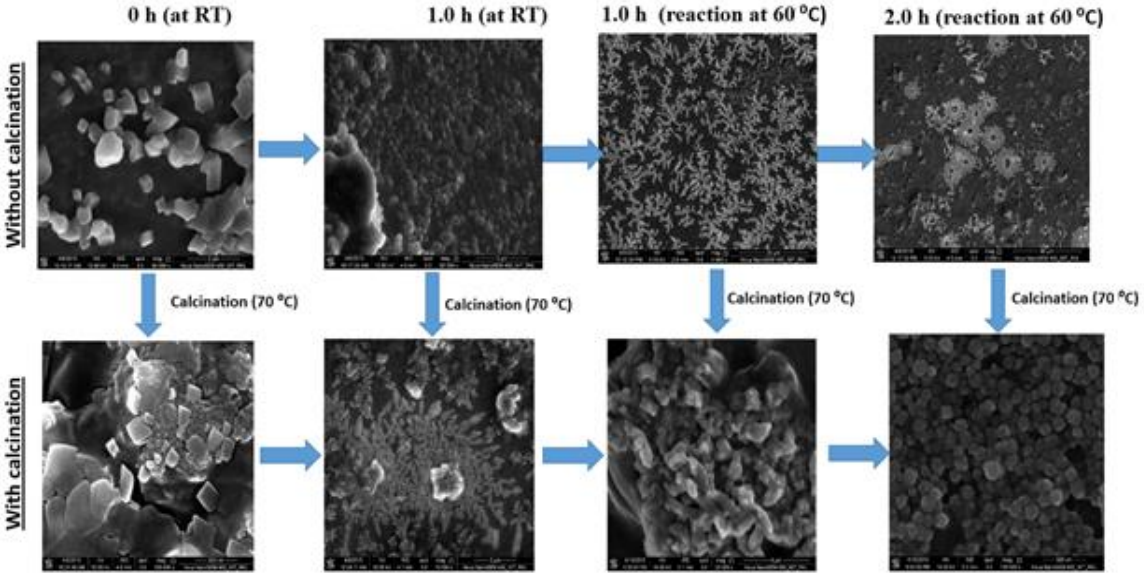

Figure S7 Self-assembly mechanism of ZnONP. The growth of the ZnONP was recorded at different time interval of the reaction before calcination (top images) and after calcination process (bottom images).

7. Effect of NP concentration in protein Fluorescence

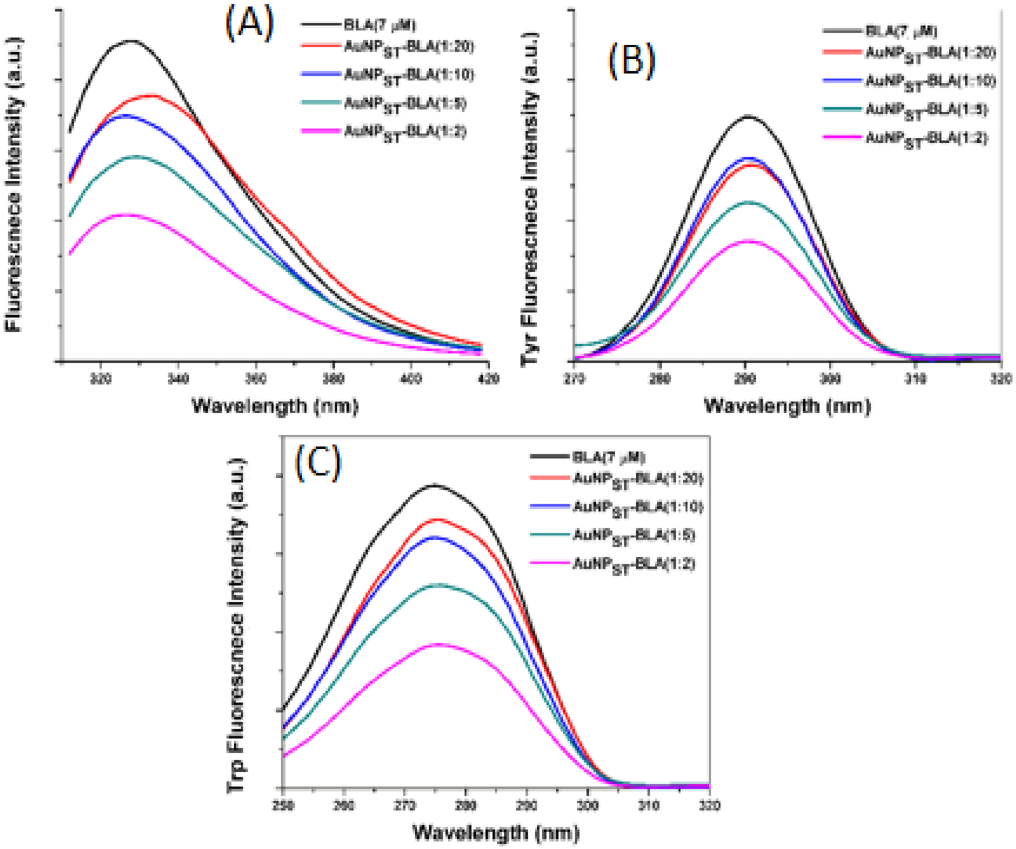

Figure S8 Fluorescence spectroscopy analysis of BLA with different molar ratio of AuNP$_{ST}$. (A) intrinsic fluorescence of BLA when excited at 295 nm. (B) Tyrosine fluorescence analysis in synchronous mode. (C) Tryptophan fluorescence analysis by synchronous fluorescence spectroscopy.

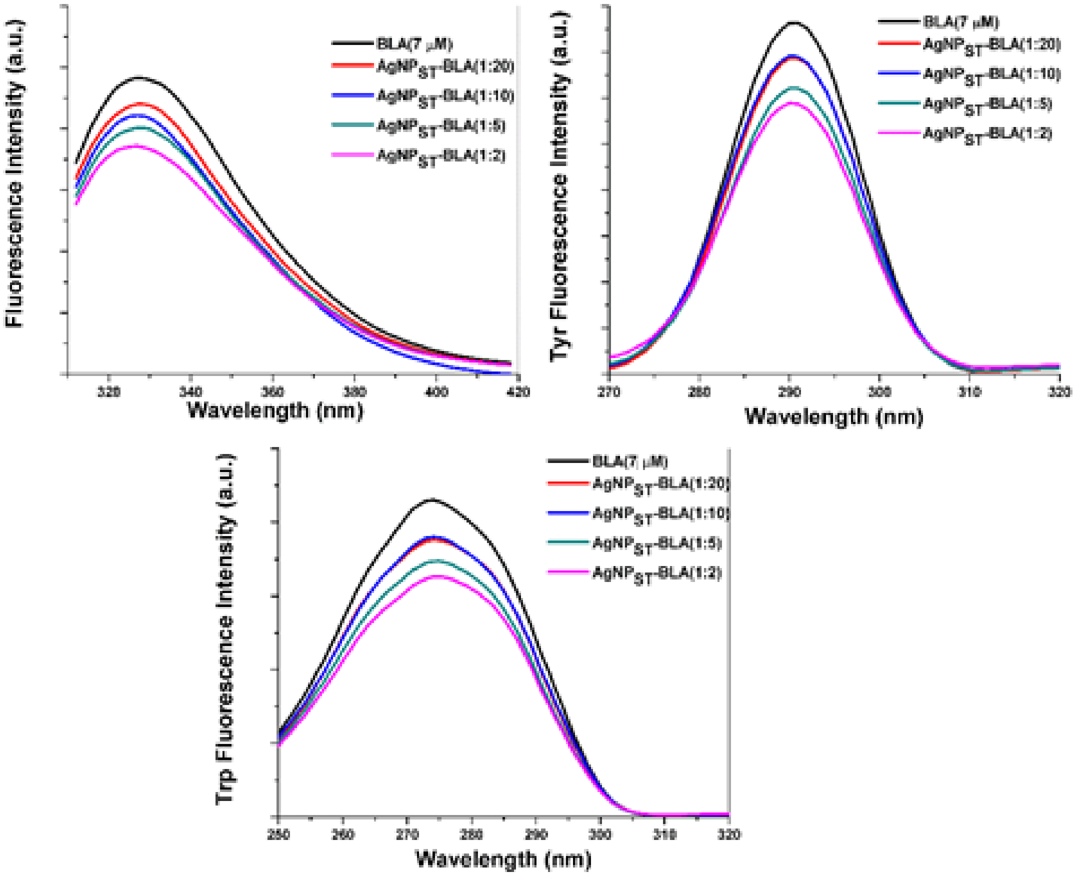

Figure S9 Fluorescence spectroscopy analysis of BLA with different molar ratio of AgNP$_{ST}$. (A) Intrinsic fluorescence of BLA when excited at 295 nm. (B) Tyrosine fluorescence analysis in synchronous mode. (C) Tryptophan fluorescence analysis by synchronous fluorescence spectroscopy.

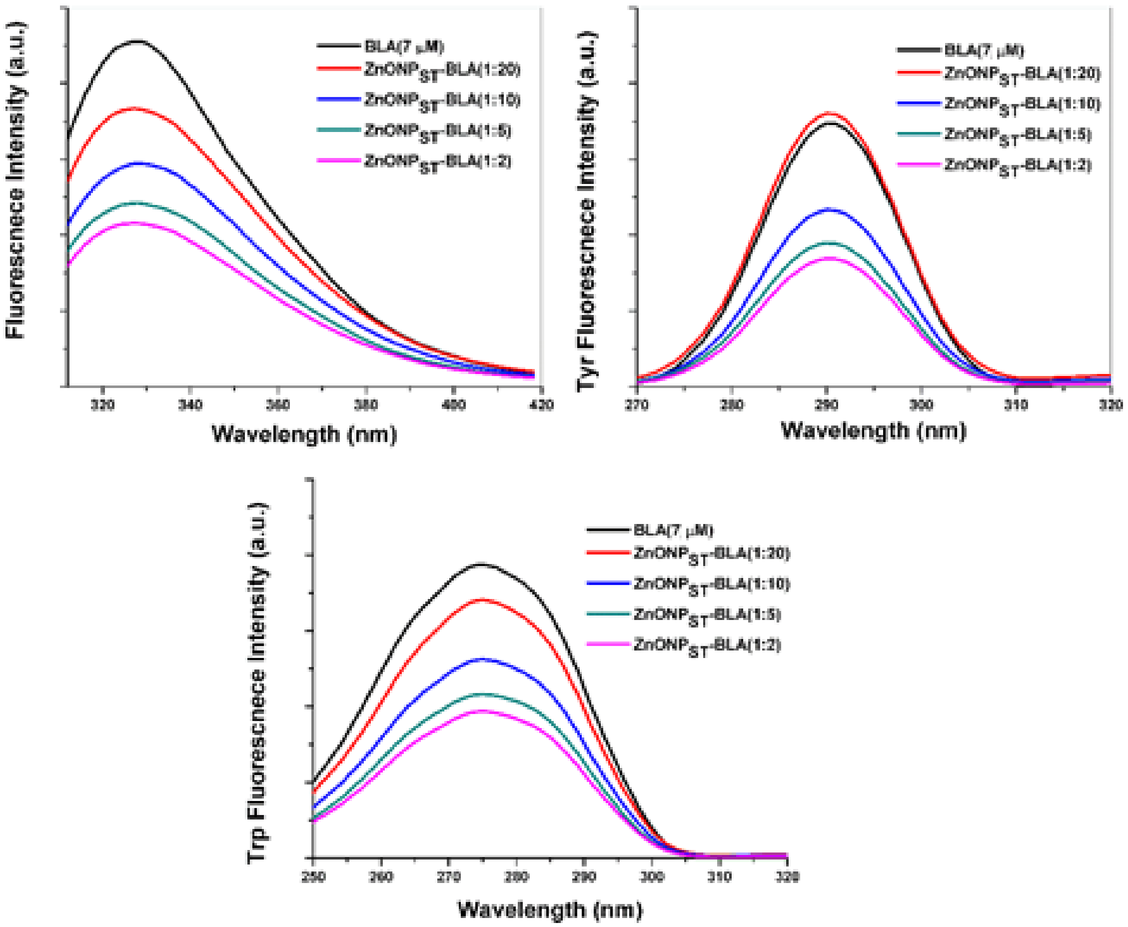

Figure S10 Fluorescence spectroscopy analysis of BLA with different molar ratio of ZnONP$_{ST}$. (A) intrinsic fluorescence of BLA when excited at 295 nm. (B) Tyrosine fluorescence analysis in synchronous mode. (C) Tryptophan fluorescence analysis by synchronous fluorescence spectroscopy.

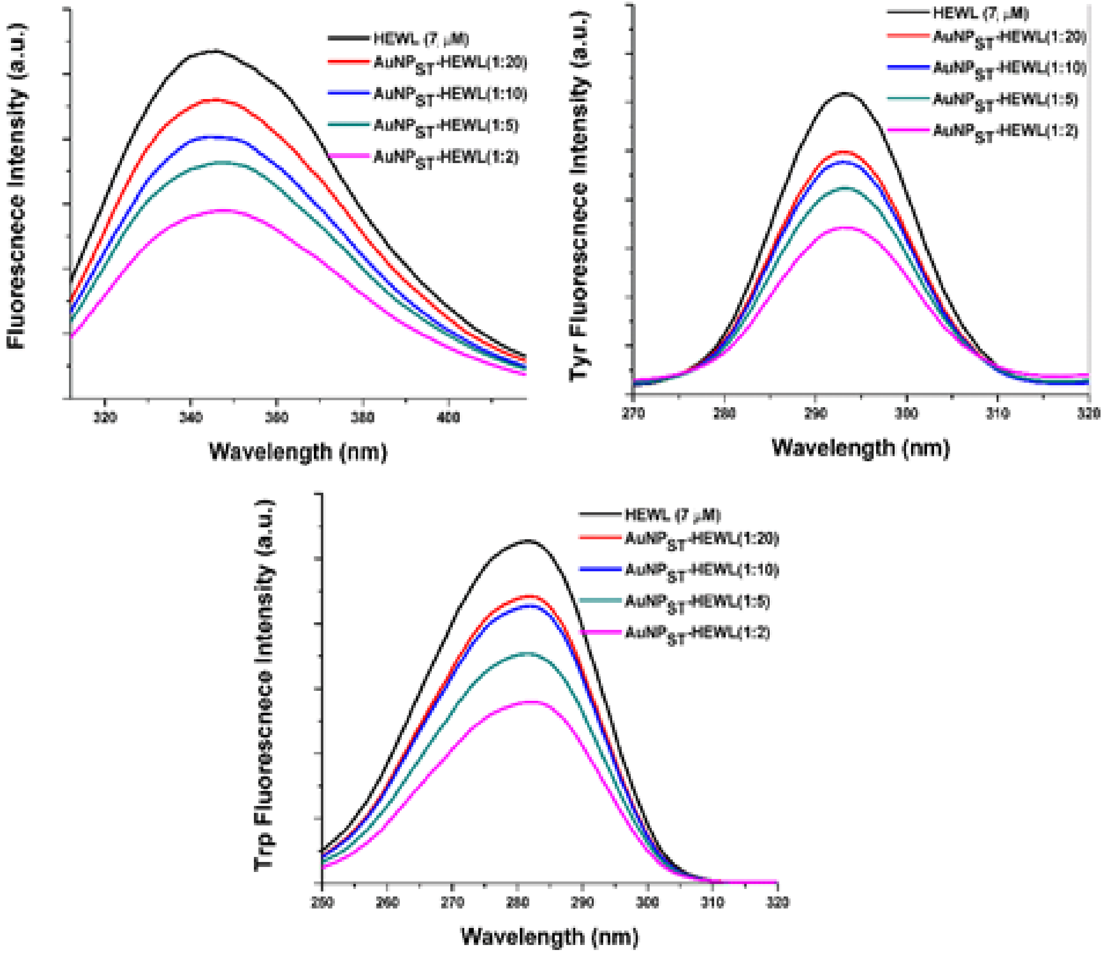

Figure S11 Fluorescence spectroscopy analysis of HEWL with different molar ratio of AuNP$_{ST}$. (A) intrinsic fluorescence of HEWL when excited at 295 nm. (B) Tyrosine fluorescence analysis in synchronous mode. (C) Tryptophan fluorescence analysis by synchronous fluorescence spectroscopy.

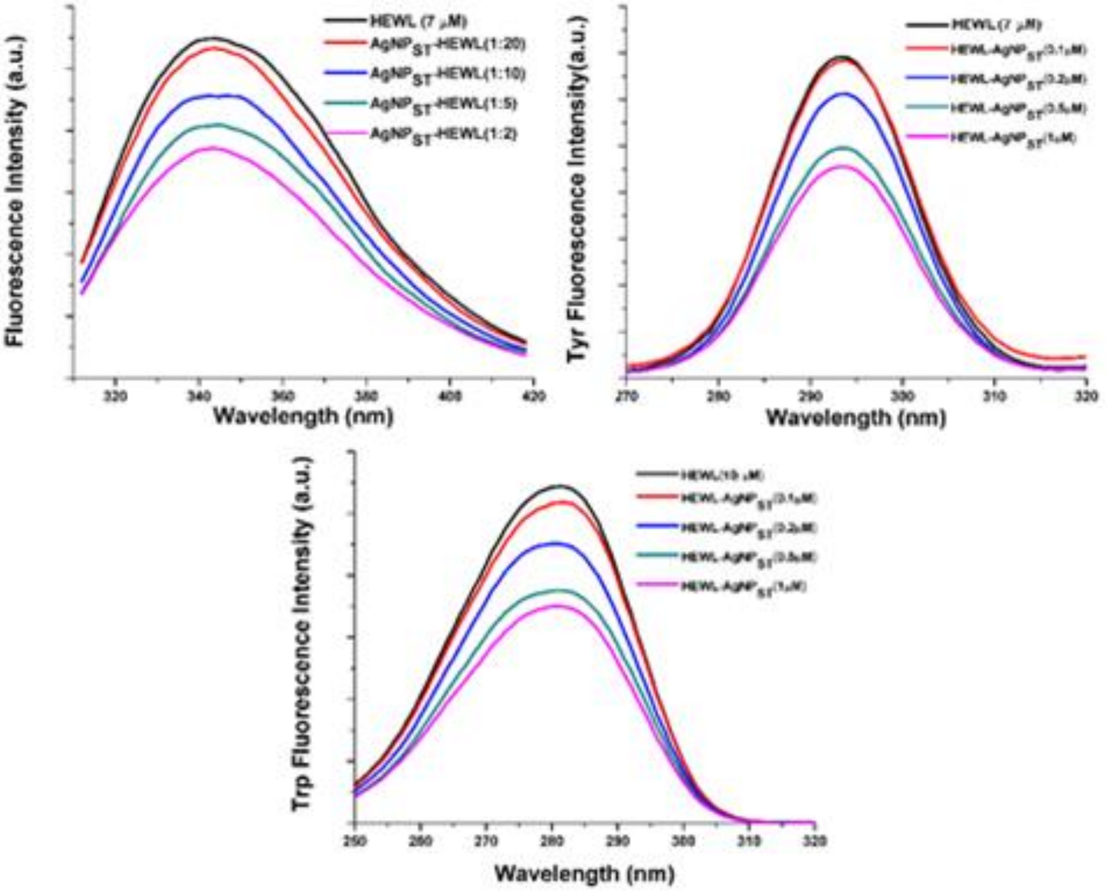

Figure S12 Fluorescence spectroscopy analysis of HEWL with different molar ratio of AgNP$_{ST}$. (A) intrinsic fluorescence of HEWL when excited at 295 nm. (B) Tyrosine fluorescence analysis in synchronous mode. (C) Tryptophan fluorescence analysis by synchronous fluorescence spectroscopy.

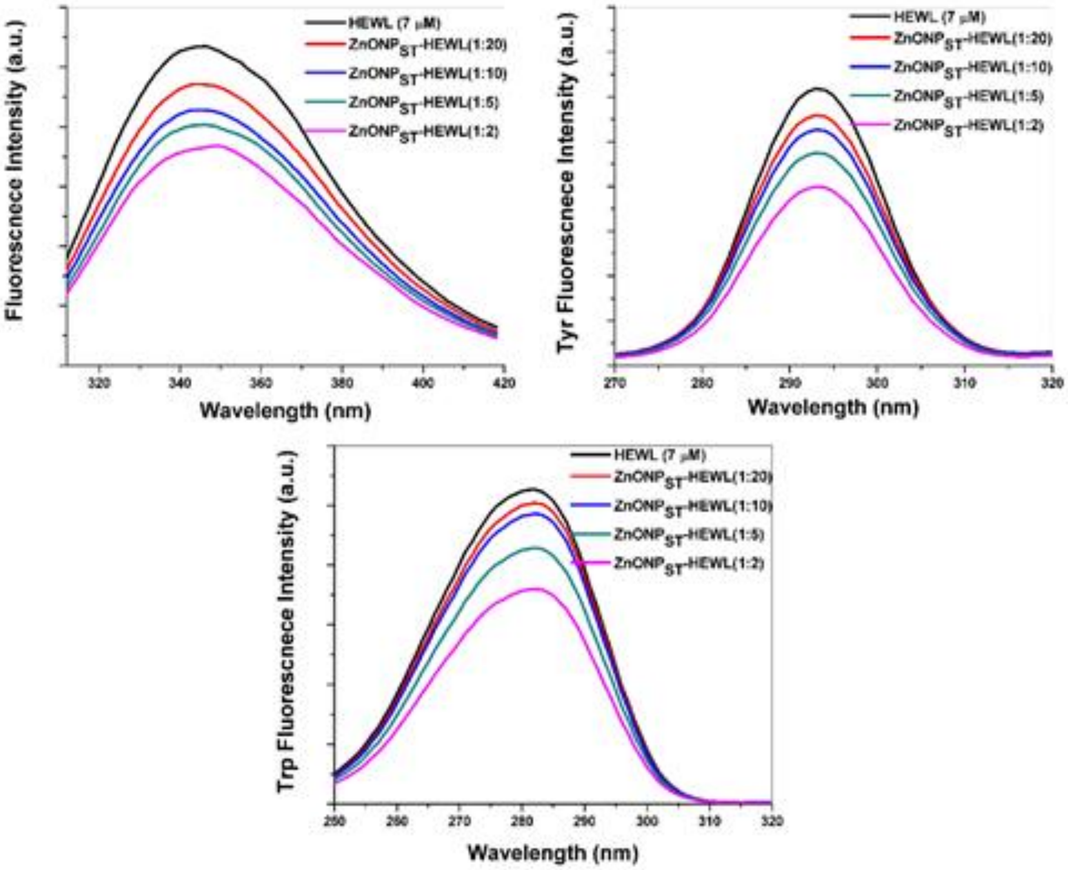

Figure S13 Fluorescence spectroscopy analysis of HEWL with different molar ratio of ZnONP$_{ST}$. (A) intrinsic fluorescence of HEWL when excited at 295 nm. (B) Tyrosine fluorescence analysis in synchronous mode. (C) Tryptophan fluorescence analysis by synchronous fluorescence spectroscopy.

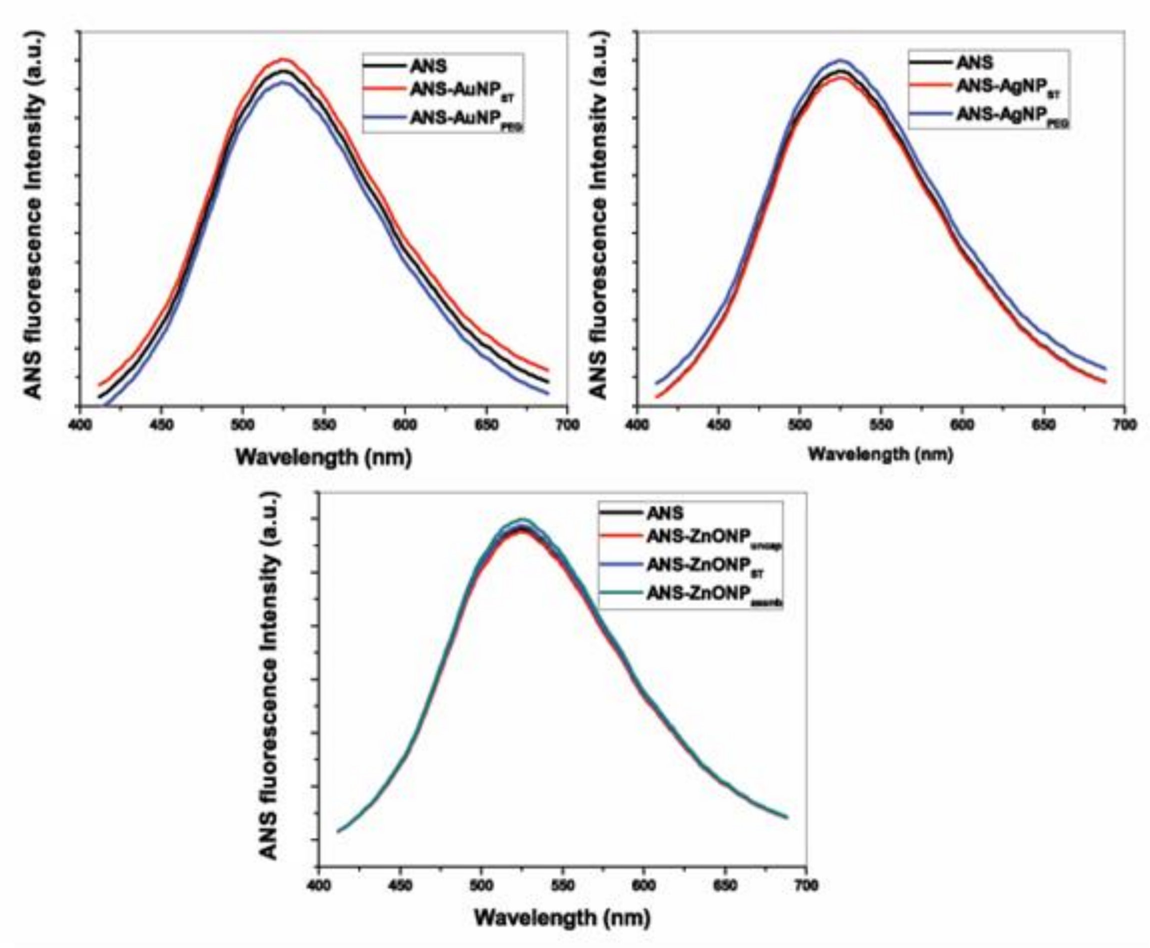

Figure S14 ANS binding with NP was analyzed. (A) ANS-AuNP, (B) ANS-AgNP, (C) ANS-ZnONP.

8. Effect of Guanidine hydrochloride

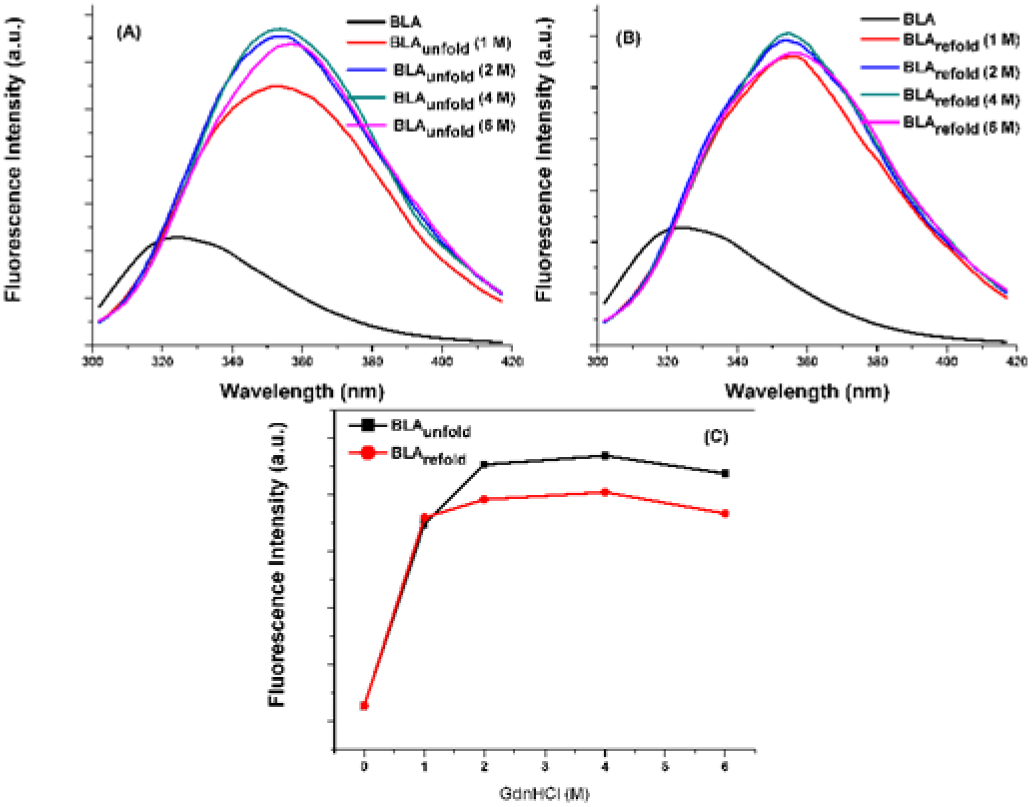

Figure S15 Fluorescence spectroscopy analysis of BLA with different concentration of guanidine hydrochloride (GdnHCl). (A) Intrinsic fluorescence of BLA when GdnHCl concentration increased from 0-6 M. (B) intrinsic fluorescence of BLA incubated in 8 M GdnHCl and further diluted in 6-1 M GdnHCl. (C) showed variation in fluorescence emission peak with 0-6 M GdnHCl.

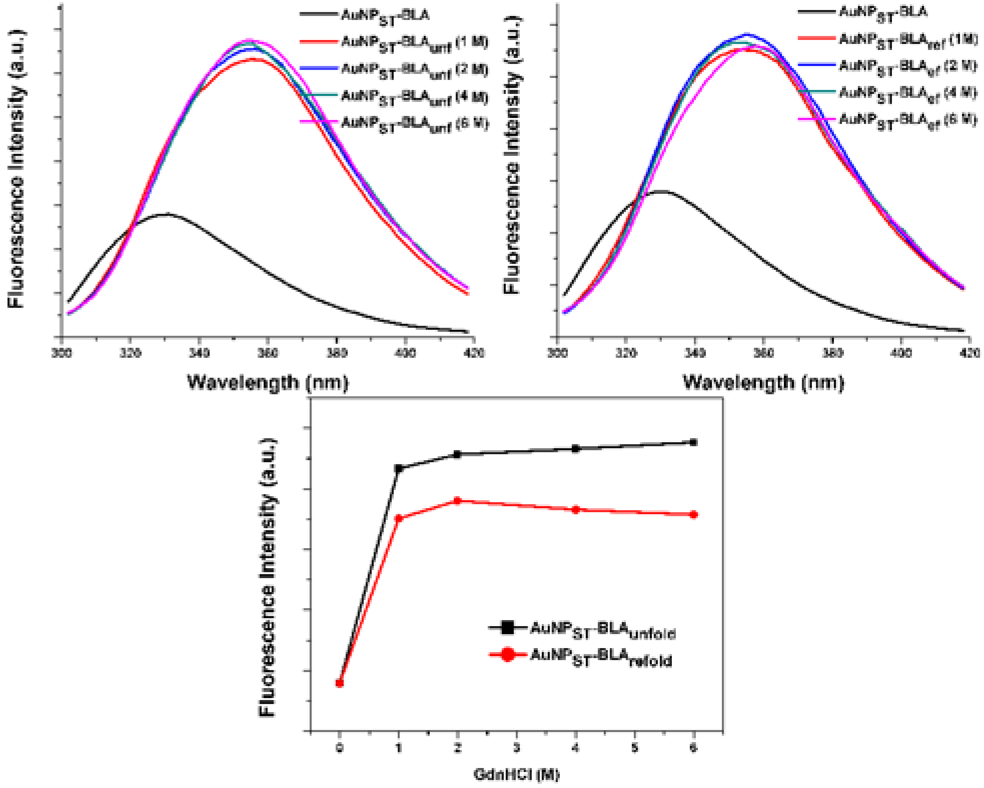

Figure S16 Fluorescence spectroscopy analysis of BLA conjugate with $AuNP_{ST}$ in different concentration of guanidine hydrochloride (GdnHCl) and 100 mM DTT. (A) Intrinsic fluorescence of BLA when GdnHCl concentration increased from 0-6 M. (B) intrinsic fluorescence of HEWL incubated in 8 M GdnHCl and further diluted in 6-1 M GdnHCl. (C) showed variation in fluorescence emission peak with 0-6 M GdnHCl during unfolding and refolding.

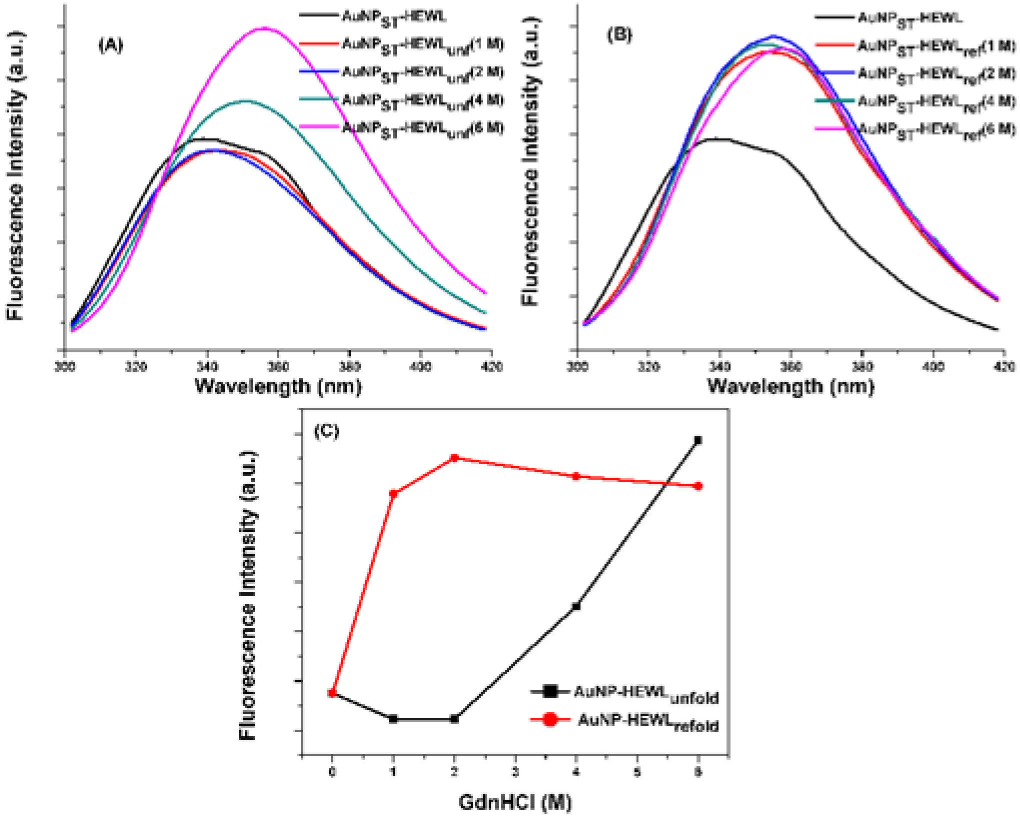

Figure S17 Fluorescence spectroscopy analysis of HEWL with AuNP$_{ST}$ in different concentration of guanidine hydrochloride (GdnHCl) and 100 mM DTT. (A) Intrinsic fluorescence of HEWL when GdnHCl concentration increased from 0-6 M. (B) intrinsic fluorescence of HEWL incubated in 8 M GdnHCl and further diluted in 6-1 M GdnHCl. (C) showed large variation in fluorescence emission peak with 0-6 M GdnHCl during unfolding and refolding.

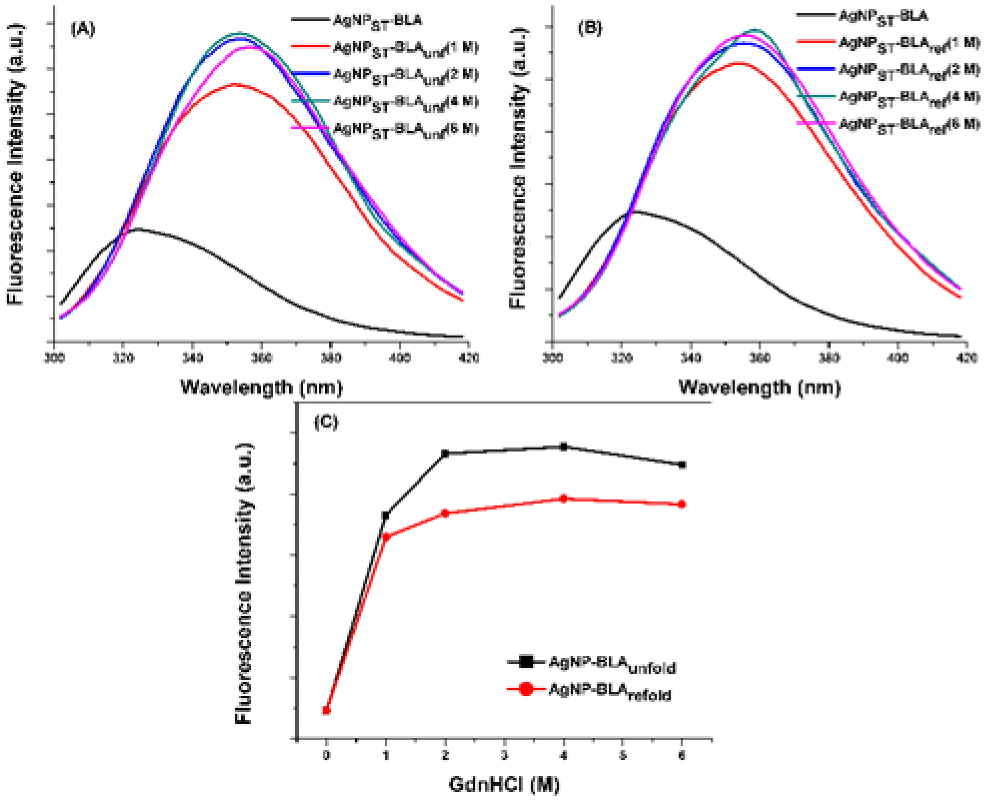

Figure S18 Fluorescence spectroscopy analysis of BLA with AgNP_{ST} in different concentration of guanidine hydrochloride (GdnHCl) and 100 mM DTT. (A) Intrinsic fluorescence of BLA when GdnHCl concentration increased from 0-6 M. (B) intrinsic fluorescence of BLA incubated in 8 M GdnHCl and further diluted in 6-1 M GdnHCl. (C) showed variation in fluorescence emission peak with 0-6 M GdnHCl during unfolding and refolding.

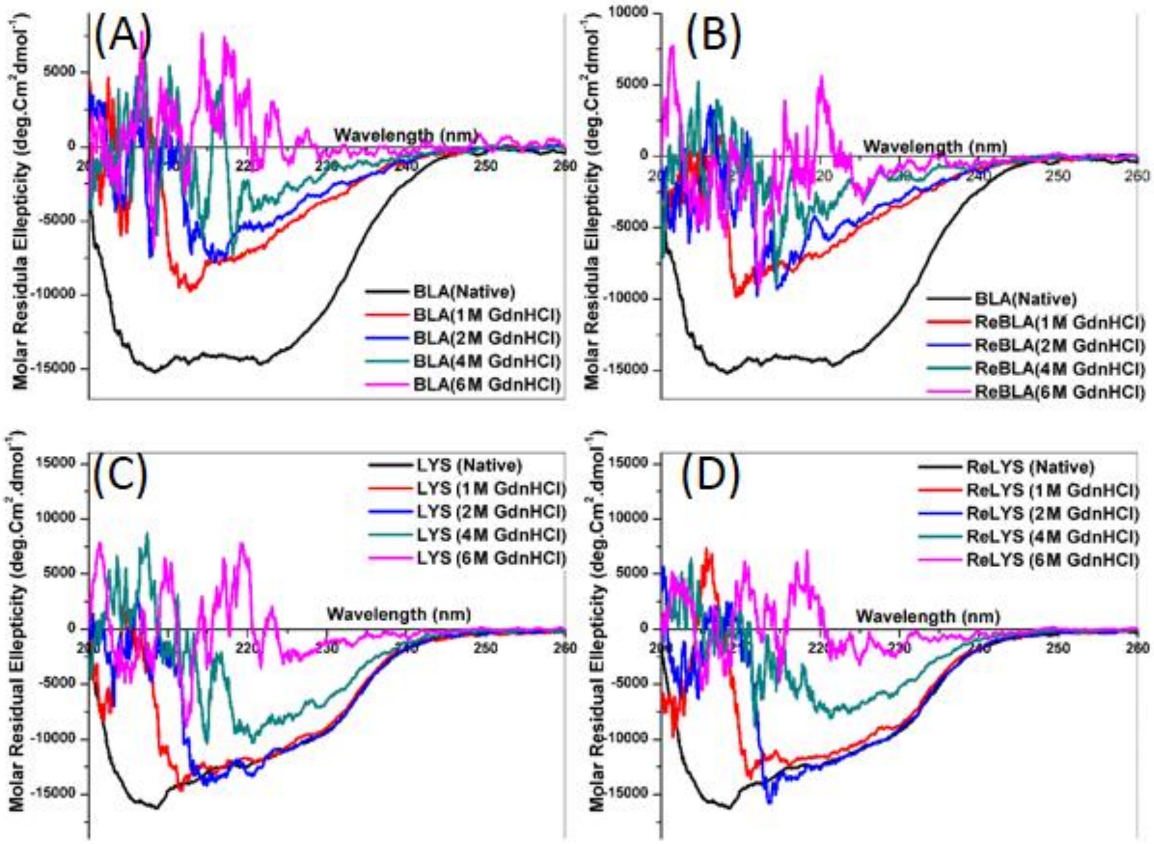

Figure S19 BLA and LYS unfolding and folding in in Different concentration of GdnHCl (0, 1, 2, 4, 6 M), at 25 ^{0}C. (A) unfolding of BLA, (B) refolding of BLA, (C) unfolding of HEWL, (D) refolding of HEWL.

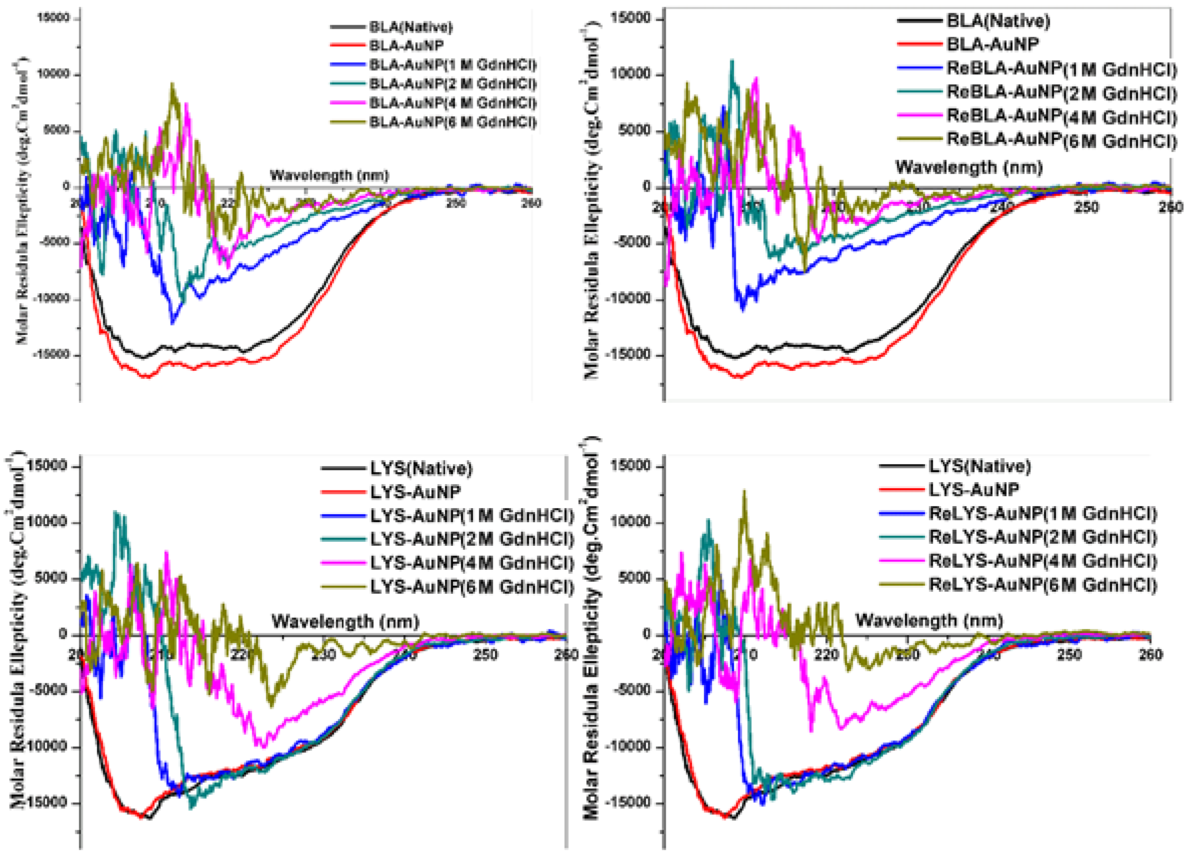

Figure S20 BLA and LYS unfolding and folding in in Different concentration of GdnHCl (0, 1, 2, 4, 6 M), at 25 ^{0}C. (A) Unfolding of BLA-AuNP$_{ST}$, (B) refolding of BLA-AuNP$_{ST}$, (C) unfolding of HEWL-AuNP$_{ST}$, (D) refolding of HEWL-AuNP$_{ST}$.

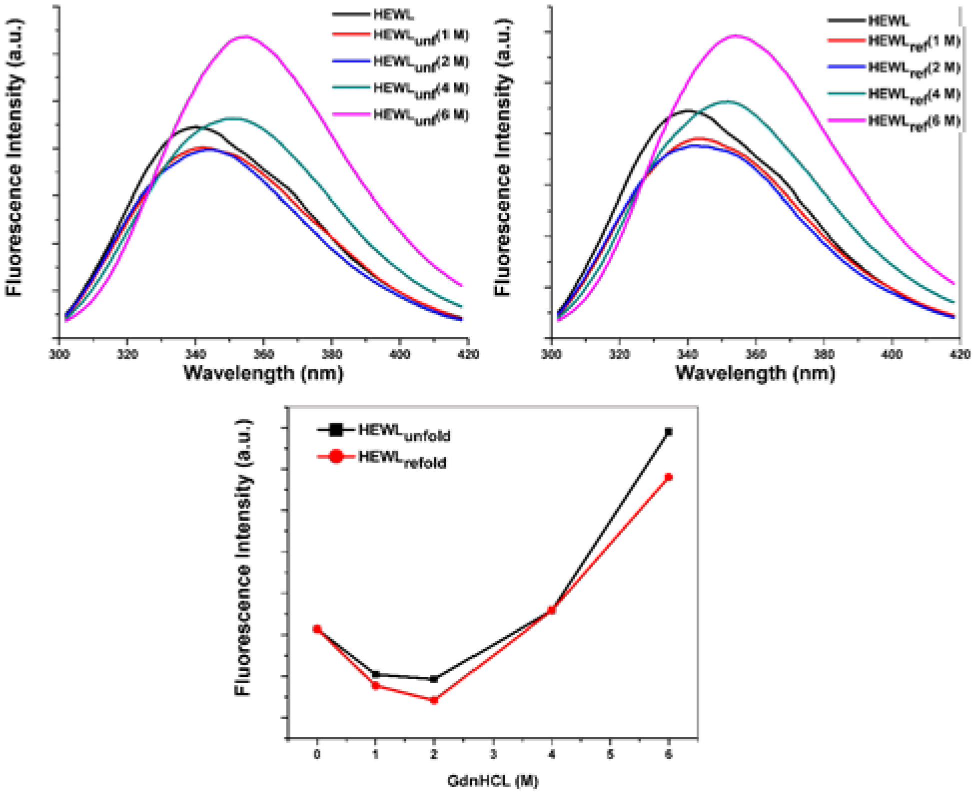

Figure S21 Fluorescence spectroscopy analysis of HEWL with different concentration of guanidine hydrochloride (GdnHCl) and 100 mM DTT. (A) Intrinsic fluorescence of HEWL when GdnHCl concentration increased from 0-6 M. (B) intrinsic fluorescence of HEWL incubated in 8 M GdnHCl and further diluted in 6-1 M GdnHCl. (C) showed variation in fluorescence emission peak with 0-6 M GdnHCl during unfolding and refolding.

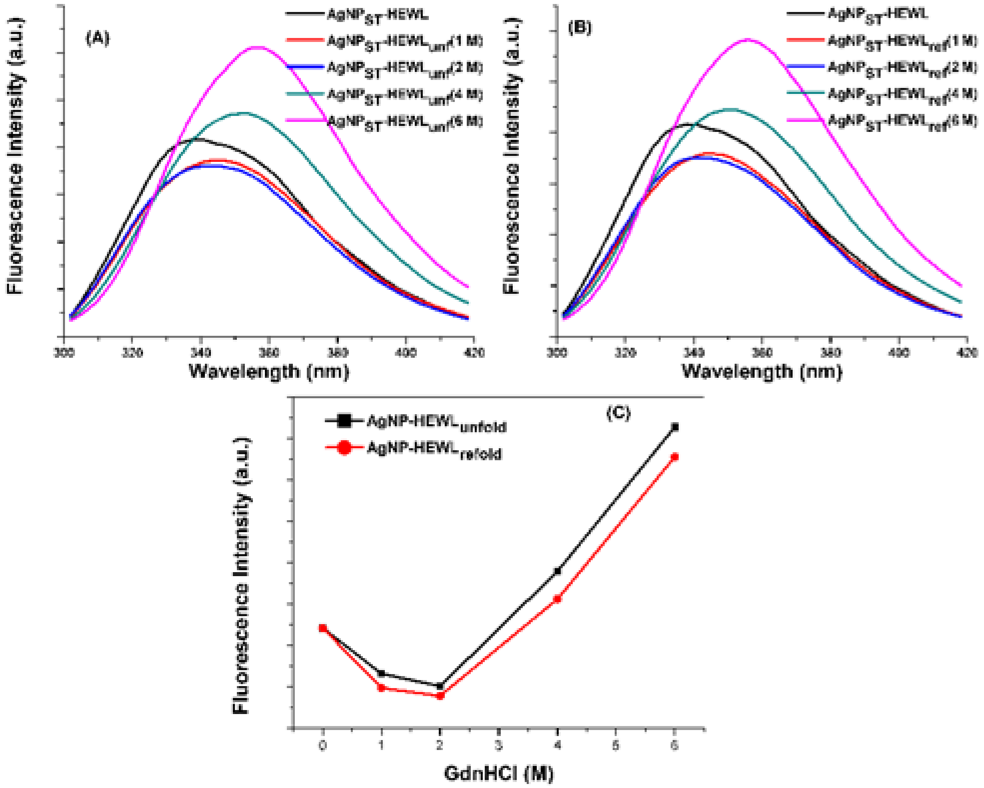

Figure S22 Fluorescence spectroscopy analysis of HEWL with AgNP$_{ST}$ in different concentration of guanidine hydrochloride (GdnHCl) and 100 mM DTT. (A) Intrinsic fluorescence of HEWL when GdnHCl concentration increased from 0-6 M. (B) intrinsic fluorescence of HEWL incubated in 8 M GdnHCl and further diluted in 6-1 M GdnHCl. (C) showed variation in fluorescence emission peak with 0-6 M GdnHCl during unfolding and refolding.

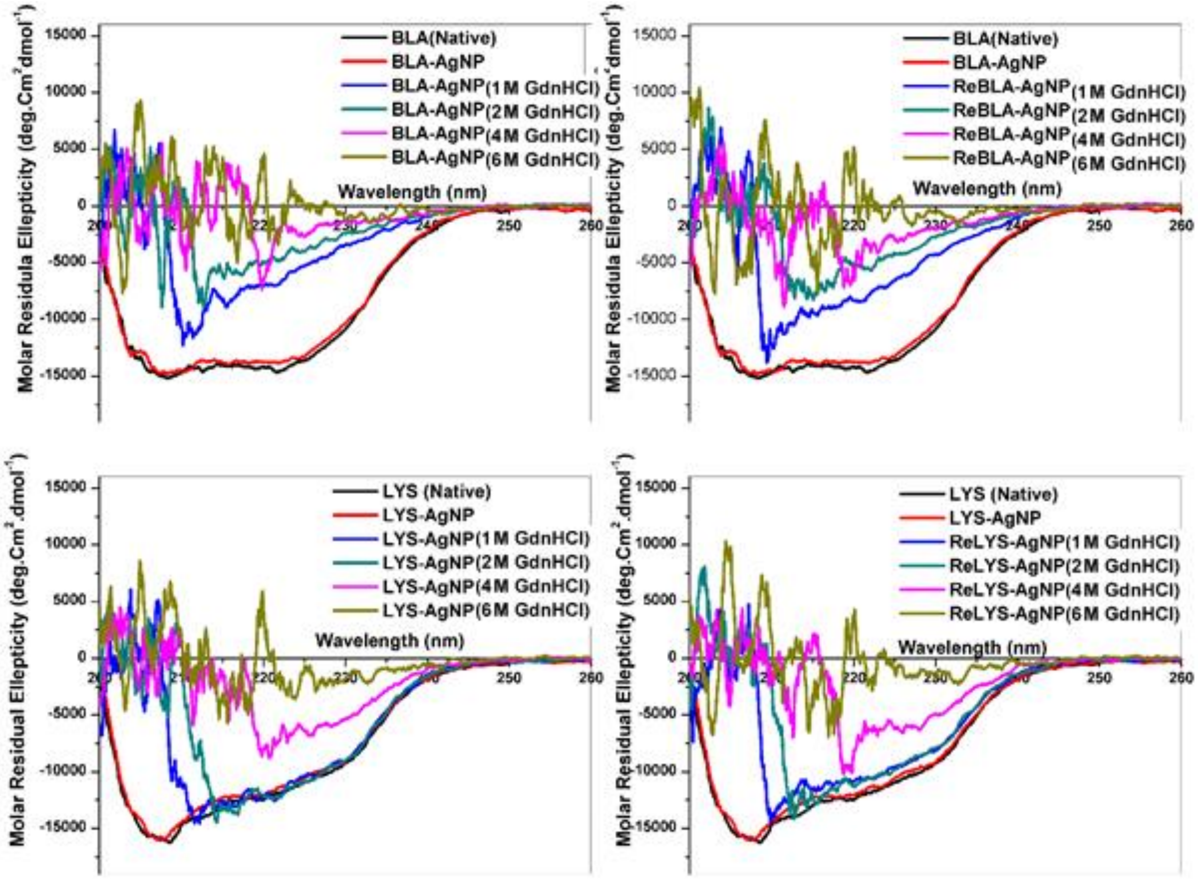

Figure S23 BLA and LYS unfolding and folding in in Different concentration of GdnHCl (0, 1, 2, 4, 6 M), at 25 ^{0}C. (A) Unfolding of BLA-AgNP$_{ST}$, (B) refolding of BLA-AgNP$_{ST}$, (C) unfolding of HEWL-AgNP$_{ST}$, (D) refolding of HEWL-AgNP$_{ST}$.

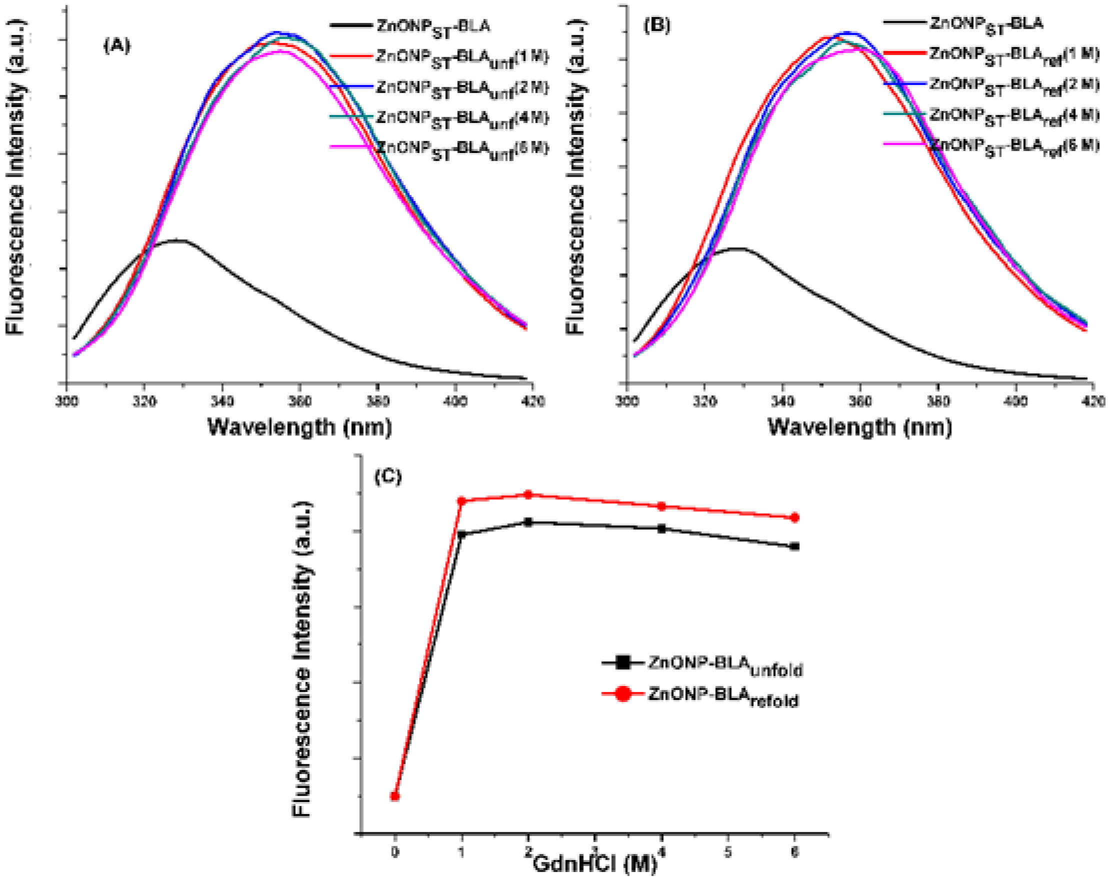

Figure S24 Fluorescence spectroscopy analysis of BLA with ZnONP$_{assmb}$ different concentration of guanidine hydrochloride (GdnHCl) and 100 mM DTT. (A) Intrinsic fluorescence of BLAwhen GdnHCl concentration increased from 0-6 M. (B) intrinsic fluorescence of BLA incubated in 8 M GdnHCl and further diluted in 6-1 M GdnHCl. (C) showed variation in fluorescence emission peak with 0-6 M GdnHCl during unfolding and refolding.

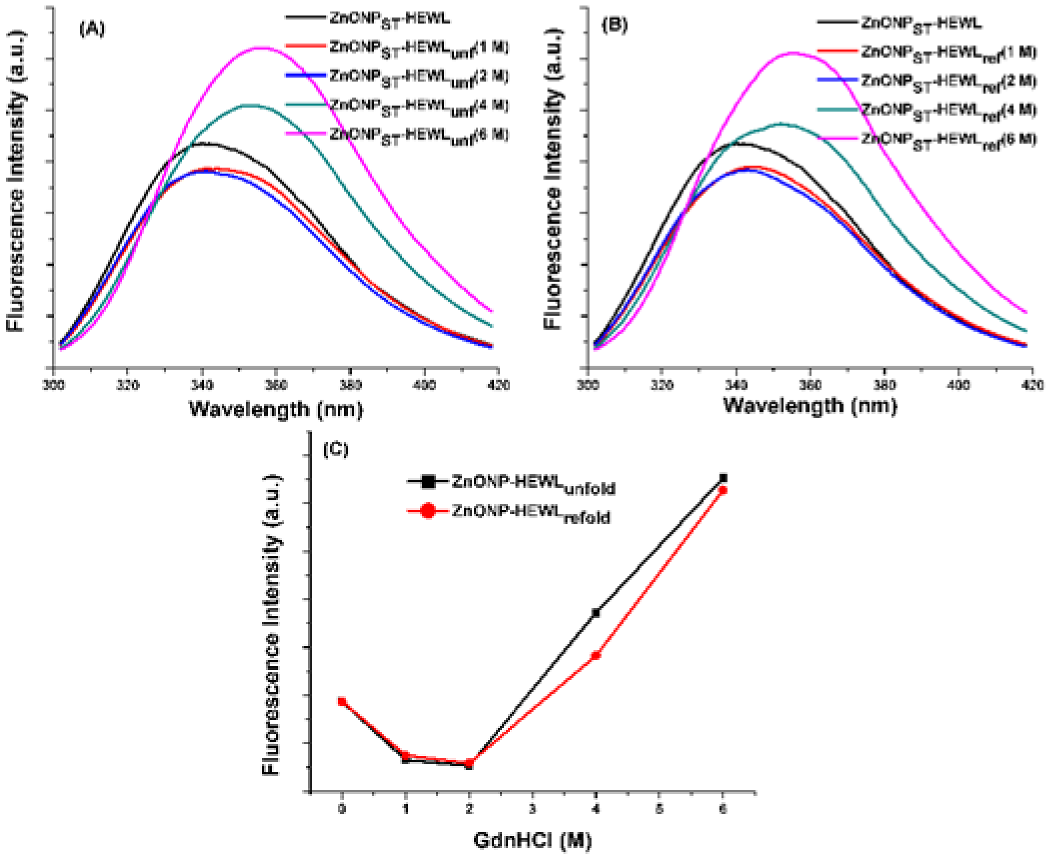

Figure S25 Fluorescence spectroscopy analysis of HEWL with ZnONP$_{ST}$ in different concentration of guanidine hydrochloride (GdnHCl) and 100 mM DTT. (A) Intrinsic fluorescence of HEWL when GdnHCl concentration increased from 0-6 M. (B) intrinsic fluorescence of HEWL incubated in 8 M GdnHCl and further diluted in 6-1 M GdnHCl. (C) showed variation in fluorescence emission peak with 0-6 M GdnHCl during unfolding and refolding.

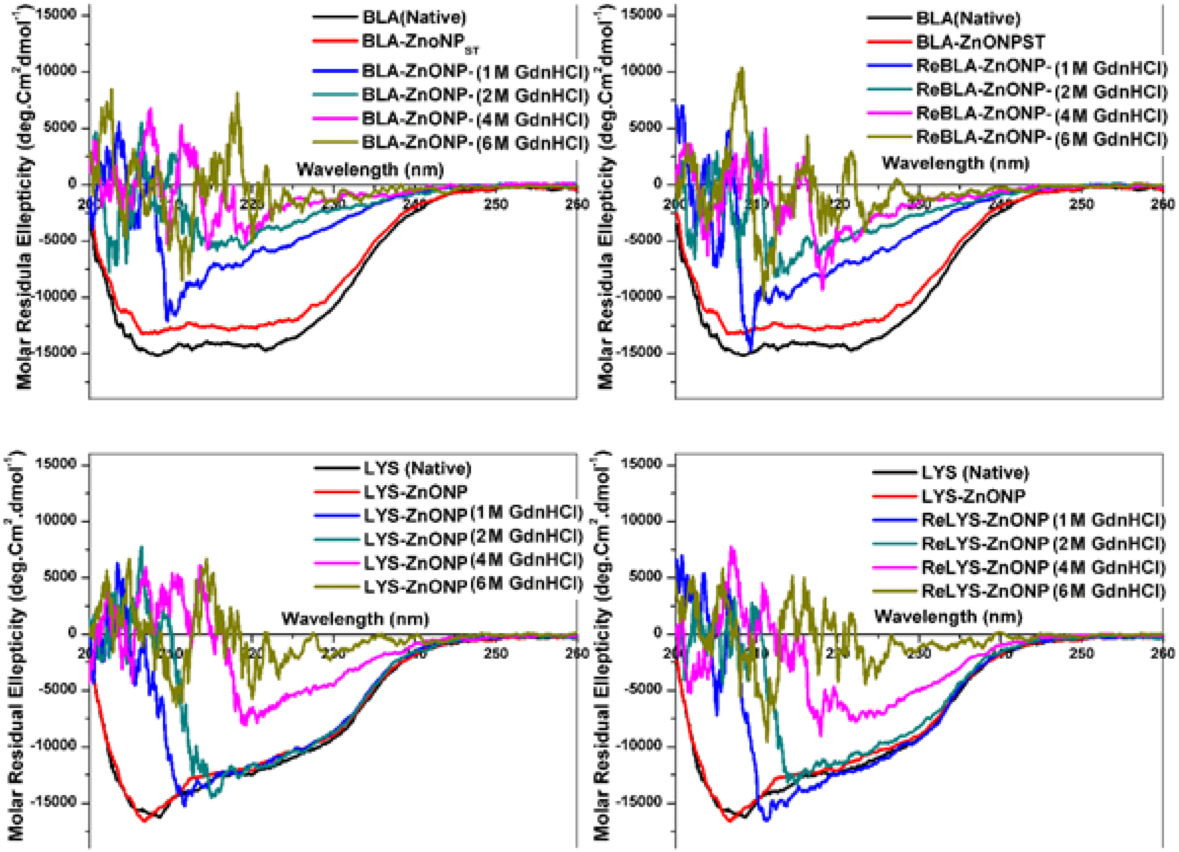

Figure S26 BLA and LYS with ZnONP, unfolding and folding in in Different concentration of GdnHCl (0, 1, 2, 4, 6 M) and 100 mM DTT, at 25 ^{0}C. Moreover, refolding was performed by dilution of protein in 8 M GdnHCl solution to 6, 4, 2, 1 M in similar condition and final concentration of protein was 10 µM in both cases. The result showed that AgNP facilitate BLA and LYS unfolding and refolding both the protein regain its initial confirmation easily.

Effect of Heating on Protein

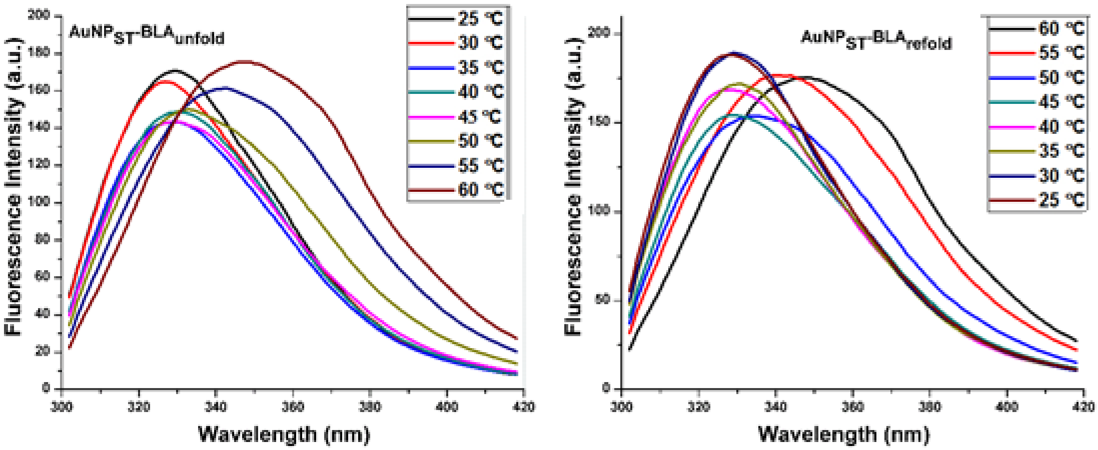

Figure S27 Fluorescence spectroscopy analysis of BLA-AuNP$_{ST}$, when sample was incubated at differ temperature (25-60 ^{0}C). (A) Intrinsic fluorescence of BLA when temperature increased from 25-60 ^{0}C with increment of 5 ^{0}C. (B) Intrinsic fluorescence of BLA when temperature decreased from 60-25 ^{0}C with decrement of 5 ^{0}C.

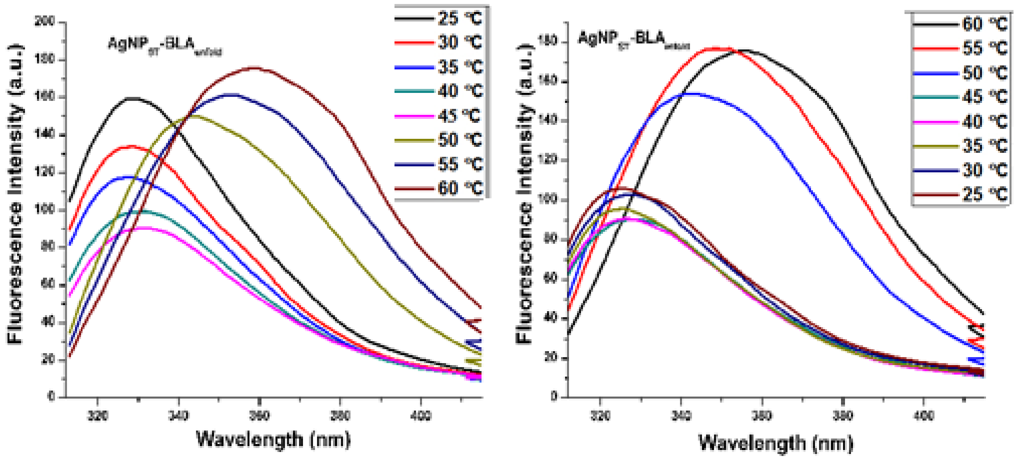

Figure S28 Fluorescence spectroscopy analysis of BLA-AgNP$_{ST}$, when sample was incubated at differ temperature (25-60 ^{0}C). (A) Intrinsic fluorescence of BLA when temperature increased from 25-60 ^{0}C with increment of 5 ^{0}C. (B) Intrinsic fluorescence of BLA when temperature decreased from 60-25 ^{0}C with decrement of 5 ^{0}C.

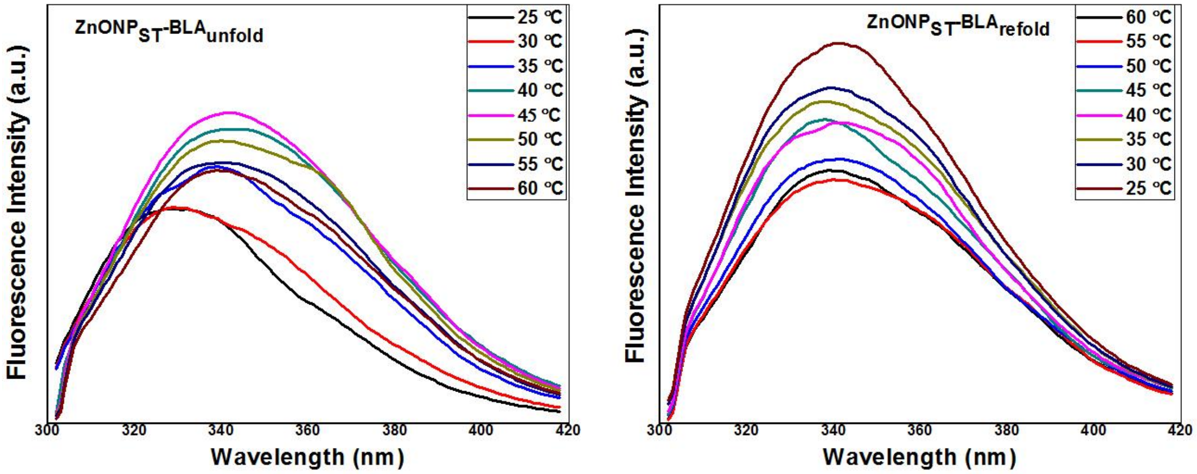

Figure S29 Fluorescence spectroscopy analysis of BLA-ZnONP$_{ST,}$ when sample was incubated at differ temperature (25-60 ^{o}C). (A) Intrinsic fluorescence of BLA when temperature increased from 25-60 ^{o}C with increment of 5 ^{o}C. (B) Intrinsic fluorescence of BLA when temperature decreased from 60-25 ^{o}C with decrement of 5 ^{o}C.

CD Spectroscopy

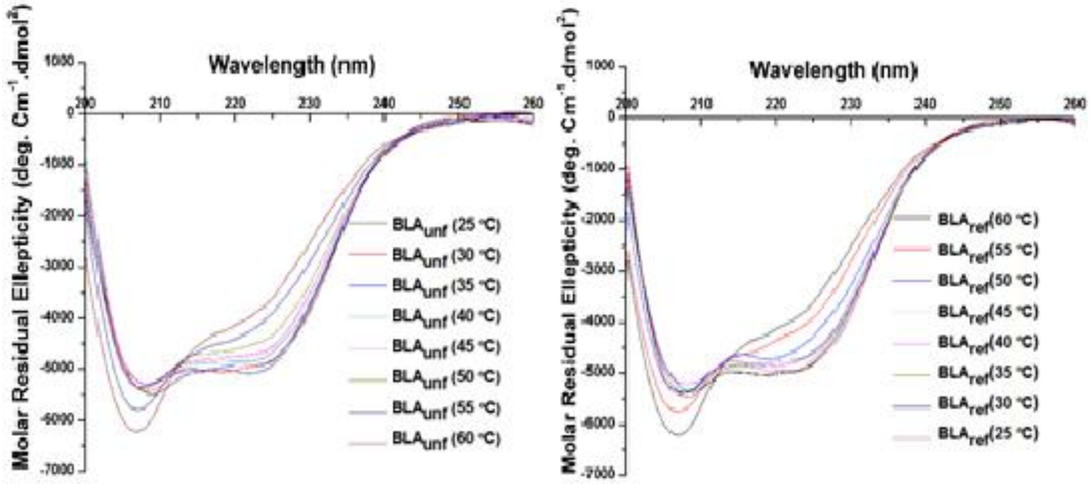

Figure S30 Circular dichroism spectroscopy analysis of BLA, when sample was incubated at differ temperature (25-60 ^{0}C). (A) Variation in spectra of BLA when temperature increased from 25-60 ^{0}C with increment of 5 ^{0}C indicated the secondary structural changes due increment of temperature. (B) Temperature dependent refolding of BLA when temperature decreased from 60-25 ^{0}C with decrement of 5 ^{0}C.

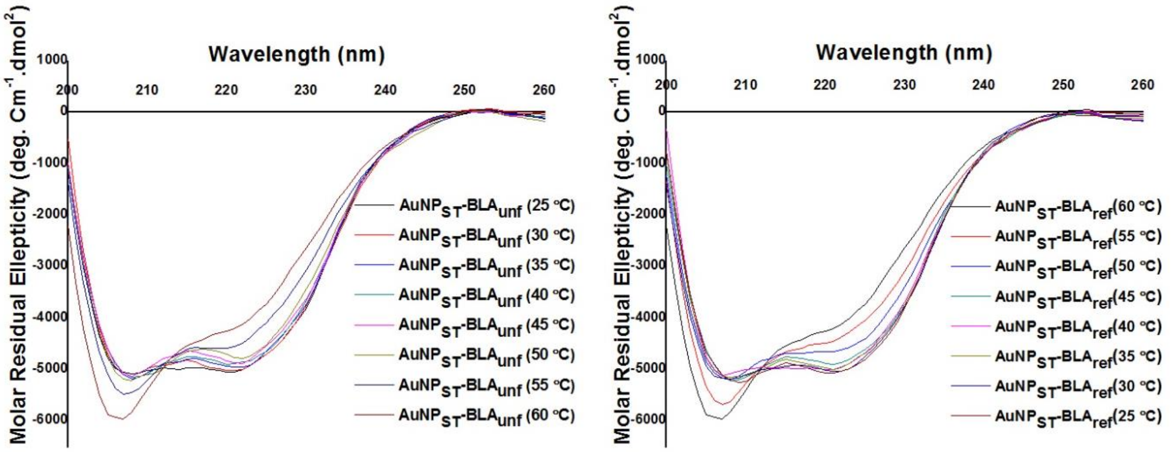

Figure S31 Circular dichroism spectroscopy analysis of AuNPST-BLA, when sample was incubated at differ temperature (25-60 ^{0}C). (A) variation in spectra of BLA when temperature increased from 25-60 ^{0}C with increment of 5 ^{0}C indicated the secondary structural changes due increment of temperature. (B) Temperature dependent refolding of BLA when temperature decreased from 60-25 ^{0}C with decrement of 5 ^{0}C.

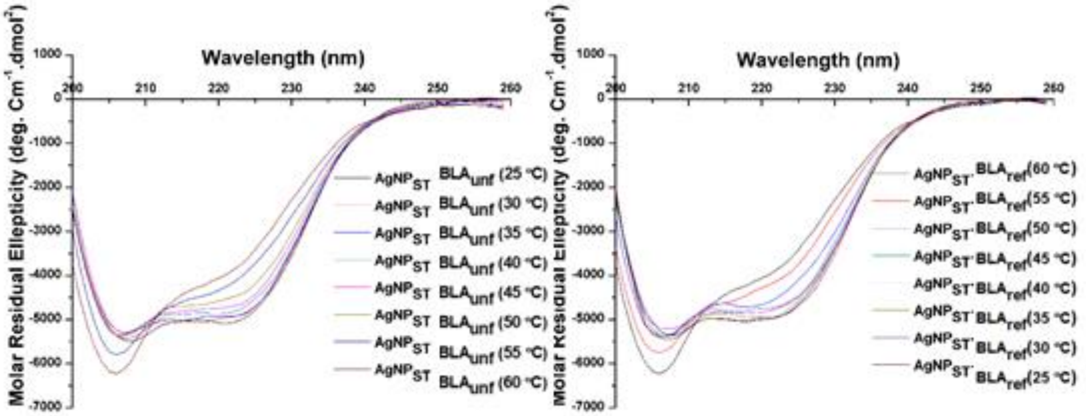

Figure S32 Circular dichroism spectroscopy analysis of AgNPST-BLA, when sample was incubated at differ temperature (25-60 ^{0}C). (A) variation in spectra of BLA when temperature increased from 25-60 ^{0}C with increment of 5 ^{0}C indicated the secondary structural changes due increment of temperature. (B) Temperature dependent refolding of BLA when temperature decreased from 60-25 ^{0}C with decrement of 5 ^{0}C.

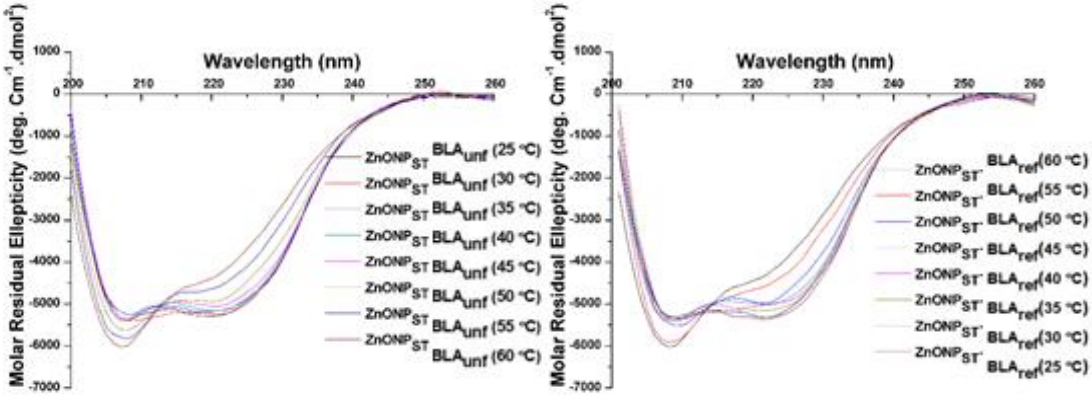

Figure S33 Circular dichroism spectroscopy analysis of ZnONPST-BLA, when sample was incubated at differ temperature (25-60 ^{0}C). (A) variation in spectra of BLA when temperature increased from 25-60 ^{0}C with increment of 5 ^{0}C indicated the secondary structural changes due increment of temperature. (B) Temperature dependent refolding of BLA when temperature decreased from 60-25 ^{0}C with decrement of 5 ^{0}C.

Fluorescence spectroscopy

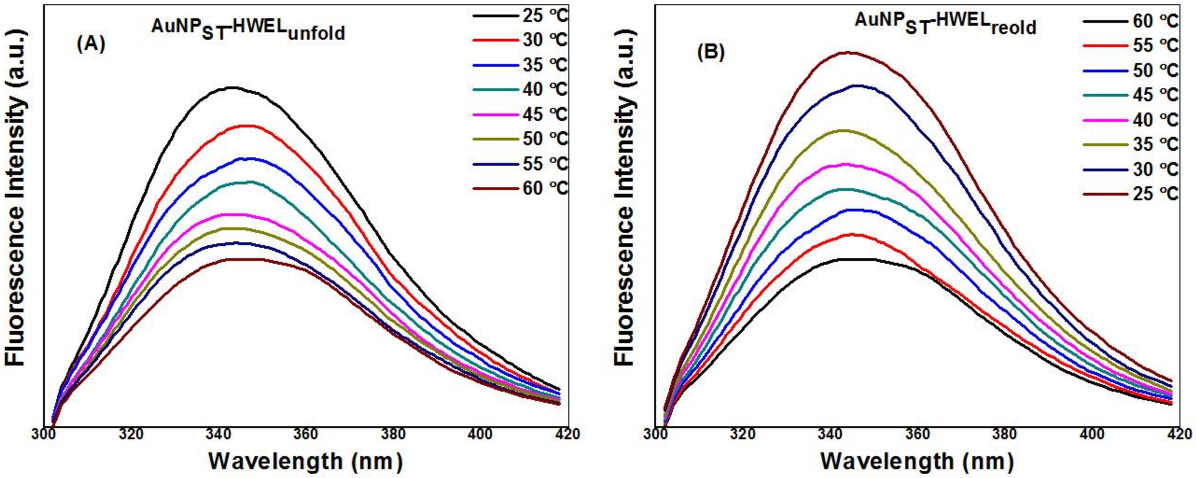

Figure S34 Fluorescence spectroscopy analysis of HEWL-AuNPST, when sample was incubated at differ temperature (25-60 ^{0}C). (A) Intrinsic fluorescence of HEWL when temperature increased from 25-60 ^{0}C with increment of 5 ^{0}C. (B) Intrinsic fluorescence of HEWL when temperature decreased from 60-25 ^{0}C with decrement of 5 ^{0}C.

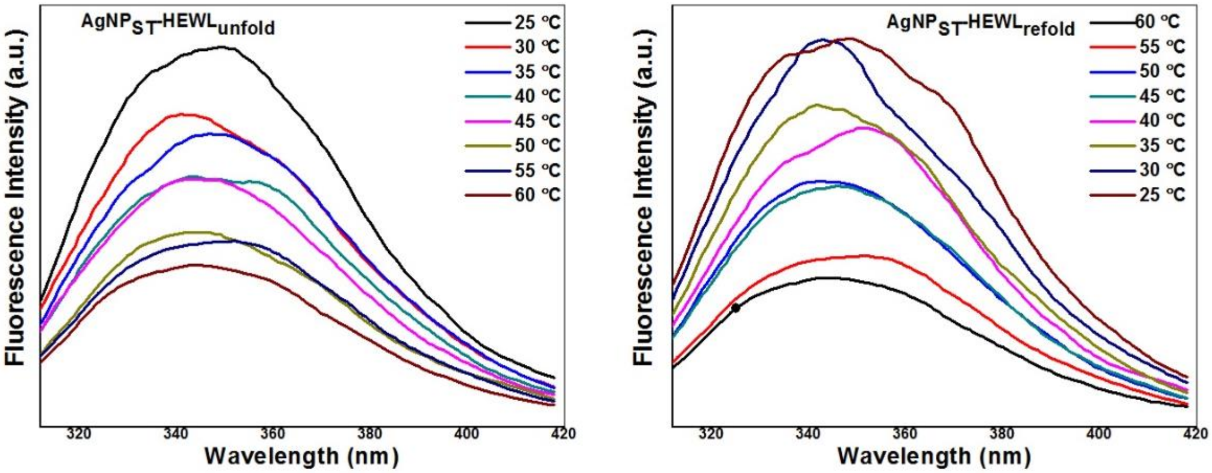

Figure S35 Fluorescence spectroscopy analysis of HEWL-AgNPST, when sample was incubated at differ temperature (25-60 ^{0}C). (A) Intrinsic fluorescence of HEWL when temperature increased from 25-60 ^{0}C with increment of 5 ^{0}C. (B) Intrinsic fluorescence of HEWL when temperature decreased from 60-25 ^{0}C with decrement of 5 ^{0}C.

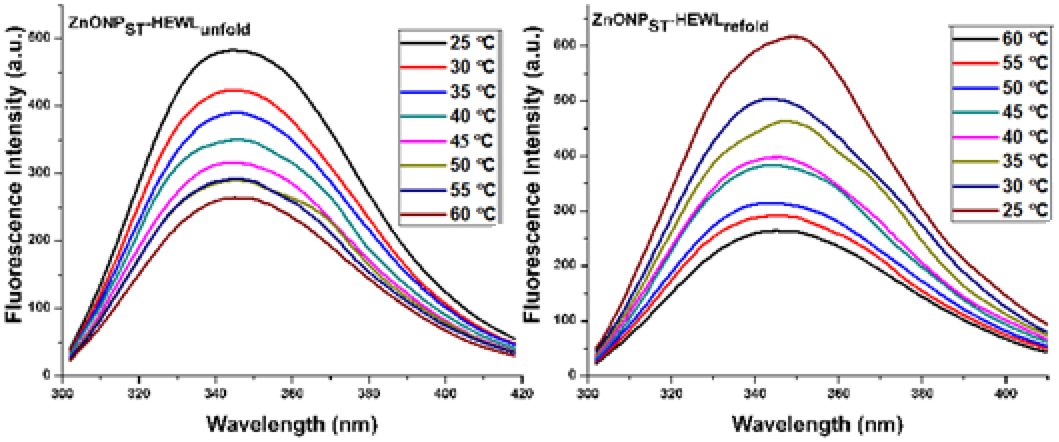

Figure S36 Fluorescence spectroscopy analysis of HEWL-ZnONPST, when sample was incubated at differ temperature (25-60 ^{0}C). (A) Intrinsic fluorescence of HEWL when temperature increased from 25-60 ^{0}C with increment of 5 ^{0}C. (B) Intrinsic fluorescence of HEWL when temperature decreased from 60-25 ^{0}C with decrement of 5 ^{0}C.

CD spectroscopy

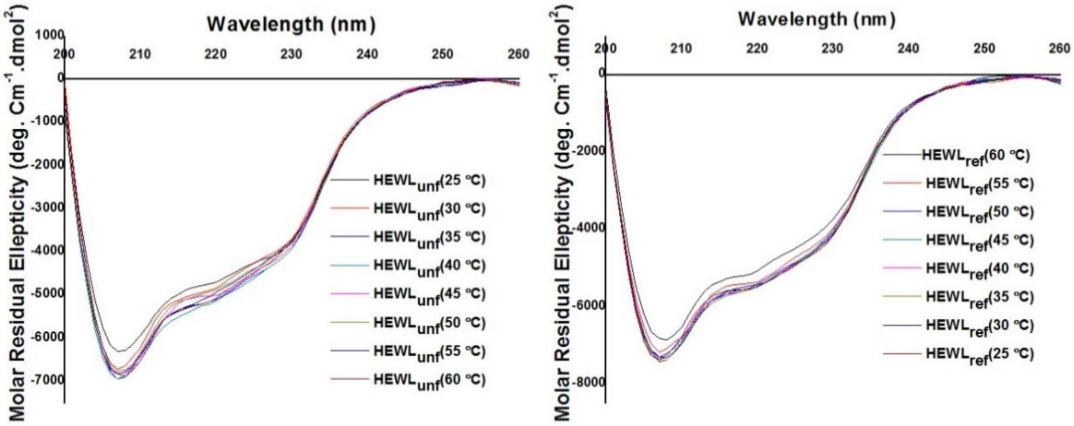

Figure S37 Circular dichroism spectroscopy analysis of HEWL, when sample was incubated at differ temperature (25-60 ^{0}C). (A) Variation in spectra of HEWL when temperature increased from 25-60 ^{0}C with increment of 5 ^{0}C indicated the secondary structural changes due increment of temperature. (B) Temperature dependent refolding of HEWL when temperature decreased from 60-25 ^{0}C with decrement of 5 ^{0}C.

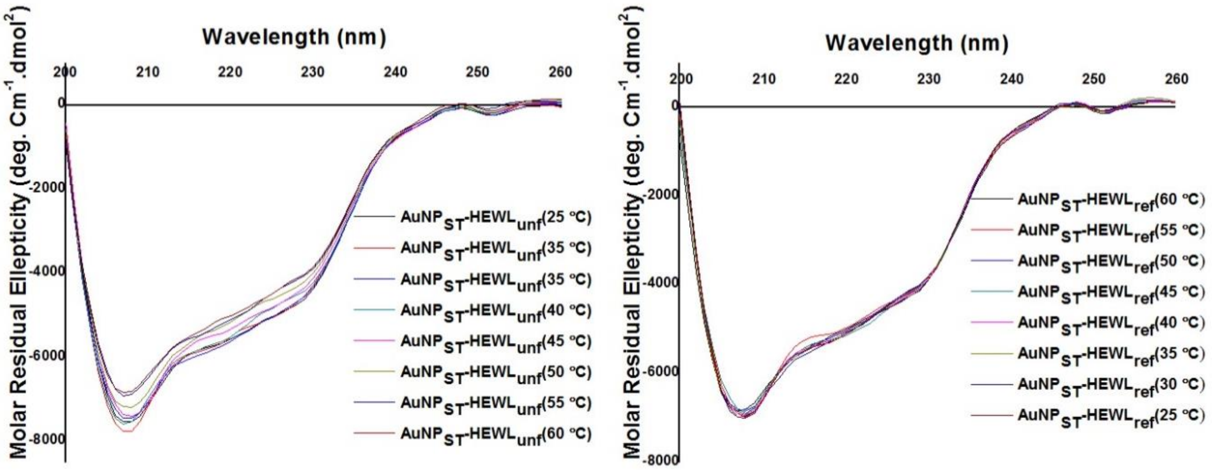

Figure S38 Circular dichroism spectroscopy analysis of HEWL with AuNPST, when sample was incubated at differ temperature (25-60 ^{0}C). (A) Variation in spectra of HEWL when temperature increased from 25-60 ^{0}C with increment of 5 ^{0}C indicated the secondary structural changes due increment of temperature. (B) Temperature dependent refolding of HEWL when temperature decreased from 60-25 ^{0}C with decrement of 5 ^{0}C.

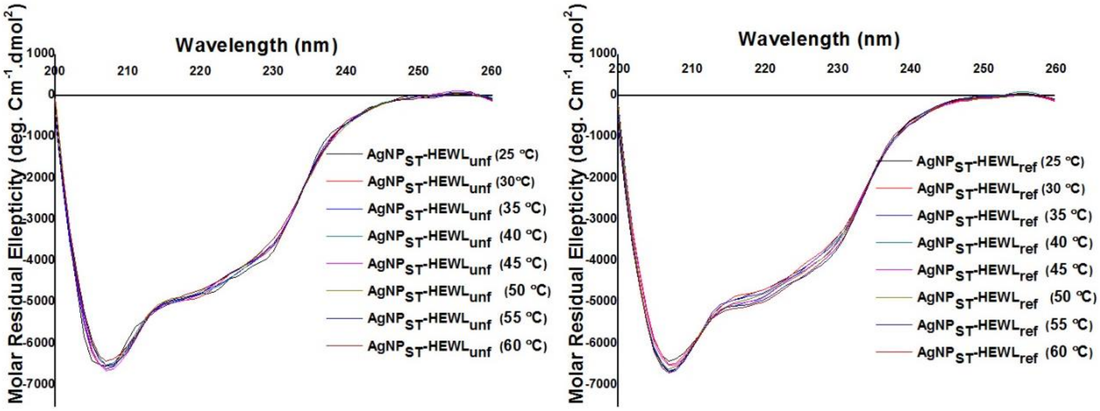

Figure S39 Circular dichroism spectroscopy analysis of HEWL with AgNPST, when sample was incubated at differ temperature (25-60 ^{0}C). (A) Variation in spectra of HEWL when temperature increased from 25-60 ^{0}C with increment of 5 ^{0}C indicated the secondary structural changes due increment of temperature. (B) Temperature dependent refolding of HEWL when temperature decreased from 60-25 ^{0}C with decrement of 5 ^{0}C.

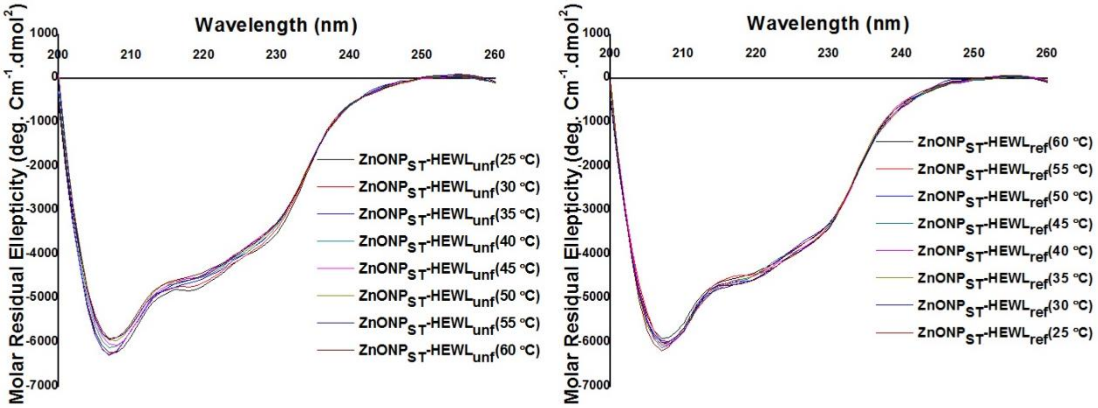

Figure S40 Circular dichroism spectroscopy analysis of HEWL with ZnONP$_{ST}$, when sample was incubated at differ temperature (25-60 ^{0}C). (A) Variation in spectra of HEWL when temperature increased from 25-60 ^{0}C with increment of 5 ^{0}C indicated the secondary structural changes due increment of temperature. (B) Temperature dependent refolding of HEWL when temperature decreased from 60-25 ^{o}C with decrement of 5 ^{o}C.

Proteinase-K digestion:

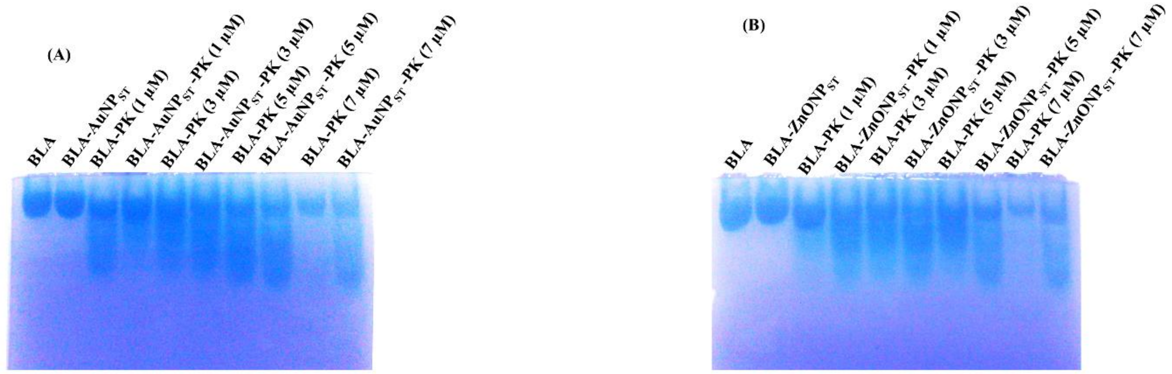

Figure S41 Proteinase-K digestion assay of various NP-BLA conjugates, 20 μl of all loading sample contains 20 μg of BLA. (A) AuNP$_{ST}$-BLA, (B) ZnONP$_{ST}$ –BLA.

Amyloid-nanoparticle interaction

Amyloid hydrodynamic size analysis:

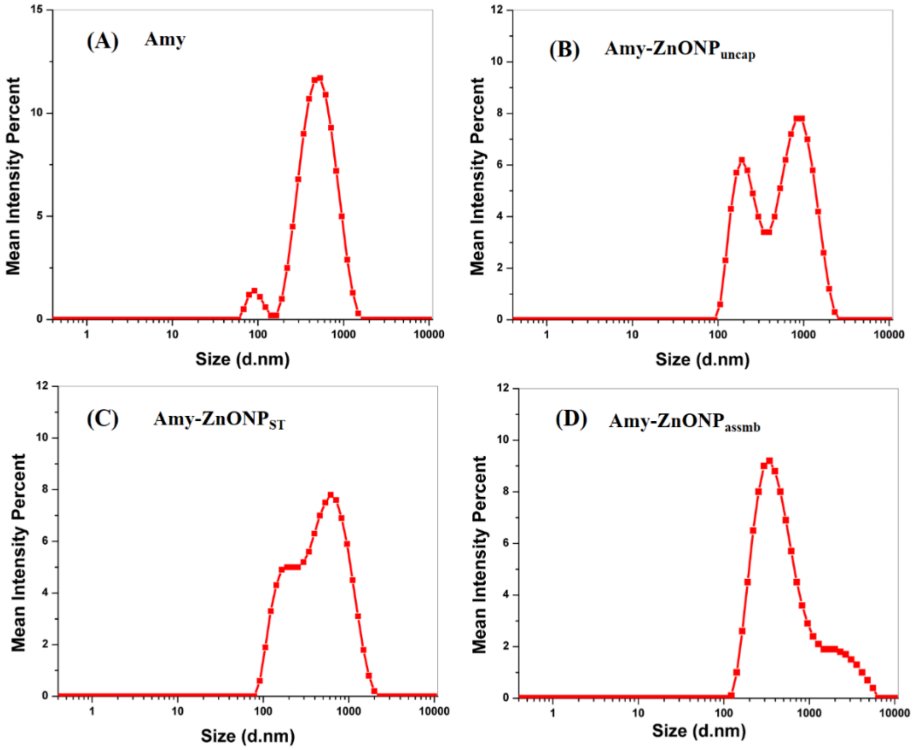

Figure S42 The DLS analysis of amyloid samples (Amy, Amy-ZnONP$_{uncap}$, Amy-ZnONP$_{ST}$, Amy-ZnONP$_{assemb}$) prepared in the presence of (A) none, (B) ZnONP$_{uncap}$, (C) ZnONP$_{ST}$, (D) ZnONP$_{assmb}$.

Far-UV circular dichroism (CD) spectral measurement of various amyloid samples:

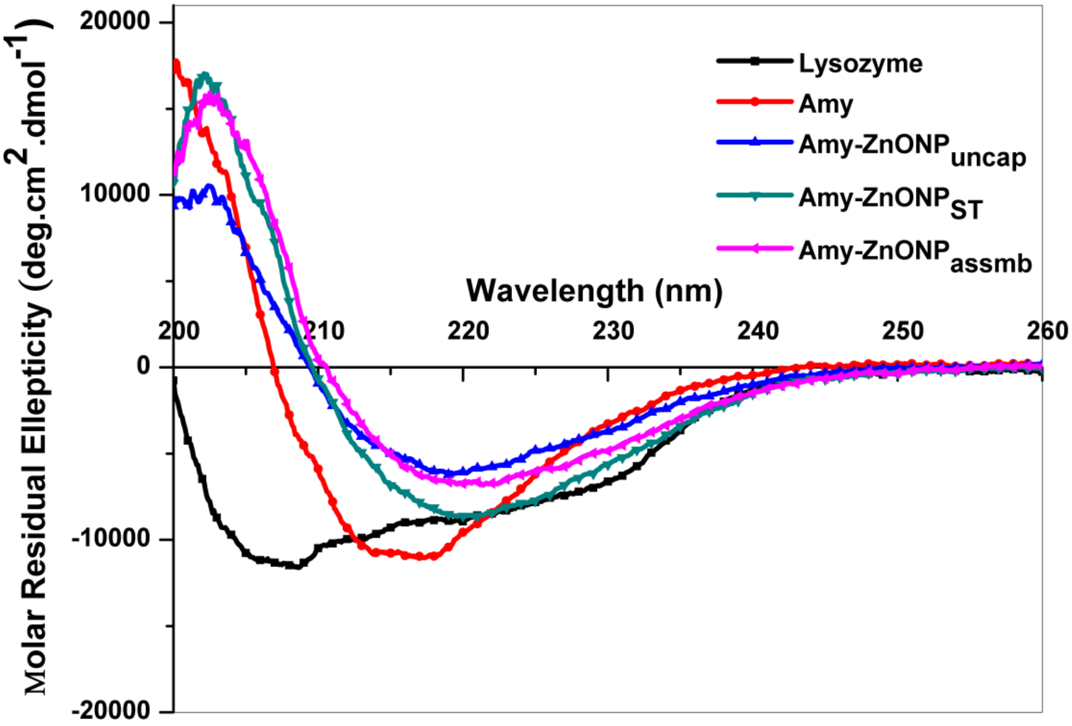

Figure S43. Circular dichroism spectroscopic analysis of different amyloid samples (Amy, Amy-ZnONP$_{uncap}$, Amy-ZnONP$_{ST}$, Amy-ZnONP$_{assmb}$) prepared with ZnONP (uncap, starch capped, and assembly). The amyloid synthesis protocol was given in 'Materials and methods' section.

Time dependent ThT fluorescence spectral measurement of various amyloid samples

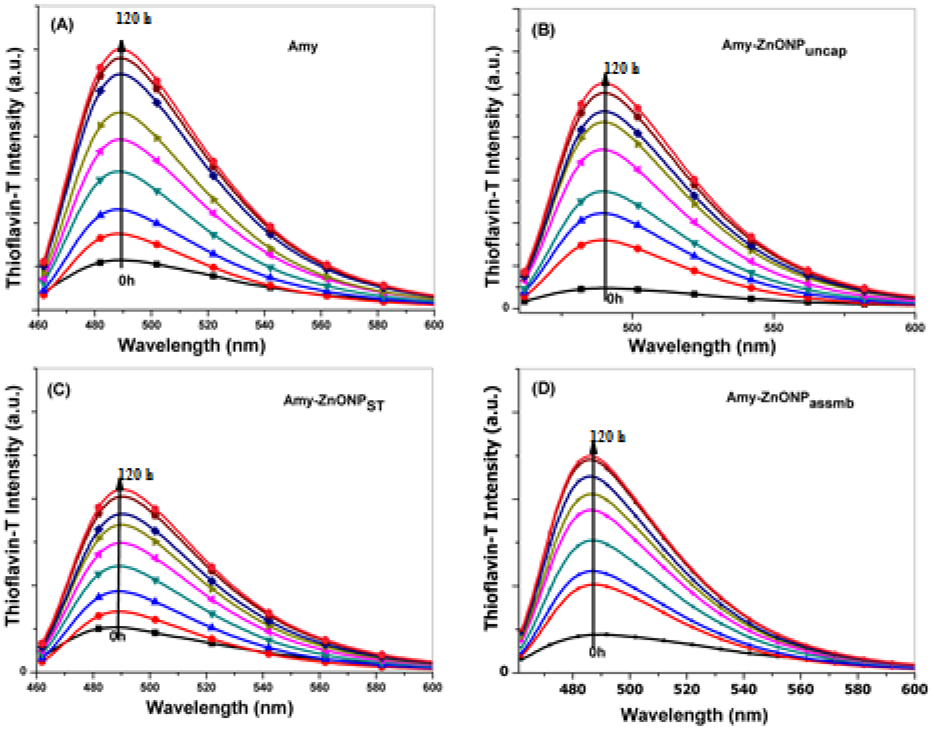

Figure S44 Thioflavin-T analysis of amyloid samples (Amy, Amy-ZnONP$_{uncap}$, Amy-ZnONP$_{ST}$, Amy-ZnONP$_{assmb}$) at every 12 h time interval and up to 120 h. (A) amyloid without NP (Amy), (B) Amy-ZnONP$_{uncap}$, (C) Amy-ZnONP$_{ST}$, (D) Amy-ZnONP$_{assmb}$.

Time dependent CD spectral measurement of various amyloid samples:

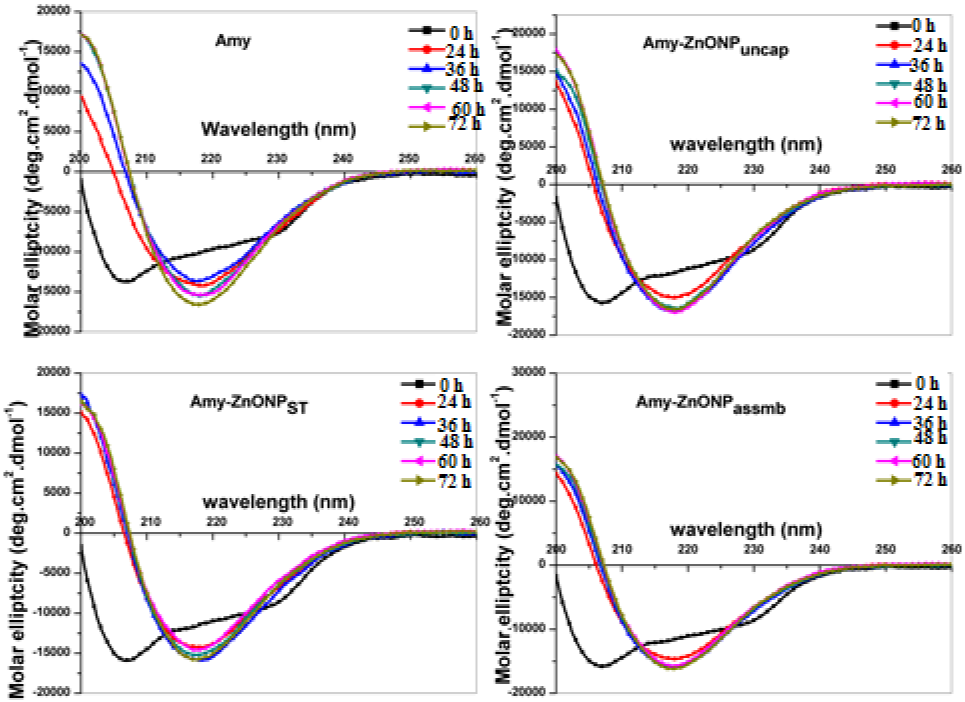

Figure S45 Circular dichroism spectral analysis of different amyloid samples (Amy, Amy-ZnONP$_{uncap}$, Amy-ZnONP$_{ST}$, Amy-ZnONP$_{assmb}$) with growth period of amyloid formation (h). (A) amyloid without NP (Amy), (B) Amy-ZnONP$_{uncap}$, (C) Amy-ZnONP$_{ST}$, (D) Amy-ZnONP$_{assmb}$.

Effect of administration time of ZnONP on amyloid formation monitored by zeta potential, ThT, and ANS fluorescence measurement:

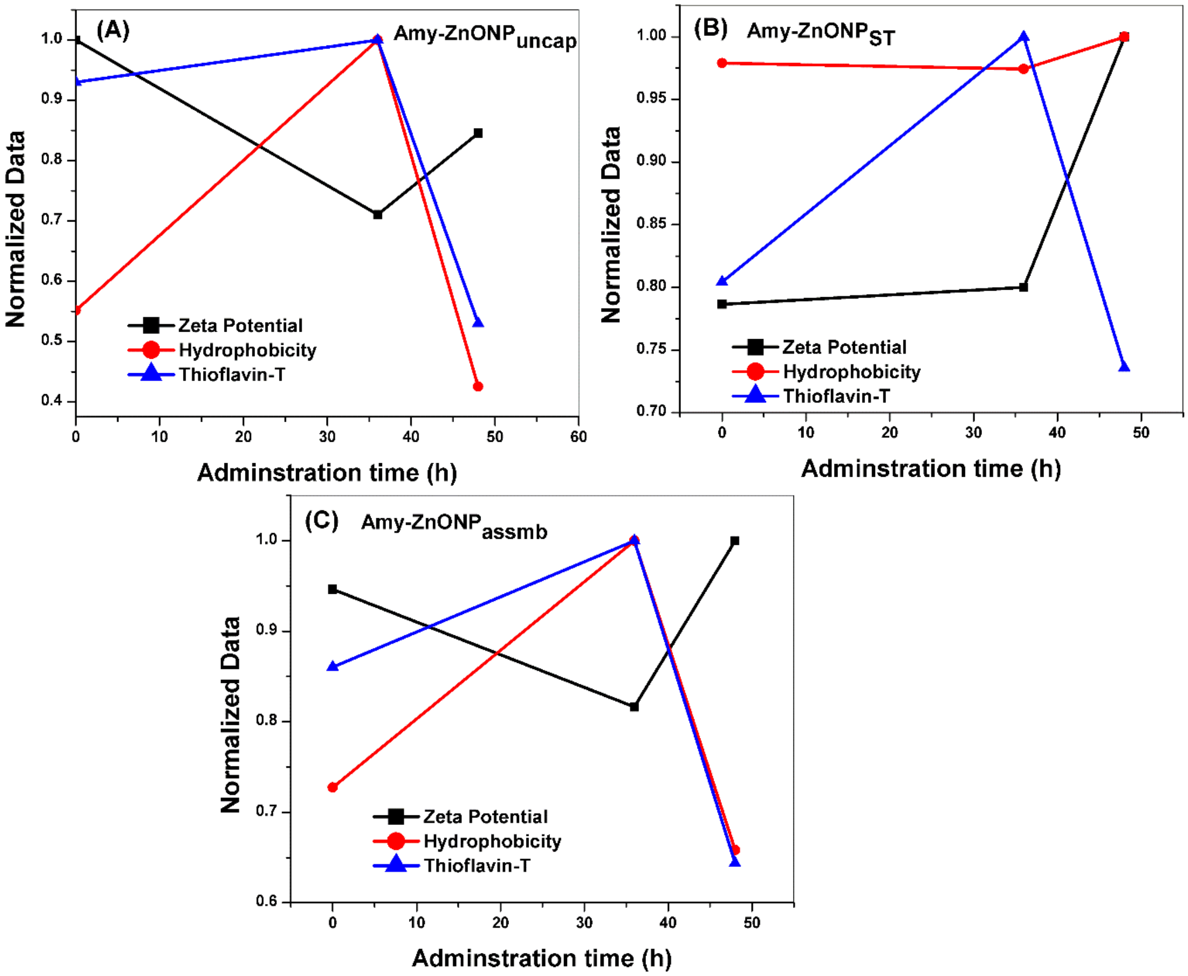

Figure S46 Measurement of zeta potential, hydrophobicity (measured at 350 nm) and Thioflavin-T fluorescence intensity (measured at 440 nm) of various amyloid samples (Amy-ZnONP$_{\text{uncap}}$, Amy-ZnONP$_{\text{ST}}$, Amy-ZnONP$_{\text{assmb}}$). ZnONP$_{\text{uncap}}$, ZnONP$_{\text{ST}}$ and ZnONP$_{\text{assmb}}$ of 10µM were administered during nucleation, elongation and maturation phase of amyloid growth. (A) Amy-ZnONP$_{\text{uncap}}$, (B) Amy-ZnONP$_{\text{ST}}$, (C) Amy-ZnONP$_{\text{assmb}}$.

Effect of administration time of ZnONP on amyloid formation monitored by FESEM imaging

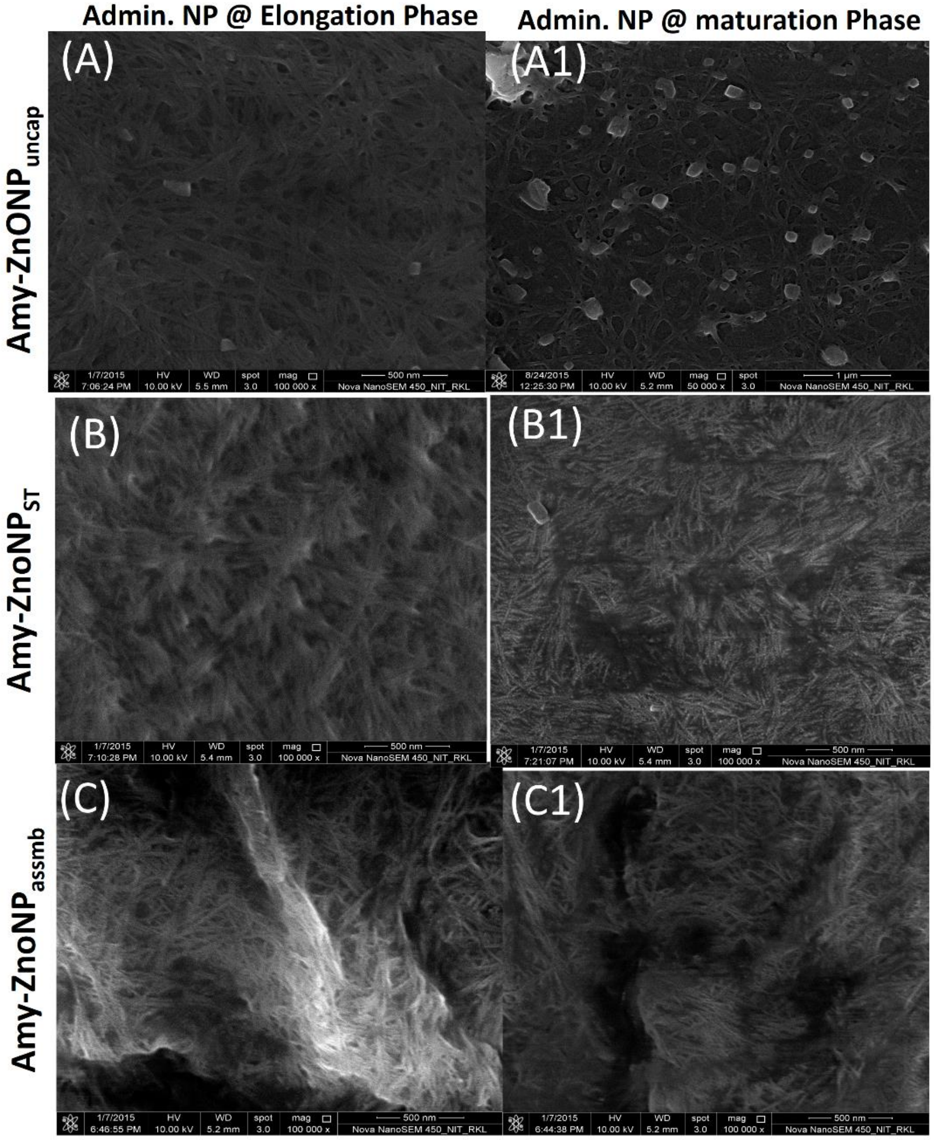

Figure S47 FESEM analysis of various amyloid samples and morphological changes due to variation in administration time (nucleation, elongation, and maturation phase); administration of (A) ZnONP$_{uncap}$, (B) ZnONP$_{ST}$ and (C) ZnONP$_{assmb}$ during elongation phase (36 h); Administration of (A1) ZnONP$_{uncap}$ (B1) ZnONP$_{ST}$ and (C1) ZnONP$_{assmb}$ during maturation phase (48 h).

REFERENCES

[1] J.F. Hainfeld, H.M. Smilowitz, M.J. O'Connor, F.A. Dilmanian, D.N. Slatkin, Nanomedicine, 8 (2012) 1601-1609.

[2] S. Lee, E.-J. Cha, K. Park, S.-Y. Lee, J.-K. Hong, I.-C. Sun, S.Y. Kim, K. Choi, I.C. Kwon, K. Kim, C.-H. Ahn, Angewandte Chemie, 120 (2008) 2846-2849.

[3] M.S. Amanda, K.B.-S. Laura, J.S. John, D. Liming, M.H. Saber, Nanotechnology, 19 (2008) 235104.

[4] K.-S. Lee, M.A. El-Sayed, The Journal of Physical Chemistry B, 110 (2006) 19220-19225.

[5] P.K. Jain, K.S. Lee, I.H. El-Sayed, M.A. El-Sayed, The Journal of Physical Chemistry B, 110 (2006) 7238-7248.

[6] N. Nath, A. Chilkoti, Analytical Chemistry, 74 (2002) 504-509.

[7] A.D. McFarland, R.P. Van Duyne, Nano Letters, 3 (2003) 1057-1062.

[8] K.J. Loh, D. Chang, Journal of Materials Science, 46 (2011) 228-237.

[9] B.P.J. de Lacy Costello, R.J. Ewen, N.M. Ratcliffe, M. Richards, Sensors and Actuators B: Chemical, 134 (2008) 945-952.

[10] Y. Kim, R.C. Johnson, J.T. Hupp, Nano Letters, 1 (2001) 165-167.

[11] Y. Cheng, A. C. Samia, J.D. Meyers, I. Panagopoulos, B. Fei, C. Burda, Journal of the American Chemical Society, 130 (2008) 10643-10647.

[12] G.F. Paciotti, L. Myer, D. Weinreich, D. Goia, N. Pavel, R.E. McLaughlin, L. Tamarkin, Drug Delivery, 11 (2004) 169-183.

[13] P. Ghosh, G. Han, M. De, C.K. Kim, V.M. Rotello, Advanced Drug Delivery Reviews, 60 (2008) 1307-1315.

[14] S.D. Brown, P. Nativo, J.-A. Smith, D. Stirling, P.R. Edwards, B. Venugopal, D.J. Flint, J.A. Plumb, D. Graham, N.J. Wheate, Journal of the American Chemical Society, 132 (2010) 4678-4684.

[15] A.G. Tkachenko, H. Xie, D. Coleman, W. Glomm, J. Ryan, M.F. Anderson, S. Franzen, D.L. Feldheim, Journal of the American Chemical Society, 125 (2003) 4700-4701.

[16] M. Jose Ruben, E. Jose Luis, C. Alejandra, H. Katherine, B.K. Juan, R. Jose Tapia, Y. Miguel Jose, Nanotechnology, 16 (2005) 2346.

[17] J. Fabrega, S.R. Fawcett, J.C. Renshaw, J.R. Lead, Environmental Science & Technology, 43 (2009) 7285-7290.

[18] J.W. Rasmussen, E. Martinez, P. Louka, D.G. Wingett, Expert Opin Drug Deliv, 7 (2010) 1063-1077.

[19] K.R. Raghupathi, R.T. Koodali, A.C. Manna, Langmuir, 27 (2011) 4020-4028.

[20] E. Casals, T. Pfaller, A. Duschl, G.J. Oostingh, V. Puntes, ACS Nano, 4 (2010) 3623-3632.

[21] S. Milani, F. Baldelli Bombelli, A.S. Pitek, K.A. Dawson, J. Rädler, ACS Nano, 6 (2012) 2532-2541.

[22] M.P. Monopoli, D. Walczyk, A. Campbell, G. Elia, I. Lynch, F. Baldelli Bombelli, K.A. Dawson, Journal of the American Chemical Society, 133 (2011) 2525-2534.

[23] J.S. Gebauer, M. Malissek, S. Simon, S.K. Knauer, M. Maskos, R.H. Stauber, W. Peukert, L. Treuel, Langmuir, 28 (2012) 9673-9679.

[24] M.E. Aubin-Tam, K. Hamad-Schifferli, Biomedical Materials, 3 (2008) 034001.

[25] S. Harper, C. Usenko, J.E. Hutchison, B.L.S. Maddux, R.L. Tanguay, Journal of Experimental Nanoscience, 3 (2008) 195-206.

[26] A.A. Vertegel, R.W. Siegel, J.S. Dordick, Langmuir, 20 (2004) 6800-6807.

[27] M.A. Dobrovolskaia, A.K. Patri, J. Zheng, J.D. Clogston, N. Ayub, P. Aggarwal, B.W. Neun, J.B. Hall, S.E. McNeil, Nanomedicine: Nanotechnology, Biology and Medicine, 5 (2009) 106-117.

[28] J.E. Gagner, M.D. Lopez, J.S. Dordick, R.W. Siegel, Biomaterials, 32 (2011) 7241-7252.

[29] R. Hong, N.O. Fischer, A. Verma, C.M. Goodman, T. Emrick, V.M. Rotello, Journal of the American Chemical Society, 126 (2004) 739-743.

[30] M.-E. Aubin-Tam, K. Hamad-Schifferli, Langmuir, 21 (2005) 12080-12084.

[31] P.P. Fu, Q. Xia, H.-M. Hwang, P.C. Ray, H. Yu, Journal of Food and Drug Analysis, 22 (2014) 64-75.

[32] J. Liu, D.A. Sonshine, S. Shervani, R.H. Hurt, ACS Nano, 4 (2010) 6903-6913.

[33] M.P. Monopoli, C. Aberg, A. Salvati, K.A. Dawson, Nat Nano, 7 (2012) 779-786.

[34] D.J. Selkoe, Nat Cell Biol, 6 (2004) 1054-1061.

[35] W. Dauer, S. Przedborski, Neuron, 39 (2003) 889-909.

[36] A.L. Horwich, J.S. Weissman, Cell, 89 (1997) 499-510.

[37] S. Linse, C. Cabaleiro-Lago, W.-F. Xue, I. Lynch, S. Lindman, E. Thulin, S.E. Radford, K.A. Dawson, Proceedings of the National Academy of Sciences, 104 (2007) 8691-8696.

[38] W.-h. Wu, X. Sun, Y.-p. Yu, J. Hu, L. Zhao, Q. Liu, Y.-f. Zhao, Y.-m. Li, Biochemical and Biophysical Research Communications, 373 (2008) 315-318.

[39] S. Hsieh, C.-w. Chang, H.-h. Chou, Colloids and Surfaces B: Biointerfaces, 112 (2013) 525-529.

[40] S. Palmal, N.R. Jana, N.R. Jana, The Journal of Physical Chemistry C, 118 (2014) 21630-21638.

[41] L. Xiao, D. Zhao, W.-H. Chan, M.M.F. Choi, H.-W. Li, Biomaterials, 31 (2010) 91-98.

[42] B. Andrea, B. Eva, K. Martina, K. Peter, V. Francesco, T. Natalia, T. Milan, B. Jaroslava, B. Fabio, G. Zuzana, Nanotechnology, 21 (2010) 065103.

[43] M.J. Osmond-McLeod, R.I.W. Osmond, Y. Oytam, M.J. McCall, B. Feltis, A. Mackay-Sim, S.A. Wood, A.L. Cook, Particle and Fibre Toxicology, 10 (2013) 54-54.

[44] K.L. Kelly, E. Coronado, L.L. Zhao, G.C. Schatz, The Journal of Physical Chemistry B, 107 (2003) 668-677.

[45] A.M. Zaniewski, M. Schriver, J. Gloria Lee, M.F. Crommie, A. Zettl, Applied Physics Letters, 102 (2013) 023108.

[46] S. Cuenot, C. Frétigny, S. Demoustier-Champagne, B. Nysten, Physical Review B, 69 (2004) 165410.

[47] S.M. Dizaj, F. Lotfipour, M. Barzegar-Jalali, M.H. Zarrintan, K. Adibkia, Materials Science and Engineering: C, 44 (2014) 278-284.

[48] A. Nel, T. Xia, L. Mädler, N. Li, Science, 311 (2006) 622-627.

[49] Y. Kong, J. Li, S. Wu, W. Cheng, R.K. Rana, J.-J. Zhu, Sensors and Actuators B: Chemical, 183 (2013) 187-193.

[50] N.R. Jana, L. Gearheart, C.J. Murphy, The Journal of Physical Chemistry B, 105 (2001) 4065-4067.

[51] T.K. Sau, C.J. Murphy, Journal of the American Chemical Society, 126 (2004) 8648-8649.

[52] J. Kimling, M. Maier, B. Okenve, V. Kotaidis, H. Ballot, A. Plech, The Journal of Physical Chemistry B, 110 (2006) 15700-15707.

[53] P. Elia, R. Zach, S. Hazan, S. Kolusheva, Z.e. Porat, Y. Zeiri, International Journal of Nanomedicine, 9 (2014) 4007-4021.

[54] H. Huang, X. Yang, Carbohydrate Research, 339 (2004) 2627-2631.

[55] S.A. Khan, A. Ahmad, RSC Advances, 4 (2014) 7729-7734.

[56] A.K. Nowinski, A.D. White, A.J. Keefe, S. Jiang, Langmuir, 30 (2014) 1864-1870.

[57] T. Serizawa, Y. Hirai, M. Aizawa, Langmuir, 25 (2009) 12229-12234.

[58] K.K. Katti, V. Kattumuri, S. Bhaskaran, K.V. Katti, R. Kannan, International Journal of Green Nanotechnology: Biomedicine, 1 (2009) B53-B59.

[59] R. Genç, G. Clergeaud, M. Ortiz, C.K. O'Sullivan, Langmuir, 27 (2011) 10894-10900.

[60] A. Fernández-Lodeiro, J. Fernández-Lodeiro, C. Núñez, R. Bastida, J.L. Capelo, C. Lodeiro, ChemistryOpen, 2 (2013) 200-207.

[61] R. Cui, C. Liu, J. Shen, D. Gao, J.-J. Zhu, H.-Y. Chen, Advanced Functional Materials, 18 (2008) 2197-2204.

[62] S. Phadtare, A. Kumar, V.P. Vinod, C. Dash, D.V. Palaskar, M. Rao, P.G. Shukla, S. Sivaram, M. Sastry, Chemistry of Materials, 15 (2003) 1944-1949.

[63] X. Liu, Q. Dai, L. Austin, J. Coutts, G. Knowles, J. Zou, H. Chen, Q. Huo, Journal of the American Chemical Society, 130 (2008) 2780-2782.

[64] D. Kim, Y.Y. Jeong, S. Jon, ACS Nano, 4 (2010) 3689-3696.

[65] L.C. Kennedy, L.R. Bickford, N.A. Lewinski, A.J. Coughlin, Y. Hu, E.S. Day, J.L. West, R.A. Drezek, Small, 7 (2011) 169-183.

[66] K. Lee, V.P. Drachev, J. Irudayaraj, ACS Nano, 5 (2011) 2109-2117.

[67] O. Yehezkeli, R. Tel-Vered, S. Raichlin, I. Willner, ACS Nano, 5 (2011) 2385-2391.

[68] S. Guerrero, J.R. Herance, S. Rojas, J.F. Mena, J.D. Gispert, G.A. Acosta, F. Albericio, M.J. Kogan, Bioconjugate Chemistry, 23 (2012) 399-408.

[69] Y. Yang, C. Li, L. Yin, M. Liu, Z. Wang, Y. Shu, G. Li, ACS Applied Materials & Interfaces, 6 (2014) 7579-7584.

[70] J.P.M. Almeida, A.Y. Lin, E.R. Figueroa, A.E. Foster, R.A. Drezek, Small, 11 (2015) 1453-1459.

[71] N. Sinha, G. Cifter, E. Sajo, R. Kumar, S. Sridhar, P.L. Nguyen, R.A. Cormack, G.M. Makrigiorgos, W. Ngwa, International Journal of Radiation Oncology*Biology*Physics, 91 (2015) 385-392.

[72] M.K. Rai, S.D. Deshmukh, A.P. Ingle, A.K. Gade, Journal of Applied Microbiology, 112 (2012) 841-852.

[73] M. Rai, A. Yadav, A. Gade, Biotechnology Advances, 27 (2009) 76-83.

[74] A.A. Chaudhari, S.L. Jasper, E. Dosunmu, M.E. Miller, R.D. Arnold, S.R. Singh, S. Pillai, Journal of Nanobiotechnology, 13 (2015) 1-17.

[75] L.J. Sherry, S.-H. Chang, G.C. Schatz, R.P. Van Duyne, B.J. Wiley, Y. Xia, Nano Letters, 5 (2005) 2034-2038.

[76] A.J. Haes, R.P. Van Duyne, Journal of the American Chemical Society, 124 (2002) 10596-10604.

[77] F. Furno, K.S. Morley, B. Wong, B.L. Sharp, P.L. Arnold, S.M. Howdle, R. Bayston, P.D. Brown, P.D. Winship, H.J. Reid, Journal of Antimicrobial Chemotherapy, 54 (2004) 1019-1024.

[78] K. Chaloupka, Y. Malam, A.M. Seifalian, Trends in Biotechnology, 28 (2010) 580-588.

[79] P. Gopinath, S.K. Gogoi, P. Sanpui, A. Paul, A. Chattopadhyay, S.S. Ghosh, Colloids and Surfaces B: Biointerfaces, 77 (2010) 240-245.

[80] Y. Hayashi, T. Miclaus, P. Engelmann, H. Autrup, D.S. Sutherland, J.J. Scott-Fordsmand, Nanotoxicology, 10 (2016) 303-311.

[81] R. Kessler, Environmental Health Perspectives, 119 (2011) A120-A125.

[82] N.S. Tulve, A.B. Stefaniak, M.E. Vance, K. Rogers, S. Mwilu, R.F. LeBouf, D. Schwegler-Berry, R. Willis, T.A. Thomas, L.C. Marr, International Journal of Hygiene and Environmental Health, 218 (2015) 345-357.

[83] E. Fröhlich, E. Roblegg, Toxicology, 291 (2012) 10-17.

[84] S. Prabhu, E.K. Poulose, International Nano Letters, 2 (2012) 1-10.

[85] J.S. Kim, E. Kuk, K.N. Yu, J.-H. Kim, S.J. Park, H.J. Lee, S.H. Kim, Y.K. Park, Y.H. Park, C.-Y. Hwang, Y.-K. Kim, Y.-S. Lee, D.H. Jeong, M.-H. Cho, Nanomedicine: Nanotechnology, Biology and Medicine, 3 (2007) 95-101.

[86] I. Sondi, B. Salopek-Sondi, Journal of Colloid and Interface Science, 275 (2004) 177-182.

[87] A. Travan, C. Pelillo, I. Donati, E. Marsich, M. Benincasa, T. Scarpa, S. Semeraro, G. Turco, R. Gennaro, S. Paoletti, Biomacromolecules, 10 (2009) 1429-1435.

[88] S. Pal, Y.K. Tak, J.M. Song, Applied and Environmental Microbiology, 73 (2007) 1712-1720.

[89] Y.K. Tak, S. Pal, P.K. Naoghare, S. Rangasamy, J.M. Song, Scientific Reports, 5 (2015) 16908.

[90] M.D. Malinsky, K.L. Kelly, G.C. Schatz, R.P. Van Duyne, Journal of the American Chemical Society, 123 (2001) 1471-1482.

[91] A.M. El Badawy, R.G. Silva, B. Morris, K.G. Scheckel, M.T. Suidan, T.M. Tolaymat, Environmental Science & Technology, 45 (2011) 283-287.

[92] E. Alarcon, M. Griffith, K.I. Udekwu, Silver Nanoparticle Applications: In the Fabrication and Design of Medical and Biosensing Devices, Springer, 2015.

[93] S.P. Tai, Y. Wu, D.B. Shieh, L.J. Chen, K.J. Lin, C.H. Yu, S.W. Chu, C.H. Chang, X.Y. Shi, Y.C. Wen, K.H. Lin, T.M. Liu, C.K. Sun, Advanced Materials, 19 (2007) 4520-4523.

[94] P. Jain, T. Pradeep, Biotechnology and Bioengineering, 90 (2005) 59-63.

[95] Y. Lv, H. Liu, Z. Wang, S. Liu, L. Hao, Y. Sang, D. Liu, J. Wang, R.I. Boughton, Journal of Membrane Science, 331 (2009) 50-56.

[96] X.-F. Sun, J. Qin, P.-F. Xia, B.-B. Guo, C.-M. Yang, C. Song, S.-G. Wang, Chemical Engineering Journal, 281 (2015) 53-59.

[97] S.A. Ansari, Q. Husain, S. Qayyum, A. Azam, Food and Chemical Toxicology, 49 (2011) 2107-2115.

[98] K.M. Reddy, K. Feris, J. Bell, D.G. Wingett, C. Hanley, A. Punnoose, Applied Physics Letters, 90 (2007) 213902.

[99] V. Nadanathangam, K. Sampath, A.A. Kathe, P.V. Varadarajan, P. Virendra, Nanotechnology, 17 (2006) 5087.

[100] X. Huang, S. Lee, X. Chen, Am J Nucl Med Mol Imaging, 1 (2011) 3-17.

[101] Q. Yuan, S. Hein, R.D. Misra, Acta Biomater, 6 (2010) 2732-2739.

[102] L. Nie, L. Gao, P. Feng, J. Zhang, X. Fu, Y. Liu, X. Yan, T. Wang, Small, 2 (2006) 621-625.

[103] Z. Zhao, W. Lei, X. Zhang, B. Wang, H. Jiang, Sensors, 10 (2010) 1216-1231.

[104] H. Zhang, B. Chen, H. Jiang, C. Wang, H. Wang, X. Wang, Biomaterials, 32 (2011) 1906-1914.

[105] A. Schöppe, H.J. Hinz, V.R. Agashe, S. Ramachandran, J.B. Udgaonkar, Protein Science : A Publication of the Protein Society, 6 (1997) 2196-2202.

[106] R. Morales, C. Duran-Aniotz, R. Diaz-Espinoza, M.V. Camacho, C. Soto, Nat. Protocols, 7 (2012) 1397-1409.

[107] F. Chiti, C.M. Dobson, Annual Review of Biochemistry, 75 (2006) 333-366.

[108] R. Nelson, M.R. Sawaya, M. Balbirnie, A.O. Madsen, C. Riekel, R. Grothe, D. Eisenberg, Nature, 435 (2005) 773-778.

[109] J.-C. Rochet, P.T. Lansbury Jr, Current Opinion in Structural Biology, 10 (2000) 60-68.

[110] M. Sunde, L.C. Serpell, M. Bartlam, P.E. Fraser, M.B. Pepys, C.C.F. Blake, Journal of Molecular Biology, 273 (1997) 729-739.

[111] C. Duran-Aniotz, R. Morales, I. Moreno-Gonzalez, P.P. Hu, C. Soto, Acta Neuropathologica Communications, 1 (2013) 1-11.

[112] D.A. Dolgikh, L.V. Abaturov, I.A. Bolotina, E.V. Brazhnikov, V.E. Bychkova, R.I. Gilmanshin, Y.O. Lebedev, G.V. Semisotnov, E.I. Tiktopulo, O.B. Ptitsyn, European Biophysics Journal, 13 (1985) 109-121.

[113] D.A. Dolgikh, R.I. Gilmanshin, E.V. Brazhnikov, V.E. Bychkova, G.V. Semisotnov, S.Y. Venyaminov, O.B. Ptitsyn, FEBS Letters, 136 (1981) 311-315.

[114] O.B. Ptitsyn, Journal of Biosciences, 8 (1985) 1-13.

[115] S.D. Durbin, G. Feher, Journal of Crystal Growth, 76 (1986) 583-592.

[116] C.C. McDonald, W.D. Phillips, J.D. Glickson, Journal of the American Chemical Society, 93 (1971) 235-246.

[117] M.F. Mossuto, A. Dhulesia, G. Devlin, E. Frare, J.R. Kumita, P.P. de Laureto, M. Dumoulin, A. Fontana, C.M. Dobson, X. Salvatella, Journal of Molecular Biology, 402 (2010) 783-796.

[118] S.S.-S. Wang, K.-N. Liu, B.-W. Wang, European Biophysics Journal, 39 (2010) 1229-1242.

[119] S. Mahanta, S. Paul, Colloids and Surfaces B: Biointerfaces, 134 (2015) 178-187.

[120] S. Mahanta, S. Paul, A. Srivastava, A. Pastor, B. Kundu, T.K. Chaudhuri, Colloids and Surfaces B: Biointerfaces, 130 (2015) 237-245.

[121] T. Kamijima, A. Ohmura, T. Sato, K. Akimoto, M. Itabashi, M. Mizuguchi, M. Kamiya, T. Kikukawa, T. Aizawa, M. Takahashi, K. Kawano, M. Demura, Biochemical and Biophysical Research Communications, 376 (2008) 211-214.

[122] C. Svanborg, H. Ågerstam, A. Aronson, R. Bjerkvig, C. Düringer, W. Fischer, L. Gustafsson, O. Hallgren, I. Leijonhuvud, S. Linse, A.-K. Mossberg, H. Nilsson, J. Pettersson, M. Svensson, HAMLET kills tumor cells by an apoptosis-like mechanism—cellular, molecular, and therapeutic aspects, in: Advances in Cancer Research, Academic Press, 2003, pp. 1-29.

[123] T. Nakamura, T. Aizawa, R. Kariya, S. Okada, M. Demura, K. Kawano, K. Makabe, K. Kuwajima, Journal of Biological Chemistry, 288 (2013) 14408-14416.

[124] G.L. Prasad, Biomedical Applications of Nanoparticles, in: J.T. Webster (Ed.) Safety of Nanoparticles: From Manufacturing to Medical Applications, Springer New York, New York, NY, 2009, pp. 89-109.

[125] F.E. Kruis, H. Fissan, A. Peled, Journal of Aerosol Science, 29 (1998) 511-535.

[126] M.C. Saha, M.E. Kabir, S. Jeelani, Materials Science and Engineering: A, 479 (2008) 213-222.

[127] P. Sharma, S. Brown, G. Walter, S. Santra, B. Moudgil, Advances in Colloid and Interface Science, 123–126 (2006) 471-485.

[128] X. Luo, A. Morrin, A.J. Killard, M.R. Smyth, Electroanalysis, 18 (2006) 319-326.

[129] M.L. Hans, A.M. Lowman, Current Opinion in Solid State and Materials Science, 6 (2002) 319-327.

[130] K. Cho, X. Wang, S. Nie, Z. Chen, D.M. Shin, American Association for Cancer Research, 14 (2008) 1310-1316.

[131] Q.A. Pankhurst, J. Connolly, S.K. Jones, J. Dobson, Journal of Physics D: Applied Physics, 36 (2003) R167.

[132] Y. Hayashi, T. Miclaus, C. Scavenius, K. Kwiatkowska, A. Sobota, P. Engelmann, J.J. Scott-Fordsmand, J.J. Enghild, D.S. Sutherland, Environmental Science & Technology, 47 (2013) 14367-14375.

[133] M.N. Ragnaill, M. Brown, D. Ye, M. Bramini, S. Callanan, I. Lynch, K.A. Dawson, European Journal of Pharmaceutics and Biopharmaceutics, 77 (2011) 360-367.

[134] D. Pozzi, V. Colapicchioni, G. Caracciolo, S. Piovesana, A.L. Capriotti, S. Palchetti, S. De Grossi, A. Riccioli, H. Amenitsch, A. Lagana, Nanoscale, 6 (2014) 2782-2792.

[135] B. Fadeel, A.E. Garcia-Bennett, Advanced Drug Delivery Reviews, 62 (2010) 362-374.

[136] A. Kunzmann, B. Andersson, T. Thurnherr, H. Krug, A. Scheynius, B. Fadeel, Biochimica et Biophysica Acta (BBA) - General Subjects, 1810 (2011) 361-373.

[137] M.A. Towler, C.G. Clapp, W. McGregor, R.F. Morgan, R.F. Edlich, Journal of Applied Biomaterials, 2 (1991) 183-186.

[138] I. Lynch, K.A. Dawson, Nano Today, 3 (2008) 40-47.

[139] J. Klein, Proceedings of the National Academy of Sciences, 104 (2007) 2029-2030.

[140] A.E. Nel, L. Madler, D. Velegol, T. Xia, E.M.V. Hoek, P. Somasundaran, F. Klaessig, V. Castranova, M. Thompson, Nat Mater, 8 (2009) 543-557.

[141] T. Cedervall, I. Lynch, M. Foy, T. Berggård, S.C. Donnelly, G. Cagney, S. Linse, K.A. Dawson, Angewandte Chemie International Edition, 46 (2007) 5754-5756.

[142] B.D. Chithrani, A.A. Ghazani, W.C.W. Chan, Nano Letters, 6 (2006) 662-668.

[143] Arnida, A. Malugin, H. Ghandehari, Journal of Applied Toxicology, 30 (2010) 212-217.

[144] L. Yildirimer, N.T.K. Thanh, M. Loizidou, A.M. Seifalian, Nano Today, 6 (2011) 585-607.

[145] J.H. Lee, J.E. Ju, B.I. Kim, P.J. Pak, E.-K. Choi, H.-S. Lee, N. Chung, Environmental Toxicology and Chemistry, 33 (2014) 2759-2766.

[146] S.H.D.P. Lacerda, J.J. Park, C. Meuse, D. Pristinski, M.L. Becker, A. Karim, J.F. Douglas, ACS Nano, 4 (2010) 365-379.

[147] T. Cedervall, I. Lynch, S. Lindman, T. Berggård, E. Thulin, H. Nilsson, K.A. Dawson, S. Linse, Proceedings of the National Academy of Sciences, 104 (2007) 2050-2055.

[148] B. Fadeel, N. Feliu, C. Vogt, A.M. Abdelmonem, W.J. Parak, Wiley Interdisciplinary Reviews: Nanomedicine and Nanobiotechnology, 5 (2013) 111-129.

[149] C.D. Walkey, W.C.W. Chan, Chemical Society Reviews, 41 (2012) 2780-2799.

[150] K. Dubey, B.G. Anand, R. Badhwar, G. Bagler, P.N. Navya, H.K. Daima, K. Kar, Amino Acids, 47 (2015) 2551-2560.

[151] J.E. Kim, M. Lee, Biochemical and Biophysical Research Communications, 303 (2003) 576-579.

[152] S. Rocha, A.F. Thünemann, M.d.C. Pereira, M. Coelho, H. Möhwald, G. Brezesinski, Biophysical Chemistry, 137 (2008) 35-42.

[153] C. Cabaleiro-Lago, F. Quinlan-Pluck, I. Lynch, S. Lindman, A.M. Minogue, E. Thulin, D.M. Walsh, K.A. Dawson, S. Linse, Journal of the American Chemical Society, 130 (2008) 15437-15443.

[154] C. Cabaleiro-Lago, F. Quinlan-Pluck, I. Lynch, K.A. Dawson, S. Linse, ACS Chemical Neuroscience, 1 (2010) 279-287.

[155] H. Skaat, R. Chen, I. Grinberg, S. Margel, Biomacromolecules, 13 (2012) 2662-2670.

[156] C. Li, D. Li, G. Wan, J. Xu, W. Hou, Nanoscale Research Letters, 6 (2011) 440.

[157] D. Goia, E. Matijević, Colloids and Surfaces A: Physicochemical and Engineering Aspects, 146 (1999) 139-152.

[158] G. Mountrichas, S. Pispas, E.I. Kamitsos, The Journal of Physical Chemistry C, 118 (2014) 22754-22759.

[159] G. Muralidharan, L. Subramanian, S.K. Nallamuthu, V. Santhanam, S. Kumar, Industrial & Engineering Chemistry Research, 50 (2011) 8786-8791.

[160] R.G. Shimmin, A.B. Schoch, P.V. Braun, Langmuir, 20 (2004) 5613-5620.

[161] M. Zhu, B. Lei, F. Ren, P. Chen, Y. Shen, B. Guan, Y. Du, T. Li, M. Liu, Scientific Reports, 4 (2014) 5259.

[162] X. Ji, X. Song, J. Li, Y. Bai, W. Yang, X. Peng, Journal of the American Chemical Society, 129 (2007) 13939-13948.

[163] H. Zhang, J.-J. Xu, H.-Y. Chen, The Journal of Physical Chemistry C, 112 (2008) 13886-13892.

[164] S. Nishimura, D. Mott, A. Takagaki, S. Maenosono, K. Ebitani, Physical Chemistry Chemical Physics, 13 (2011) 9335-9343.

[165] N. Vigneshwaran, R.P. Nachane, R.H. Balasubramanya, P.V. Varadarajan, Carbohydrate Research, 341 (2006) 2012-2018.

[166] V.K. Sharma, R.A. Yngard, Y. Lin, Advances in Colloid and Interface Science, 145 (2009) 83-96.

[167] X. Jiang, W. Chen, C. Chen, S. Xiong, A. Yu, Nanoscale Res Lett, 6 (2010) 32.

[168] M.B. Kasture, P. Patel, A.A. Prabhune, C.V. Ramana, A.A. Kulkarni, B.L.V. Prasad, Journal of Chemical Sciences, 120 (2008) 515-520.

[169] E.G. Goh, X. Xu, P.G. McCormick, Scripta Materialia, 78–79 (2014) 49-52.

[170] R. Zamiri, A. Zakaria, H.A. Ahangar, M. Darroudi, A.K. Zak, G.P.C. Drummen, Journal of Alloys and Compounds, 516 (2012) 41-48.

[171] A. Becheri, M. Dürr, P. Lo Nostro, P. Baglioni, Journal of Nanoparticle Research, 10 (2008) 679-689.

[172] D. Shugar, Biochimica et Biophysica Acta, 8 (1952) 302-309.

[173] C.-C. You, O.R. Miranda, B. Gider, P.S. Ghosh, I.-B. Kim, B. Erdogan, S.A. Krovi, U.H.F. Bunz, V.M. Rotello, Nat Nano, 2 (2007) 318-323.

[174] J.-M. Nam, C.S. Thaxton, C.A. Mirkin, Science, 301 (2003) 1884.

[175] J. Jiang, G. Oberdörster, P. Biswas, Journal of Nanoparticle Research, 11 (2009) 77-89.

[176] S. Patil, A. Sandberg, E. Heckert, W. Self, S. Seal, Biomaterials, 28 (2007) 4600-4607.

[177] Y. Zhang, M. Yang, N.G. Portney, D. Cui, G. Budak, E. Ozbay, M. Ozkan, C.S. Ozkan, Biomedical Microdevices, 10 (2008) 321-328.

[178] G.D. Rose, A.R. Geselowitz, G.J. Lesser, R.H. Lee, M.H. Zehfus, Science, 229 (1985) 834-838.

[179] Z. Yan-Ling, P. Xian-Ming, Z. Jun-Mei, IUBMB Life, 44 (1998) 949-960.

[180] V. Vagenende, M.G.S. Yap, B.L. Trout, Biochemistry, 48 (2009) 11084-11096.

[181] E.Y. Chi, S. Krishnan, T.W. Randolph, J.F. Carpenter, Pharmaceutical Research, 20 (2003) 1325-1336.

[182] I. Gryczynski, W. Wiczk, M.L. Johnson, J.R. Lakowicz, Biophysical Chemistry, 32 (1988) 173-185.

[183] D.W. Piston, G.-J. Kremers, Trends in Biochemical Sciences, 32 (2007) 407-414.

[184] F.W.J. Teale, Biochemical Journal, 76 (1960) 381-388.

[185] A.K. Lala, P. Kaul, Journal of Biological Chemistry, 267 (1992) 19914-19918.

[186] V.I. Teichberg, N. Sharon, FEBS Letters, 7 (1970) 171-174.

[187] S. Chakraborti, T. Chatterjee, P. Joshi, A. Poddar, B. Bhattacharyya, S.P. Singh, V. Gupta, P. Chakrabarti, Langmuir, 26 (2010) 3506-3513.

[188] S. Chakraborti, S. Sarwar, P. Chakrabarti, The Journal of Physical Chemistry B, 117 (2013) 13397-13408.

[189] L. Shang, Y. Wang, J. Jiang, S. Dong, Langmuir, 23 (2007) 2714-2721.

[190] G. Holzwarth, P. Doty, Journal of the American Chemical Society, 87 (1965) 218-228.

[191] N.J. Greenfield, G.D. Fasman, Biochemistry, 8 (1969) 4108-4116.

[192] C. Wiedemann, P. Bellstedt, M. Görlach, Bioinformatics, 29 (2013) 1750-1757.

[193] P. Relkin, D.M. Mulvihill, Critical Reviews in Food Science and Nutrition, 36 (1996) 565-601.

[194] A. Fersht, Structure and Mechanism in Protein Science: A Guide to Enzyme Catalysis and Protein Folding, W. H. Freeman, 1999.

[195] N.J. Greenfield, Nature protocols, 1 (2006) 2527-2535.

[196] Y. Hiraoka, S. Sugai, International Journal of Peptide and Protein Research, 23 (1984) 535-542.

[197] G. Vanderheeren, I. Hanssens, Journal of Biological Chemistry, 269 (1994) 7090-7094.

[198] A. Blumlein, J.J. McManus, Biochimica et Biophysica Acta (BBA) - Proteins and Proteomics, 1834 (2013) 2064-2070.

[199] J.-Y. Chang, L. Li, FEBS Letters, 511 (2002) 73-78.

[200] M. Ikeguchi, K. Kuwajima, M. Mitani, S. Sugai, Biochemistry, 25 (1986) 6965-6972.

[201] K. Kuwajima, Y. Hiraoka, M. Ikeguchi, S. Sugai, Biochemistry, 24 (1985) 874-881.

[202] F. Ahmad, C.C. Bigelow, Journal of Biological Chemistry, 257 (1982) 12935-12938.

[203] R. Tomar, V.K. Dubey, M.V. Jagannadham, Biochimie, 91 (2009) 951-960.

[204] M. Biancalana, S. Koide, Biochimica et Biophysica Acta, 1804 (2010) 1405-1412.

[205] M. Groenning, Journal of Chemical Biology, 3 (2010) 1-18.

[206] V. Vetri, C. Canale, A. Relini, F. Librizzi, V. Militello, A. Gliozzi, M. Leone, Biophysical Chemistry, 125 (2007) 184-190.

[207] K.E. Marshall, K.L. Morris, D. Charlton, N. O'Reilly, L. Lewis, H. Walden, L.C. Serpell, Biochemistry, 50 (2011) 2061-2071.

[208] B. Raman, E. Chatani, M. Kihara, T. Ban, M. Sakai, K. Hasegawa, H. Naiki, C.M. Rao, Y. Goto, Biochemistry, 44 (2005) 1288-1299.

[209] S. Dominguez-Medina, L. Kisley, L.J. Tauzin, A. Hoggard, B. Shuang, A.S. D. S. Indrasekara, S. Chen, L.-Y. Wang, P.J. Derry, A. Liopo, E.R. Zubarev, C.F. Landes, S. Link, ACS Nano, 10 (2016) 2103-2112.

[210] S. Radic, T.P. Davis, P.C. Ke, F. Ding, RSC Advances, 5 (2015) 105489-105498.

[211] B. Moores, E. Drolle, S.J. Attwood, J. Simons, Z. Leonenko, PLoS ONE, 6 (2011) e25954.

[212] M. Zhu, P.O. Souillac, C. Ionescu-Zanetti, S.A. Carter, A.L. Fink, Journal of Biological Chemistry, 277 (2002) 50914-50922.

[213] H. Du, P. Chandaroy, S.W. Hui, Biochimica et Biophysica Acta (BBA) - Biomembranes, 1326 (1997) 236-248.

[214] J.L. Perry, K.G. Reuter, M.P. Kai, K.P. Herlihy, S.W. Jones, J.C. Luft, M. Napier, J.E. Bear, J.M. DeSimone, Nano Letters, 12 (2012) 5304-5310.

[215] A.L. Gharibyan, V. Zamotin, K. Yanamandra, O.S. Moskaleva, B.A. Margulis, I.A. Kostanyan, L.A. Morozova-Roche, Journal of Molecular Biology, 365 (2007) 1337-1349.

[216] H. Kadowaki, H. Nishitoh, F. Urano, C. Sadamitsu, A. Matsuzawa, K. Takeda, H. Masutani, J. Yodoi, Y. Urano, T. Nagano, H. Ichijo, Cell Death Differ, 12 (2005) 19-24.

[217] J. Bieschke, J. Russ, R.P. Friedrich, D.E. Ehrnhoefer, H. Wobst, K. Neugebauer, E.E. Wanker, Proceedings of the National Academy of Sciences, 107 (2010) 7710-7715.

[218] B. Mannini, E. Mulvihill, C. Sgromo, R. Cascella, R. Khodarahmi, M. Ramazzotti, C.M. Dobson, C. Cecchi, F. Chiti, ACS Chemical Biology, 9 (2014) 2309-2317.

[219] T.L. Riss, R. Moravec, A. Niles, H. Benink, T. Worzella, L. Minor, (2004).

[220] C. Galvagnion, A.K. Buell, G. Meisl, T.C.T. Michaels, M. Vendruscolo, T.P.J. Knowles, C.M. Dobson, Nat Chem Biol, 11 (2015) 229-234.

[221] L.H. Russell, E. Mazzio, R.B. Badisa, Z.-P. Zhu, M. Agharahimi, E.T. Oriaku, C.B. Goodman, Anticancer Research, 32 (2012) 1595-1602.

CURRICULUM VITAE

DEEPENDRA KUMAR BAN
Research Scholar,
Structural Biology and Nanomedicine Laboratory,
Department of Biotechnology and Medical Engineering,
National Institute of Technology, Rourkela,
Rourkela-769008, Odisha, India.
Email: deependrakban29@gmail.com,
deependrakban@yahoo.com
Contact: +91-9778550704(M)

RESEARCH EXPERIENCE

Jan 2011-	**Doctoral Research**
July 2016	**Interaction of metal-based nanoparticles with proteins: Relation to structure, function and amyloid forming propensity of lysozyme and α-lactalbumin.** (*Supervisors: Prof. Subhankar Paul and Co-Supervisor: Prof. Swadesh Kumar Pratihar, N.I.T, Rourkela, India.*) (Thesis submitted)
Apr 2009 –	**Master's Research**
Mar 2010	**Purification and characterization of sucrase from *Termitomyces clypeatus* in aggregation with cellobioase.** (*Supervisor: Dr. Suman Khowala, Indian Institute of Chemical Biology (CSIR), Kolkata, India.*)
June 2009-	**Master's Short Term Research**
May 2010	**Optimization of solid-state fermentation of citric acid production by utilizing Sugarcane Baggase.** (*Supervisor: Dr. Hironmay Gongopadhyay, Jadavpur University, Kolkata, India.*)
June 2007-	**Bachelor's Research**
May 2008	**Study the Cellulose Decomposition by Fungus *Chaetomium globosum*** (*Supervisor: **Mr. Ajai Singh,** College of Biotechnology and Allied Sciences (Allahabad Agricultural Institute-Deemed University, Allahabad, India*)

EDUCATION

2011-2016 **Ph.D.**

Department of Biotechnology and Medical Engineering, NIT Rourkela, India; CGPA: 8.8.

2008-2010 **M. Tech (Master of Technology)**

Department of Food Technology & Biochemical Engineering, Jadavpur University, Kolkata, India; CGPA: 8.11

2004-2008 **B. Tech (Bachelor of Technology)**

Department of Biotechnology, Allahabad Agricultural Institute- Deemed University, Allahabad, India; SGPA: 8.9

TECHNICAL SKILL

1. **Biophysical Techniques** such as Circular Dichroism Spectroscopy, Fluorescence Spectroscopy, FTIR.
2. **Nanomaterial characterization techniques** such as UV-Vis, DSC/TGA, dynamic light scattering and zeta potential analysis, X-ray diffraction analysis, electron microscopy (FESEM and TEM), atomic force microscopy (AFM).
3. **Molecular technique** like DNA, RNA, and protein extraction, purification, and estimation, Chromatographic techniques like HPLC, FPLC, SDS-PAGE, Native-PAGE.
4. **Cell Culture Techniques:** microbial culture such as bacteria e.g. *E. coli*, *B. subtilis* etc. and fungus e.g. *Termitomyces clypeatus*, *Aspergillus niger*, *saccharomyces cerevisiae* and animal cell culture such as N2a (mice neuroblastoma), HaCaT (human Keratinocyte). Cell viability and ROS based death analysis.

PUBLICATIONS

1. **Ban, D. K.,** Paul S (2016) " Nano Zinc Oxide Inhibits Fibrillar Growth and Suppresses Cellular Toxicity of Lysozyme Amyloid." **ACS Applied Materials and Interface,** 31587–31601. **(Impact Factor 7.1)**
2. **Ban, D. K.** and Paul, S (2016). "Protein corona over silver nanoparticles triggers conformational change of proteins and drop in bactericidal potential of nanoparticles: Polyethylene glycol capping as preventive strategy." **Colloidal and Surface-B: Bio-interface**, 146: 577–584. **(Impact Factor 4.2)**

3. **Ban, D. K**., Pratihar S. K. and Paul, S (2015). "Controlled modification of starch in the synthesis of gold nanoparticles with tunable optical properties and their application in heavy metal sensing." **RSC Advances**, 5(99): 81554-81564. **(Impact Factor 3.2)**
4. **Ban, D. K.,** Pratihar S. K. and Paul, S (2015). "An investigation of optical properties of zinc oxide nanoparticle synthesized by starch mediated assembly and its application in photocatalytic bleaching of methyl green and rhodamine-B." **Materials Science in Semiconductor Processing**, 39: 691-701. **(Impact Factor 2.2)**
5. **Ban, D. K.** and Paul, S (2014). "Zinc Oxide Nanoparticles Modulates the Production of β-Glucosidase and Protects its Functional State Under Alcoholic Condition in Saccharomyces cerevisiae." **Applied Biochemistry and Biotechnology,** 173(1): 155-166. **(Impact Factor 1.6)**
6. Karmakar, R., **Ban, D. K**. and Ghosh, U. (2014) Comparative study of native and modified starches isolated from conventional and nonconventional sources. **International Food Research Journal**; 21(2), 597-602.
7. Karmakar, R, Mondal, T, Saha, B, **Ban, D. K**, Dey, B, Ghosh Dastidar, P. and Goswami, R. **(2011)** Arsenic induced Biochemical perturbation in Swiss Albino Mice and Cytoprotective activities of Curcumin. **International Journal of Environmental Sciences**; 2(1), 240-248.
8. Karmakar, R., **Ban, D. K.,** Ali, S. W. and Ghosh, A. K. **(2011)** Production and characterization of thermostable α-amylase by microorganisms isolated from the soil in Kolkata. **Indian Science Cruiser**; 25(1): 16-20**.** (Only printed version available).

Manuscript under preparation

9. **Ban, D. K.,** Paul S. " Gold and silver nanoparticles capping and its effects on the amyloid forming propensity of Hen egg white lysozyme and cellular toxicity.
10. **Ban, D. K.,** Paul S " Effect of metal-based nanoparticles in structure, function, and folding of model proteins."
11. **Ban, D. K.,** Paul S " Silver nanoparticle synthesis, characterization, and its application in sensing."

CONFERENCE PROCEEDINGS

1. Paul, S and **Ban, D. K.** (2014), "Synthesis and Characterization of Zinc oxide nanoparticle and its application in Biotechnology" **ICBEE conference-2014**, Bangkok.
2. **Ban, D. K.,** and Paul S. (2012), "Synthesis and application of silver nanoparticle" **International Symposium on protein folding and dynamics**, 15-17th October 2012, organized by National Center for biological sciences, TIFR Bangalore, India.

3. Karmakar, R and **Ban, D. K.** (2011). Fermentative production and characterization of methionine by bacteria isolated from soil. **98th Indian Science Congress;** Section of new biology, 3-7th January 2011, Chennai, India.
4. **Ban D. K.,** Gangopadhyay H. (2010). Spicy Medicine: Study the Potential of Spices as Alternative Medicine, Abstract No: BT-17, Proceeding of **West Bengal State Science & Technology Congress**, 4th – 5th March 2010, Kolkata, India.
5. **Ban D. K.,** Gangopadhyay H. (2010). Application of spices as food preservative**,** Abstract No: 28 Proceedings of the UGC-Sponsored National Level Symposium on "**Recent Trends in Microbiological Research**" 13th-14th February, 2010, Kolkata, India.
6. **Ban, D. K**., Bhattacharjee, P. (2010). Design of fruit snacks for the Indian market, **International conference on Food Technology: Edition II;** October 2010, Thanjavur, Tamil Nadu, India.
7. **Ban, D. K.** (2005) 'Edible Vaccine' in Biotech. A Seminar, 'BIO-CON-2005' at Sai College of Medical Science & Technology, Kanpur, India (Jan-2005) (Poster presentation).

TRAINING/WORKSHOPS

1. **Short-term course on Scattering Techniques for material characterization (SDTMC2012),** 10-15th December 2012, Department of Physics, NIT Rourkela, India.
2. **SERB school on 'Introduction to system and synthetic biology for scientists and engineers'**, April 30-May 3, 2012, organized by IIT Bombay, India.
3. **Certificate course on nanotechnology,** 11-15th May-2011, organized by University Department of Chemical Technology, North Maharashtra University, Jalgaon, India.
4. **'Training Program on Laboratory Safety: Radiation Safety, Chemical Safety and Bio-Safety',** 7th September 2009, organized by Indian Institute of Chemical Biology (CSIR), Kolkata, India.
5. **Undergraduate training program on "clinical pathology and allied techniques",** June-July-2007, Apollo Clinic, Allahabad, Uttar Pradesh, India.
6. **Advance Diploma course in "Molecular Biology and Genetic Engineering",** July-2006 at Sangene Institute of biosciences, Bangalore, Karnataka, India.

FELLOWSHIP, AWARDS, AND HONORS

1. NIT Rourkela Institute Ph.D. Research Fellowship from Ministry of Human Resource Development, Government of India (January 2011-present).
2. Qualified Graduate Aptitude Test in Engineering (GATE) (2008) with 97.46 percentile, Organized by all IITs and Indian Institute of Sciences, Bangalore and got a fellowship for M. Tech study.

3. Travelling grant by IIT Bombay for participating in workshop “SERB school on ‘Introduction to system and synthetic biology for scientists and engineers”, April 30-May 3, 2012.
4. Travelling grant by National Center for biological sciences, TIFR Bangalore, India to participate in International symposium on protein folding and dynamics, 15-17th October 2012.
5. Certificate from Indian Association of Physics teachers and selected as top 10% student appear for the exam from School V.P.I.C, Kanpur, Uttar Pradesh
6. Cleared a Unified Scholarship Exam and National fellowship for talented student and awarded Fellowship up to class 12th.

REFERENCES

---

1. Dr. Subhankar Paul, Associate Professor,

Department of Biotechnology and Medical Engineering, N.I.T, Rourkela-769008, Odisha, India., email: spaul@nitrkl.ac.in

2. Dr. Swadesh Kumar Pratihar, Associate Professor

Department of Ceramic Engineering, N.I.T, Rourkela-769008, Odisha, India

email: skpratihar@nitrkl.ac.in

3. Dr. Mukesh Kumar Gupta, Associate Professor

Department of Biotechnology and Medical Engineering, N.I.T, Rourkela-769008, Odisha, India., email: guptam@nitrkl.ac.in

Place: Rourkela Deependra Kumar Ban

Date: 28/12/2016